

# Novel Whiffing-Inspired Gapped Wings as Control Surfaces

by

Piper Sigrest

A dissertation submitted in partial fulfillment  
of the requirements for the degree of  
Doctor of Philosophy  
(Aerospace Engineering)  
in The University of Michigan  
2023

Doctoral Committee:

Professor Daniel J. Inman, Chair  
Professor Diann Brei  
Professor Joaquim R. R. A. Martins  
Assistant Professor Gökçin Çınar

Despite its public claims of being a leader in Diversity, Equity, and Inclusion, the Rackham Graduate School does not currently allow students to include their pronouns on the title and identifier pages of their dissertations. This practice is outdated and transphobic. Due to a lack of support from Rackham itself, I reached out to the Spectrum Center for help. The Spectrum Center is currently advocating to remedy this critical issue. In the meantime, I have included my pronouns here, as they deserved to appear on the title page:

*they/them*



Piper Sigrest

psigrest@umich.edu

ORCID iD: 0000-0003-1688-8676

© Piper Sigrest 2023

To those who love me for me, and to my trans siblings who continue to pave the way:  
may you live authentically, joyfully, and intentionally.

## ACKNOWLEDGEMENTS

This dissertation is the culmination of years of learning, frustration, and discovery. In addition to the challenges of grad school, it was during these five years that I realized my transgender identity. Transitioning while earning my PhD was probably the hardest thing I've ever done—and also the most rewarding. I'm grateful to everyone who stood by my side, showed me kindness and respect, and loved me for me. I am proud beyond compare to present this dissertation wholly as myself.

Firstly, thank you to my advisor, Dr. Inman, for his continued encouragement, perspective, patience, and understanding. You were a true mentor and guide to me on this journey. By being yourself, you drew incredible people to the AIMS Lab, and gave me a safe space to learn and grow as both a researcher and a person.

Naturally, it was the people who made the AIMS Lab amazing. I could not have done this without my life-long friends and labmates. Special thanks to Christina, Kevin, Greta, Lawren, Krystal, Lori, and Kayc for learning and laughing with me. I'm grateful for your mentorship and friendship, and I cannot imagine grad school without you all. A part of me will always be AIMS-less in Ann Arbor!

To my incredible siblings—especially Dell and Nor—thank you for your unconditional love and support. I love you all so much, and am so grateful to have you by my side. Della, you're my best friend. You carried me through the lows and celebrated the highs with me. I can always count on you to remind me to sharpen my tool, and call me on my B.S. I can't wait to be back in the same city as you! Eleanor, it's brought me so much joy to grow closer to you, and watch you blossom on your own journey. You always help me laugh when the chips were down. Your nine-year-old words shall always be wisened.

Hugs and love to my chosen family and friends. Lizzy, you first helped me to be brave and come to Michigan. Katey and Rose, you made Michigan my home. Cara, AJ, Audrey, and Ana, you kept me smiling through all the hard times! Andrew, Isabel, Faith, Maria—I appreciate your support no matter the distance, through long phone calls and impromptu visits. To my Aero friends, especially Marco, Neil, Leanne, Elliot, and Hannah, thanks for putting up with my constant muttering, and commiserating over Reviewer #2! Zooey, Elle, Oliver, Stevie, Nika, Dottie, Sophia, and my whole queer community—thank you for always cheering me on. To my mentors Indra, Rob, and Sarah, I’m so grateful to have you in my corner, and for your confidence in me.

I would be remiss not to acknowledge the talented medical teams that made my transition possible. Thank you for changing the lives of trans people like myself for the better. Della, Sures, Nor, and Cara, special thanks for taking care of me emotionally and physically as I prepared and recovered from my surgeries. I could not have done it without you!

I’d also like to thank several Aero staff members who always went the extra mile. Ruthie, Shani, and Tanner, you were pivotal parts of my grad school experience. You always had my back, from managing difficult logistics to just being a listening ear. Chris, Terry, Tom, Dave, and the Tech Center staff were so supportive and kind, from setting up wind tunnel lifting mechanisms to machining a finicky part.

Further thanks to the faculty and staff in the CREES department, especially Liz, Charlie, Prof. Von Moltke, and Prof. Paloff. From day one, you made me feel so welcome in the department. You gave me a much needed creative outlet, and the support I needed to concurrently earn my certificate in Russian Studies.

Special shout-out to Dozer Coffee, my go-to thesis writing destination, and a place where I always felt safe to be myself.

Finally, to JRK, my other half. I love you, buddy.

This dissertation is based upon work supported by the US Air Force Office of Scientific Research under grant number FA9550-16-1-0087 “Avian-Inspired Multifunctional Morphing Vehicles” and grant number FA9550-21-1-0325 “Towards Neural Control for Fly-by-Feel Morphing”, both monitored by Dr. B.L. Lee. Support was also provided by the National Science Foundation (NSF) under Grant No. EFRI C3 SoRo 1935216 and the NSF Graduate Research Fellowship Program under Grant No. DGE 1256260. Any opinions, findings, and conclusions or recommendations expressed in this material are those of the author and do not necessarily reflect the views of the National Science Foundation.

# TABLE OF CONTENTS

DEDICATION . . . . .	ii
ACKNOWLEDGEMENTS . . . . .	iii
LIST OF FIGURES . . . . .	ix
LIST OF TABLES . . . . .	xvi
LIST OF APPENDICES . . . . .	xvii
LIST OF ABBREVIATIONS . . . . .	xviii
LIST OF SYMBOLS . . . . .	xix
ABSTRACT . . . . .	xxvii
<b>CHAPTER</b>	
<b>I. Introduction . . . . .</b>	<b>1</b>
1.1 Bioinspiration . . . . .	1
1.2 Avian whiffing . . . . .	2
1.3 The whiffing-inspired gapped wing . . . . .	4
1.4 Novelty and significance of gapped wings . . . . .	7
<b>II. A Gapped Wing Created Roll at High Lift Coefficients . . . . .</b>	<b>9</b>
2.1 Overview . . . . .	9
2.2 Motivation and background . . . . .	10
2.3 Methods . . . . .	10
2.3.1 Experimental setup for gapped wings . . . . .	10
2.3.2 Data analysis . . . . .	14
2.3.3 Gapped wing actuation work estimates . . . . .	16
2.3.4 Representative spoiler . . . . .	17
2.3.5 Representative aileron . . . . .	21
2.4 Results and discussion . . . . .	22

2.4.1	Gaps decreased lift with insignificant drag change . . . . .	23
2.4.2	Gapped wings were less effective than spoiler for descent . . . . .	25
2.4.3	Nine-gap wing outperformed aileron at high angles . . . . .	29
2.5	Limitations . . . . .	35
2.6	Chapter summary . . . . .	36
2.7	Data availability . . . . .	37
<b>III.</b>	<b>Gaps Re-Energized the Boundary Layer and Required Less Work Than Single Aileron for Large Rolling Moments . . . . .</b>	<b>38</b>
3.1	Overview . . . . .	38
3.2	Motivation and background . . . . .	39
3.3	Methods . . . . .	40
3.3.1	SI-gapped wing experimental validation . . . . .	43
3.3.2	JH-aileron wing experimental validation . . . . .	45
3.3.3	SI-aileron wing for direct comparison . . . . .	46
3.3.4	General comments on work estimates . . . . .	47
3.4	Mesh convergence study . . . . .	47
3.5	Experimental validation . . . . .	49
3.6	Results and discussion . . . . .	52
3.6.1	Gaps affected the flow field over the wing . . . . .	52
3.6.2	Flow within a gap informed actuation requirements . . . . .	54
3.6.3	Gaps required less work than single aileron at high roll . . . . .	59
3.7	Chapter summary . . . . .	64
3.8	Data availability . . . . .	65
<b>IV.</b>	<b>A Gapped Wing was Less Effective for Roll Than Two Ailerons . . . . .</b>	<b>66</b>
4.1	Overview . . . . .	66
4.2	Motivation and background . . . . .	67
4.3	Methods . . . . .	67
4.3.1	Simulation setup . . . . .	67
4.3.2	CFD-based work estimate of JH-gapped wing . . . . .	70
4.3.3	Semi-empirical two-aileron JH-wing . . . . .	71
4.4	Validating the two-aileron JH-wing simulations . . . . .	72
4.5	Two ailerons produced more roll than gapped wing . . . . .	74
4.6	Gapped wing offered some drag and yaw benefits . . . . .	75
4.7	Chapter summary . . . . .	79
4.8	Data availability . . . . .	80
<b>V.</b>	<b>Refining Gap Dimensions Could Maximize Roll per Work . . . . .</b>	<b>81</b>
5.1	Overview . . . . .	81
5.2	Motivation and background . . . . .	82
5.3	Methods . . . . .	83

5.3.1	Conducting the parameter sweep . . . . .	83
5.3.2	Building the linear models . . . . .	85
5.4	Effects on rolling moment coefficient . . . . .	87
5.5	Effects on actuation work . . . . .	90
5.6	Gap configuration could be designed to maximize normalized roll . . . . .	94
5.7	Linear model validation . . . . .	96
5.8	Gaps could be gradually actuated for smooth roll control . . . . .	97
5.9	Chapter summary . . . . .	99
5.10	Data availability . . . . .	100
<b>VI.</b>	<b>Gapped Wings Altered Trim and Alleviated Gusts . . . . .</b>	<b>101</b>
6.1	Overview . . . . .	101
6.2	Motivation and background . . . . .	102
6.3	Methods . . . . .	102
6.3.1	Modelling the equations of motion . . . . .	102
6.3.2	Defining the trim state . . . . .	106
6.3.3	Characterizing the free response . . . . .	107
6.3.4	Defining the gust profile . . . . .	107
6.3.5	Modelling the aircraft . . . . .	109
6.4	Results and discussion . . . . .	121
6.4.1	Gaps shifted the aerodynamic center forward . . . . .	122
6.4.2	Gapped wings steepened glide, increased velocity at trim . . . . .	122
6.4.3	Natural modes were generally benefited by gaps . . . . .	124
6.4.4	Gapped wings improved aircrafts' gust responses . . . . .	129
6.5	Chapter summary . . . . .	132
6.6	Data availability . . . . .	133
<b>VII.</b>	<b>Conclusion . . . . .</b>	<b>134</b>
7.1	Summary of results and impact . . . . .	135
7.1.1	A gapped wing created roll at high lift coefficients . . . . .	135
7.1.2	Gaps reenergized flow and produced high rolling moment coefficients . . . . .	135
7.1.3	A gapped wing produced less roll than two ailerons, but favorable yaw in some cases . . . . .	136
7.1.4	Gap dimensions could be optimized for roll per work . . . . .	136
7.1.5	Gapped wings effectively altered trim and mitigated gusts . . . . .	137
7.2	Limitations of the gapped wings . . . . .	138
7.3	Future work . . . . .	138
<b>APPENDICES</b>	<b>. . . . .</b>	<b>141</b>
<b>BIBLIOGRAPHY</b>	<b>. . . . .</b>	<b>188</b>



## LIST OF FIGURES

### Figure

1.1	Birds whiffle to lose altitude, move laterally, and respond to gusts. Airflow through gaps between primary flight feathers likely causes aerodynamic changes such as decreased lift. To whiffle, the bird flies inverted and the resulting airflow twists the primary flight feathers open, creating gaps in the trailing edge. . . . .	3
1.2	Visual comparison of (A) gaps due to feather rotation on a whiffing bird wing and (B) whiffing-inspired gaps on a UAV wing. . . . .	5
2.1	Fully assembled five-gap wing with end plates and mounting rod. . . . .	11
2.2	Wind tunnel setup. PT is the pressure transducer, LC the load cell, T the thermocouple, and P the pitot tube. The wing is a right semi-span. Moments were taken about the yellow point $O$ at the quarter-chord of the wing root. Data were reported in the wind axes [59]. . . . .	13
2.3	Isometric cross-section view of a gapped wing in two configurations, with the gap covers shown in light blue. (A) Gaps open. (B) Gaps closed. . . . .	16
2.4	Geometry of Sun’s representative spoiler on a wing of chord $c$ (in m) [63]. $\delta_{s,0}$ is the spoiler angle when undeflected and flush against the airfoil (rad). $\delta_s$ is the deflection angle of the spoiler (rad), with upwards deflection negative. $c_s$ is the chord of the spoiler (as a fraction of wing chord). $x_{cg,s}$ is the location of the spoiler’s center of gravity along its length, with respect to its hinge line (m). . . . .	18
2.5	Gaps significantly decreased lift but generally did not impact drag. (A) Lift coefficient. The dotted vertical lines indicate the stall angle of attack. (B) Drag coefficient. Statistically significant data are marked with $\odot$ and insignificant data are marked with $\cdot$ (Appendix C). The transparent ribbons show the expanded uncertainty at an approximately 95% level of confidence. . . . .	24
2.6	Gaps do not decrease lift as much as a spoiler and negligibly impact drag. (A) Incremental lift coefficient. (B) Incremental drag coefficient. Dotted lines show the equivalent spoiler deflections [63]. Statistically significant data are marked with $\odot$ and insignificant data are marked with $\cdot$ (Appendix C). The transparent ribbons show the expanded uncertainty at approximately 95% level of confidence. . . . .	26

2.7	The gapped wings were not suitable for rapid descent. (A) The gapped wings produced decreases in lift coefficient equivalent to very low spoiler deflection angles. (B) The gapped wings also did not increase drag as much as the equivalent spoilers. Finally, the gapped wings (C) required less force but (D) required more work than the equivalent spoilers. . . . .	28
2.8	Gaps produced comparable roll and less yaw than an aileron [2]. (A) Rolling moment coefficient. (B) Yawing moment coefficient. Dotted lines are various aileron deflection angles [2]. Statistically significant data are marked with $\odot$ and insignificant data are marked with $\cdot$ (Appendix C). The transparent ribbons show expanded uncertainties at an approximately 95% level of confidence. . . . .	30
2.9	Gaps were effective for roll control in some cases. (A) Maximum rolling moment coefficient of each gapped wing and equivalent aileron (equal by design). (B) Yawing moment coefficient. (C) Required actuation force (N). (D) Required actuation work (mJ). The percent decreases in force and work of the gapped wing compared to the aileron are below each pair. . . . .	34
3.1	Using STAR-CCM+, we created unstructured polyhedral meshes with prism layers. (A) Cross-section of the volume mesh for the SI-gapped wing. (B) Detailed view of the volume mesh cross-section. (C) Surface mesh on the wing. Data were reported in wind axes [19] with a positive rolling moment as shown. (D) Detailed view of the surface mesh near the gaps. . . . .	43
3.2	The gapped wing actuation work was based on a model with gap covers (dark brown) that slid spanwise to open and close the gaps. (A) Gaps closed. (B) Gaps open. (C) Cross-section of a gap. Force was measured on the full gap face (light blue) in the spanwise direction. The gap cover face (dark brown) was used to analytically estimate the work. . . . .	45
3.3	We performed a mesh convergence study on the SI-gapped wing to determine an appropriate mesh density for each wing configuration. We investigated (A) rolling moment coefficient and (B) lift coefficient, both at $3^\circ$ angle of attack. . . . .	48
3.4	The SI-gapped wing CFD results agreed well with previous experimental data from Chapter II, considering the (A) lift, (B) rolling moment, and (C) drag coefficient. The data point at $12^\circ$ angle of attack was partially converged, likely indicating stall. The grey transparent ribbon around the experimental data represents the uncertainty at an approximately 95% confidence level. . . . .	50
3.5	The JH-aileron wing CFD results agreed well with previous experimental data [2], comparing the (A) rolling moment and (B) hinge moment coefficient at $10^\circ$ angle of attack. Negative deflection angles are upwards. . . . .	51
3.6	The gaps affected the thickness and velocity of the local boundary layer at $10^\circ$ angle of attack, indicating re-energization of the boundary layer. The SI-gapped wing is shown without endplates for visual clarity. Velocities over a baseline wing section are shown at the wing root. Velocities are also plotted 0.0254 mm inboard of the central gap's root face. . . . .	53

3.7	Each gap created a pair of strong vortices, similar to those produced by an aileron. The gap vortex nearest the wing root extended farthest downstream. (A) iso-surface of the SI-gapped wing with a Q-criterion of $1 \text{ s}^{-2}$ . (B) SI-gapped wing with a Q-criterion of $50 \text{ s}^{-2}$ . (C) SI-aileron wing with a Q-criterion of $1 \text{ s}^{-2}$ . (D) SI-aileron wing with a Q-criterion of $50 \text{ s}^{-2}$ . Both wings are at $2^\circ$ angle of attack and the aileron is deflected $-15.3^\circ$ . . . . .	55
3.8	Streamwise flow through the gap recirculated then exited over the suction side at the trailing edge. (A) Velocity field at $2^\circ$ angle of attack. (B) Velocity field at $10^\circ$ . (C) Due to the consistent spanwise pressure distribution, data from the central gap was used. Velocity data were from the blue plane with its normal along the $y$ -axis and positioned in the middle of the gap to avoid boundary layers. . . . .	56
3.9	The flow within a gap was largely streamwise. (A) Velocity field at $2^\circ$ angle of attack. (B) Pressure contours at $2^\circ$ angle of attack, and pressure coefficients along the dotted white chord line. (C) Velocity field at $10^\circ$ angle of attack. (D) Pressure contours at $10^\circ$ angle of attack. (E) We used data from the central gap: pressure contours from the gap's root face and velocity from the blue plane with a $z$ -axis normal and origin on the chord line. . . . .	57
3.10	The flow over the aileron featured large pressure spikes and positive hinge moments that increased as deflection angle increased. (A) Velocity field over the $-4.7^\circ$ deflected aileron at $2^\circ$ angle of attack. (B) Corresponding pressure coefficient plot. (C) Velocity field over the $-15.3^\circ$ deflected aileron at $2^\circ$ angle of attack. (D) Corresponding pressure coefficient plot. (E) Data were taken at the midspan of the aileron. . . . .	59
3.11	The SI-gapped wing required less work than the SI-aileron wing to produce rolling moment coefficients above 0.0182, and produced a higher maximum coefficient. The aileron was simulated at $2^\circ$ angle of attack and deflection angles from $0^\circ$ to $-30^\circ$ , and the gapped wing was simulated across angles of attack from $0^\circ$ to $12^\circ$ . Grey data points were stalled and "x" indicates partial convergence. The SI-gapped wing values depended on the area ratio $R$ . . . . .	61
4.1	The three-dimensional mesh for the JH-gapped wing was created using STAR-CCM's built-in tools. (A) Surface mesh over the JH-gapped wing, with a detail view of the gaps and wingtip. (B) Cross-section of the bullet-shaped domain. The detail view shows prism layers over a gap. . . . .	69
4.2	Sample residual convergence plot of the JH-gapped wing at $2^\circ$ angle of attack.	70
4.3	The JH-gapped wing was modelled with gap covers (yellow) that slid along the wing span to (A) open the gaps (B) and close them. (C) The force used to estimate actuation work was calculated on the red gap face. (D) $R$ was calculated using the green gap cover area (Eqn. 3.1). . . . .	71
4.4	CFD simulations of the two-aileron JH-wing agreed well with semi-empirical estimates of the (A) rolling moment coefficient and (B) yawing moment coefficient across aileron deflection magnitude, and (C) work versus rolling moment coefficient at several angles of attack. In the legend, (JH) indicates semi-empirical estimates based on single-aileron data [2]. . . . .	73

4.5	(A) The JH-gapped wing required more work than the two-aileron JH-wing at low rolling moment coefficients. At its higher coefficients, the gapped wing required comparable work to the ailerons at $10^\circ$ angle of attack. (B) Detail view. . . . .	76
4.6	The JH-gapped wing provided some drag and yaw benefits over the two-aileron JH wing. (A) The two aileron wing produced adverse yaw across all rolling moment coefficients, while the JH-gapped wing produced favorable yaw at low rolling moment coefficients. (B) The JH-gapped wing produced less drag than the two-aileron wing at $10^\circ$ angle of attack for low rolling moment coefficients. . . . .	77
5.1	A range of gap widths and gap lengths were simulated, resulting in various gap aspect ratios. The initial gaps were $\frac{2c}{3}$ long and $\frac{b}{48}$ wide (Chapters II and III). . . . .	84
5.2	Each gap dimension was tested on (A) a wing with nine gaps and (B) a wing with five outboard gaps. (C) A two-gap wing with $\frac{2c}{3} \times \frac{b}{5}$ gaps was also simulated. Parts (A) and (B) show wings with $\frac{2c}{3} \times \frac{b}{48}$ gaps for illustrative purposes. . . . .	85
5.3	Rolling moment coefficient increased as gap length and gap width increased. Five- and nine-gap wings with various gap lengths and widths were simulated at $0^\circ$ , $2^\circ$ , $7^\circ$ , and $10^\circ$ angle of attack. . . . .	88
5.4	Gap cover work increased as gap length and gap width increased. Each gap configuration was simulated at $0^\circ$ , $2^\circ$ , $7^\circ$ , and $10^\circ$ angle of attack on five- and nine-gap wings. . . . .	91
5.5	Normalized roll increased as gap length and width increased. Wings were simulated at $2^\circ$ , $7^\circ$ , and $10^\circ$ angle of attack on five- and nine-gap wings. Wings at $0^\circ$ angle of attack produced negligible roll and were excluded. . .	95
5.6	(A) The linear model for the rolling moment of the five- and nine-gap wings fit with higher residuals at higher angles of attack. (B) The linear model for the actuation work of the five- and nine-gap wings fit very accurately. . . .	98
6.1	The aircraft consisted of a wing, tail, and a stringer fuselage. The wing and tail were mounted by their respective centers of gravity at incidence angles $i^{wing}$ and $i^{tail}$ . In trim, the aircraft glided at an angle $\gamma_0$ below the local horizon with velocity $U_0$ . The longitudinal axis of the fuselage was at an angle of attack $\alpha_0$ with respect to the velocity vector. The weight of the aircraft $mg$ acted down towards the center of the Earth. The body axes, denoted by the subscript $b$ , were respective to the aircraft longitudinal axis. The stability axes, denoted with the subscript $s$ , were taken with respect to the velocity vector. . . . .	110
6.2	Gaps generally decreased the wing's pitching moment coefficient about the aircraft's center of gravity ( $C_{MCG}^{wing}$ ). The solid black line is the baseline wing, the dashed blue line is the gapped wing with the smallest impact on gust response, and the dotted yellow line is the gapped wing with the largest impact on gust response. The $C_{MCG}^{wing}$ curves of all the aircraft are plotted in Appendix K. . . . .	123

6.3	The gapped wings (A) decreased trim angle of attack, (B) steepened trim glide angle, and (C) increased trim velocity. The filled dot is the baseline aircraft, + are five-gap aircraft, and o are nine-gap aircraft. Aircraft are color-coded based on gap length and plotted against gap width on the $x$ -axis.	125
6.4	The gapped wings decreased the natural frequency and increased the damping of the phugoid mode. They also increased the natural frequency and decreased the damping of the short period mode. The filled dot is the baseline aircraft. Each + is five-gap aircraft and each o is a nine-gap aircraft. The aircraft are color-coded by their gap length and plotted against their gap width on the $x$ -axis. . . . .	126
6.5	Gapped wings improved the aircraft's gust response by reducing the amplitude and increasing the damping of oscillations. The changes in (A),(E) forward velocity; (B),(F) heave velocity; (C),(G) pitch rate; and (D),(H) pitch angle are plotted against time in response to streamwise and transverse $1-\cos$ gusts. The solid black line is the baseline aircraft, the dashed blue line is the gapped wing with the smallest impact on response, and the dotted yellow line is the gapped wing with the largest impact. All aircraft responses are in Appendix K. . . . .	130
B.1	The gapped wings and aileron wings exhibited similar work curves in both the SI and JH configurations, despite differences in geometry and flow. (A) Work versus rolling moment coefficient of the JH wings. (B) Work curves of the SI wings. The work to actuate the full gap face (before scaling by $R$ ) is included as dashed lines. We varied deflection angle for the aileron wings and angle of attack for the gapped wings. . . . .	144
B.2	The pressure distribution along the chord of the SI-gapped wing was not significantly affected by spanwise location, but varied more greatly along the span of the JH-gapped wing. Data were taken at $2^\circ$ and $10^\circ$ angles of attack, at three spanwise locations near the root, midspan, and wingtip of each wing as indicated with dashed lines in Figure B.3. . . . .	146
B.3	Tip effects did not substantially impact the pressure distribution over the upper surface of the gapped semi-spans. (A) SI-gapped wing at $2^\circ$ angle of attack. (B) SI-gapped wing at $10^\circ$ angle of attack. (C) JH-gapped wing at $2^\circ$ angle of attack. (D) JH-gapped wing at $10^\circ$ angle of attack. The black dotted lines in (A) and (C) show the sampling locations used for Figure B.2.	147
D.1	Validation of the experimental SI-baseline wing lift curve, compared to previously published NACA 0012 data [6], [93], [105]. The experimental data agreed well with the previously published data . . . . .	152
E.1	The SI-baseline wing CFD data agreed well with the previous experimental results, comparing (A) lift coefficient and (B) drag coefficient. The baseline wing was simulated as the SI-aileron wing with a $0^\circ$ deflection at angles of attack from $0^\circ$ to $10^\circ$ . . . . .	154
E.2	Compared to the pressure coefficients over the SI-baseline wing (brown), the pressure coefficients over the SI-gapped wing (yellow) oscillated to local minima and maxima. The SI-baseline wing also experienced a slightly higher pressure coefficient at the trailing edge than the SI-gapped wing. . . . .	155

F.1	(A) The Riemann sum work estimate was lower than the constant force estimate for the SI-gapped wing with $\frac{2c}{3} \times \frac{b}{48}$ gaps. (B) The force on the vertical gap faces decreased as the gaps widened. The gap widths used for the Riemann sum estimates are shown with solid lines, and unused gap widths are shown as dotted lines. The force is plotted at each simulated angle of attack: $\alpha = [0^\circ, 2^\circ, 7^\circ, 10^\circ]$ . . . . .	159
F.2	(A) The Riemann sum work estimates were lower than the constant hinge moment estimates. (B) Hinge moment coefficient decreased as aileron deflection magnitude decreased. Hinge moment and work are plotted against aileron deflection angle at several representative angles of attack. . . . .	160
F.3	Comparing the Riemann sum work estimates of the SI-gapped wing and SI-aileron wing, the intersection increased to a rolling moment coefficient of 0.0236 (compared to 0.0182 in Figure 3.11). Grey points indicate partial aileron stall. . . . .	162
G.1	The rolling moment coefficient versus gap width for the five- and nine- gap wings, as well as the two-gap wing, all with a gap length of $\frac{2c}{3}$ . Data are plotted at (A) $0^\circ$ , (B) $2^\circ$ , (C) $7^\circ$ , and (D) $10^\circ$ angle of attack. . . . .	164
G.2	The actuation work versus gap width for the five- and nine- gap wings, as well as the two-gap wing, all with $\frac{2c}{3}$ -long gaps. Data are plotted at (A) $0^\circ$ , (B) $2^\circ$ , (C) $7^\circ$ , and (D) $10^\circ$ angle of attack. . . . .	166
G.3	The normalized roll versus gap width for the five- and nine- gap wings, as well as the two-gap wing, all with a gap length of $\frac{2c}{3}$ . Data are plotted at (A) $2^\circ$ , (B) $7^\circ$ , and (C) $10^\circ$ angle of attack. . . . .	167
H.1	The linear models for (A) rolling moment coefficient and (B) actuation work of the SI-gapped wing agreed well with the validation data (five- and nine-gap wings with $\frac{2c}{3} \times \frac{b}{48}$ gaps), when the models were built only using those same validation data points. . . . .	169
I.1	The asymmetric parameter sweep data was corrected to a symmetric configuration (blue line). I validated the corrected estimates with direct CFD simulations of a symmetric gapped wing (black circles). I validated the gapped wing configuration with nine $\frac{3c}{4} \times \frac{b}{16}$ gaps. (A) lift coefficient, (B) drag coefficient, and (C) pitching moment coefficient about the quarter-chord. . . . .	172
J.1	The tail planform was elliptical, with different minor axes $d_{LE}$ and $d_{TE}$ for the leading edge and trailing edge portions, respectively. Both ellipses had a major axis $D$ . The aerodynamic centers of the airfoil sections fell along the same spanwise axis of the tail. . . . .	175
K.1	(A) Gaps decreased the wing's pitching moment coefficient about the aircraft's center of gravity. (B) - (I) Gapped wings improved the aircraft gust response by reducing amplitude and increasing damping of the changes in state variables. We plot the changes in forward velocity, heave velocity, pitch rate, and pitch angle in response to streamwise and transverse 1-cos gusts. The solid black line is the baseline aircraft, and each color dashed or dotted line is a different gapped wing aircraft. . . . .	179

L.1	The AC-mounted aircraft was defined with the wing and tail mounted by their respective aerodynamic centers, per common aerodynamic texts [73], [88]. . . . .	181
L.2	This configuration of the AC-mounted aircraft trimmed at generally lower angles of attack, similar glide angles, and higher forward velocities compared to the CG-mounted aircraft from Chapter VI. The gapped wings exhibited the same effects on trim state as they did for the CG-mounted aircraft. . .	184
L.3	AC-mounting the wings and tail had modest effects on the natural modes of the aircraft. Notably, the gapped wings exhibited the same pattern of effects on the natural modes as they did for the CG-mounted aircraft. . . .	185
L.4	The gust responses of the AC-mounted aircraft were very similar to those of the CG-mounted aircraft (Chapter VI), and the gapped wings had the same impacts on responses of the AC-mounted aircraft. . . . .	186
L.5	Gapped wings had similar effects on the gust responses of the AC-mounted aircraft as they did on the CG-mounted aircraft (Chapter VI). (A) Gaps decreased the wing’s pitching moment coefficient about the aircraft’s center of gravity. (B) - (I) Gapped wings improved the aircraft gust response by reducing amplitude and increasing damping of the changes in state variables. We plot the changes in forward velocity, heave velocity, pitch rate, and pitch angle in response to streamwise and tranverse 1–cos gusts. The solid black line is the baseline aircraft, and each color dashed or dotted line is a different gapped wing aircraft. . . . .	187

## LIST OF TABLES

### Table

2.1	Actuation requirements of nine-gap wing and $-15.0^\circ$ equivalent spoiler, at $11.8^\circ$ angle of attack. This scenario was the best rapid descent performance of the gapped wings. . . . .	27
2.2	Equivalent aileron deflection angle and associated angle of attack of each gapped wing. . . . .	29
3.1	Three wing configurations were simulated using CFD, to allow for experimental validation and direct comparison of the aileron and gapped wings. .	41
4.1	The JH-gapped wing and two-aileron JH-wing were simulated using CFD, to allow for experimental validation and direct comparison of the aileron and gapped wings in the JH-configuration. . . . .	68



## LIST OF APPENDICES

### Appendix

A.	Airfoil ordinates . . . . .	142
B.	Aerodynamic Effects of Endplates, and Comparison of SI- and JH-Wings . . .	143
C.	Experimental Uncertainty Analysis . . . . .	148
D.	Validation of Experimental Setup . . . . .	151
E.	Comparison of SI-Gapped Wing and SI-Baseline Wing . . . . .	153
F.	Refined Work Estimates Based on Integral Approximations . . . . .	156
G.	Parameter Sweep With the Two-Gap Wing . . . . .	163
H.	Simplified Linear Models of Roll and Work, for Validation . . . . .	168
I.	Validation of Symmetric Wing Data Corrections . . . . .	171
J.	Modeling Aircraft Wing and Tail for Rigid Body Dynamics . . . . .	173
K.	Gust Responses of all Aircraft . . . . .	178
L.	Dynamics of Aircraft With AC-Mounted Wing and Tail . . . . .	180

## LIST OF ABBREVIATIONS

<b>CFD</b>	computational fluid dynamics
<b>GUM</b>	Guide to the Expression of Uncertainty in Measurement [1]
<b>JH</b>	Johnson and Hagerman
<b>LES</b>	large eddy simulation
<b>RANS</b>	Reynolds-averaged Navier-Stokes
<b>TKE</b>	turbulent kinetic energy
<b>SDR</b>	specific dissipation rate
<b>SI</b>	Sigrest and Inman
<b>UAV</b>	uncrewed aerial vehicle
<b>AC</b>	aerodynamic center
<b>CG</b>	center of gravity
<b>DATCOM</b>	U.S. Air Force Data Compendium

## LIST OF SYMBOLS

$\alpha$	Angle of attack (rad)
$\alpha^{tail}$	Angle of attack of the tail
$\alpha^{wing}$	Angle of attack of the wing
$\alpha_0$	Trim angle of attack (rad)
<b>A</b>	Matrix of aircraft stability derivatives modifying the state variables
<b>C</b>	Matrix of aircraft stability derivatives modifying the gust disturbance vector
<b>x</b>	Changes in aircraft state variables
$\Delta\alpha$	Angle of attack increment
$\Delta\delta$	Change in control surface deflection angle
$\Delta\theta$	Change in pitch angle (rad)
$\Delta C_D^{spoiler}$	Incremental coefficient of drag caused by the spoiler
$\Delta C_L^{spoiler}$	Incremental coefficient of lift caused by the spoiler
$\Delta C_L^{wing}$	Incremental coefficient of lift of the gapped wings
$\Delta q$	Change in pitch rate (rad/s)
$\Delta u$	Change in forward velocity (m/s)
$\Delta w$	Change in heave velocity (m/s)
$\Delta x$	Linear extension of actuator
$\delta_a$	Deflection angle of the aileron
$\delta_s$	Deflection angle of the spoiler
$\delta_{s,0}$	Initial angle of the spoiler when undeflected and flush against the airfoil (rad)
$\ell^{fuse}$	Distance from the fuselage point mass to the aircraft CG (m)
$\ell_b$	Rolling moment of the baseline wing

$\ell_g$	Measured rolling moment of the semi-span gapped wing (N-m)
$\ell_{AC}^{tail}$	Distance from the tail's aerodynamic center to the aircraft's CG
$\ell_{AC}^{wing}$	Distance from the wing's aerodynamic center to the aircraft's center of gravity
$\ell_{QC-GC}$	Distance from the tail's quarter-chord to its center of gravity
$\epsilon$	Downwash from the wing at the horizontal tail
$\eta$	Tail efficiency factor
$\eta_a$	Efficiency of the actuation system
$\frac{d\epsilon}{d\alpha}$	Variation of the downwash with angle of attack (per rad)
$\gamma_0$	Trim glide angle (rad)
$\gamma_D$	Incidence influence function for spoiler drag
$\gamma_L$	Incidence influence function for spoiler lift
$\Im$	Imaginary part of the eigenvalues
$\Lambda$	Sweep angle of the wing
$\lambda$	Taper ratio of the wing
$\lambda_i$	Eigenvalues of the aircraft state space system
$\mu$	Coefficient of static friction
$\omega_n$	Natural frequency of the longitudinal modes (rad/s)
$\omega_{n,SP}$	Natural frequency of the short period mode (rad/s)
$\Re$	Real part of the eigenvalues
$\rho$	Air density (kg/m <sup>3</sup> )
$\zeta$	Damping ratio of the longitudinal modes
$a_0$	Two-dimensional NACA 0012 lift curve slope (per rad)
$A_{gc}$	Area of the vertical gap cover face (m <sup>2</sup> )
$A_g$	Area of the full vertical gap face (m <sup>2</sup> )
$AR_g$	Aspect ratio of a gap
$AR_t$	Aspect ratio of the tail
$AR_w$	Aspect ratio of the wing

$b$	Wing semi-span (m)
$b_g$	Width of a gap (m)
$c$	Wing chord (m)
$C_\ell^{C,U}$	Corrected rolling moment coefficient produced by the upwards aileron
$C_\ell^{M,D}$	Measured rolling moment coefficient produced by the downwards aileron
$C_\ell^{M,U}$	Measured rolling moment coefficient produced by the upwards aileron
$C_\ell^{norm}$	Rolling moment coefficient normalized by actuation work (normalized roll)
$C_\ell^T$	Rolling moment coefficient produced by two oppositely-deflected ailerons
$C_\ell^{wing}$	Rolling moment coefficient of the full asymmetric gapped wing
$c_a$	Chord of the aileron (m)
$C_D$	Drag coefficient of the aircraft
$c_d$	Two-dimensional/profile drag coefficient of the NACA 0012
$C_D^{base}$	Drag coefficient measured from the full symmetric baseline wing CFD
$C_D^{meas}$	Drag coefficient measured from the full asymmetric gapped wing CFD
$C_D^{tail}$	Drag coefficient of the tail
$C_D^{wing}$	Drag coefficient of the wing
$c_g$	Length of a gap (m)
$C_L$	Lift coefficient of the aircraft
$c_l$	Two-dimensional lift coefficient
$C_L^{base}$	Lift coefficient measured from the full symmetric baseline wing CFD
$C_L^{meas}$	Lift coefficient measured from the full asymmetric gapped wing CFD
$C_L^{tail}$	Lift curve of the tail
$C_L^{wing}$	Lift coefficient of the wing
$C_M$	Net pitching moment coefficient of the aircraft at trim
$C_M$	Pitching moment coefficient of the aircraft
$c_s$	Chord/length of the spoiler (m)
$C_{D,s}$	Drag coefficient of the deflected spoiler

$C_{D0}$	Drag coefficient at trim
$C_{D\alpha}$	Slope of the drag curve (per radian)
$C_{D_u}$	Change in drag coefficient with forward speed
$C_{D_i}^{tail}$	Induced drag coefficient of the tail
$C_{h,a}$	Hinge moment coefficient of the aileron
$C_{L0}$	Lift coefficient at trim
$C_{L\alpha}$	Slope of the lift curve (per radian)
$C_{L\alpha}^{tail}$	Lift curve slope of the tail (per rad)
$C_{L_u}$	Change in lift coefficient with forward velocity
$C_{L\alpha}^{tail}$	Slope of the tail's lift curve (per rad)
$C_{L\alpha}^{wing}$	Slope of the wing's lift curve (per rad)
$C_{M,QC\alpha}^{wing}$	Slope of the wing's moment curve about the quarter-chord (per rad)
$C_{M\alpha}$	Slope of the pitching moment curve (per radian)
$C_{M_q}$	Change of the pitching moment coefficient with pitch rate
$C_{M_u}$	Change in pitching moment coefficient with forward speed
$C_{M\dot{\alpha}}$	Change of the pitching moment coefficient with time rate of change of angle of attack
$C_{MAC}^{wing}$	Pitching moment coefficient of the wing about its aerodynamic center
$C_{MAC}^{wing}$	Wing's pitching moment coefficient about its aerodynamic center
$C_{MCG}^{tail}$	Pitching moment coefficient of the tail about the aircraft's center of gravity
$C_{MCG}^{wing}$	Pitching moment coefficient of the wing about the aircraft's center of gravity
$C_{MQC}^{base}$	Pitching moment coefficient measured at the quarter-chord from the full symmetric baseline wing CFD
$C_{MQC}^{meas}$	Pitching moment coefficient measured at the quarter-chord from the full asymmetric gapped wing CFD
$C_{MQC}^{wing}$	Wing's pitching moment coefficient about its quarter-chord
$c_{root}^{tail}$	Root chord of the tail
$C_{Z_q}$	Change in the Z-force coefficient due to pitch rate

$D$	Major axis of the tail elliptical planform
$d$	General expression for minor axis of the tail planform ellipse
$d_{LE}$	Minor axis of the leading edge ellipse of the tail planform
$d_{TE}$	Minor axis of the trailing edge ellipse of the tail planform
$e$	Planform efficiency factor
$F_g$	Force acting on all of the full vertical gap faces (N)
$F_N$	Normal force acting on one gap cover (N)
$F_s$	Force to deflect the spoiler to a given angle
$F_{fr}$	Friction force acting on one gap cover (N)
$F_{gc}$	Force required to actuate all the gap covers (N)
$F_{x,0}$	Net force acting on the aircraft in the $x$ -direction at trim
$F_{z,0}$	Net force acting on the aircraft in the $z$ -direction at trim
$G$	Grid factor of the mesh
$g$	Acceleration due to gravity ( $m/s^2$ )
$G_k$	Gearing ratio of control surface actuation system
$h$	Height of the tail ellipsoid
$h_H$	Height between the tail's aerodynamic center and the wing's chord line (m)
$i^{tail}$	Incidence angle of the tail
$i^{wing}$	Incidence angle of the wing
$I_y$	Mass moment of inertia of the aircraft about the $y$ -axis at its center of gravity ( $kg \cdot m^2$ )
$I_y^{half}$	Moment of inertia of each half-ellipse of the tail planform
$I_y^{tail}$	Tail moment of inertia about its quarter-chord
$I_{y,CG}$	Aircraft's mass moment of inertia about the $y$ -axis acting at its center of gravity ( $kg \cdot m^2$ )
$I_{y,CG}^{tail}$	Mass moment of inertia of the tail about the $y$ -axis at the aircraft's center of gravity ( $kg \cdot m^2$ )
$I_{y,CG}^{wing}$	Mass moment of inertia of the wing about the $y$ -axis at the aircraft's center of gravity ( $kg \cdot m^2$ )

$K$	Correction factor for aileron measurements from Johnson and Hagerman [2]
$K_\lambda$	Wing taper ratio factor
$K_A$	Wing aspect ratio factor
$K_{h_H}$	Horizontal tail location factor
$L_b$	Measured lift force of the baseline semi-span wing (N)
$L_g$	Measured lift force of the gapped semi-span wing (N)
$l_h$	Distance between the wing and the tail's aerodynamic centers parallel to the wing's chord line (m)
$m$	Total aircraft mass (kg)
$m^{base}$	Mass of the baseline wing (kg)
$m^{fuse}$	Mass of the fuselage (kg)
$m^{tail}$	Mass of the tail (kg)
$m^{wing}$	Mass of the wing (kg)
$M_a$	Hinge moment of the aileron (N-m)
$m_a$	Mass of the aileron (kg)
$m_i$	Mass of the $i^{th}$ of the tail
$M_s$	Hinge moment of the spoiler
$m_s$	Mass of the spoiler (kg)
$m_{gc}$	Mass of a single gap cover (kg)
$M_{y0}$	Net pitching moment acting on the aircraft at trim
$N$	Parameter relating short period natural frequency and aircraft load factor
$n$	Number of gaps in the wing
$N_{cells}$	Number of cells in volume mesh
$Q$	Dynamic pressure (Pa)
$Q_0$	Dynamic pressure at the trim state (N/m <sup>2</sup> )
$R$	Area ratio of gap to gap cover vertical areas
$Re$	Reynolds number



$S^{tail}$	Planform area of the tail
$S_a$	Surface area of the aileron (m <sup>2</sup> )
$S_b$	Area of the baseline semi-span wing (m <sup>2</sup> )
$S_e$	Exposed wing or tail planform area
$S_g$	Area of the gapped semi-span wing (m <sup>2</sup> )
$S_s$	Surface area of the spoiler (m <sup>2</sup> )
$S_{fa}$	Full asymmetric wing area (m <sup>2</sup> )
$S_{fs}$	Full symmetric wing planform area (m <sup>2</sup> )
$t$	Time (s)
$t_a$	Time to halve the initial amplitude (s)
$t_m$	Time at which the gust reaches its maximum velocity (s)
$U_0$	Forward velocity at the trim state (m/s)
$U_g(t)$	Gust velocity profile over time (m/s)
$V$	Freestream velocity (m/s)
$V_H$	Volume fraction of the tail
$V_l$	Air velocity at the spoiler location (m/s)
$v_{gq}$	Gust velocity about the $y$ -axis (m/s)
$v_{gx}$	Gust velocity along the $x$ -axis (m/s)
$v_{gz}$	Gust velocity along the $z$ -axis (m/s)
$W_a$	Work to deflect the aileron to a given angle (N-m)
$W_a^R$	Work to actuate the SI-aileron wing based on Riemann sum integral approximation
$W_a^D$	Work to actuate the downwards ailerons
$W_a^T$	Work to actuate the wing with two ailerons
$W_a^U$	Work to actuate the upwards ailerons
$w_g$	Maximum gust velocity (m/s)
$W_s$	Work to deflect the spoiler to a given angle
$W_{gc}$	Work to actuate all of the gap covers (N-m)

$W_{gc}^R$	Work to actuate the SI-gap covers based on Riemann sum integral approximation
$x_{ac}^{tail}$	Distance from the aerodynamic center of the tail to the CG of the full aircraft (m)
$x_{AC}^{wing}$	Location of the aerodynamic center relative to the wing's leading edge (m)
$x_{cg,a}$	Location of the center of gravity of the aileron along its chord, relative to its hinge axis
$x_{CG,i}$	Location of the tail's $i^{th}$ slice center of gravity along its chord
$x_{cg,s}$	Location of the center of gravity of the spoiler along its chord, relative to its hinge axis
$x_{CG}$	Distance from the nose to the aircraft's center of gravity (m)
$x_{CG}^{fuse}$	Distance from the nose to the fuselage's center of gravity (m)
$x_{CG}^{t0}$	Location of the tail's CG along its chord, relative to the tail's leading edge
$x_{CG}^{tail}$	Distance from the nose to the tail's center of gravity (m)
$x_{CG}^{wing}$	Distance from the nose to the wing's center of gravity (m)
$\zeta$	Gust disturbance vector
W	Weight of the aircraft

## ABSTRACT

Some bird species fly inverted (“whiffle”) to lose altitude, move laterally, and respond to gusts. Inverted flight twists the primary feathers, creating gaps along the trailing edge and decreasing lift. Whiffing shares parallels to conventional spoilers and ailerons on uncrewed aerial vehicles (UAVs). However, the maneuver had yet to inspire aircraft design. Here, I investigate the capabilities of a novel UAV control surface – a wing with gaps in the trailing edge – using the feather rotation mechanism as a new source of bio-inspiration. Wind tunnel tests revealed that the gapped wings did not reduce lift as much as a spoiler. However, at high angles of attack, a gapped wing produced a greater rolling moment coefficients than a maximum-deflected single aileron. I then simulated a gapped wing with a commercial computational fluid dynamics solver to estimate its work requirements. The gapped wing required higher work than a single aileron at low rolling moment coefficients. However, the gapped wing required less work at higher rolling moment coefficients and ultimately produced a higher maximum rolling moment coefficient. The results also highlighted the fluid dynamics mechanisms underlying the behavior the gapped wings. I additionally compared the gapped wing to a realistic wing with two ailerons. Compared to the two-aileron wing, the gapped wing produced smaller rolling moment coefficients, but favorable yaw at low rolling moment coefficients. A parameter sweep of gap size and configuration further implied that gap geometry could be tailored to maximize rolling moment coefficient per actuation work. Finally, I analytically modelled the rigid body dynamics of aircraft with varying gapped wings. The gaps generally improved the longitudinal modes. They also effectively damped and reduced the amplitude of the gust response. Ultimately, despite several limitations, the gapped wings could be a useful gust mitigation or roll control surface in certain situations.

# CHAPTER I

## Introduction

### 1.1 Bioinspiration

Bioinspired engineering is the practice of studying and understanding natural phenomena, then leveraging their useful aspects to improve technology. Birds and other natural flyers are often taken as sources of bioinspiration for aerospace engineering. They provide a wealth of behaviors, mechanisms, and flight techniques that could be adapted to aircraft and uncrewed aerial vehicles (UAVs). However, due to evolutionary pressures, birds are not necessarily optimized for any specific form of flight [3]. Thus, bioinspired innovations frequently come with their own advantages and disadvantages [3]. While bioinspired engineering has its benefits, it is important to fully explore new ideas and concepts before implementing them on UAVs. Ultimately, avian bioinspiration provides a multidisciplinary lens for approaching aerospace problems. This knowledge exchange is bidirectional: bioinspired engineering can also provide important context and data for the biological sciences.

Many avian mechanisms have been taken as bioinspiration for UAVs. Smooth camber morphing [4]–[6], wing sweep [7], tail morphing [8], alulas and wingtip slots [9], and others are well-characterized examples of bioinspired UAV technologies. Despite the large body of information that exists on avian bioinspiration, there is still much left to explore.

In this dissertation, I identified a little-understood avian behavior (whiffing) as a previously unused source of bioinspiration for a novel control surface. This concept took the form

of a rectangular wing with gaps along the trailing edge. I then investigated if the gapped wings provided desirable control capabilities, possibly similar to the avian whiffing maneuver. A combination of experimental, computational, and analytical studies were employed to build confidence in the results and develop a variety of useful tools. In particular, I focused on understanding the affects of the gaps on the aerodynamic performance of a wing, and the underlying fluid mechanics. In the spirit of bioinspiration, this dissertation served as an initial assessment of the advantages and disadvantages of the gapped wings. Since the control surface concept and its bioinspiration were unique and novel, the work here provided a foundation of knowledge for future engineers and biologists. Finally, note that this work was founded on the principle of bioinspiration, rather than biomimicry. The goal was not to replicate avian whiffing. Rather, I observed the behavior and used it as the motivation for a novel control surface.

## 1.2 Avian whiffing

Some species of birds invert mid-flight while keeping their heads level, a maneuver known as whiffing or dumping [10]–[12]. Various species of birds have been observed whiffing, especially waterfowl like geese and ducks. It is hypothesized that birds whiffle to evade predators, lose altitude for landing, descend rapidly, move laterally, and respond to gusts and atmospheric disturbances, among other reasons [10]–[13]. It is currently unknown if whiffing in response to a gust is active or passive [12]. Larger birds such as the black stork (*Ciconia nigra*) have also been observed whiffing during courtship displays [14]. Whiffing has been qualitatively described as “a swift zig-zagging, side-slipping erratic fall” [10], “aerobatic” [12], side-slipping and tumbling [15], [16], and losing altitude “at a rapid rate” [12]. Amateur videos of whiffing show similar qualities, with the whiffing birds descending at a steep near-vertical angle [17]. Birds typically only whiffle for a moment, and either flap or glide while inverted [12]. Previous publications on whiffing are largely qualitative and observational, and the maneuver has not been rigorously studied in either the biological or engineering

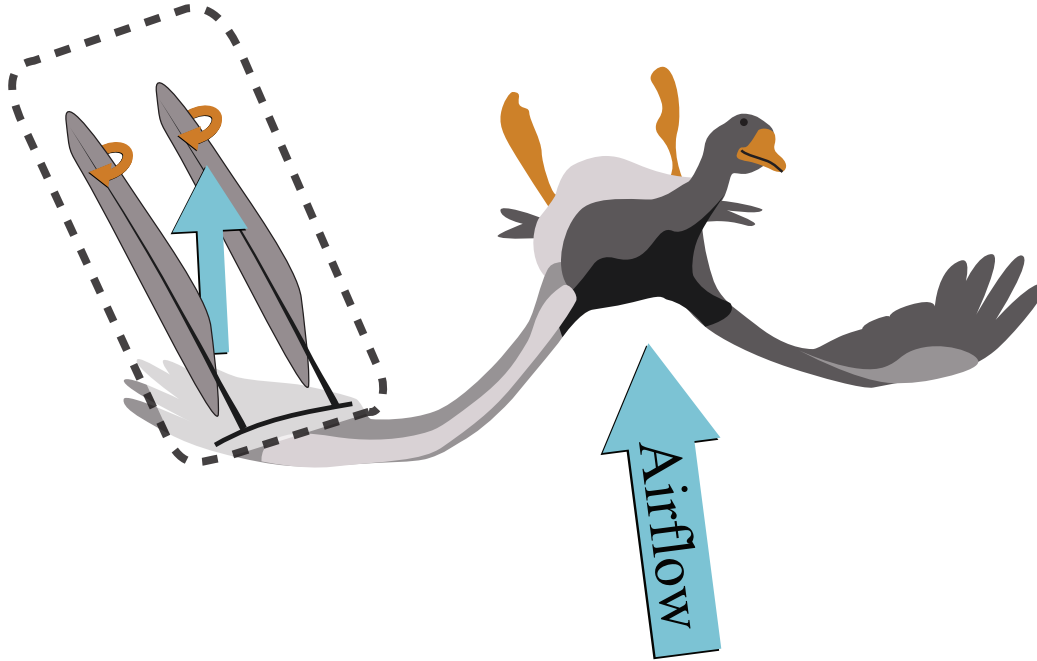


Figure 1.1: Birds whiffle to lose altitude, move laterally, and respond to gusts. Airflow through gaps between primary flight feathers likely causes aerodynamic changes such as decreased lift. To whiffle, the bird flies inverted and the resulting airflow twists the primary flight feathers open, creating gaps in the trailing edge.

domains. There are large gaps in the literature on the mechanisms and aerodynamics of whiffing. Recent engineering studies did point to whiffing as an example of avian neck control and head stabilization [18], [19]. However, the maneuver had yet to inspire aircraft design.

During whiffing, airflow from the back (dorsal) to the belly (ventral) side of the bird causes the primary flight feathers to twist open [20]. The resulting gaps between the feathers likely allow air to pass through the wing, leading to changes in aerodynamic forces and moments such as decreased lift (Fig. 1.1). While primary feathers are known to twist in dorsal-to-ventral airflow [21]–[23], there are no quantified results of secondary feathers twisting while whiffing. Note that the term “whiffing” refers to the behavior of flying upside down, while feather rotation is a mechanism that occurs during the whiffing behavior (and other situations characterized by dorsal-to-ventral airflow). It is possible that camber, or wing curvature, also plays a role in whiffing. Bird wings typically have camber [24] which

likely inverts during whiffing, contributing to a decrease in lift. However, the extent to which camber inversion and feather rotation interact to affect whiffing is unclear.

Due to its high maneuverability and rapid descent, whiffing could be an advantageous new source of bio-inspiration for aircraft control surfaces. The effects of whiffing on a bird's flight path can be compared to two control surfaces found on UAVs: spoilers and ailerons. Like spoilers, whiffing decreases the lift-to-drag ratio and leads to descent. Hypothetically whiffing just one wing, while not known to be possible for birds, could lead to a rolling moment like an aileron due to the resulting asymmetric lift distribution across the full wingspan. Both spoilers and ailerons can also be used to alleviate gusts, like whiffing.

### 1.3 The whiffing-inspired gapped wing

To effectively translate the whiffing maneuver to UAVs, I first simplified and idealized the mechanisms of a whiffing wing. Whiffing is related to both camber inversion and feather rotation. Inverted-camber wings and bioinspired camber morphing have already been extensively studied and characterized [3], [4], [25], [26]. Conversely, feather rotation has not been investigated or applied to aircraft design. It provides a novel solution to a classic problem. I therefore focus on feather rotation instead of camber morphing.

Combining the feather rotation mechanism of whiffing with practical energy considerations, I designed whiffing-inspiring rectangular wings with a series of gaps in the trailing edge (Fig. 1.2). While conventional control surfaces—like spoilers, ailerons, flaps, and camber morphing wings—deflect into the flow, the gapped wing would actuate in the same plane as the wing. Thus, the gapped wing has no deflecting components. This planar actuation is a new method of control for UAVs that differs from the traditional deflection-based control surfaces. I anticipated that the planar nature of the gapped wings would hold both energetic and aerodynamic benefits over deflecting control surfaces.

Whiffing-inspired gapped wings could be beneficial to UAVs in terms of energy costs. Both birds and UAVs are energy-constrained [27]–[30]. Limited battery capacities restrict

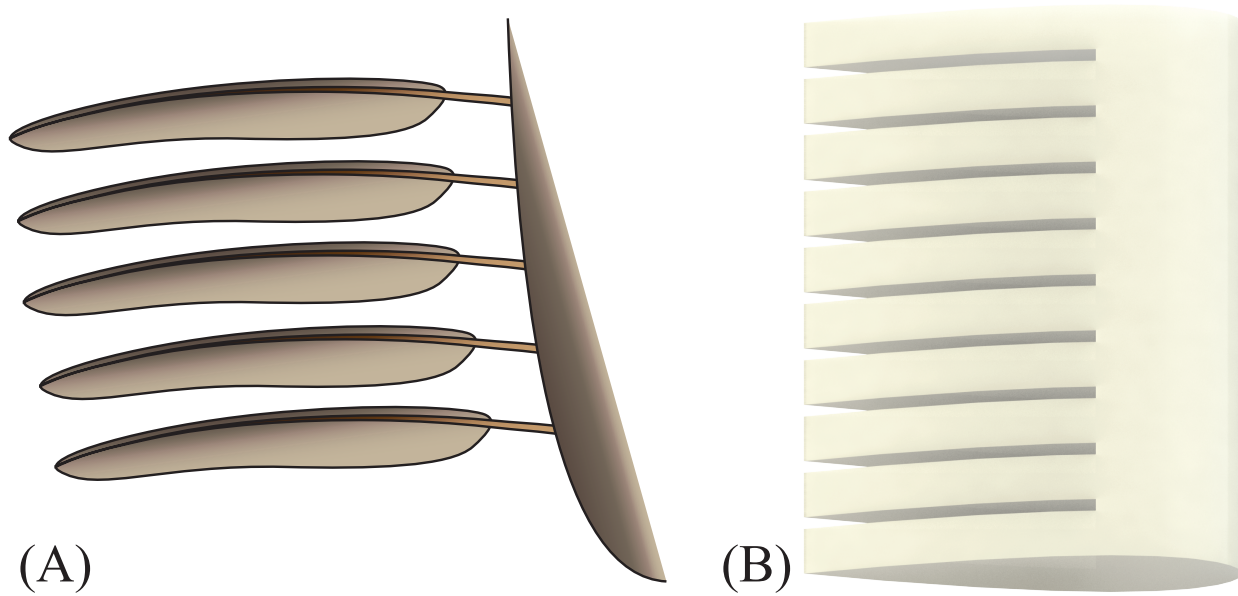


Figure 1.2: Visual comparison of (A) gaps due to feather rotation on a whiffing bird wing and (B) whiffing-inspired gaps on a UAV wing.

important UAV mission parameters like flight duration, range, and payload weight [29], [30]. Thus, while maneuvering costs may represent a small portion of a UAV's total energy budget, it is nevertheless important to consider and minimize the energy consumption of all aspects of flight in order to make the most of battery capacity. Maneuvering costs would be particularly relevant for missions involving loitering or extensive actuation. Evaluating and reducing the energy cost of actuators for maneuvering is an active area of study [31], [32]. The passive nature of feather rotation and apparent ease of the whiffing maneuver suggest that a whiffing-inspired control surface may require less work than conventional deflecting control surfaces. In particular, I hypothesized that actuating the gaps in the plane of the wing would require less work than deflecting a flap or aileron.

The gaps' planar nature could hold aerodynamic benefits as well. Most ailerons only deflect  $20^\circ$  to  $30^\circ$  to minimize the risk of flow separation [2], [33]. At high angles of attack, the risk of aileron-induced flow separation and stall becomes even greater. Conversely, gaps along the trailing edge may not be subjected to the same risk of premature stall at high angles or rolling moment coefficients. While the gaps would likely produce vortices that



alter the flow and aerodynamics of the wing, they may not exacerbate flow separation as much as a large aileron deflection.

Overall, the gapped wings could be very useful for small UAVs in a variety of scenarios. The gapped wings could decrease the lift-to-drag ratio of an aircraft, similarly to a whiffing bird. This would enable UAVs to land and maneuver with agility in crowded environments, potentially at a lower energy cost compared to conventional control surfaces. In turn, the lower energy costs would reserve precious battery capacity for extending mission duration or carrying heavier payloads.

The gaps in the trailing edge were initially sized based on naturally occurring features in bird wings. There is no quantitative data on the size of the gaps caused by feather rotation. However, there is a large repository of information on molt gaps in bird wings. Molting is the process by which birds replace worn feathers with new feathers [34]. Notably, molting often leaves visible gaps in between flight feathers [35]–[40]. Molt gaps have been shown to decrease flight performance during both gliding and flapping flight [5], [35]–[38], [41]–[45], similarly to the decreased lift observed during whiffing. Due to this relationship, we initially sized the gaps based on the dimensions of typical molt gaps in birds [35].

The proposed gapped wings are similar to other technologies such as serrated trailing edges, split flaps, slotted spoilers, slotted airfoils, and porous wings. Serrated trailing edges have been studied mainly for noise reduction [46], but few aerodynamic analyses have been conducted. Furthermore, serrated trailing edges are physically distinct from the wing gaps investigated in the current study [46]. Split flaps perforated with circular holes [47], [48] and slots [47] have been studied as dive brakes, but their purposes were to limit dive speed, reduce buffeting, and increase aileron control effectiveness during dives, rather than descending, rolling, or mitigating gusts [47], [48]. Furthermore, dive brakes on powered aircraft were intentionally designed to have minimal impact on lift production, which is unfavorable for rapid descent [47]. Slotted spoilers have also been investigated, but as a method of increasing aileron control effectiveness during a dive, rather than a method of descent [49]. Slotted

airfoils have also been used to increase lift and delay flow separation at high angles of attack [50]–[53]. However, such slots are typically cut along the span of the wing, perpendicular to orientation of the gaps in this study. Finally, porous wings have been used to bleed airflow through a wing and control global forces and moments [54], [55]. The concept of flow bleed is similar to that of the whiffing-inspired gaps: air is allowed to flow from the pressure to the suction side of the wing. However, previous bleed ports were concentrated near the trailing edge, and did not extend as far along the chord as the whiffing-inspired gaps.

## 1.4 Novelty and significance of gapped wings

This dissertation intersected biology and aircraft design to provide contributions to basic science, aerodynamics, and practical engineering knowledge. Firstly, I proposed the gapped wing as a novel bioinspired UAV control surface. I then assessed the gapped wing’s capabilities for rapid descent, roll control, and gust alleviation, three hypothesized uses of the avian whiffing maneuver [12].

A gapped wing was found to provide comparable performance to a conventional aileron, for a fraction of the actuation cost (Chapter II). Computational fluid dynamics helped build an understanding of the flow over the novel wing geometry (Chapter III). I also estimated the gapped wing actuation requirements based on aerodynamic loading. These results were then expanded to compare the gapped wing to a wing with two ailerons (Chapter IV). I further investigated the effects of gap configuration on roll performance and actuation cost, providing a spring-board for future optimization studies (Chapter V). Finally, I showed that gapped wings had beneficial impacts on the trim, natural modes, and gust response of an aircraft (Chapter VI). Throughout this dissertation, I discussed relevant advantages and disadvantages of the gapped wings to provide a holistic picture of their capabilities as a control surface. The gapped wings were not well-suited for all situations, and were faced with several limitations. Addressing these disadvantages provided useful data for aircraft designers to implement the gapped wings. Ultimately, the findings suggested that the novel

gapped wings could be suitable for roll control and gust alleviation in some situations, such as for small energy-constrained UAVs at high lift coefficients.

This work represented the first time that whiffing was leveraged as a starting point for aerodynamic design. I also presented the first computational study of flow over a wing with this streamwise gap geometry, and the first study of the impacts of gaps on aircraft rigid body dynamics. Very little prior knowledge existed on either whiffing or streamwise gaps. Thus, this dissertation provided a starting point for both biologists and engineers to study the whiffing behavior and apply it to future bio-inspired work.

## CHAPTER II

# A Gapped Wing Created Roll at High Lift Coefficients

### 2.1 Overview

Here, we investigated if gaps in the trailing edge of a wing, similar to those caused by feather rotation during whiffing, could provide an effective method for rapid descent and banking of UAVs. To address this question, we performed a wind tunnel test of 3D printed wings with a varying amount of trailing edge gaps. Then, we compared the lift and rolling moment coefficients generated by the gapped wings to those of a traditional spoiler and aileron. Next, we used an analytical analysis to estimate the force and work required to actuate the gaps, spoiler, and aileron. Our results showed that gapped wings did not reduce lift as much as a spoiler and required more work. However, we found that at high angles of attack, the gapped wings produced rolling moment coefficients equivalent to an aileron deflected as much as  $32.7^\circ$  upwards, while requiring substantially less actuation force and work. Thus, while the gapped wings did not provide a noticeable benefit over spoilers for rapid descent, they provided an effective alternative to an aileron at high lift coefficients. These findings suggested a novel control method that may be advantageous for small fixed-wing UAVs, particularly energy-constrained aircraft.

## 2.2 Motivation and background

Two hypothesized uses of whiffing are rapid descent and lateral movement [12]. These functions are analogous to a UAV using spoilers or ailerons to control their flight paths. Thus, it was speculated that the novel whiffing-inspired gapped wings could provide benefits in these applications. The gapped wings have not been previously studied in the context of aircraft design and control. Thus, the first step in assessing their capabilities as control surfaces was measuring how they impacted the forces and moments of a UAV wing. This data enabled us to determine if the gapped wings could provide effective alternatives to spoilers and ailerons.

## 2.3 Methods

### 2.3.1 Experimental setup for gapped wings

Wings with zero, three, five and nine gaps ( $n = [0, 3, 5, 9]$ ) spaced evenly along the trailing edge (“gapped wings”) were tested in a wind tunnel. We 3D printed the wings with ABS plastic on a Dimension Elite printer. Each wing had a rectangular planform with a 16 in. semi-span ( $b = 16$  in.) and a 9 in. chord ( $c = 9$  in.), yielding an aspect ratio of 3.56. A NACA 0012 airfoil was used for each wing, because of its symmetry and the wide availability of previously published aerodynamic data. The airfoil ordinates were modelled according to Appendix A. The size of the gaps was held constant, with a gap length equal to  $\frac{2}{3}$  the chord ( $c_g = 6$  in.) and width equal to  $\frac{1}{48}$  of the semi-span ( $b_g = \frac{1}{3}$  in.). For the nine-gap wing, this gap size yielded an area 12.5% less than the area of the wing with no gaps. We used the wing with no gaps as a “baseline wing” to provide a reference point for the gapped wings.

We installed circular end plates on either side of each wing to simulate two-dimensional flow, to study the effects of the gaps independently from the effects of wingtip vortices (Fig. 2.1) [6]. Due to the use of end plates, the data did not capture three-dimensional wing effects, also known as tip effects. Tip effects tend to reduce the lift coefficient and the lift

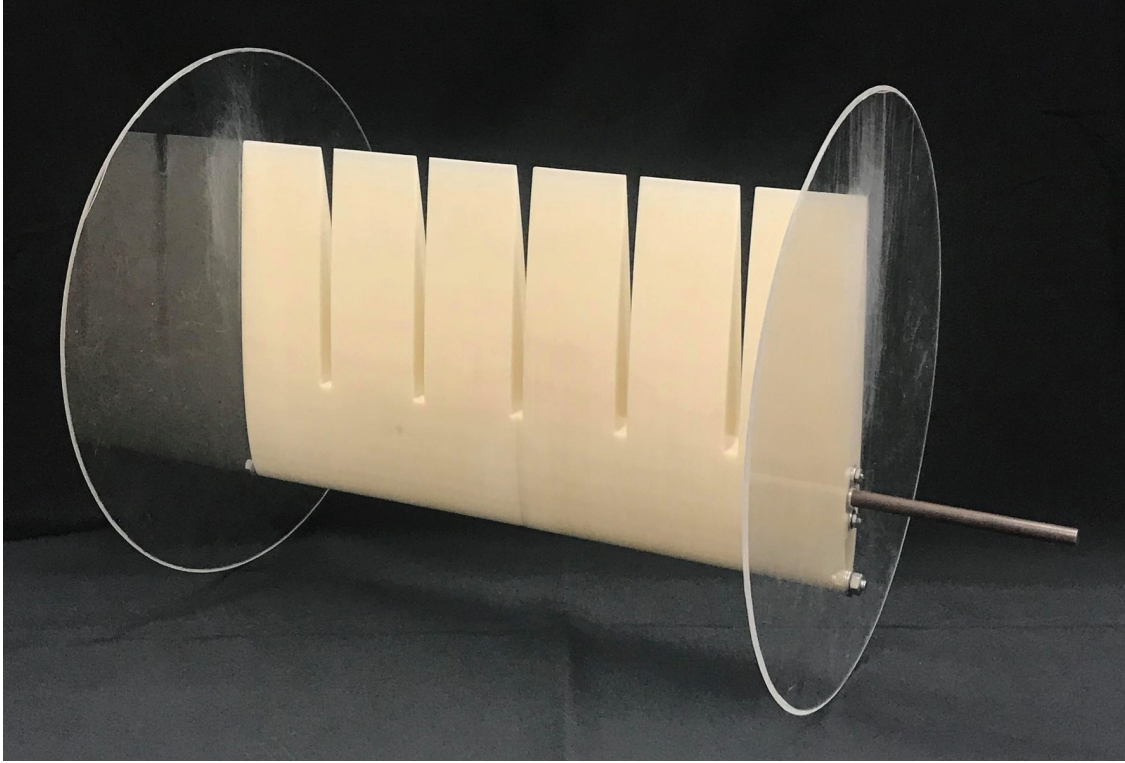


Figure 2.1: Fully assembled five-gap wing with end plates and mounting rod.

curve slope. They also typically increase drag through the creation of induced drag [56]. It has also been found that, for a wing with a retractable aileron (morphologically similar to a spoiler deployed on the upper surface of one wing), increasing aspect ratio tends to increase rolling moment coefficient [57]. Two-dimensional wings do not have tip effects, and can be approximated as wings with an aspect ratio approaching infinity. Thus, this trend implies that tip effects tended to decrease rolling moment. The same study found as aspect ratio increased, the yawing moment became more favorable (in the same direction as roll) at low angles of attack, but more adverse (in the opposite direction as roll) at higher angles [57]. However, since adverse yaw is a result of tip effects, we refrain from describing the gapped wing yawing moment coefficients as “adverse” or “proverse.” The two-dimensional effects of the endplates were verified through computational visualization techniques (Appendix B).

The wing assembly was mounted to a 6-axis ATI Delta Force/Torque Sensor load cell with a rod at the quarter-chord. The load cell was affixed to a Parker Rotary Positioner 30012-S

powered by a Vexta Stepper Motor PK266-03B. This rotary table was installed inverted on top of the test section. The wings were considered as semi-span right wings, with the root closest to the tunnel ceiling.

We conducted testing in a 2ft×2ft open-loop wind tunnel with a freestream turbulence level of 0.7% along the centerline, and approximately 1.8% near the edges of the tunnel [58]. The wings were mounted vertically from the test section ceiling with 3.25 in. of clearance between the end plate and the ceiling of the tunnel, to ensure the wing was sufficiently outside the wall boundary layer. We measured temperature data with a type T thermocouple, and dynamic pressure with a pitot tube and Omega PX-2650 pressure transducer. Load cell data were collected at each angle of attack for 5 seconds at a rate of 3600 Hz. We automated the tests and data collection using MATLAB scripts. Figure 2.2 shows the test setup.

We performed three trials of each wing at a Reynolds number ( $Re$ ) of  $2.33 \times 10^5$ , corresponding to a velocity ( $V$ ) of 16.1 m/s. The  $Re$  was within a range comparable to birds and UAVs [60]. Before each trial, we ran a tare sweep from  $-20^\circ$  to  $0^\circ$  in  $1^\circ$  increments, with the wind tunnel off. We found the tare to be consistent across angles based on its low standard deviation across angle of attack. Therefore, for ease of calculations, we used the tare values at  $0^\circ$  angle of attack in subsequent data analysis. The zero-degree angle of attack was found by sweeping through a small range of near-zero angles, then interpolating to find the angle at which the normal force on the wing vanished. Following from the airfoil’s symmetry, we set this zero-lift angle of attack to be  $0^\circ$  angle of attack. During each trial, we swept the wing from  $0^\circ$  to  $10^\circ$  ( $1^\circ$  increments) and from  $10^\circ$  to  $20^\circ$  ( $0.5^\circ$  increments), which provided sufficient resolution in the stalled regions. The effective angle of attack range experienced by the wings varied slightly from this commanded range due to data corrections. We found that hysteresis effects within a single trial were negligible.

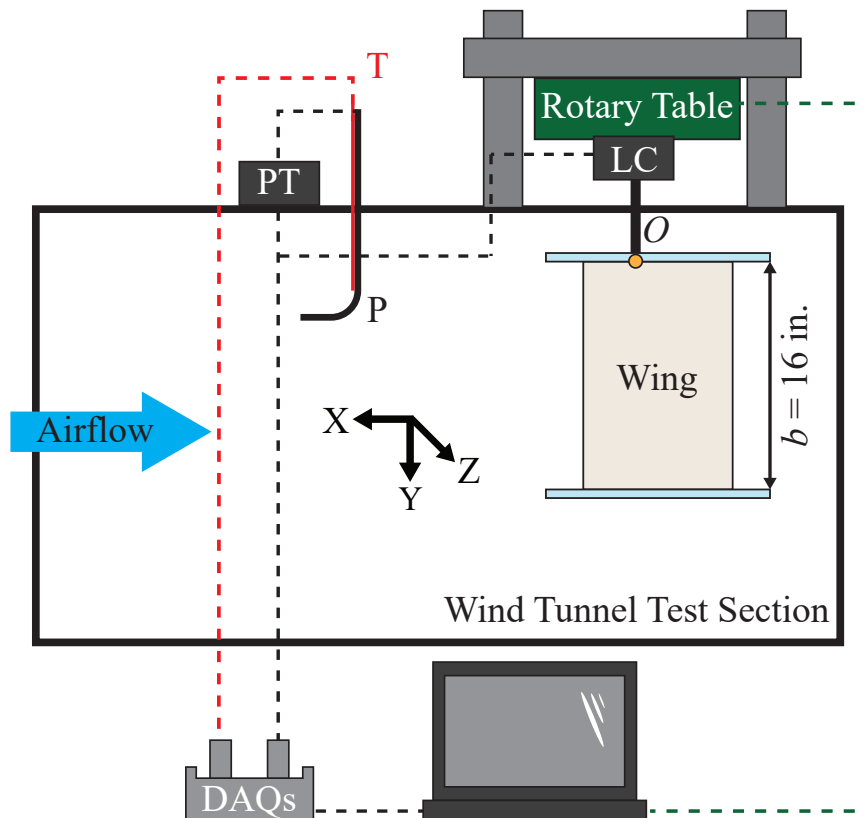


Figure 2.2: Wind tunnel setup. PT is the pressure transducer, LC the load cell, T the thermocouple, and P the pitot tube. The wing is a right semi-span. Moments were taken about the yellow point  $O$  at the quarter-chord of the wing root. Data were reported in the wind axes [59].



### 2.3.2 Data analysis

We averaged the results of the three trials at each angle of attack to present cumulative data, because each wing's individual trials were highly repeatable. The data were corrected for solid blockage, wake blockage, and jet boundaries following Barlow et al. [59]. These corrections approximated freestream conditions and allowed for more direct comparison with other previously published data. No other corrections were made because they were deemed negligible. Given the thinness of the endplates, they were not included in the wing planform area when calculating the aerodynamic force and moment coefficients. We calculated the experimental uncertainty of the data according to the Guide to the Expression of Uncertainty in Measurements (GUM) and reported the expanded uncertainty of the data with a level of confidence of approximately 95% [1]. To quantify if the differences between each gapped wing and the baseline wing were statistically significant, we calculated the expanded uncertainty of the difference of means at an approximately 95% confidence level. Appendix C further details the uncertainty and statistical analyses.

To avoid conflating the aerodynamic effects of the end plates with the effects of varying the number of gaps, we reported the aerodynamic parameters as incremental values, that is, the difference between the gapped wing and the baseline wing values. The results are therefore intended to be taken in a comparative context between wings with different numbers of gaps. For rapid descent, we also considered the gapped wings to be symmetrical (having the same number of gaps on the left and right semi-spans), since spoilers are deployed symmetrically. For example, the incremental lift coefficient  $\Delta C_L^{wing}$  was calculated as the difference between the lift coefficient of the baseline wing and the gapped wing:

$$\Delta C_L^{wing} = \frac{L_g}{QS_g} - \frac{L_b}{QS_b} \quad (2.1)$$

where  $\Delta C_L^{wing}$  is the incremental lift coefficient,  $L_g$  is the measured lift force of the gapped semi-span wing (N),  $L_b$  is the measured lift force of the baseline semi-span wing (N), and  $Q$  is

the dynamic pressure (Pa). The area of the baseline semi-span wing  $S_b$  ( $\text{m}^2$ ) was calculated according to:

$$S_b = bc \quad (2.2)$$

The area of the gapped semi-span wing  $S_g$  ( $\text{m}^2$ ) was calculated by subtracting the planform area of the gaps from the planform area of the baseline wing, per:

$$S_g = bc - nb_g c_g \quad (2.3)$$

Note that the lift coefficient of the gapped wings (used in Eqn. 2.1) was normalized by the gapped wing planform area calculated by Eqn 2.3. By doing so, we interpreted changes in lift coefficient as results of the gaps themselves, rather than the decreased wing area. We calculated the incremental drag coefficient in the same manner.

For the moments, we adopted the sign convention in which the positive moment directions are consistent with the positive conventions on the wind axes (Fig. 2.2) [59]. Thus, a positive rolling moment is a roll towards the right wing [33]. To create a rolling moment, a UAV would need to use an asymmetric wing configuration, be it with ailerons or different gapped wings on each side. Pairing a right gapped semi-span with a left baseline semi-span would initiate a positive roll towards the right gapped wing due to the difference in lift production. Thus, a right gapped wing was comparable to an upwards deflected aileron on the right semi-span. We presented the experimental moment results as a full wing with a right semi-span gapped wing and a left semi-span baseline wing.

Moment coefficients were calculated about the point on the inner surface of the end plate at the wing root, at the quarter-chord (yellow point  $O$  in Fig. 2.2). We calculated the moment coefficients of the full asymmetric wing by subtracting the moment coefficients of the baseline wing from those of the gapped wings [59]. The measured moments were normalized by the full wing area and span [59]. For example, the rolling moment coefficient

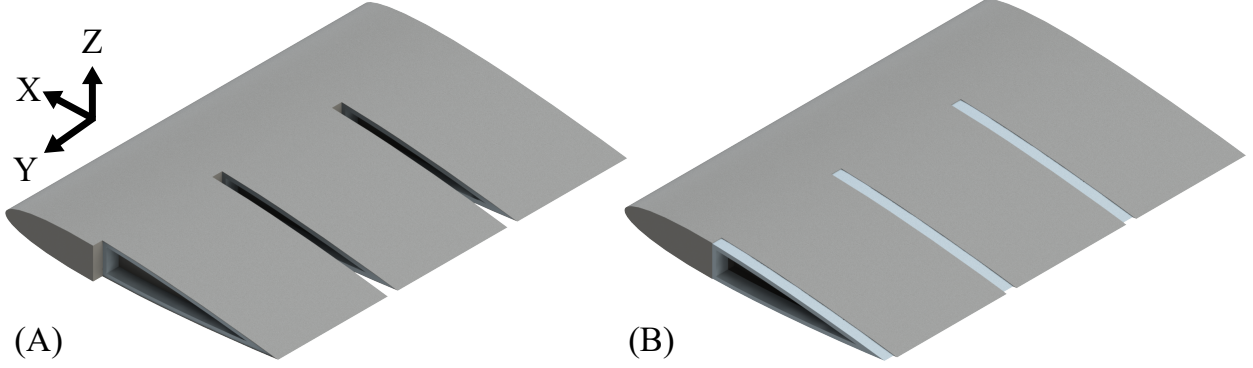


Figure 2.3: Isometric cross-section view of a gapped wing in two configurations, with the gap covers shown in light blue. (A) Gaps open. (B) Gaps closed.

$C_\ell^{wing}$  of the full asymmetric wing was calculated according to:

$$C_\ell^{wing} = \frac{\ell_g}{2QS_{fa}b} - \frac{\ell_b}{2QS_{fa}b} \quad (2.4)$$

and

$$S_{fa} = S_g + S_b = (bc) + (bc - nb_gc_g) \quad (2.5)$$

where  $\ell_g$  is the measured rolling moment of the semi-span gapped wing (N-m),  $\ell_b$  is the measured rolling moment of the semi-span baseline wing (N-m), and  $S_{fa}$  is the full asymmetric wing area. We calculated the yawing moment coefficient in the same manner. Note that it is more desirable for the rolling moment to result in a yaw with the same sign, that is, in the same direction as the roll.

### 2.3.3 Gapped wing actuation work estimates

To calculate the force and work required to actuate the gaps, we considered an actuation scheme in which the gaps were nominally blocked by covers (the unactuated configuration). To actuate, the covers slid spanwise into recesses in the wing, leaving the gaps exposed (the actuated configuration). The recesses were thin walled, so the outer mold line of the unactuated wing represented the baseline wing as closely as possible. A digital mock-up is shown in Figure 2.3 with the gap covers in light blue.

We estimated the force required to actuate the gap covers based on kinematics:

$$F_{gc} = nF_{fr} = n\mu F_N \quad (2.6)$$

where  $F_{gc}$  is the force required to actuate all the gap covers (N),  $F_{fr}$  is the friction force acting on one gap cover (N),  $\mu$  is the coefficient of static friction,  $F_N$  is the normal force acting on one gap cover (N), and  $n$  is the number of gaps. The lift force acting on the covers was estimated in the normal force term:

$$F_N = m_{gc}g - L_b \frac{b_g c_g}{b_c} \quad (2.7)$$

where  $m_{gc}$  is the mass of a single gap cover (kg) and  $g$  is the acceleration due to gravity ( $\text{m/s}^2$ ). To make comparisons between the gapped wings and conventional control surfaces as direct as possible, we used the baseline wing lift measured at the angle of attack corresponding to the equivalent control surface deflection. The work required to actuate all of the gap covers (J) was given by:

$$W_{gc} = F_{gc} b_g \quad (2.8)$$

For the gapped wings, we used a static coefficient of friction of 0.28 and a density of 1.01  $\text{g/cm}^3$ , which are typical values for a generic ABS plastic [61], [62]. The volume of a single gap cover as modelled in CAD was 10.35  $\text{cm}^3$ .

### 2.3.4 Representative spoiler

For the rapid descent comparison, we considered a model of a representative spoiler developed by Sun [63]. Spoilers reduce lift to cause descent, and increase drag to prevent excessive buildup of speed. Sun's model described a full-span spoiler with a chord that was 10% of the wing chord, positioned at 70% chord, with a maximum deflection of 60° (Fig. 2.4). The model was built with data from various spoilers with chords ranging from 5%

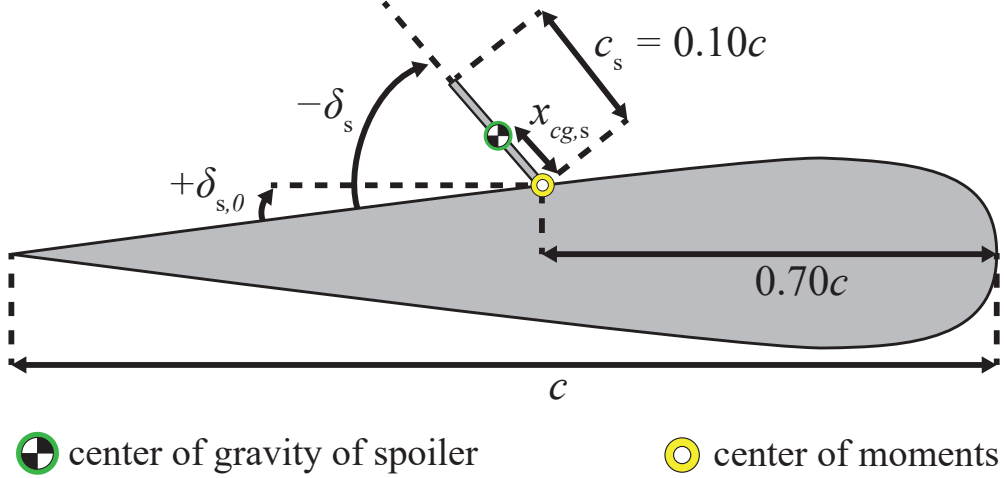


Figure 2.4: Geometry of Sun’s representative spoiler on a wing of chord  $c$  (in m) [63].  $\delta_{s,0}$  is the spoiler angle when undeflected and flush against the airfoil (rad).  $\delta_s$  is the deflection angle of the spoiler (rad), with upwards deflection negative.  $c_s$  is the chord of the spoiler (as a fraction of wing chord).  $x_{cg,s}$  is the location of the spoiler’s center of gravity along its length, with respect to its hinge line (m).

to 15% wing chord, locations from 65% to 73% wing chord, on a variety of airfoils, at an  $Re$  from  $2.8 \times 10^5$  to  $71 \times 10^6$  [63]. The spoilers were mostly three-dimensional, with the exception of several two-dimensional studies [63].

Since our gapped wing experimental data extended up to  $20^\circ$  angle of attack, we used Sun’s model that accounted for large angles of attack, where the incremental lift coefficient  $\Delta C_L^{spoiler}$  and incremental drag coefficient  $\Delta C_D^{spoiler}$  were given by [63]:

$$\Delta C_L^{spoiler} = 0.32\gamma_L\delta_s + 0.51\gamma_L \sin \delta_s \quad (2.9)$$

$$\Delta C_D^{spoiler} = -0.1\gamma_D\delta_s \quad (2.10)$$

$$\gamma_L(\alpha) = \begin{cases} 1.0 & \text{for } -10^\circ \leq \alpha \leq 10^\circ \\ 2.0 - \frac{\alpha}{10.0} & \text{for } 10^\circ \leq \alpha \leq 20^\circ \end{cases} \quad (2.11)$$

$$\gamma_D(\alpha) = 1.0 - \frac{\alpha}{15.0} \text{ for } -15^\circ \leq \alpha \leq 20^\circ \quad (2.12)$$

where  $\alpha$  is the angle of attack (degrees) and  $\delta_s$  is the deflection of the spoiler (radians).

Sun defined the incidence influence functions  $\gamma_L$  and  $\gamma_D$  to generalize the lift and drag spoiler models (respectively) to larger angles of attack. Upwards spoiler deflections were negative (Fig. 2.4), yielding negative lift coefficient increments and positive drag coefficient increments.

To compare the spoiler model to the gapped wing data, we calculated equivalent spoiler deflection angles for the representative spoiler on a wing with the same geometry and flow conditions as the baseline wing. We first determined the greatest reduction of lift coefficient of each gapped wing, and the angle of attack at which it occurred. Since the focus of the rapid descent comparison was on lift reduction, this point represented the best-case performance of each gapped wing. Then, using Sun’s model, we calculated the spoiler deflection that created an equivalent lift coefficient reduction at the same angle of attack. After comparing the aerodynamics of the spoiler and gapped wings, we considered actuation requirements. Spoiler actuation requirements are typically specified as hinge moments [32], [33]. However, since the gapped wings operated in-plane and thus do not have hinge moments, we converted the spoiler hinge moments to be in terms of force and work. We calculated the hinge moment of the spoiler  $M_s$  at the equivalent deflection for each gapped wing by [64]:

$$M_s = \frac{1}{2}\rho V_l^2 \left( \frac{1}{2}C_{D,s} \sin^2(\delta_s) \right) S_s c_s + (m_s g) x_{cg,s} \cos(|-\delta_s| - \delta_{s,0} - \alpha) \quad (2.13)$$

where  $\rho$  is the air density ( $\text{kg}/\text{m}^3$ ),  $V_l$  is the air velocity at the spoiler location ( $\text{m}/\text{s}$ ),  $C_{D,s}$  is the drag coefficient of the deflected spoiler,  $S_s$  is the area of the spoiler ( $\text{m}^2$ ),  $c_s$  is the chord of the spoiler,  $m_s$  is the mass of the spoiler ( $\text{kg}$ ),  $\alpha$  is the angle of attack (in radians) and  $g$  is the acceleration due to gravity ( $\text{m}/\text{s}^2$ ). The first term of Eqn. 2.13 approximated the hinge moment due to aerodynamic forces, as proposed by Scholz [64]. We used Scholz’s suggested values for  $C_{D,s}$  of 1.8 and  $V_l$  of  $1.14 \times V$  [64]. The second term of Eqn. 2.13 was the hinge moment due to the weight of the spoiler, assuming a flat plate and geometry shown in Figure 2.4. From our CAD model of the representative spoiler on a wing with the same

geometry as the baseline wing, the volume was  $7.37 \text{ cm}^3$ ,  $x_{cg,s}$  was  $0.011 \text{ m}$ , and  $\delta_{s,0}$  was  $0.105$  radians. We used a density of  $1.01 \text{ g/cm}^3$  for a generic ABS plastic [35]. We estimated the work according to [32]:

$$W_s = -M_s \delta_s \quad (2.14)$$

Recall that deflection angle of the spoiler was defined with negative upwards. Furthermore, the negative sign in Eqn. 2.14 accounted for the fact that we sought the work required of the spoiler actuation system. The product  $M_s \delta_s$  represented the work “done” by the airflow on the spoiler surface. Thus, I took the negative of that product to determine the work required to overcome the aerodynamic forces on the spoiler.

Calculating the spoiler actuation force  $F_s$  required us to make several assumptions about the mechanics of the spoiler actuation system. Chakraborty proposed [32]:

$$F_s = \frac{G_k M_s}{\eta_a} \quad (2.15)$$

where  $G_k$  is the gearing ratio of the control surface actuation system (rad/m) and  $\eta_a$  is the efficiency of the actuation system. The gearing ratio  $G_k$  described the change in control surface deflection  $\Delta\delta$  per linear extension  $\Delta x$  of the actuator [32]:

$$G_k = \frac{\Delta\delta}{\Delta x} \quad (2.16)$$

We stipulated that the spoiler was actuated by a servo motor with a control horn of radius  $0.015\text{m}$ . We assumed a one-to-one ratio between servo deflection and control surface deflection: a  $60^\circ$  servo rotation yielded a linear extension of  $0.013\text{m}$ , a spoiler deflection of  $60^\circ$ , and a gearing ratio of  $80.6 \text{ m}^{-1}$ . To make the comparison between gapped wings and spoiler conservative, and because no efficiency factor was applied to the gapped wing control surface, we used an efficiency of 100%.

### 2.3.5 Representative aileron

For roll control, we compared the gapped wings to a three-dimensional wing with a representative aileron [2]. The aileron had a chord of 25% of the full wing chord and a span of 24.2% of the full span, positioned at the outboard tip of the right semi-span [2]. These dimensions fell within the range of common aileron sizes [33], and there was published data on this aileron configuration from Johnson and Hagerman [2]. Most ailerons typically have a maximum deflection less than  $25^\circ$  to  $30^\circ$  [2], [33], as deflections past  $20^\circ$  to  $25^\circ$  could lead to flow separation and loss of control authority [33].

While Johnson and Hagerman used a symmetric NACA 64A010 airfoil [2], the NACA 64A010 and NACA 0012 two-dimensional lift coefficient curves were nearly identical below stall [65], and had comparable stall angles on wings with similar aspect ratios [2]. The NACA 64A010 had a higher two-dimensional drag coefficient [65], but the primary conclusions of this paper are based on lift coefficient and rolling moment coefficient. Therefore, the difference in airfoils did not preclude comparison of the gapped wings with Johnson and Hagerman’s aileron data.

According to the sign convention, an upwards right aileron deflection was negative, and yielded a positive rolling moment towards the right wing [33]. Thus, we compared the moments of a wing with a right gapped semi-span and a left baseline semi-span, to those of a wing with a single upwards-deflected aileron on the right semi-span.

We compared the representative aileron to each gapped wing using equivalent aileron deflection angles, for the representative aileron on a wing with the same geometry and flow conditions as the baseline wing. Since a higher rolling moment coefficient indicated better roll control, we first determined the maximum rolling moment coefficient of each gapped wing, and its corresponding angle of attack. Then, we linearly interpolated Johnson and Hagerman’s data to find the aileron deflection that produced an equivalent rolling moment coefficient at the same angle of attack [2]. These equivalent aileron deflection angles were likely conservative: Johnson and Hagerman tested at a higher  $Re$  of  $4.5 \times 10^6$ , meaning



the ailerons likely produced larger lift coefficients and rolling moment coefficients than they would at the  $Re$  of  $2.33 \times 10^5$  used here [66]. At this lower  $Re$ , the aileron may create lower lift coefficients and rolling moment coefficients, resulting in even higher equivalent aileron deflection angles.

Similarly to the spoiler, we calculated the aileron force and work from its hinge moments. We first interpolated Johnson and Hagerman’s hinge moment coefficient data for the equivalent aileron deflections of each gapped wing. Johnson and Hagerman normalized the hinge moment by the first moment of area of the aileron [2], which was mathematically and numerically equivalent to normalizing by the product of the aileron area and aileron chord, as done here [2], [33]. We calculated the hinge moments  $M_a$  of each by:

$$M_a = \frac{1}{2}\rho V^2 C_{h,a} S_a c_a + (m_a g) x_{cg,a} \cos(|\delta_a| - \alpha) \quad (2.17)$$

Where  $V$  is the freestream velocity (m/s),  $S_a$  is the surface area of the aileron,  $c_a$  is the chord of the aileron,  $m_a$  is the mass of the aileron (kg),  $C_{h,a}$  is the hinge moment coefficient of the aileron, and  $x_{cg,a}$  is the chordwise location of the center of gravity of the aileron with respect to the hinge line (m). The first term of Eqn. 2.17 was the moment due to aerodynamic loading, and the second term was the moment due to gravity acting on the aileron. We used the density of ABS plastic, an aileron volume of  $41.06 \text{ cm}^3$ , and an  $x_{cg,a}$  of  $0.0196 \text{ m}$ . The physical properties were found from our CAD model of the representative aileron on a wing with the same geometry as the baseline wing. We then estimated the force and work required to deflect the aileron using the same method as the spoiler (Eqn. 2.14, Eqn. 2.15, and Eqn. 2.16) assuming a gearing ratio  $G_k$  of  $80.6 \text{ m}^{-1}$  and efficiency  $\eta_a$  of 100%.

## 2.4 Results and discussion

The objective of the current research was to assess the gapped wings as alternatives to spoilers and ailerons for rapid descent and roll control of energy-constrained UAVs. In the

following subsections, we first present the aerodynamic results of the gapped wings, then discuss effective control surface deflection angles and compare the aerodynamic results to spoilers and ailerons. Finally, we compare the actuation requirements of the gapped wings to the spoiler and aileron.

#### **2.4.1 Gaps decreased lift with insignificant drag change**

We found that increasing the number of gaps significantly decreased the lift coefficient below stall and lowered the maximum lift coefficient of the wing (Fig. 2.5), even when normalized by the smaller gapped wing area. As the number of gaps increased, the wings stalled at a higher angle of attack. For example, the stall angle of attack increased by about  $1^\circ$  between the baseline and the nine-gap wing. The gapped wings also exhibited a sharper stall, indicated by more pointed peaks. Notably, the gapped wings experienced a smaller overall loss of lift due to stall than the baseline wing. A comparison of the baseline wing lift coefficient with previously published NACA 0012 data can be found in Appendix D.

We found that trailing edge gaps generally had an insignificant impact on the drag coefficient. Minimal drag is typically considered advantageous for straight and level flight, climbs, and maneuvers, because lower drag requires less thrust and thus less energy to achieve the same airspeed. However, in the case of rapid descent, a larger drag coefficient can be beneficial in preventing excessive buildup of speed. At high angles of attack in the post-stall regime, the gapped wings did increase drag significantly compared to the baseline wing. But, the increase did not seem dependent on the number of gaps. For example, the nine-gap wing did not appear to produce significantly more drag than the three-gap wing.

The lift and drag phenomena exhibited by the gapped wing could be explained by airflow through the gaps from the pressure side of the wing to the suction side. This type of venting has been seen on slotted wings to reenergize the flow over the trailing edge and delay separation [50]. Wings with various slot configurations generally exhibit similar lift behaviors to the gapped wings: decreased (or unaffected) lift at low angles of attack and increased lift

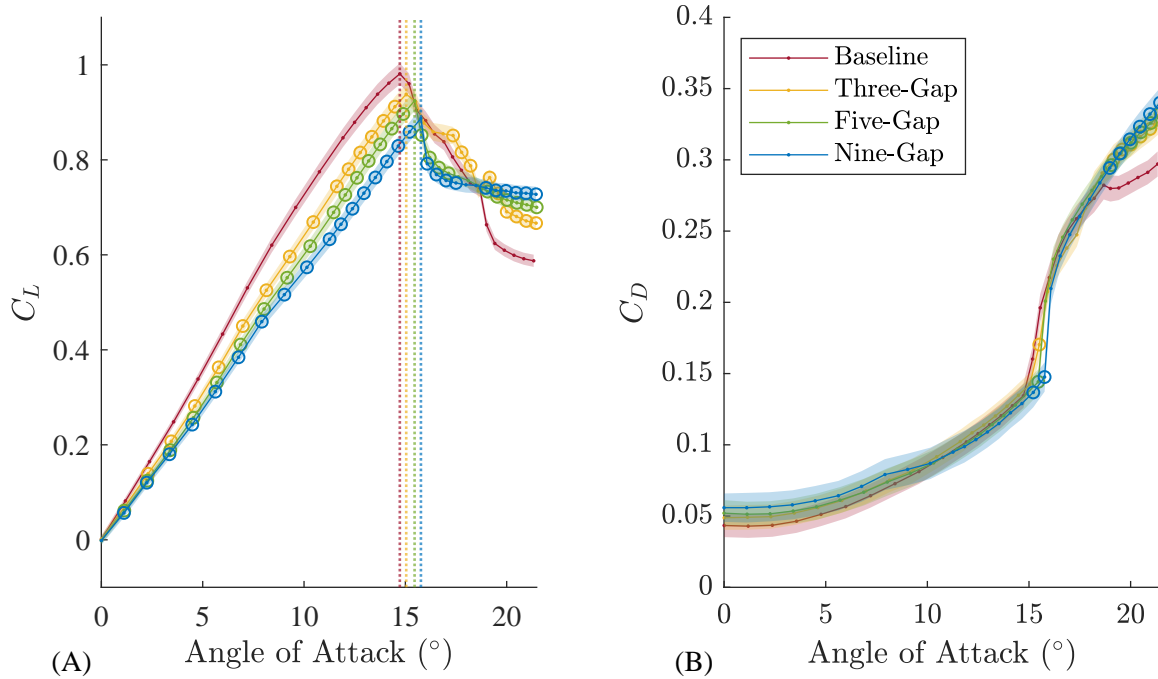


Figure 2.5: Gaps significantly decreased lift but generally did not impact drag. (A) Lift coefficient. The dotted vertical lines indicate the stall angle of attack. (B) Drag coefficient. Statistically significant data are marked with  $\odot$  and insignificant data are marked with  $\cdot$  (Appendix C). The transparent ribbons show the expanded uncertainty at an approximately 95% level of confidence.

at higher angles, relative to a baseline wing [50]–[53]. Some slotted wings also delayed stall [53], and others experienced a sharper stall [51], like the gapped wings. Furthermore, slotted airfoils generally increase drag, although the effects are usually small [50]–[53], much like the drag coefficient of the gapped wings. While the performance similarities between the gapped wings and slotted wings may suggest they share similar flow mechanisms, further work is required to confirm this hypothesis for the gapped wings.

The lift and drag performance of the gapped wings in the post-stall region (specifically, above approximately  $18.5^\circ$ ), has interesting implications for existing UAV rapid descent maneuvers that are performed at high angles of attack, like deep-stall [67]. To perform a deep-stall maneuver, a UAV increases angle of attack past stall, leading to flow separation and rapid lift reduction, in order to make a controlled descent [67]. At high angles of attack,

increasing the number of gaps in the wing reduced the decay of lift, leading to a higher lift coefficient than the baseline wing. Initially, it would therefore seem the gapped wings may be less attractive for deep-stall. However, the gapped wings could provide a method to regulate descent during deep-stall, without requiring full stall recovery. For example, momentarily opening the gaps could recover a small amount of lift production, enabling a temporary lessening of the rate of descent. Further, the increased drag of the gapped wings at these high angles could enable a UAV to reduce its airspeed compared to the baseline wing. This effect would be particularly useful just prior to touchdown, if using a deep-stall maneuver to land, similar to birds [68]. Deep-stall is characterized by an extremely steep and fast descent [67], which requires stronger (and thus heavier) airframe to prevent damage upon touchdown. Opening gapped wings just prior to touchdown could soften the landing and reduce the need for heavier structures.

#### 2.4.2 Gapped wings were less effective than spoiler for descent

Figure 2.6 plots the incremental lift coefficient and incremental drag coefficient of the gapped wings compared to Sun’s spoiler model at the equivalent deflection angles [63]. Figure 2.6 presents the same gapped wing data as Figure 2.5, but in incremental format for comparison with the spoiler.

The greatest lift reduction of the gapped wings occurred with the nine-gap wing at  $11.8^\circ$  angle of attack, for which we calculated an equivalent spoiler deflection of  $-15.0^\circ$ . In the most optimistic case, the gapped wings only captured the range of performance of a spoiler deflected  $-15^\circ$ . However, recall that the maximum spoiler deflection angle is  $-60^\circ$ . At lower angles of attack more commonly used for cruising and maneuvering flight, the gapped wings were even less effective at decreasing the lift coefficient: at about  $5^\circ$  angle of attack the nine-gap wing decreased the lift coefficient only as much as a  $-6.3^\circ$  deflected spoiler.

As dictated by Sun’s model, the spoiler incremental lift coefficient was constant for low angles of attack, then linearly increased above  $10^\circ$  angle of attack [63]. Conversely, the

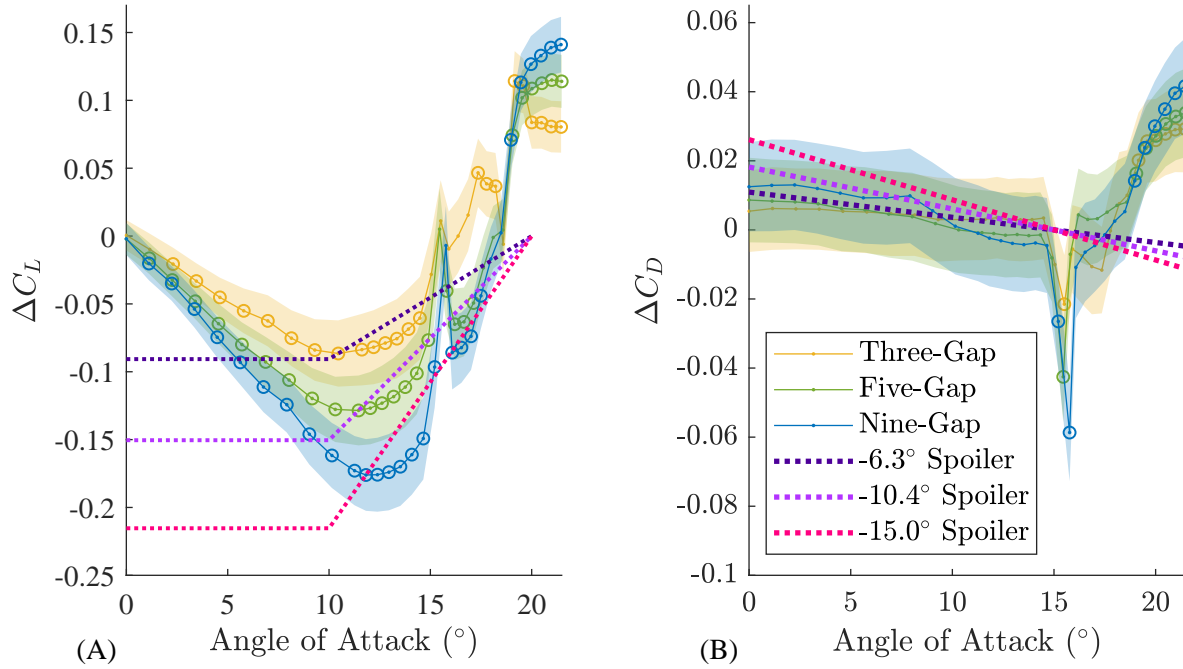


Figure 2.6: Gaps do not decrease lift as much as a spoiler and negligibly impact drag. (A) Incremental lift coefficient. (B) Incremental drag coefficient. Dotted lines show the equivalent spoiler deflections [63]. Statistically significant data are marked with  $\odot$  and insignificant data are marked with  $\cdot$  (Appendix C). The transparent ribbons show the expanded uncertainty at approximately 95% level of confidence.

incremental lift coefficient of the gapped wings was highly dependent on angle of attack. The lift reduction of both the gapped wings and the representative spoiler degraded at angles of attack above approximately  $10^\circ$  to  $12^\circ$ , making both control methods less effective for rapid descent at higher angles. However, while the spoiler could produce its greatest lift reduction across a range of angles of attack, the gapped wing could only achieve optimal performance at a narrow range of higher angles of attack.

The incremental drag coefficients of the gapped wings were nearly constant below approximately  $8^\circ$  angle of attack. From  $8^\circ$  to  $14^\circ$ , the incremental drag coefficient decreased gradually as the number of gaps increased. In the vicinity of stall, the incremental drag coefficient of the gapped wings sharply became negative, before becoming positive again at high angles of attack. Except for high angles of attack, the gapped wings produced a small

Table 2.1: Actuation requirements of nine-gap wing and  $-15.0^\circ$  equivalent spoiler, at  $11.8^\circ$  angle of attack. This scenario was the best rapid descent performance of the gapped wings.

	$-15.0^\circ$ spoiler	Nine-gap wing
Hinge moment	0.0033 N-m	N/A
Actuation force	0.267 N	0.182 N
Actuation work	0.865 mJ	1.54 mJ

and insignificant incremental drag coefficient. This effect was not necessarily desirable for rapid descent, because an increase in drag would help manage airspeed. Conversely, the spoiler drag coefficient was positive below stall and generally produced greater drag than the corresponding gapped wings. The spoiler drag coefficient gradually decreased as angle of attack increased.

To summarize the aerodynamic comparison between the gapped wings and representative spoiler, we found the gapped wings produced a less favorable response for rapid descent (Fig. 2.7). The spoiler model was characterized by a significant decrease in lift and increase in drag, thus meeting our definition for rapid descent. However, the gapped wings resulted in modest lift reduction and insignificant drag increase, so they did not meet all our requirements for rapid descent. Furthermore, the lift reduction of the gapped wings was highly dependent on angle of attack, while the spoiler lift reduction was constant below stall. Thus, the gapped wings appeared less aerodynamically desirable for rapid descent.

While the gapped wings did not perform as well as the representative spoiler, it was possible that the gapped wings could require less actuation force or work due to their planar operation, thus providing an advantage over the traditional spoiler. We calculated the force and work of the best-case scenario of the gapped wings (the nine-gap wing at  $11.8^\circ$  angle of attack), which corresponds to the spoiler model at the equivalent deflection angle  $-15.0^\circ$  (Table 2.1). Note that by design, the spoiler achieves rapid descent in this equivalent deflection case. The nine-gap wing required 31.7% less force but 78.3% more work than the

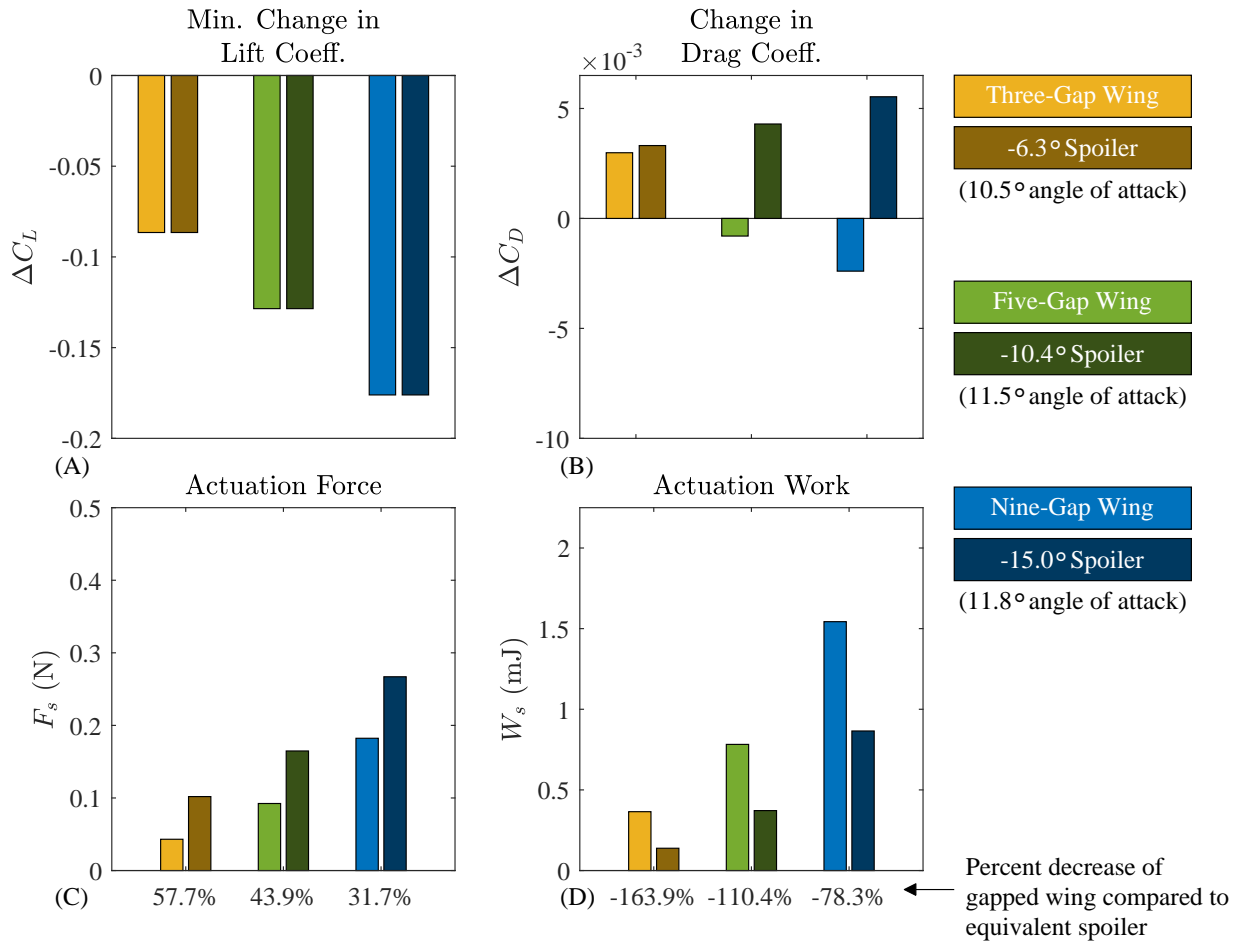


Figure 2.7: The gapped wings were not suitable for rapid descent. (A) The gapped wings produced decreases in lift coefficient equivalent to very low spoiler deflection angles. (B) The gapped wings also did not increase drag as much as the equivalent spoilers. Finally, the gapped wings (C) required less force but (D) required more work than the equivalent spoilers.

equivalent spoiler (Fig. 2.7).

In all, our aerodynamic and actuation results showed that the gapped wings did not provide a significant advantage for rapid descent over conventional spoilers (Fig. 2.7). The gapped wings only captured the lift coefficient reduction of small spoiler deflections (up to  $-15.0^\circ$ ) and required higher actuation work.

Table 2.2: Equivalent aileron deflection angle and associated angle of attack of each gapped wing.

Gapped wing	Equivalent deflection angle	At angle of attack
Three-gap	$-12.2^\circ$	$10.5^\circ$
Five-gap	$-18.7^\circ$	$12.0^\circ$
Nine-gap	$-32.7^\circ$	$13.5^\circ$

### 2.4.3 Nine-gap wing outperformed aileron at high angles

We found that increasing the number of gaps significantly increased the rolling moment coefficient (Fig. 2.8). The five-gap wing had an equivalent aileron deflection of  $-18.7^\circ$  (at  $12.0^\circ$  angle of attack). This meant that the five-gap wing captured comparable performance to nearly the full range of the representative aileron, since maximum aileron deflections are typically  $20^\circ$  to  $30^\circ$  [2], [33]. Further, the nine-gap wing had an equivalent deflection angle of  $-32.7^\circ$  (at  $13.5^\circ$  angle of attack) and was thus capable of producing rolling moment coefficients in excess of the maximum deflected aileron. Johnson and Hagerman only tested up to  $\pm 30^\circ$  of aileron deflection, so we linearly extrapolated their data to determine the equivalent deflection angle of  $-32.7^\circ$  for the nine-gap wing [2]. The equivalent deflection angles are summarized in Table 2.2, and Figure 2.9 shows the rolling moment coefficient and angle of attack used to determine each gapped wing’s equivalent deflection. Note that the equivalent aileron deflections were calculated at angles of attack below stall of the respective gapped wing. Figure 2.8 displays the closest aileron deflections to the equivalent angles, rather than interpolations and extrapolations of Johnson and Hagerman’s data [2].

Roll control effectiveness of an aileron can be estimated as the change in rolling moment coefficient per change in deflection angle [33]. However, since the gapped wings do not deflect, the equivalent aileron deflection angle served as a measure of their roll control effectiveness. For example, at  $13.5^\circ$  angle of attack, a  $-32.7^\circ$  aileron produced a rolling moment coefficient of 0.0305, yielding an estimated roll control effectiveness of 0.0534 per radian (given no rolling moment at the neutral aileron position [2]). The nine-gap wing produced the same rolling



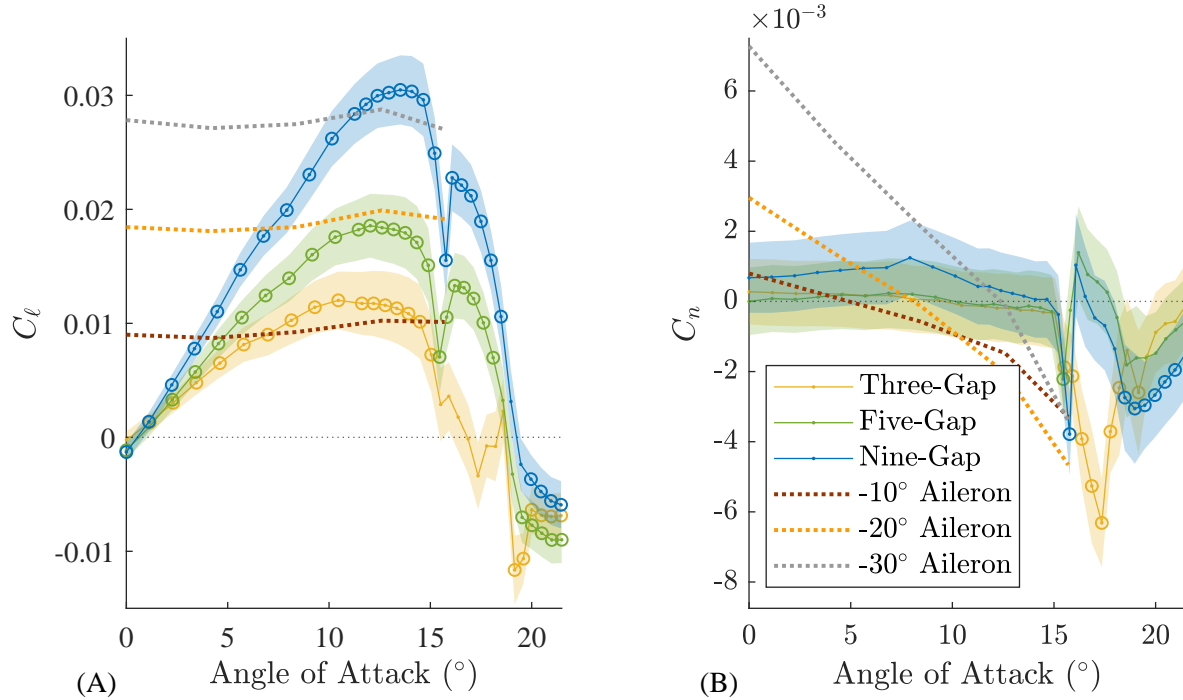


Figure 2.8: Gaps produced comparable roll and less yaw than an aileron [2]. (A) Rolling moment coefficient. (B) Yawing moment coefficient. Dotted lines are various aileron deflection angles [2]. Statistically significant data are marked with  $\odot$  and insignificant data are marked with  $\cdot$  (Appendix C). The transparent ribbons show expanded uncertainties at an approximately 95% level of confidence.

moment coefficient at this angle of attack, giving it an equivalent roll control effectiveness of 0.0534 per radian. Therefore, “opening” nine gaps in the trailing edge had the same roll control effectiveness as deflecting an aileron  $32.7^\circ$  upwards, at that angle of attack. Since the rolling moment coefficient of the aileron remained fairly constant over angle of attack (Fig. 2.8), its roll control effectiveness also stayed relatively constant. Conversely, the rolling moment coefficient of the gapped wings varied strongly across angle of attack (Fig. 2.8): as angle of attack changed, so did the equivalent aileron deflection, and relatedly the roll control effectiveness. Thus, while the roll control effectiveness of the  $-32.7^\circ$  aileron only dropped slightly as angle of attack went to zero, the roll control effectiveness of the nine-gap wing approached zero. In contrast, as angle of attack increased towards stall, the roll control effectiveness of the nine-gap wing exceeded that of the representative aileron, since

the rolling moment coefficient of the nine-gap wing was greater than that of a maximum-deflected aileron.

Unlike the traditional aileron, which had relatively constant rolling moment coefficients over angle of attack, the coefficients of the gapped wings were highly dependent on lift. di Luca et al. found similar trends with a bio-inspired morphing wing that folded its wing tips to change wing area [7]. Like di Luca’s findings, we observed the gapped wings to be most effective at high lift coefficients, meaning low-speed flight. According to di Luca, this low-speed regime is ideal for high maneuverability for small drones, and in these conditions, gapped wing roll control was superior to aileron control. However, the gapped wings did not create as large rolling moment coefficients as conventional ailerons at lower lift coefficients. di Luca proposed a simple control work-around for the gapped wings’ dependence on angle of attack: pairing the gapped wing actuation with a quick pitch-up movement would instantaneously increase lift coefficient to achieve the maximum rolling moment coefficient [7]. The gapped wings could also be augmented with another control surface, such as a slotted flap or aileron, to provide higher rolling moment coefficients at lower lift coefficients.

On a related note, gapped wings may also be more advantageous than ailerons at higher angles of attack because they increased stall angle of attack, and exhibited larger rolling moment coefficients at high angles of attack than the maximum deflected aileron. Aileron deflection angles above  $20^\circ$  to  $25^\circ$  tend to decrease stall angle of attack [2], [33]. Thus, if a UAV flying at a high angle creates a rolling moment with a large aileron deflection, it is at risk of stalling. Conversely, the gapped wings delayed stall angle of attack. So, if a UAV flying at a high angle creates a rolling moment by opening gaps, it is at a lower risk of triggering stall. In addition, as seen in Figure 2.8, the gapped wings created a much higher rolling moment coefficient than the maximum deflected aileron ( $30^\circ$ ) at high angles of attack.

These effects are especially poignant during flight at high angles of attack and low air-speed, such as short-field takeoff and slow-flight. Consider a UAV in slow-flight, flying in the vicinity of stall, that needs to perform a banking maneuver with ailerons. It can only

make small aileron deflections or it risks stalling, and thus has a limited attainable rolling moment coefficient. If the UAV makes too large aileron deflections to achieve a higher rolling moment coefficient, it could stall prematurely. However, a UAV in slow flight with gapped wings would be able to create a much larger rolling moment coefficient with a lower risk of stall, because the gapped wings increase the stall angle of attack, and offer higher rolling moment coefficients than the maximum deflected aileron. Thus, the gapped wings may enable UAVs to roll at higher angles of attack and expand the maneuvering envelope.

At high angles of attack above about  $18^\circ$ , the rolling moment coefficient of the gapped wings became negative. This counter-intuitively indicated a roll away from the gapped wing, and was due to the fact that the gapped wings produced a higher lift coefficient than the baseline wing at these high angles (Fig. 2.5). The switch in rolling moment coefficient sign and the dependence of the rolling moment coefficient on angle of attack may require a more complex controller that is capable of handling nonlinear aircraft models [69].

Note that the gapped wing rolling moment coefficients were slightly negative at  $0^\circ$  angle of attack. Since the gaps preserved the symmetry of the airfoil, and thus produced the same zero-lift as the baseline wing at  $0^\circ$ , we expected the rolling moment coefficient to be zero here. However, all the wings, including the baseline wing, produced a small (less than 0.01) but measurable rolling moment coefficient (before taking the difference with the baseline wing). Therefore, we attributed the non-zero rolling moment coefficient at  $0^\circ$  not to the gaps, but to experimental sources of variance that we were not reasonably able to quantify for the uncertainty analysis. These sources potentially included small manufacturing defects or asymmetries in the wings [59], slight compliance in the mounting scheme, or the Type B variance of the load cell (discussed in Appendix C).

The significant increase in rolling moment coefficient of the gapped wings was accompanied by a negligible rise in drag coefficient (Fig. 2.5). While the insignificant change in drag coefficient was not necessarily desirable for rapid descent, it is more advantageous for roll control since a larger drag would require more thrust to maintain airspeed and altitude

while banking. Higher drag differentials could also be tied to larger yawing moments.

In general, the yawing moment coefficient was not significantly impacted by the gaps, with the exception of some higher angles of attack (Fig. 2.8). The yawing moment coefficient was relatively constant below stall, unlike the aileron, which steadily decreased as angle of attack increased. At low angles of attack, the gapped wings' yawing moment coefficient was the same sign as the rolling moment coefficient (positive). The three-gap and five-gap wing yawing moment coefficients became the opposite sign from roll around  $10^\circ$ , and the nine-gap wing around  $15^\circ$ . At higher angles of attack, the yawing moment coefficient of the three-gap wing remained the same sign as roll, while the sign of the five- and nine-gap wing switched again before ultimately returning to the same sign as the rolling moment coefficient. The roll-yaw coupling, and the fact that it changed sign multiple times, may require a more complex controller [70]. The coupling trend was also distinct from that of the ailerons: tip effects caused the aileron yawing moment coefficient to become steadily more negative as angle of attack increased, and the rolling moment coefficient stayed positive [2].

Figure 2.9 summarizes the rolling and yawing moment coefficients of the gapped wings and equivalent aileron deflections and illustrates several key trends. Firstly, as intended, the rolling moment coefficient of each gapped wing was equal to its equivalent aileron and increased as the gaps increased. Secondly, the gapped wing yawing moment coefficients grew steadily less negative as the number of gaps increased, such that the nine-gap wing yawing moment coefficient was positive (the same sign as the rolling moment coefficient). However, the yawing moment coefficients of the equivalent aileron deflections were all negative, and the opposite sign of the rolling moment coefficients.

While the gapped wings produced rolling moment coefficients equivalent to, and occasionally higher than, traditional ailerons, it was also important to compare actuation requirements. We found the gapped wings decreased actuation force by at least 88.4% and decreased actuation work by at least 80.4% compared to the equivalent aileron deflections (Fig. 2.9). The results of the aileron comparison indicated that the gapped wings may be

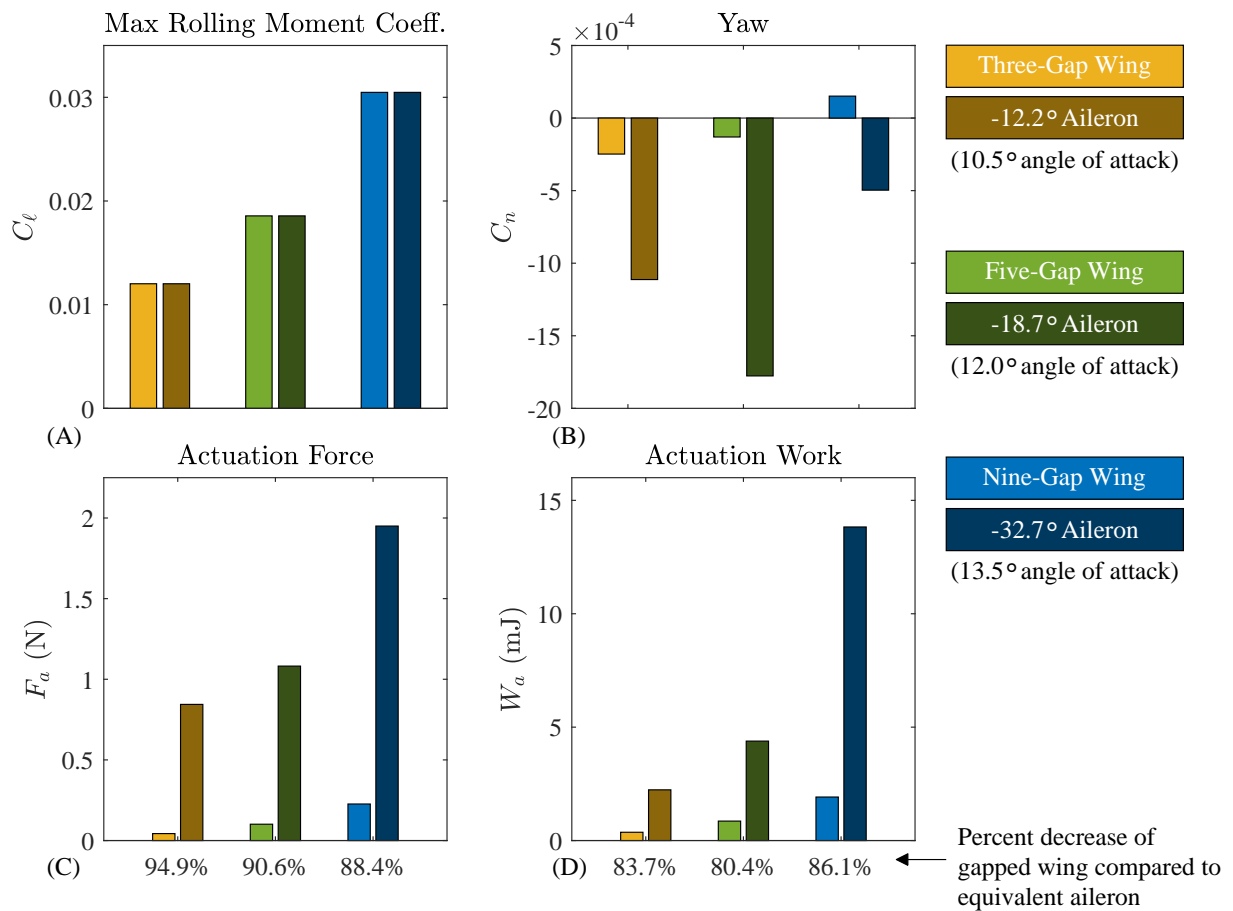


Figure 2.9: Gaps were effective for roll control in some cases. (A) Maximum rolling moment coefficient of each gapped wing and equivalent aileron (equal by design). (B) Yawing moment coefficient. (C) Required actuation force (N). (D) Required actuation work (mJ). The percent decreases in force and work of the gapped wing compared to the aileron are below each pair.

a useful alternative to ailerons for roll control. The gapped wings fully captured the range of rolling moment coefficients produced by a representative aileron. While there was not a clear benefit in yawing moment coefficients, the gapped wings required a fraction of the actuation work and force of the ailerons. The comparable roll control and lowered actuation costs make the gapped wings a potentially beneficial alternative to traditional ailerons for banking control of energy-constrained UAVs, particularly at lower flight speeds.

## 2.5 Limitations

The current chapter focused on the aerodynamic effects of trailing edge gaps on a symmetric airfoil. We neglected the potential role of bird wings' camber in our whiffing-inspired design. It is possible that replicating this work with a cambered wing would better approximate whiffing and produce greater changes in the lift coefficient, rolling moment coefficient, and other parameters.

Since the spoiler model and representative aileron were three-dimensional wings, and the gapped wings approximated two-dimensional flow, it is important to consider the potential impact of tip effects on the comparisons. It was shown that the gapped wings do not decrease lift comparably to a spoiler. The lack of tip effects may have artificially increased the lift of the gapped wings [56], meaning this conclusion was conservative and three-dimensional gapped wings may have performed even less desirably than a spoiler. Conversely, because tip effects tend to increase drag [56], three-dimensional gapped wings may have a higher drag coefficient closer to that of the spoiler. In terms of roll control, decreasing aspect ratio tends to decrease the rolling moment coefficient [57]. This tip effect makes the comparison of the two-dimensional gapped wings to the representative aileron less conservative, since the three-dimensional gapped wing rolling moment coefficient may be lower than we measured. Decreasing aspect ratio makes the yawing moment more favorable at high angles of attack [57], but since the gapped wings were two-dimensional and thus could not produce adverse yaw, it is difficult to comment on how tip effects may impact the sign of the yawing moment coefficients relative to the rolling moment coefficients of the gapped wings.

The gapped wings have several limitations. Firstly, the gapped wings do not appear to be beneficial for rapid descent applications. While the gapped wings showed promise for roll control actuation, the moment coefficients of the gapped wings were highly dependent on the lift coefficient, which could require more complex controllers. Further, the gapped wings did not create as much rolling moment coefficient at lower lift coefficients as conventional ailerons. The gaps may also be mechanically complex to implement.

Finally, note that these comparisons were performed for a single gap dimension ( $\frac{2c}{3} \times \frac{b}{48}$ ). Thus, the results cannot be generalized to all gapped wing configurations. Chapter V addresses how varying gap size, number of gaps, and other parameters alters the performance of the gapped wing. Tailoring the gap parameters could thus also improve the performance of the gapped wing relative to the aileron and spoiler.

## 2.6 Chapter summary

Here we investigated if whiffing-inspired gapped wings could provide advantageous alternatives to spoilers for rapid descent or ailerons for banking. To do this, we tested wings with various numbers of gaps along the trailing edge at a low  $Re$  in a wind tunnel and extracted the lift, drag, rolling moment and yawing moment coefficients. Next, we calculated equivalent spoiler and aileron deflection angles based on previously published aerodynamic data, and compared the results to the gapped wings. Finally, we estimated the actuation force and work required to operate a gapped wing concept and compared to previously published actuation data on the representative spoiler and aileron. To the best of our knowledge, this is the first time that avian whiffing served as inspiration for a UAV control surface.

We found that, except for high angles of attack, increasing the number of gaps in the wing decreased the lift coefficient, delayed stall, had negligible impact on the drag coefficient, increased the rolling moment coefficient, and resulted in yaw in the same direction as roll both at low and very high angles of attack. The gapped wings did not decrease the lift coefficient as much as a fully deflected spoiler, did not significantly increase the drag coefficient, and required greater work to operate. Thus, they may not be a suitable alternative to spoilers for rapid descent.

The gapped wings did provide comparable aerodynamic performance to conventional ailerons: the nine-gap wing was able to produce an equivalent rolling moment coefficient to a representative aileron deflected  $32.7^\circ$  upwards at  $13.5^\circ$  angle of attack. Additionally, the nine-gap wing required 88.4% less force and 86.1% less work to achieve the same rolling

moment coefficient as the equivalent deflected aileron, making the gapped wings an attractive alternative to conventional ailerons for roll control of energy-constrained UAVs. Furthermore, these benefits occurred at a high lift coefficient, suggesting that the gapped wing would be most suitable for a UAV flying at low airspeeds, and that it would be ideal to perform a pitch-up maneuver prior to banking to capture the maximum performance of the gapped wings. Their performance at high lift coefficients also indicates that the gapped wings could extend the envelope over which UAVs perform roll maneuvers. In all, morphing trailing edge gaps inspired by whiffing could provide a novel actuation method for roll control in energy-constrained UAVs.

## **2.7 Data availability**

All raw data and MATLAB codes used for post-processing and analysis are available publicly at DOI: [10.6084/m9.figshare.c.5735009](https://doi.org/10.6084/m9.figshare.c.5735009).



## CHAPTER III

# Gaps Re-Energized the Boundary Layer and Required Less Work Than Single Aileron for Large Rolling Moments

### 3.1 Overview

It is speculated that feather rotation-inspired gaps could be used as roll control surfaces on UAVs. However, the understanding of the fluid mechanics and required actuation work of this novel gapped wing were rudimentary. Here, we used a commercial computational fluid dynamics solver to model the flow over a whiffing-inspired gapped wing and compare its analytically estimated work requirements to an aileron. The simulation results agreed well with previous experimental data. While the gaps thickened the local boundary layer over the wing, they re-energized the flow over the suction side of the trailing edge. Further, each gap produced a pair of strong vortices, with the gap nearest to the wing root producing the largest vortex. The flow within a gap recirculated, and moved largely in the streamwise direction. These flow mechanics caused the gapped wing to require higher actuation work than the aileron at low rolling moment coefficients. However, above rolling moment coefficients of 0.0182, the gapped wing required less work and ultimately produced a higher maximum rolling moment coefficient. Despite the variable control effectiveness, the data suggested that the gapped wings could be a useful roll control surface for energy-constrained UAVs at

high lift coefficients, when compared to a single aileron.

## 3.2 Motivation and background

The previous experimental work investigated novel wings with different numbers of gaps in the trailing edge (Chapter II). The gapped wings were not a suitable alternative to spoilers, since they did not decrease lift as much as a spoiler and required greater work to actuate. Conversely the results implied that the gapped wings could be beneficial for roll control compared to a wing with a single deflected aileron. The gapped wings produced a greater maximum rolling moment coefficient than the aileron for less work, showing promise for roll control at high lift coefficients for energy-constrained UAVs.

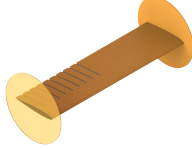
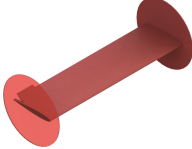
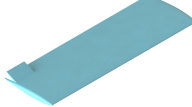
However, the aerodynamic effects of the gaps on the airflow over the wing remained unknown. Furthermore, the previous work estimates were rudimentary, and based more on classical mechanics as opposed to aerodynamic loading. Here we used Siemens STAR-CCM+, a commercial computational fluid dynamics (CFD) software, to simulate the gapped wing and representative aileron. The CFD simulations built insight into the aerodynamic effects of the gaps on the overall flow field, as well as flow phenomena present within a gap. Further, they informed more accurate actuation work estimates based on aerodynamic loading. Ultimately, the simulations provided additional evidence that gapped wings may require less work than an aileron at high rolling moment coefficients, and may produce a higher maximum rolling moment coefficient. To the best of our knowledge, this work represented the first computational study of flow through gaps along the chord of a wing, and an important step in assessing the capabilities of novel whiffing-inspired wings as control surfaces.

### 3.3 Methods

Our use of CFD appropriately complemented the previous experimental study. The experimental work identified the general performance and behaviors of the gapped wings. The simulations then provided a deeper understanding of underlying flow mechanisms without the need for complex experimental setups. The CFD simulations also directly calculated aerodynamic forces on all surfaces of the wing, allowing us to estimate actuation work without costly prototypes, equipment, and instruments. Furthermore, simulating the gapped wing enabled future cost-effective and timely parameter sweeps, optimization studies, and design iterations. Finally, experimentally validating the computational simulations demonstrated the reliability of both datasets.

Before conducting our CFD study, we defined the wing configurations to be simulated (Table 3.1). The first configuration (SI-gapped wing) is the same wing geometry and flow parameters as Sigrest and Inman’s previously conducted gapped wing experiments (Chapter II). We also simulated a baseline SI wing without gaps (SI-baseline wing), which is discussed further in Appendix E. The second configuration (JH-aileron wing) is the same wing geometry and flow parameters as Johnson and Hagerman’s previously conducted aileron experiments [2]. These two configurations were used to experimentally validate the CFD simulations, and a mesh convergence study was conducted on the SI-gapped wing. However, the JH-aileron wing and SI-gapped wing had different geometries and flow parameters. To reconcile these differences, we simulated an aileron of the same relative dimensions as the JH-aileron, but with the wing geometry and flow conditions of the gapped wing (SI-aileron wing). Simulating the SI-aileron wing allowed us to directly compare rolling moment coefficients and actuation work of the gaps and aileron [2]. We also simulated gaps on a wing with the geometry and flow conditions of the JH-configuration (JH-gapped wing). We found that the JH-gapped wing behaved very similarly to the SI-gapped wing. Therefore, we focused here on just the SI-gapped wing results. We address the JH-gapped wing more closely in Chapter IV and Appendix B. While the previous experimental study compared the gapped wings to a spoiler

Table 3.1: Three wing configurations were simulated using CFD, to allow for experimental validation and direct comparison of the aileron and gapped wings.

	SI-Gapped Wing	SI-Aileron Wing	JH-Aileron Wing
			
Data sources	Experiment, CFD	CFD	Experiment, CFD
Airfoil	NACA 0012	NACA 0012	NACA 64A010
Velocity (m/s)	16	16	86.2629
$Re$	$2.33 \times 10^5$	$2.33 \times 10^5$	$4.5 \times 10^6$
Simulated angles of attack	$0^\circ$ to $12^\circ$	$0^\circ$ to $10^\circ$	$10^\circ$
Density (kg/m <sup>3</sup> )	1.1565	1.1565	1.225
Kinematic Viscosity (Pa-s)	$1.58 \times 10^{-5}$	$1.58 \times 10^{-5}$	$1.4607 \times 10^{-5}$
Ref. Area (m <sup>2</sup> )	0.1742	0.1858	1.8
Ref. Length (m)	0.8128	0.8128	2.3622
Hinge Moment Ref. Area (m <sup>2</sup> )	–	0.0056	0.0544
Hinge Moment Ref. Length (m)	–	0.0572	0.1905

and aileron (Chapter II), we focused solely on the aileron comparison because the gapped wings were not found to be beneficial for rapid descent. We also only simulated the wing with nine gaps, since it produced the greatest rolling moment coefficients in the previous study. All airfoil ordinates were obtained as described in Appendix A. Note that Table 3.1 presents the relevant dimensions with units, because these are the values that were directly used to model the wings and run the CFD simulations. The dimensional values also highlight the importance of modeling the SI-aileron wing as a direct comparison to the SI-gapped wing.

We used Siemens STAR-CCM+ to perform steady-state three-dimensional Reynolds-averaged Navier-Stokes (RANS)-based CFD simulations. Compared to higher-fidelity CFD approaches such as scale-resolving simulations, RANS provided us with an appropriate balance between simulation accuracy and computational cost. Since we sought to measure average force and moment values and capture the general effects of the gaps on the flow field, RANS was suitable for our needs. We were primarily interested in high-lift configurations and chose the  $k - \omega$  SST turbulence model for its ability to capture flow separation, particularly in the low- $Re$  flow regime [71], [72]. We used the uncoupled solver for the

JH-aileron wing and SI-aileron wing, and the coupled solver for the SI-gapped wing since it presented more of a challenge to converge. We monitored the unscaled residuals and terminated the simulation after  $x$ -momentum,  $y$ -momentum,  $z$ -momentum, continuity, and turbulent kinetic energy (TKE) were all below  $1 \times 10^{-4}$ , and after specific dissipation rate (SDR) was reduced by at least four orders of magnitude. In two cases, SDR only relatively fell below  $7.5 \times 10^{-4}$ . This typically took about 500 iterations for the SI-gapped wing, between 200 and 850 iterations for the SI-aileron wing, and between 700 and 875 iterations for the JH-aileron wing.

The three-dimensional volume mesh was generated using STAR-CCM+'s built-in tools (Fig. 3.1). We used an unstructured polyhedral mesh with extruded prism layers near the wing surface to capture the boundary layer. The prism layer parameters were chosen such that the wall  $y^+$  value remained below one for the majority of the wing surface and the growth ratio was less than 1.3. The prism layers were also applied to the vertical gap faces. Wake refinement was applied about two chord lengths behind the wing and endplates.

We normalized the force and moment coefficients by the planform area of the full wing, minus the planform area of the endplates and gaps where applicable. The rolling and yawing moment coefficients were also normalized by the full wingspan, and the pitching moment coefficient was further normalized by wing chord, as is standard [73]. The reference areas and lengths are shown in Table 3.1. Moment coefficients were measured and reported about the quarter-chord at the wing root. The previously conducted experiments tested half-span models in a wind tunnel using the reflection plane methodology, then corrected the data to a full asymmetric wingspan with the control surface on only the right semi-span [2] (Chapter II). Conversely, we simulated the full asymmetric span in a bullet-shaped domain to avoid reflection plane corrections in post-processing. The CFD domain boundaries were 12.3 times the wingspan of the SI-gapped wing and SI-aileron wing and 10 times the wingspan of the JH-aileron wing. All data were reported in the wind axes [59]. According to sign conventions, a negative aileron deflection angle was upwards and a positive aileron hinge

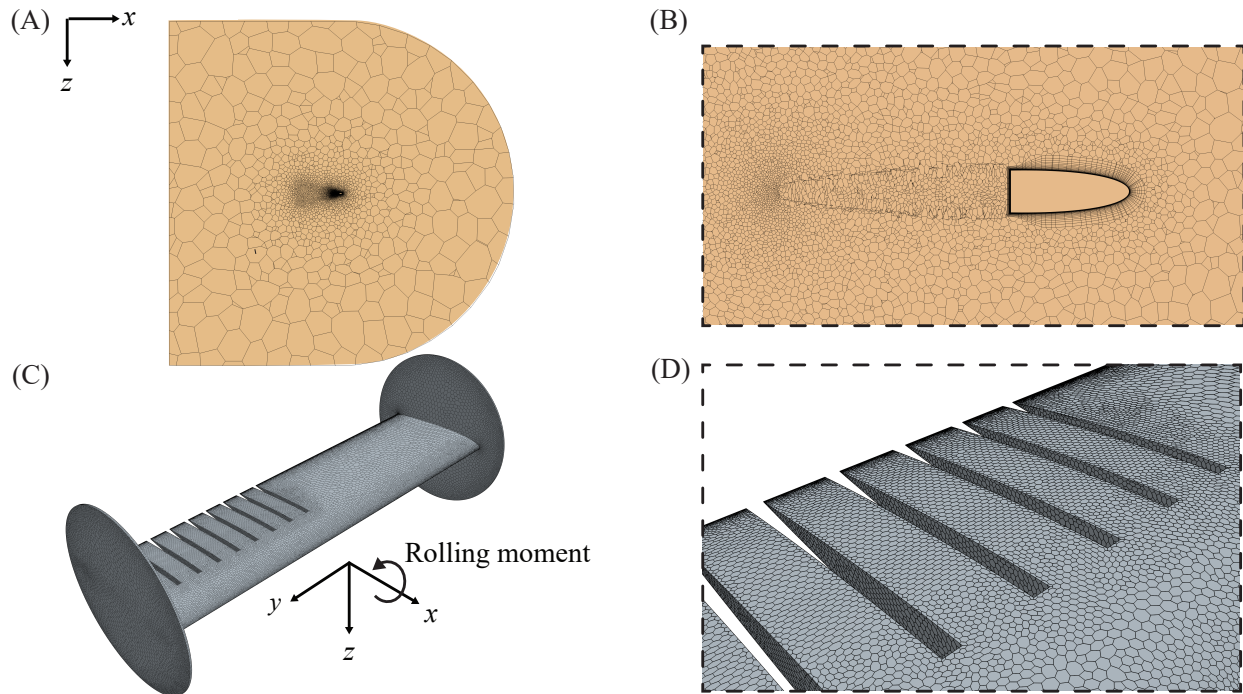


Figure 3.1: Using STAR-CCM+, we created unstructured polyhedral meshes with prism layers. (A) Cross-section of the volume mesh for the SI-gapped wing. (B) Detailed view of the volume mesh cross-section. (C) Surface mesh on the wing. Data were reported in wind axes [19] with a positive rolling moment as shown. (D) Detailed view of the surface mesh near the gaps.

moment was downwards towards the neutral position [33], [59]. Positive rolling moments were produced by an upwards aileron deflection and open gaps.

### 3.3.1 SI-gapped wing experimental validation

To experimentally validate the SI-gapped wing—the nine gap wing tested by Sigrest and Inman (Chapter II)—we replicated the experimental geometry and flow conditions in CFD (Table 3.1). Each gap had a length  $\frac{2}{3}$  of the wing chord and a width  $\frac{1}{48}$  of the half-span. Additionally, we simulated the SI-baseline wing without gaps, presented in Appendix E. The previous experimental work also provides an in-depth comparison of the behavior of the gapped wing and baseline wing (Chapter II). In the previous experiment, two circular endplates were used to reduce tip effects and approximate two-dimensional flow over the wing. We included the endplates in the simulations to ensure that the model was appropriately

validated. The effects of the endplates on the flow are detailed in Appendix B. We simulated the SI-gapped wing at angles of attack from  $0^\circ$  to  $12^\circ$ .

The previous experiment and current CFD simulations used two different approaches to estimate the actuation work of the gapped wing. Both methods considered a model with “gap covers” that slid along the span of the wing to cover the gaps (Fig. 3.2 (A)) or open them (Fig. 3.2 (B)). In the previous experiment, the work to open the gaps was estimated as a friction force acting on the gap covers over the width of the gap, with the normal force estimated as the lift on the gap covers minus their weight (Chapter II, Eqn. 2.8). In the current study, we sought a more accurate estimate based on aerodynamic loading as opposed to classical mechanics. We calculated the actuation work directly from aerodynamic forces on the gaps, combining the CFD results with an analytical approach. We assumed that only aerodynamic forces acted on the gap covers, and excluded gravity, friction, and other forces. From the CFD data, we measured the force acting on all nine vertical gap faces (light blue in Figure 3.2 (C)) in the spanwise direction. Then, we multiplied the force by the width of a gap. This quantity represented the work required to open the gaps by retracting the entire gap face into the wing, assuming a constant force over the actuation distance. We assumed a constant force because the models are static and rigid, thus the gaps remain a constant width. However, this work was calculated on a larger face than is realistic. The work should only be calculated on the area corresponding to the gap cover (dark brown in Figure 3.2 (C)), since only this gap cover would move during actuation. Therefore, we analytically estimated the work to actuate the gap covers by scaling by the ratio of the two areas  $R$ , according to:

$$W_{gc} = RF_g b_g \quad (3.1)$$

$$R = \frac{A_{gc}}{A_g} \quad (3.2)$$

This equation represented the work required to slide just the gap covers to open the gaps. We analytically scaled the work because of the limitations of modelling small features

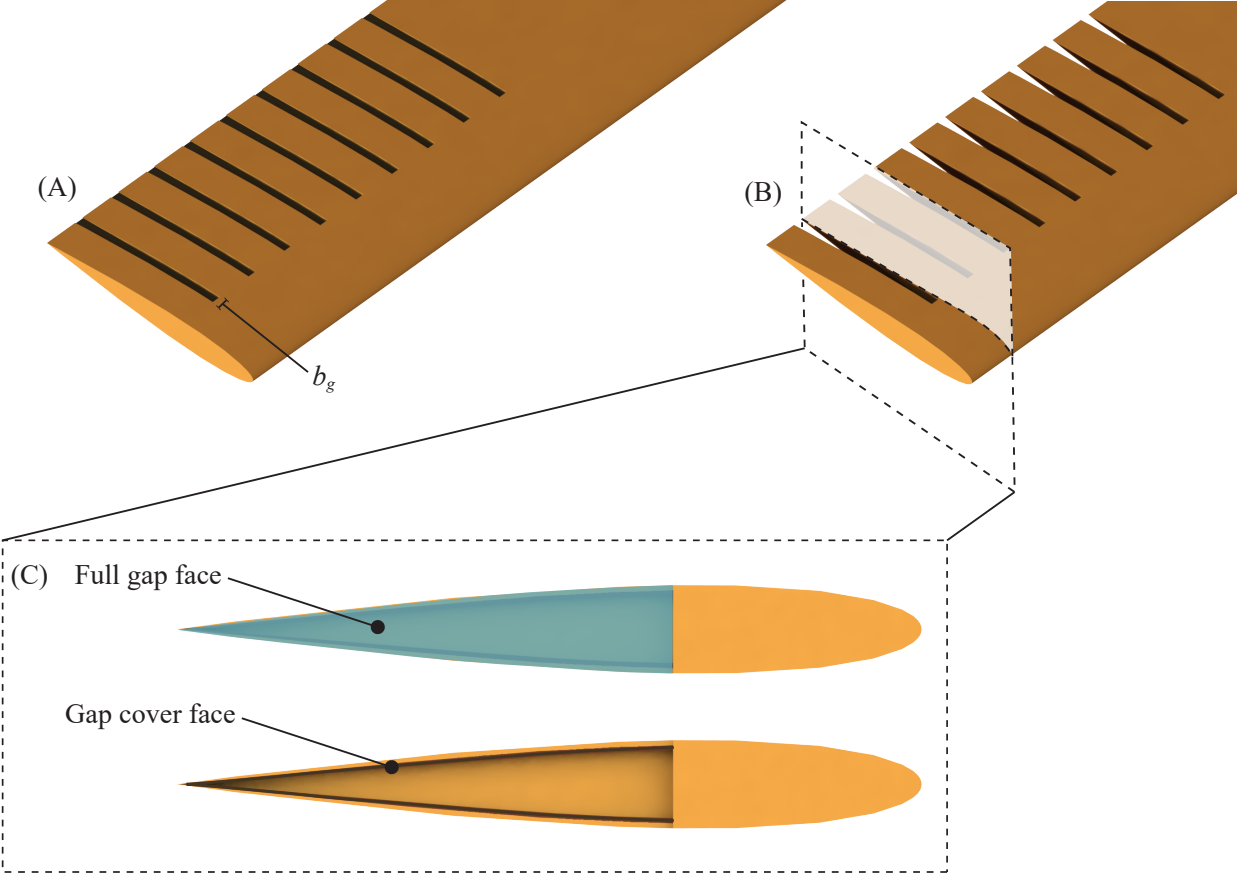


Figure 3.2: The gapped wing actuation work was based on a model with gap covers (dark brown) that slid spanwise to open and close the gaps. (A) Gaps closed. (B) Gaps open. (C) Cross-section of a gap. Force was measured on the full gap face (light blue) in the spanwise direction. The gap cover face (dark brown) was used to analytically estimate the work.

in CFD. However, using Eqn. 3.1 made the work estimate dependent on the geometry of the gapped wing model, specifically the area ratio  $R$ . Thus, the results were dependent on the assumed geometry of the gap covers. The unscaled work values (for  $R = 1$ ) are included in Figure B.1 for completeness. Here, we assumed an area ratio  $R$  of 0.0964 based on a CAD model with 0.794mm ( $\frac{1}{32}$  in.) thick gap covers.

### 3.3.2 JH-aileron wing experimental validation

We also experimentally validated the JH-aileron wing using the geometry and flow conditions from Johnson and Hagerman [2] (Table 3.1). Experimental values for air density and



viscosity were not provided, so we assumed standard atmospheric conditions. We simulated a single aileron on the right semi-span, with a chord of 25% of wing chord and a span 24.2% of the semi-span starting at 72.6% of the half span [2] because this is the same configuration used in Chapter II and these dimensions are within the typical range for an aileron [33]. We calculated the aileron hinge moment about the hinge axis at 75% of wing chord and normalized it by aileron area and aileron chord. Since the rolling moment coefficient of the aileron was largely constant across angle of attack [2], we simulated the wing at a constant 10° angle of attack, varying aileron deflection angle from 0° to −30°. We estimated the work to deflect the aileron against aerodynamic loads by directly measuring the hinge moment from the CFD results, then multiplying it by deflection angle:

$$W_a = -M_a \delta_a \tag{3.3}$$

Similarly to the gapped wing, this work estimate assumed that only aerodynamic forces are acting on the aileron, and that the hinge moment was constant across deflection. The constant hinge moment assumption was due to the static and rigid nature of the model.

### 3.3.3 SI-aileron wing for direct comparison

There were several differences in the wing geometry and flow parameters of the JH-aileron wing and the SI-gapped wing (Table 3.1). Thus, in order to directly compare the aileron with the gaps, we simulated an aileron on the right semi-span of a wing with the same geometry and flow conditions as Sigrest and Inman’s wing (Table 3.1). This SI-aileron wing had a 0.2286m chord, 0.4064m semi-span, and circular endplates as per Chapter II. The aileron retained the same relative dimensions as the JH-aileron wing: a width 24.2% of the semi-span and a length 25% of the chord with the hinge axis at 75% wing chord. We simulated this wing at angles of attack from 0° to 10° and with aileron deflections between 0° to −30°. We estimated the actuation work according to Eqn. 3.3, assuming a constant hinge moment.

### 3.3.4 General comments on work estimates

To keep our comparison between gapped wing and aileron wing actuation one-to-one, our estimates (Eqn. 3.1 and Eqn. 3.3) did not include the work required to pitch either wing to the simulated angle of attack. We considered the gapped wing to already be positioned at the angle of attack when actuated. Thus, it was not necessary to include the pitch work in our estimates. Since the rolling moment coefficient of the aileron is insensitive to angle of attack [2], we assumed it was already angled when actuated and exclude the pitch work. In addition, angle of attack is typically controlled by an elevator, flaps, or other symmetrically deployed control surfaces. Estimating the work to change angle of attack would require modelling a full hypothetical UAV. Making these assumptions to estimate pitch work would not necessarily improve the fidelity of the actuation work estimates, because such assumptions can greatly alter aircraft performance. Thus we simulated just the wings with the single relevant roll control surface, and neglected the work required to change the wing's angle of attack.

The work estimates for the SI-aileron wing and SI-gapped wing were likely over-predictions because we assumed constant force over gap cover displacement, and constant hinge moment over aileron deflection. In reality, hinge moment increases with deflection [2] and the force on the gaps likely changes as they open. This topic is addressed in Chapter V and Appendix F.

## 3.4 Mesh convergence study

We conducted a mesh refinement study on the SI-gapped wing, for the lift coefficient and rolling moment coefficient at 3° angle of attack (Fig. 3.3). Five meshes were generated with approximately 1.0 million, 2.5 million, 3.5 million, 6.1 million, and 9.0 million cells. The meshes were locally refined around areas of fine geometry, such as the gaps and endplate edges. We computed the grid factor of each mesh according to [74]:

$$G = N_{cells}^{-2/3} \quad (3.4)$$

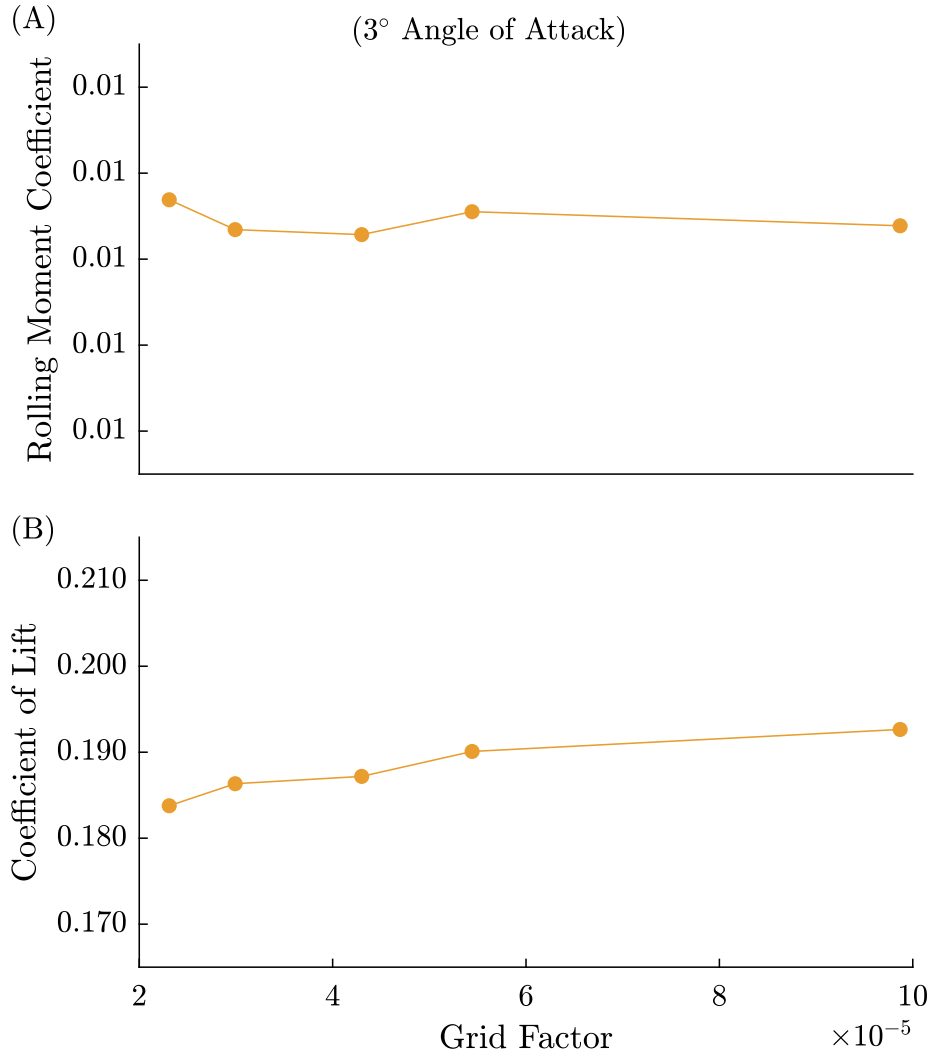


Figure 3.3: We performed a mesh convergence study on the SI-gapped wing to determine an appropriate mesh density for each wing configuration. We investigated (A) rolling moment coefficient and (B) lift coefficient, both at  $3^\circ$  angle of attack.

Neither the lift coefficient nor the rolling moment coefficient behaved linearly as the mesh is refined, but this was expected due to uneven refinement of the polyhedral mesh and the complex flow field (Fig. 3.3). In particular, the rolling moment coefficient results were in line with typical moment predictions in CFD. For example, the pitching moment coefficients computed as part of the AIAA CFD Drag Prediction Workshop showed not only considerable spread between entries, but also differing trends [75]. Some solvers converged from below and

others from above, and a substantial number of entries did not obtain a linear convergence region during refinement [75]. Based on the mesh refinement study, we used the 3.5 million cell mesh for the SI-gapped wing, 2.6 to 3 million cells for the SI-aileron wing, and 2.2 to 2.8 million cells for the JH-aileron wing. The exact number of cells depended on aileron deflection and angle of attack. This refinement study ensured that we used an appropriate level of mesh density for each case. For the mesh density chosen, we found good agreement between the CFD simulations and previous experimental data.

### 3.5 Experimental validation

The SI-gapped wing CFD results generally agreed well with the previous experimental results from Chapter II (Fig. 3.4). We simulated the wing at several angles of attack ranging from  $0^\circ$  to  $12^\circ$ . The lift coefficient predictions were within experimental uncertainty except for the data point at  $10^\circ$  angle of attack, which differed from the experiment by 0.013, and the data point at  $12^\circ$  angle of attack, which was partially converged likely indicating separated flow and stall. Excluding the stalled data point, the drag coefficient fell within experimental uncertainty. The rolling moment coefficient was generally within experimental uncertainty and differed by at most 0.0038. The  $12^\circ$  stall angle of attack predicted by CFD was lower than the stall angle of  $14.7^\circ$  angle of attack found experimentally. It is common for RANS to under-predict stall angle [76]. The experimental validation of the SI-baseline wing also matched well (Appendix E).

The CFD results of the JH-aileron wing also agreed well with the experimental data (Fig. 3.5) [2]. We compared simulated and experimental data across a range of upwards aileron deflections from  $0^\circ$  to  $-30^\circ$ , at a constant  $10^\circ$  angle of attack. The rolling moment coefficient differed from the experimental data by less than 0.0012, and the hinge moment coefficient differed by less than 0.022.

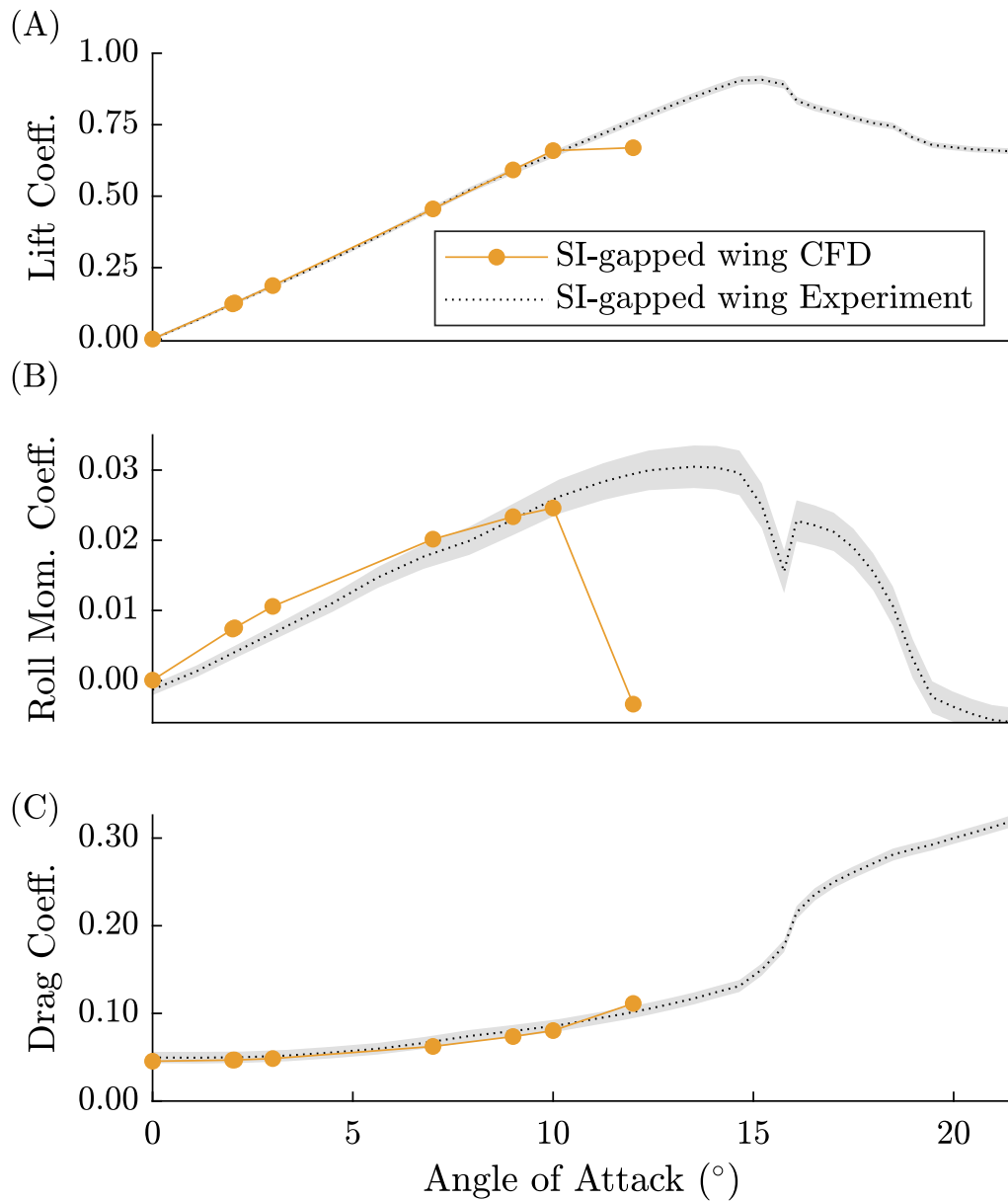


Figure 3.4: The SI-gapped wing CFD results agreed well with previous experimental data from Chapter II, considering the (A) lift, (B) rolling moment, and (C) drag coefficient. The data point at 12° angle of attack was partially converged, likely indicating stall. The grey transparent ribbon around the experimental data represents the uncertainty at an approximately 95% confidence level.

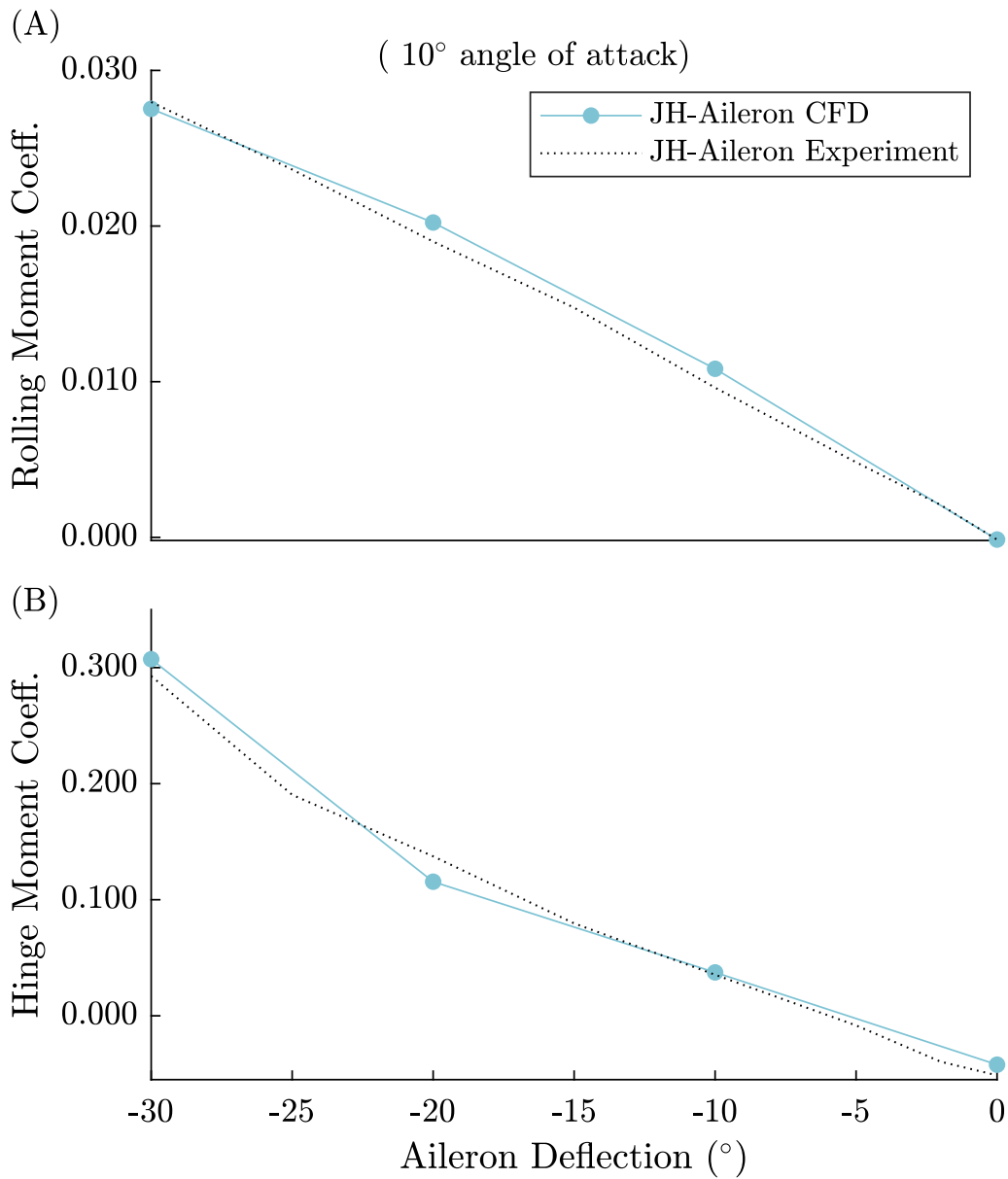


Figure 3.5: The JH-aileron wing CFD results agreed well with previous experimental data [2], comparing the (A) rolling moment and (B) hinge moment coefficient at 10° angle of attack. Negative deflection angles are upwards.

## 3.6 Results and discussion

### 3.6.1 Gaps affected the flow field over the wing

First, we investigated the aerodynamic effects of the gaps on the broader flow field over the wing. While there have been studies on the airflow over geometries related to the gapped wing—including wings with serrated trailing edges [77], [78], steps [79], [80], and slotted airfoils [51], [52]—this is the first instance of modelling flow over a wing with this gap geometry to the best of the authors’ knowledge. Thus, the flow information presented here could provide context and insight into flows over other similar geometries.

Compared to a baseline wing section, the presence of a gap affected the velocity and thickness of the local boundary layer, as measured at  $10^\circ$  angle of attack (Fig. 3.6). The flow over the baseline wing section was nominal for a NACA 0012 airfoil. Conversely, the gap noticeably changed the local boundary layer. The flow through the gap was more vertical, and appeared to double the thickness of the boundary layer in the vicinity of the gap. The boundary layer near the gap also began growing at a chord-wise position closer to the leading edge. However, a much thinner portion of the boundary layer experienced very low velocities near the wing surface, compared to the boundary layer over the baseline section. This increased velocity within the boundary layer indicated that the flow through the gap re-energized the boundary layer over the suction side of the trailing edge [52]. This effect could have been one cause of the gapped wing’s delayed stall, which was previously observed experimentally (Chapter II). Note that the flow outside of the boundary layer remained largely unaffected by the presence of the gap (Fig. 3.6).

Each gap also produced a pair of vortices, due to the gaps’ sharp corners and resulting discontinuities in the wing surface (Fig. 3.7). While there were regions of vorticity along the gap length, the coherent vortex structures formed at the trailing edge. We qualified the strength of the vortices in terms of the Q-criterion, an established method of vortex detection based on the vorticity and strain rate tensors [81]–[83], as well as the magnitude

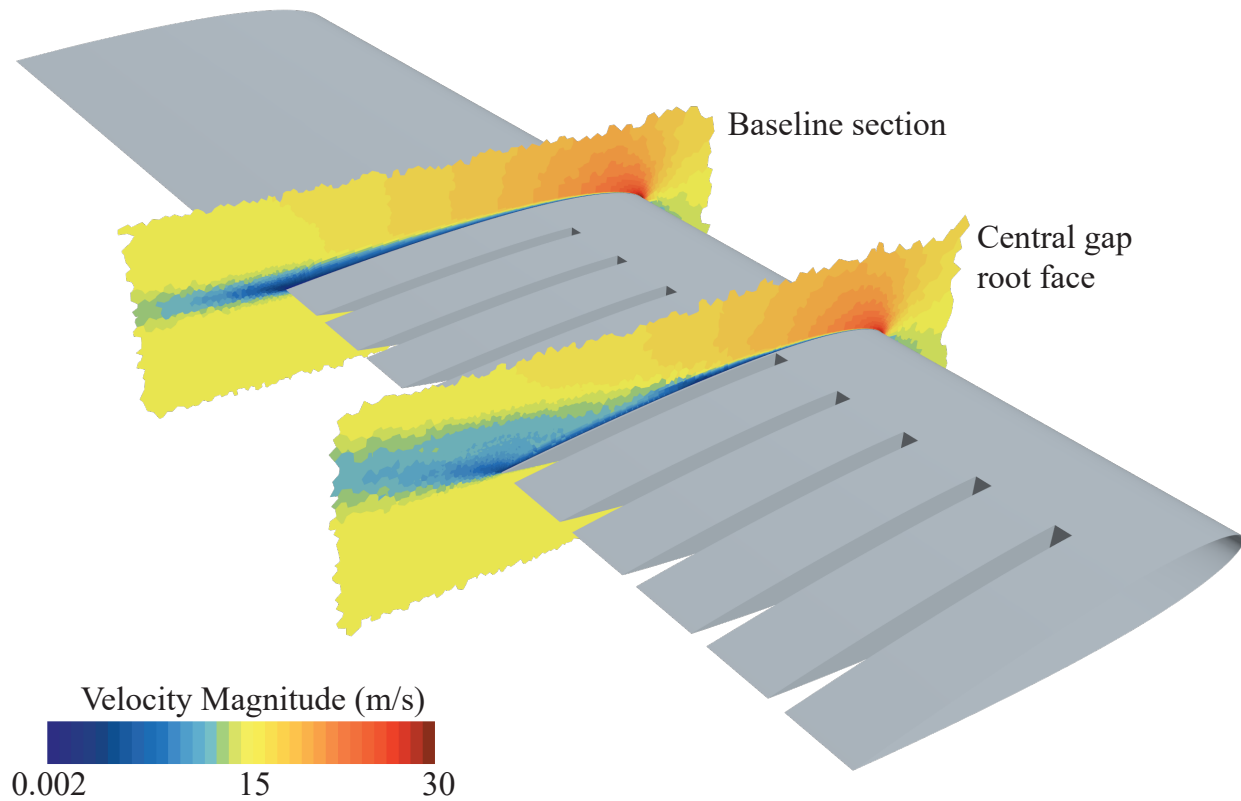


Figure 3.6: The gaps affected the thickness and velocity of the local boundary layer at  $10^\circ$  angle of attack, indicating re-energization of the boundary layer. The SI-gapped wing is shown without endplates for visual clarity. Velocities over a baseline wing section are shown at the wing root. Velocities are also plotted 0.0254 mm inboard of the central gap's root face.

of the vorticity. Higher  $Q$ -criterion and higher vorticity magnitude both indicate a stronger vortex, and vice versa. The vortices were strongest at the trailing edge and weakened as they travelled downstream (Fig. 3.7). Vortex strength appeared generally constant across the gaps, with several exceptions. The gap vortex nearest the wingtip appeared to interact and merge with the vortex from the endplate. This effect was likely due to the physical proximity of this outboard gap to the endplate. The gap vortex nearest the wing root was generally the same vorticity as the other gap vortices. However, this vortex grew to a larger diameter and extended farther downstream of the wing. The central gap vortices were much smaller and dissipated faster, likely because they were bound by the larger vortices from the endplate and most inboard gap. Additionally, the mutual interactions between the central



gap vortices may have impacted their size and dissipation. The most inboard gap vortex was free to grow because it was far from the endplate vortices and other large flow structures. Generally, the vortices on the wing root side of the gaps also extended farther downstream than the vortices on the wingtip sides. Note that the vortex produced by the endplate was characterized by much lower vorticity and Q-criterion. This indicated that the vortices shed by the gaps were stronger than those created by the endplates.

We also investigated the vortices present on the SI-aileron wing deflected  $-15.3^\circ$  at  $2^\circ$  angle of attack, as a comparison to the SI-gapped wing. As expected, each edge of the aileron produced a strong vortex structure, similar in vorticity magnitude and Q-criterion to the vortices produced by the gapped wing. Like the gap vortices, the aileron vortices were strongest near the trailing edge and weakened downstream. The aileron vortices were also larger in diameter, like the most inboard gap vortex. Both the SI-gapped wing and SI-aileron wing had comparable levels of vorticity over the leading edge of the wing surface and endplates. This behavior was similar to that over the baseline semi-span. This result implied that neither the gaps nor the aileron drastically increased the upstream vorticity compared to a baseline wing.

### **3.6.2 Flow within a gap informed actuation requirements**

With an understanding of how the gaps affected the broader flow field over a wing, we investigated the behavior of the flow through the gap itself (Fig. 3.8). We examined the flow through the central gap in the SI-gapped wing at  $2^\circ$  and  $10^\circ$  angle of attack. While we simulated the SI-gapped wing at a broader range of angles, we studied these two cases more closely to understand the representative behavior at low and high angles of attack. We also examined the velocity field on two orthogonal planes, to enable us to characterize the streamwise and spanwise components of the flow individually. Since the pressure distribution over the SI-gapped wing did not appear to be greatly affected by the endplates or span location (Appendix B), we measured the velocity and pressure in the

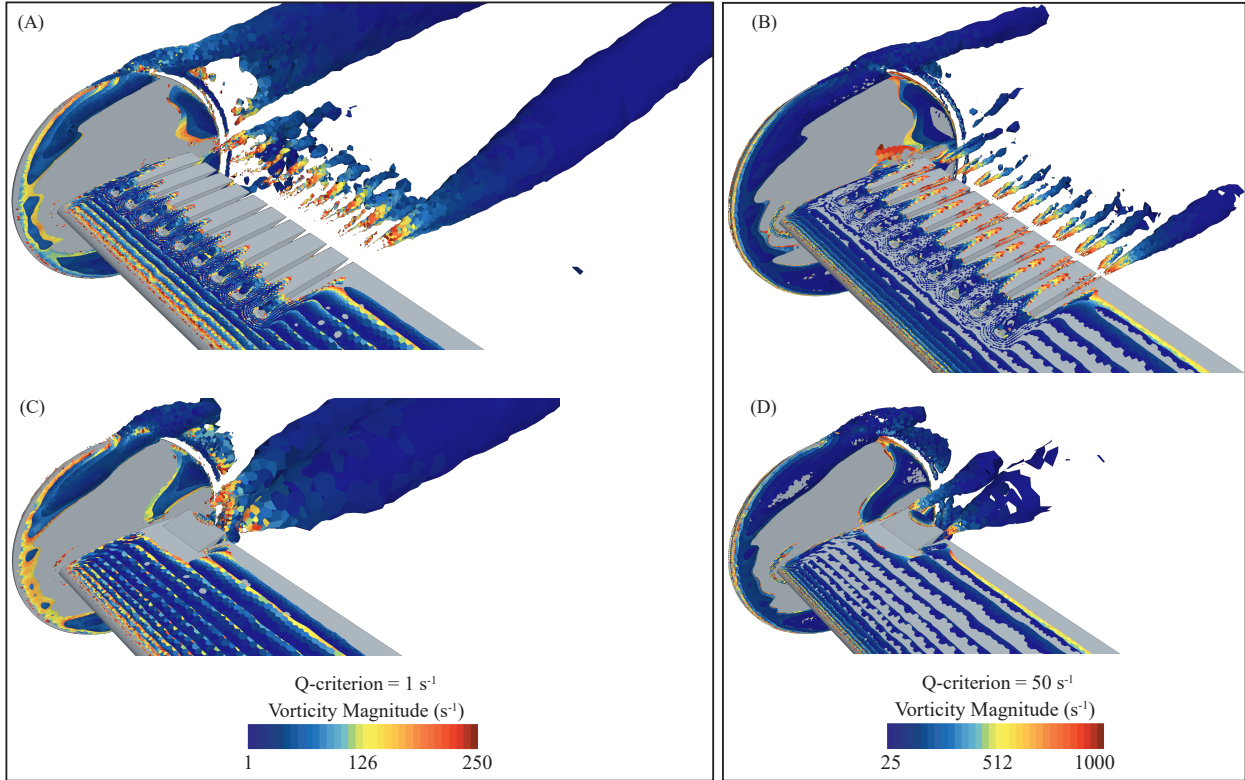


Figure 3.7: Each gap created a pair of strong vortices, similar to those produced by an aileron. The gap vortex nearest the wing root extended farthest downstream. (A) iso-surface of the SI-gapped wing with a Q-criterion of  $1 \text{ s}^{-2}$ . (B) SI-gapped wing with a Q-criterion of  $50 \text{ s}^{-2}$ . (C) SI-aileron wing with a Q-criterion of  $1 \text{ s}^{-2}$ . (D) SI-aileron wing with a Q-criterion of  $50 \text{ s}^{-2}$ . Both wings are at  $2^\circ$  angle of attack and the aileron is deflected  $-15.3^\circ$ .

central gap as a representative set.

In general, the gapped wing decreased lift compared to the baseline wing by allowing airflow through the gaps from the pressure to the suction side. For completeness, Appendix E experimentally validates the SI-baseline wing simulations, and briefly compares the pressure coefficients over the baseline wing to the gapped wing. The previous experimental work also thoroughly compares the gapped wing and baseline wing in terms of aerodynamic force and moment coefficients, descent, and roll (Chapter II).

The streamwise velocity field within the gap itself showed slow-moving recirculating flow at the start of the gap (Fig. 3.8). Such recirculation regions are also a general flow characteristic of flows over backwards-facing steps [79], [80]. As angle of attack increases from  $2^\circ$

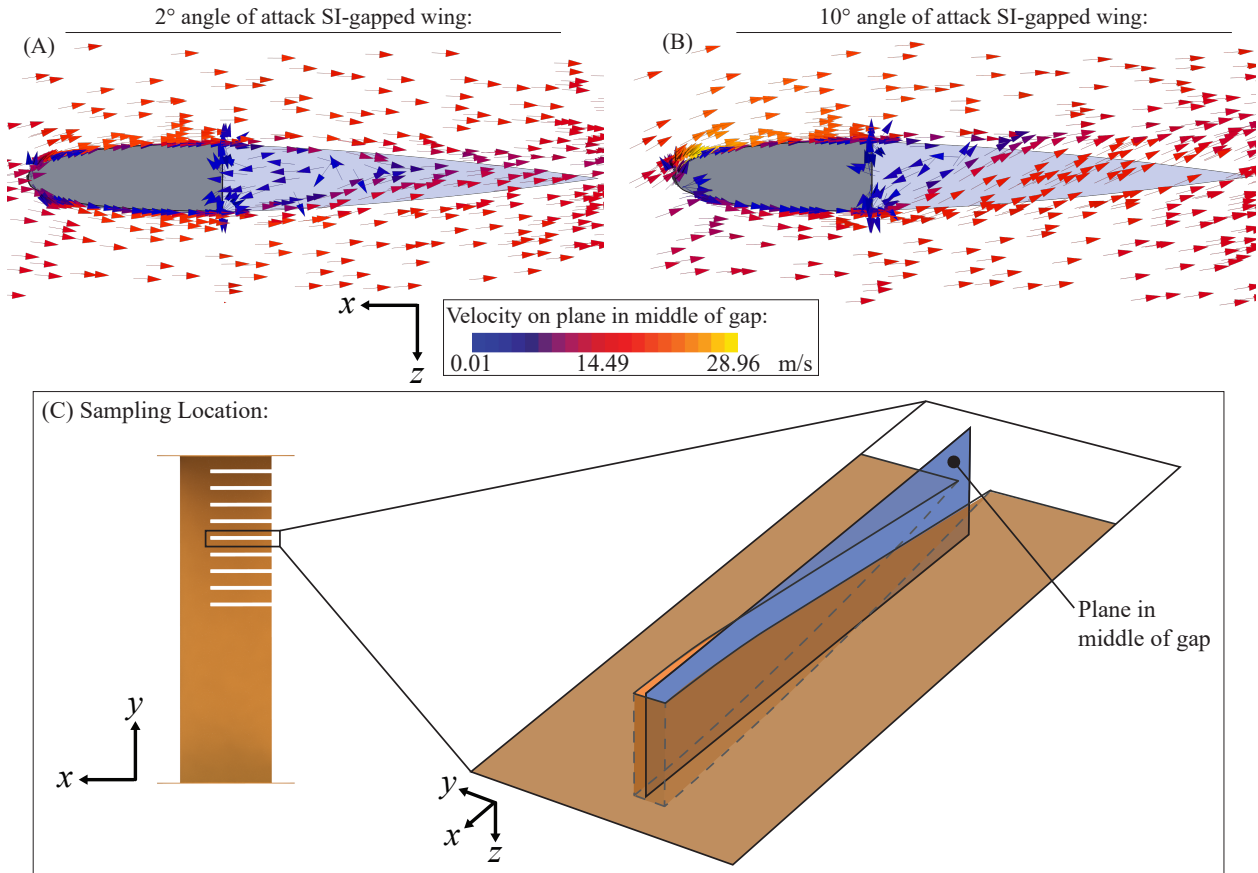


Figure 3.8: Streamwise flow through the gap recirculated then exited over the suction side at the trailing edge. (A) Velocity field at 2° angle of attack. (B) Velocity field at 10°. (C) Due to the consistent spanwise pressure distribution, data from the central gap was used. Velocity data were from the blue plane with its normal along the  $y$ -axis and positioned in the middle of the gap to avoid boundary layers.

to 10°, the flow through the gap became more vertical and the recirculation region appeared to shorten in the freestream direction. This behavior was expected given that increasing the angle of attack increased the vertical component of the freestream. Shortly downstream, the flow passed through the gap with an upward vertical component. As seen in Figure 3.6, this re-energized flow on the suction side of the trailing edge similarly to flow through a slot along the wing span [51], [52] and may have helped delay stall (Fig. 2.5).

The flow within the gap itself was largely in the streamwise direction, with noticeable spanwise components only at the recirculation region and trailing edge of the wing where the gap vortices formed (Fig. 3.9). The spanwise flow components may have been small because

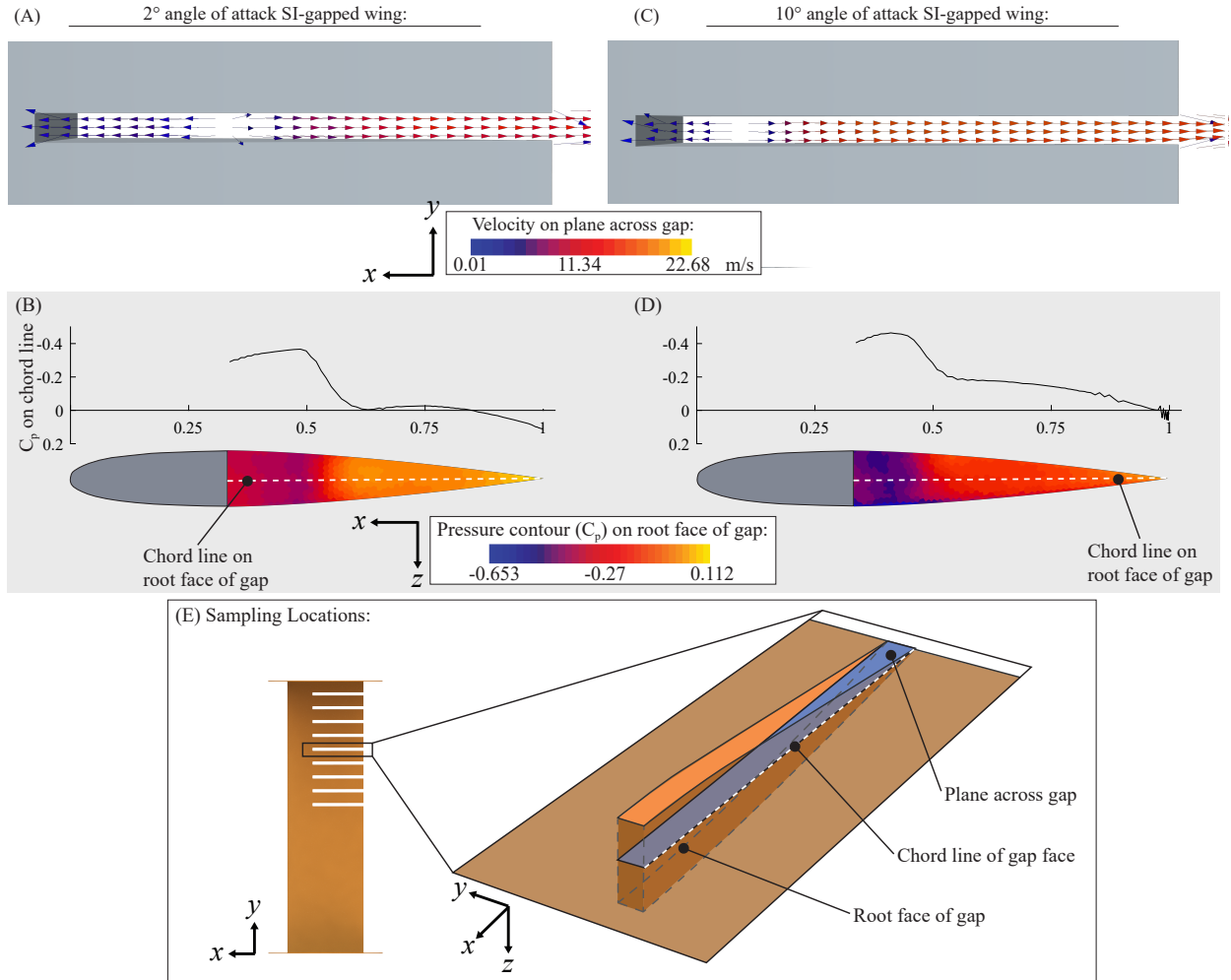


Figure 3.9: The flow within a gap was largely streamwise. (A) Velocity field at 2° angle of attack. (B) Pressure contours at 2° angle of attack, and pressure coefficients along the dotted white chord line. (C) Velocity field at 10° angle of attack. (D) Pressure contours at 10° angle of attack. (E) We used data from the central gap: pressure contours from the gap’s root face and velocity from the blue plane with a  $z$ -axis normal and origin on the chord line.

of the narrow width of the gap; it is possible that spanwise flow structures did not have time to fully develop in the confined gap space. Future studies will help validate this hypothesis.

The pressure contours on the gap face closest to the wing root also agreed with the behavior of the velocity field (Fig. 3.9 (B) and (D)). The pressure was relatively constant over the height of the gap in the  $z$ -axis direction, even at 10° angle of attack despite the strong vertical flow component. This consistency occurred because airflow from the upper and lower

wing surfaces were free to mix and equalize pressures in the gap. Thus we highlighted the general pattern by plotting pressure coefficients along the chord line of the gap face—that is, at the intersection of the mid-plane across the gap and the root face of the gap, shown as a dotted white line in Figure 3.9 (E). At the start of the gap, there was a slight favorable pressure gradient that reached a minimum negative value towards the end of the recirculation region. Moving further downstream, the pressure gradient remained generally adverse, reaching first a local maximum at about 50% to 60% chord at the end of the recirculation region, and then a global maximum pressure coefficient at the trailing edge. Overall, this pressure distribution shared a similar trend to that of a laminar separation bubble on an airfoil [84]. The majority of the gap face experienced negative pressure coefficients, implying a suction force over a large portion of the gap face that pulled the gap cover in towards the center of the gap. Thus, work was required to hold the gap covers open. The pressure coefficient curve shifted more negative as angle of attack increased, corresponding to an increase in actuation work as rolling moment coefficient increased.

Figure 3.10 shows representative velocity fields and pressure coefficients measured over the SI-aileron wing deflected  $4.7^\circ$  and  $15.3^\circ$  upwards, at  $2^\circ$  angle of attack. While we simulated the SI-aileron wing at a larger range of deflections, these two cases demonstrated the representative behavior at small and large aileron deflections. In both deflection cases, the pressure coefficients were generally negative on the lower surface and positive on the upper surface of the aileron, indicating a positive hinge moment that pushed the aileron down towards the neutral position. There were noticeable pressure spikes near the hinge axis at 75% chord, which is typical for ailerons due to the abrupt change in flow direction [85]. Greater aileron deflections led to larger pressure spikes and higher hinge moments. Similar pressure distributions over ailerons have been observed in other studies [85]–[87].

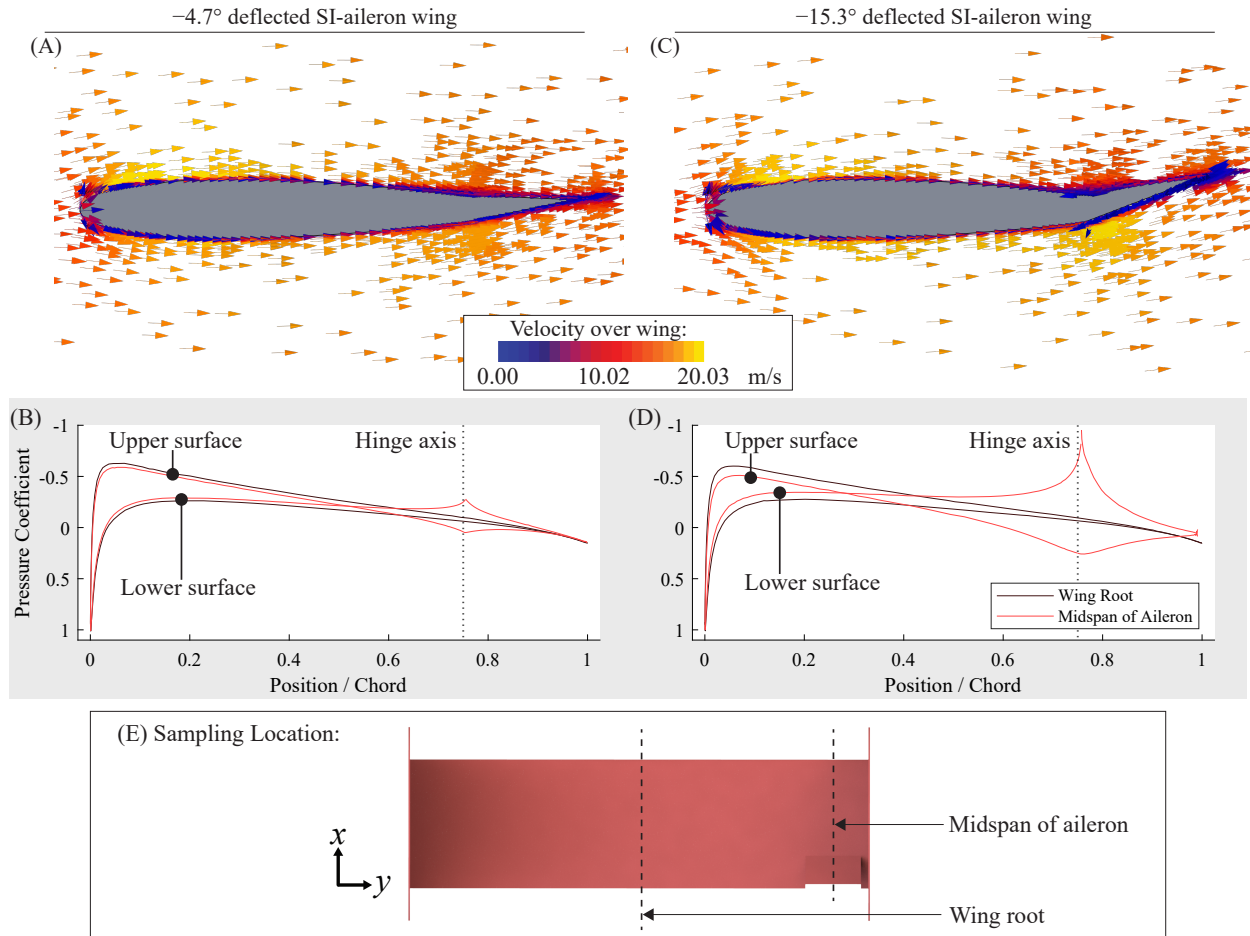


Figure 3.10: The flow over the aileron featured large pressure spikes and positive hinge moments that increased as deflection angle increased. (A) Velocity field over the  $-4.7^\circ$  deflected aileron at  $2^\circ$  angle of attack. (B) Corresponding pressure coefficient plot. (C) Velocity field over the  $-15.3^\circ$  deflected aileron at  $2^\circ$  angle of attack. (D) Corresponding pressure coefficient plot. (E) Data were taken at the midspan of the aileron.

### 3.6.3 Gaps required less work than single aileron at high roll

With an understanding of the flows over the gapped wing and aileron, we plotted the work requirements against rolling moment coefficient (Fig. 3.11). We used rolling moment coefficient as our independent parameter because it was an indicator of control performance. Furthermore, since the behavior of the SI-aileron wing was more dependent on deflection angle and the SI-gapped wing was more dependent on angle of attack, the rolling moment coefficient served as a useful common factor between the two wings. To vary rolling moment

coefficient, we simulated the gapped wing across angle of attacks from  $0^\circ$  to  $12^\circ$  and the aileron deflected from  $-0^\circ$  to  $-30^\circ$  at a constant  $2^\circ$  angle of attack.

Counter to what we expected, the gapped wing actuation work was higher than that of the aileron for low rolling moment coefficients (Fig. 3.11). Both wings had a nonlinear relationship between work and rolling moment coefficient. However, at zero rolling moment coefficient, the aileron required zero work while the gapped wing required a nonzero baseline work. This was because it always took work to actuate the gaps regardless of whether they produced roll. The NACA 0012 is a symmetric airfoil, meaning that at  $0^\circ$  angle of attack, zero lift was produced by either semi-span and thus zero rolling moment was produced. At any other angle of attack, exerting work to actuate the gapped wing resulted in a rolling moment. In fact, the gapped wing work curve was shallower than the aileron work curve. The curves intersected at a rolling moment coefficient of 0.0182, indicating that the gapped wing required less work than the aileron wing for rolling moment coefficients above this point.

Note that the CFD simulations of the SI-gapped wing may have predicted higher actuation work than expected for both methodological and fluid dynamics reasons. Firstly, it is challenging to resolve flows in RANS simulations in the vicinity of small geometric features such as the gaps. As a result, there may have been large errors associated with the gap force predicted by CFD simulations. RANS provided an appropriate compromise between accuracy and cost for this study, and yielded good agreement between simulated and experimental results. However, future work could employ higher fidelity simulation tools to confirm the work estimates and resolve finer details in the flow. The choice of turbulence model could have further affected the work predictions [76]. The higher work of the gapped wing at lower rolling moment coefficients could also have been due to the fluid mechanics in the gaps. The flow through the gaps created a stronger force than the airflow over the aileron at lower rolling moment coefficients. However, at higher rolling moment coefficients, the greater magnitudes of the pressure coefficients over the aileron led to a larger hinge mo-

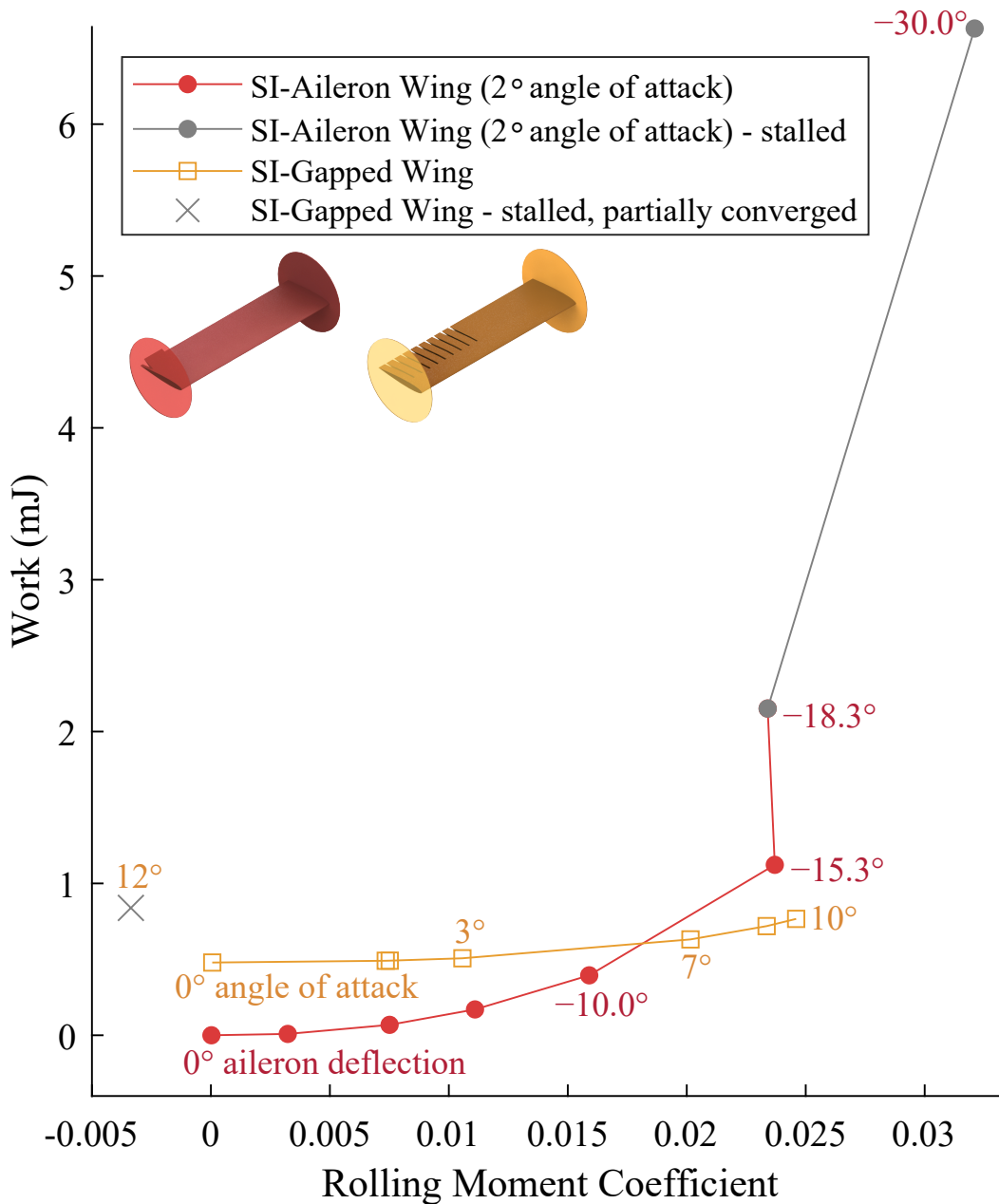


Figure 3.11: The SI-gapped wing required less work than the SI-aileron wing to produce rolling moment coefficients above 0.0182, and produced a higher maximum coefficient. The aileron was simulated at  $2^\circ$  angle of attack and deflection angles from  $0^\circ$  to  $-30^\circ$ , and the gapped wing was simulated across angles of attack from  $0^\circ$  to  $12^\circ$ . Grey data points were stalled and “x” indicates partial convergence. The SI-gapped wing values depended on the area ratio  $R$ .



ment on the aileron than the suction force on the gaps. As the rolling moment coefficient increased, the work required to actuate the gaps did not increase as quickly as the work required to actuate the aileron, leading to the flatter gapped wing work curve.

The gapped wing and aileron wing also had different roll control behaviors post-stall (Fig. 3.11). The aileron work curve exhibited a nearly vertical jump at a rolling moment coefficient of 0.0237, indicating that the aileron was likely partially stalled above this rolling moment coefficient: any increase in deflection angle led to a slight increase in rolling moment coefficient but a large penalty in work requirements. This result may have been because the aileron work curve was taken at  $2^\circ$  angle of attack. Thus, the semi-span with the aileron stalled because of the high deflection angles, while the clean semi-span did not stall due to the low angle of attack. In this situation the wing continued to produce a positive rolling moment because the clean semi-span still produced more lift than the semi-span with the stalled aileron. Conversely, the gapped wing reached a higher maximum rolling moment coefficient of 0.0246 before stalling. At this point, the rolling moment coefficient dropped drastically while actuation work remained constant. Here, both semi-spans of the gapped wing were at a high angle of attack of  $12^\circ$ , so the flow over the whole wing was likely separated. The gaps were completely enveloped by this separated flow, meaning their presence had little bearing on the forces and moments produced by the wing. That is, the stalled gapped wing behaved like a wing without gaps and produced very small rolling moments. Recall that the SI-gapped wing data point at  $12^\circ$  angle of attack was partially converged (indicated by the grey ‘×’ in Figure 3.11). This point was included in Figure 3.11 to demonstrate the qualitative post-stall behavior of the SI-gapped wing.

The gapped wing reached a greater maximum rolling moment coefficient than the aileron before stalling (Fig. 3.11). The simulations under-predicted the maximum rolling moment coefficient of the SI-gapped wing (Fig. 3.4). It was likely that the simulations under-predicted the maximum rolling moment coefficient of the SI-aileron wing as well. Despite these conservative predictions, Figure 3.11 showed that the gapped wing still achieved a higher rolling

moment coefficient than the aileron wing before stall. The SI-gapped wing produced a maximum rolling moment coefficient of 0.0246 at  $10^\circ$  angle of attack (Fig. 3.11). This value was equivalent to the aileron deflected more than  $18.3^\circ$ , at which point the aileron had already partially stalled. Further, recall that the aileron was plotted at a low angle of attack of  $2^\circ$  in Figure 3.11. It is possible that the aileron may stall at lower deflections when at a higher angle of attack like the gapped wing [2], [33]. In these scenarios, the aileron wing would produce an even lower maximum rolling moment coefficient, because aileron performance is generally proportional to deflection angle but constant across angle of attack [2]. Therefore, the SI-gapped wing could likely produce greater maximum rolling moment coefficients for less work compared to the SI-aileron wing. In an experimental setting, we expect the aileron and gapped wing work curves would continue on similar pre-stall trends to even higher rolling moment coefficients than found using CFD. Given this advantage, it is important to note that the gapped wing lost control effectiveness after stall, while the aileron wing retained some effectiveness at the simulated  $2^\circ$  angle of attack due to its partial stall.

The dependence of the gapped wing's control effectiveness on angle of attack could make implementing the gaps more complex. Since the gapped wings were less effective at lower lift coefficients, they may need to be augmented with an additional control surface at those flight conditions. For example, at low angles of attack, roll could be primarily controlled by an aileron with the gaps assuming control at higher angles to lower work costs and delay stall. Alternatively, a hybrid control surface could take the form of an aileron with gaps along its surface. The gaps could open at higher aileron deflections to delay stall and remain closed at lower deflections to take advantage of lower aileron work costs. Further investigation is needed to determine the validity of this concept. The gapped wings also could require a complex controller that is able to manage the changing control surface effectiveness across angle of attack. Similarly, the gapped wing could be paired with an instantaneous pitch-up maneuver before actuation, to capture maximum rolling performance at the high lift coefficient [7]. This approach would assume that the gapped wing is necessarily changing

angle of attack before rolling, so including the work to perform the pitch-up maneuver could provide a more complete picture of the design space.

### 3.7 Chapter summary

Here, we performed the first CFD simulations of flow over a novel whiffing-inspired gapped wing. We experimentally validated the simulations, estimated the actuation work requirements of a gapped wing, and compared the results to those of a conventional aileron. The CFD data agreed well with previous experimental data of both a gapped wing and conventional aileron [2]. Examining the flow over the entire wing revealed that despite thickening the boundary layer, the gaps re-energized flow over the suction side of the trailing edge. Additionally, each gap produced a pair of vortices. The gap vortices were generally stronger than the vortices shed by the endplates. Furthermore, the gap vortex nearest to the wing root was much larger than the central gap vortices. The simulations further showed that flow within a gap itself was characterized by a recirculation region then re-energization of the flow. In addition, the flow through a gap was largely in the streamwise direction, with spanwise components only in the recirculation region and at the trailing edge. These general flow characteristics are similar to those of flow over a backwards-facing step [79], [80] and flow through a slotted airfoil [51], [52], and could provide useful intuition for other related flows. The actuation work requirements for both control surfaces were based directly on aerodynamic loading. Compared to the aileron, the gapped wing required less work for rolling moment coefficients above 0.0182 and produced a greater maximum rolling moment coefficient. However, the gapped wing lost control effectiveness post-stall. Since the gapped wing effectiveness varied across angle of attack, it may require a more complex controller or augmentation by another control surface at low rolling moments. Overall, the CFD simulations indicated that the gapped wings could be an alternative method of roll control for energy-constrained aircraft when higher rolling moment coefficients are required, compared to a single aileron.

### 3.8 Data availability

The data and scripts that support the findings of this study are openly available on figshare. Supplementary materials for the SI-configuration are located at DOI: [10.6084/m9.figshare.c.6284877.v3](https://doi.org/10.6084/m9.figshare.c.6284877.v3). Supplementary materials for the JH-configuration are located at DOI: [10.6084/m9.figshare.c.6284874.v1](https://doi.org/10.6084/m9.figshare.c.6284874.v1). Scripts were written and run in MATLAB R2022a.

## CHAPTER IV

# A Gapped Wing was Less Effective for Roll Than Two Ailerons

### 4.1 Overview

Previously, gapped wings and wings with a single aileron were simulated in a commercial CFD solver. The results implied that the gapped wings held some advantages for roll control of UAVs. In particular, the gapped wings produced higher maximum rolling moment coefficients than the single aileron, and required less work at high roll coefficients. However, ailerons are typically implemented as asymmetrically-deflected pairs—with one upwards and one downwards aileron—as opposed to a single flap on one semi-span. Here, I simulated a JH-wing with two ailerons, and compared its rolling moment coefficient and actuation work to a gapped wing in the JH configuration (“JH-gapped wing”). The gapped wing required more work than the aileron at low rolling moment coefficients. Furthermore, the gapped wing produced a lower maximum rolling moment coefficient compared to the two-aileron wing. In the upper range of gapped wing rolling moment coefficients, it required similar work to the ailerons at  $10^\circ$  angle of attack. Despite the relatively lower roll performance, the gapped wings provided some benefits by decreasing adverse yaw and drag in certain cases. Overall, the two-aileron comparison provided a more complete picture of how the gapped wings perform relative to conventional control surfaces. This work demonstrated both the

more practical shortcomings of the gapped wings, as well as their advantages. This holistic knowledge of the gapped wings will provide useful context for future aircraft designers.

## 4.2 Motivation and background


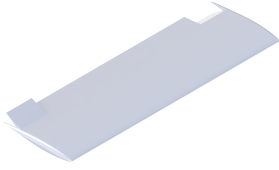
In Chapters II and III, the gapped wings were compared to a wing with a single aileron on one semi-span. This kept the comparisons as direct as possible within the existing literature, and provided initial data on the gapped wing’s aerodynamic performance. However, ailerons are usually implemented in pairs that deflect in opposition to one another. Thus, it is most realistic to compare the gapped wing to a wing with two ailerons. Here, I expanded the CFD simulations from Chapter III to compare a gapped wing to a wing with two ailerons. This work was necessary to provide a more complete picture of the gapped wings’ performance relative to conventional control surfaces.

## 4.3 Methods

### 4.3.1 Simulation setup

Here, I simulated two new wing configurations (Table 4.1). Firstly, I simulated a JH-aileron wing with two ailerons as opposed to one (“two-aileron JH-wing”). While it is possible for aileron pairs to deflect to slightly different angles in the real world [33], I assumed that the ailerons deflected equal and opposite amounts. The aileron on the right semi-span was deflected upwards, and the left aileron was deflected downwards. I also simulated the “JH-gapped wing,” which featured nine gaps of dimension  $\frac{2c}{3} \times \frac{b}{48}$  on the right semi-span of a wing with the baseline dimensions and flow conditions as the JH-aileron wing (Table 3.1). Both the two-aileron JH-wing and the JH-gapped wing were simulated as full asymmetric spans in a bullet-shaped domain, to avoid reflection plane corrections in post-processing. The wings were rectangular with a 0.762m chord, 1.1811m semi-span, and rounded wingtips with no endplates [2]. Since Johnson and Hagerman did not specify flow conditions beyond Reynolds

Table 4.1: The JH-gapped wing and two-aileron JH-wing were simulated using CFD, to allow for experimental validation and direct comparison of the aileron and gapped wings in the JH-configuration.

	JH-Gapped Wing	Two-Aileron JH-Wing
		
Data sources	CFD	CFD, Semi-empirical
Airfoil	NACA 64A010	NACA 64A010
Velocity (m/s)	86.2629	86.2629
$Re$	$4.5 \times 10^6$	$4.5 \times 10^6$
Simulated angles of attack	$0^\circ$ to $12^\circ$	$2^\circ$ , $10^\circ$
Density (kg/m <sup>3</sup> )	1.225	1.225
Kinematic Viscosity (Pa-s)	$1.4607 \times 10^{-5}$	$1.4607 \times 10^{-5}$
Ref. Area (m <sup>2</sup> )	1.69	1.8
Ref. Length (m)	2.3622	2.3622
Hinge Moment Ref. Area (per aileron, m <sup>2</sup> )	—	0.0544
Hinge Moment Ref. Length (per aileron, m)	—	0.1905

number, we assumed standard atmospheric conditions [2]. Just as the SI-aileron wing enabled us to directly compare gaps and ailerons in the SI-configuration, the JH-gapped wing allowed us to directly compare gaps and ailerons in the JH-configuration. It was necessary to simulate the JH-gapped wing due to differences in the Johnson and Hagerman setup and the Sigrest and Inman setup. Johnson and Hagerman tested at a higher Reynolds number, without a wingtip endplate, on a larger wing with a rounded wingtip and a different airfoil [2]. The work curve of the JH-gapped wing is discussed in detail in Appendix B.

As done in Chapter III, the meshes for the JH-gapped wing and two-aileron JH-wing were built using tools within STAR-CCM+. The meshes were three-dimensional and prism layers were applied to all wing surfaces. The prism layers were constructed such that the wall  $y^+$  value remained below one for the majority of the wing surface, and the growth ratio was about 1.3. Wake refinement was applied about two chord-lengths behind the wings. The

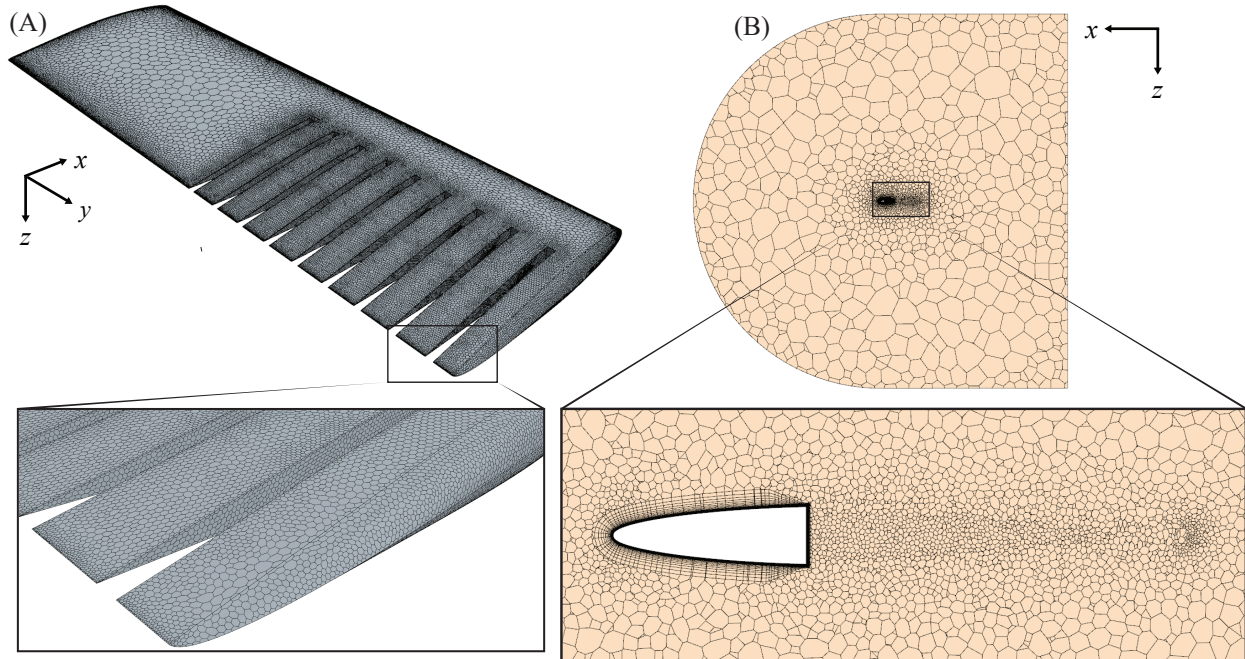


Figure 4.1: The three-dimensional mesh for the JH-gapped wing was created using STAR-CCM’s built-in tools. (A) Surface mesh over the JH-gapped wing, with a detail view of the gaps and wingtip. (B) Cross-section of the bullet-shaped domain. The detail view shows prism layers over a gap.

boundaries of the bullet-shaped domain were ten times the JH wingspan. Based on the mesh refinement study (Section 3.4), the JH-gapped wing was simulated with 3.8 to 4.3 million cells depending on angle of attack. The two-aileron JH-wing was simulated with 2.1 to 3.1 million cells depending on deflection angle.

Steady-state three-dimensional RANS simulations were performed in the commercial CFD solver Siemens STAR-CCM+. I used the uncoupled solver for the two-aileron JH-wing at  $0^\circ$  and  $10^\circ$  deflection, and the coupled solver for  $20^\circ$  and  $30^\circ$  deflection. For the JH-gapped wing, the coupled solver was used at small angles of attack, and the uncoupled solver was used for higher angles of attack for ease of convergence. Simulations were terminated after the unscaled residuals of  $x$ -momentum,  $y$ -momentum,  $z$ -momentum, continuity, and TKE were below  $1 \times 10^{-4}$ , and after SDR was reduced by at least four orders of magnitude. In two cases of the two-aileron JH-wing, SDR only fell below  $1.6 \times 10^{-3}$ . In two instances of the JH-gapped wing,  $x$ -momentum,  $y$ -momentum,  $z$ -momentum, continuity, and TKE only



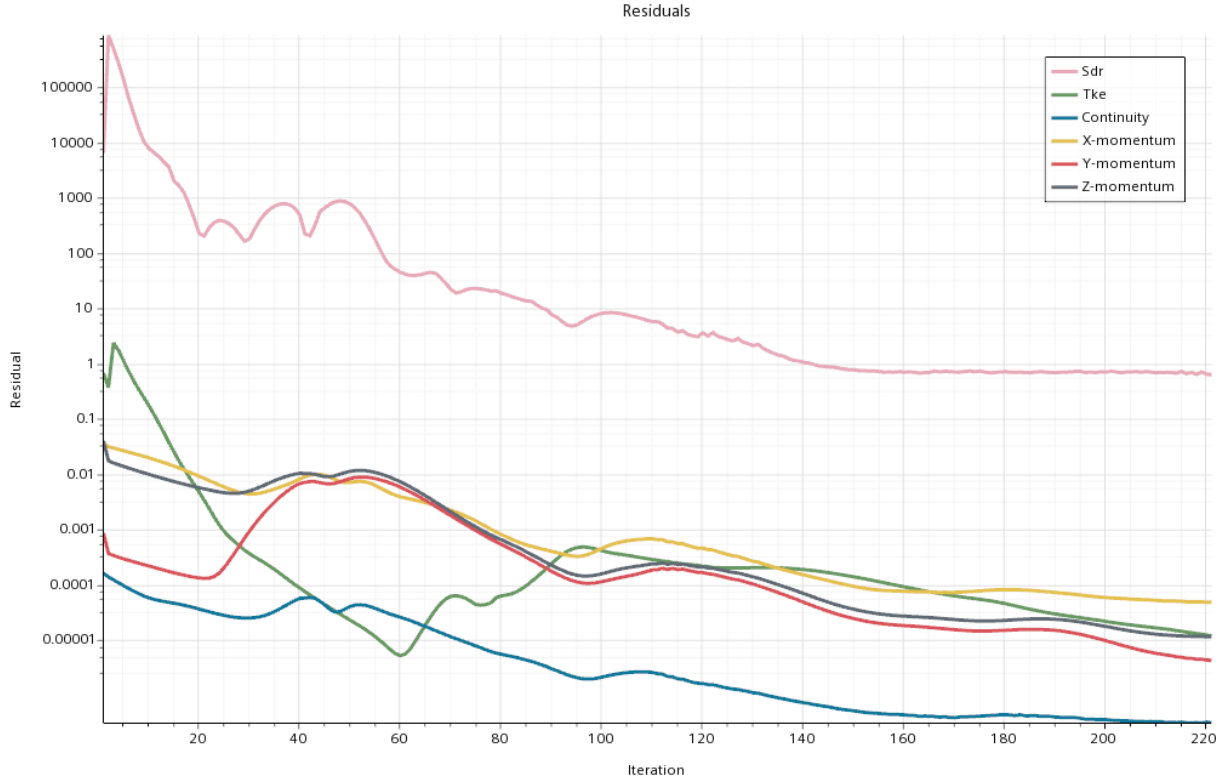


Figure 4.2: Sample residual convergence plot of the JH-gapped wing at  $2^\circ$  angle of attack. reached  $5.3 \times 10^{-4}$ . Convergence was typically achieved within 300 to 3400 iterations for the two-aileron JH-wing and 200 to 1200 iterations for the JH-gapped wing.

I additionally simulated the SI-aileron wing with two ailerons. The SI and JH configuration behaved similarly, as they did for the one-aileron comparison (Appendix B). Therefore, I focused on the JH configuration here because it was closest to a real-world UAV given its slightly higher aspect ratio and lack of endplates. Furthermore, using the JH configuration allowed us to semi-empirically validate the two-aileron CFD data.

### 4.3.2 CFD-based work estimate of JH-gapped wing

Like the SI-gapped wing, the JH-gapped wing was considered to have gap covers that slid along the span of the wing to open or close the gaps (Fig. 4.3). The gap covers were assumed to be  $1/8$  in. thick, yielding an area ratio  $R$  of 0.1257 for the JH-gapped wing

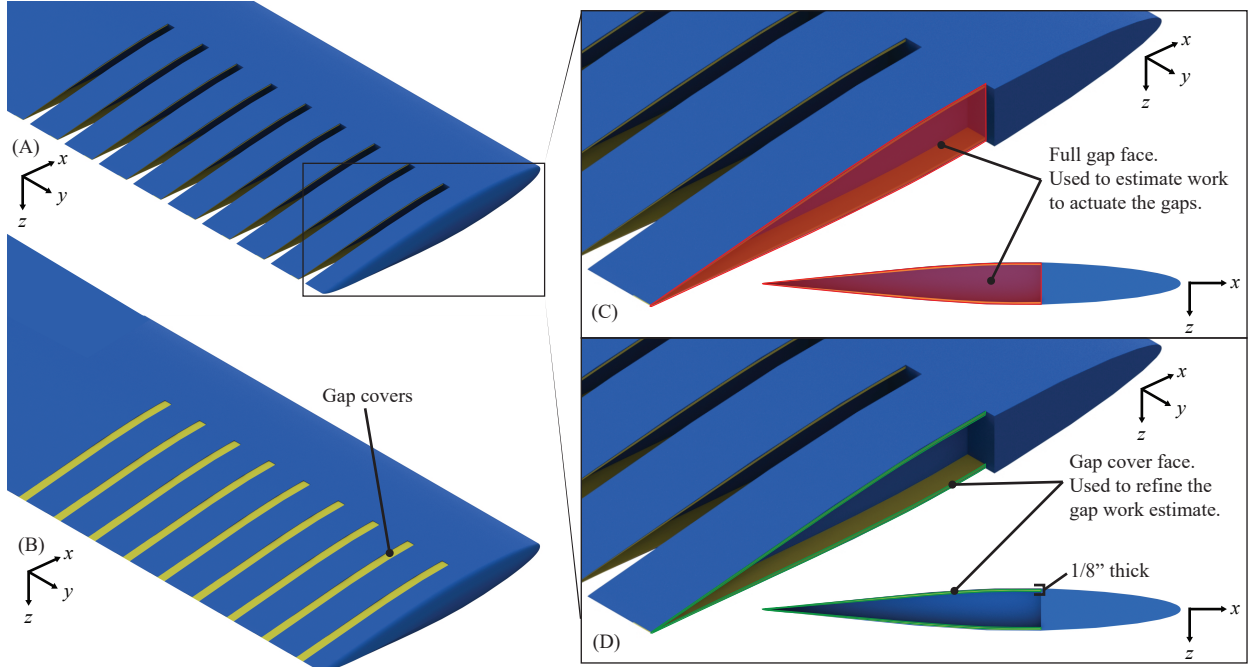


Figure 4.3: The JH-gapped wing was modelled with gap covers (yellow) that slid along the wing span to (A) open the gaps (B) and close them. (C) The force used to estimate actuation work was calculated on the red gap face. (D)  $R$  was calculated using the green gap cover area (Eqn. 3.1).

(Eqn. 3.2). The work to actuate the gap covers of the JH-gapped wing was thus estimated from the CFD data according to Eqn. 3.1.

### 4.3.3 Semi-empirical two-aileron JH-wing

Johnson and Hagerman's single aileron experimental data were used to analytically estimate the performance of a wing with two ailerons [2]. The semi-empirical results were then used to validate the two-aileron JH-wing simulations. The two ailerons were assumed to deflect equal and opposite amounts. I calculated the rolling and yawing moment coefficients of the two-aileron wing as the difference in moments caused by up- and down-deflected ailerons [59]. For example, the rolling moment coefficient of the two-aileron JH-wing was analytically estimated as:

$$C_\ell^T = C_\ell^{M,U} - C_\ell^{M,D} \quad (4.1)$$

where  $C_\ell^{M,U}$  is the measured rolling moment coefficient of the upwards aileron and  $C_\ell^{M,D}$  is the measured rolling moment coefficient of the downwards aileron. The measured rolling and yawing moment coefficients were calculated by factoring out a correction factor,  $K$  [2]. For example, the measured rolling moment coefficient from an upwards aileron deflection was calculated by [2]:

$$C_\ell^{M,U} = \frac{C_\ell^{C,U}}{K} \quad (4.2)$$

where  $C_\ell^{C,U}$  is the corrected rolling moment coefficient that was reported by Johnson and Hagerman. Unlike the rolling and yawing moment coefficients, the measured hinge moment coefficients were not corrected by  $K$  [2]. Therefore, I directly used the reported hinge moment coefficient data. Thus, the work to actuate the two-aileron JH wing was semi-empirically estimated according to:

$$W_a^T = W_a^U + W_a^D \quad (4.3)$$

where  $W_a^U$  is the work to deflect the aileron up, and  $W_a^D$  is the work to deflect the aileron down. Each of these values was found according to:

$$W_a^{D,U} = -M_a(\pm\delta_a) \quad (4.4)$$

and

$$M_a = \frac{1}{2}\rho V^2 S_a c_a C_{h,a} \quad (4.5)$$

Per Eqn. 2.14, the negative sign in Eqn. 4.4 accounted for the fact that I sought the work done by the hypothetical actuation system, rather than the work of the airflow on the aileron.

#### 4.4 Validating the two-aileron JH-wing simulations

The CFD simulations of the two-aileron JH-wing agreed well with the semi-empirical estimates of rolling moment coefficient, yawing moment coefficient, and acuation work (Fig. 4.4). As expected from theory, the two-aileron JH-wing produced slightly less than twice the rolling

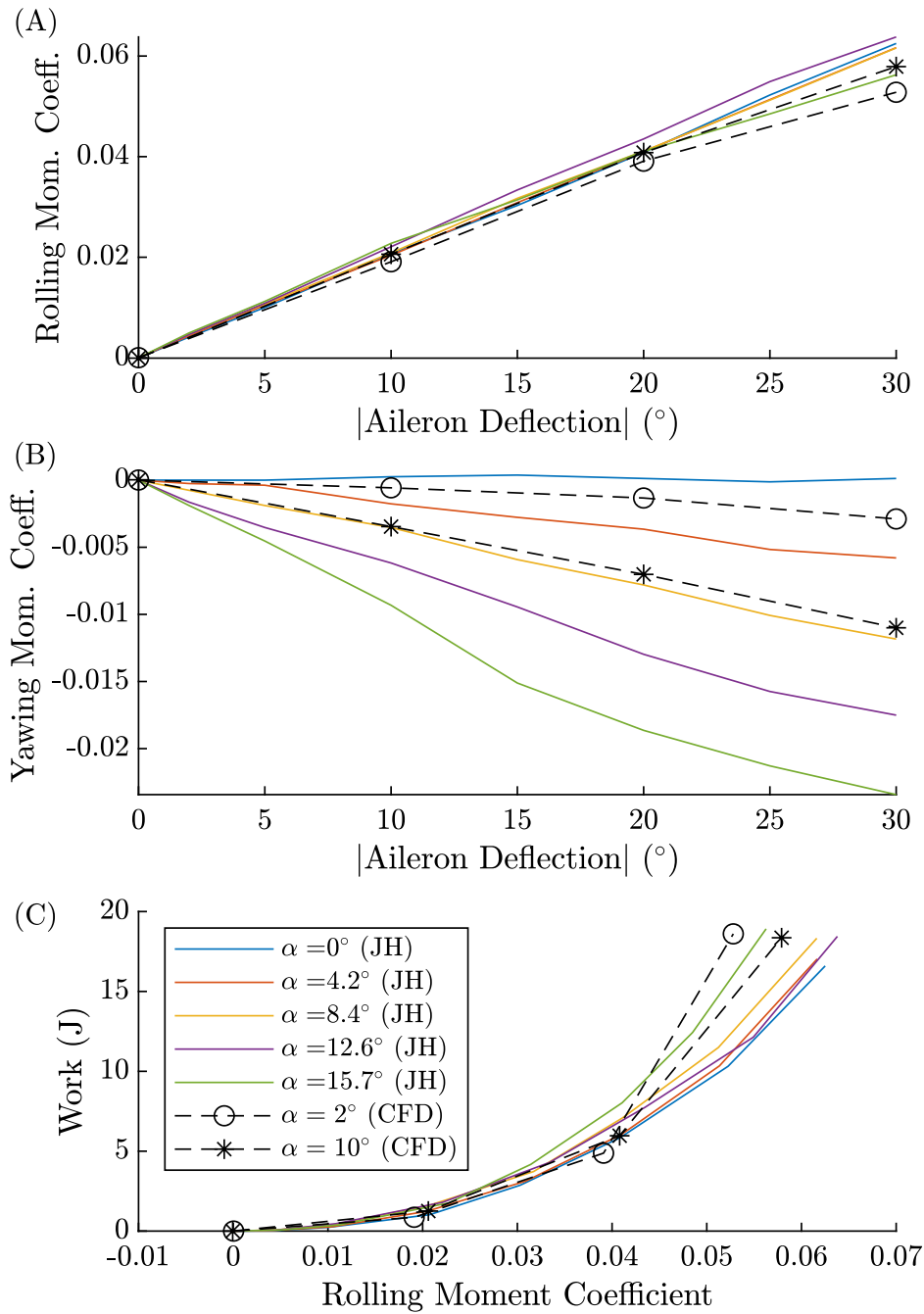


Figure 4.4: CFD simulations of the two-aileron JH-wing agreed well with semi-empirical estimates of the (A) rolling moment coefficient and (B) yawing moment coefficient across aileron deflection magnitude, and (C) work versus rolling moment coefficient at several angles of attack. In the legend, (JH) indicates semi-empirical estimates based on single-aileron data [2].

moment coefficient of the single JH-aileron wing (Fig. 3.5) [59]. In general, the CFD results under-predicted rolling moment coefficient and over-predicted the hinge moment coefficients when the aileron was at higher deflection angles. These effects led to the CFD over-predicting work as a function of rolling moment coefficient. These discrepancies were expected, given the likelihood of flow separation at high deflection angles and the difficulty of capturing separated flow in RANS. Note that Figure 4.4 includes semi-empirical estimates at several angles of attack from  $0^\circ$  to  $15.7^\circ$  [2] and the CFD results at  $2^\circ$  and  $10^\circ$  angle of attack, to capture variation of the yawing and hinge moment coefficients across angle of attack [2].

## 4.5 Two ailerons produced more roll than gapped wing

Previous chapters found that a nine-gap SI-gapped wing at a high angle of attack produced an equivalent rolling moment coefficient to a single  $32.7^\circ$  upwards aileron (Chapter II). Chapter III showed that the SI-gapped wing required more work than the aileron at low rolling moment coefficients. However, the gapped wing produced a larger maximum rolling moment coefficient, and required less work in this highly maneuverable regime.

Here, the addition of a second oppositely deflected aileron changed the relationship between the gapped wing and aileron wing work curves. Deflecting two ailerons to a given angle required approximately twice as much work as deflecting a single aileron to the same angle. However, the two ailerons correspondingly produced a rolling moment coefficient about twice as high as the single aileron. Thus, the two-aileron work curve did not steepen with the addition of the second aileron. Rather, the curve extended to higher rolling moment coefficients along a similar trend. In other words, the two ailerons each needed to deflect approximately half as much as a single aileron to produce the same rolling moment coefficient. Since aileron hinge moment is generally proportional to deflection angle [2], this effect roughly halved the hinge moment of each aileron, and the total work remained similar to that for a single aileron producing the same rolling moment coefficient. Ultimately, the two-aileron JH-wing produced much higher rolling moment coefficients for negligible increases in

work compared to both the single JH-aileron wing and the JH-gapped wing.

The JH-gapped wing produced a much lower maximum rolling moment coefficient than the two-aileron JH-wing (Fig. 4.5). The maximum rolling moment coefficient produced by the JH-gapped wing was only equivalent to the two-aileron JH-wing deflected  $\pm 7^\circ$  (based on a linear interpolation of the two-aileron JH-wing CFD data at  $10^\circ$  angle of attack). Furthermore, the JH-gapped wing did not provide a clear benefit in terms of work. The JH-gapped wing required more work than the two-aileron JH-wing to produce low rolling moment coefficients. The gapped wing and aileron wing work curves intersected at a rolling moment coefficient of 0.0115, indicating that the gapped wing required less work above this point. In this regime, the JH-gapped wing did not provide significant work reduction. Rather, the JH-gapped wing required comparable work to the two-aileron JH-wing at  $10^\circ$  angle of attack. Thus, the main disadvantage of the JH-gapped wing was that it did not produce as high rolling moment coefficients as the two-aileron JH-wing.

Recall that the work of the JH-gapped wing was highly dependent on the specific assumed geometry of the gap, the  $R$  area ratio in particular (Eqn. 3.1). Refining the wing geometry to lower the value of  $R$  would decrease the magnitude of the JH-gapped wing work curve. The gap geometry could also be optimized to lower work costs, as discussed next in Chapter V. Finally, the JH-gapped wing had a non-zero work intercept due to the nature of opening the gaps in a symmetric airfoil (Chapter III). Using an asymmetric airfoil with a non-zero zero-lift angle could possibly shift the JH-gapped wing work curve to the left along the rolling moment coefficient axis, effectively reducing the work per rolling moment coefficient of the JH-gapped wing.

## 4.6 Gapped wing offered some drag and yaw benefits

The JH configuration did not have endplates, and thus was three-dimensional and had tip effects. This meant I could describe the JH wings as having adverse or favorable yaw. Adverse yaw is yaw in the opposite direction (the opposite sign, in the chosen convention)

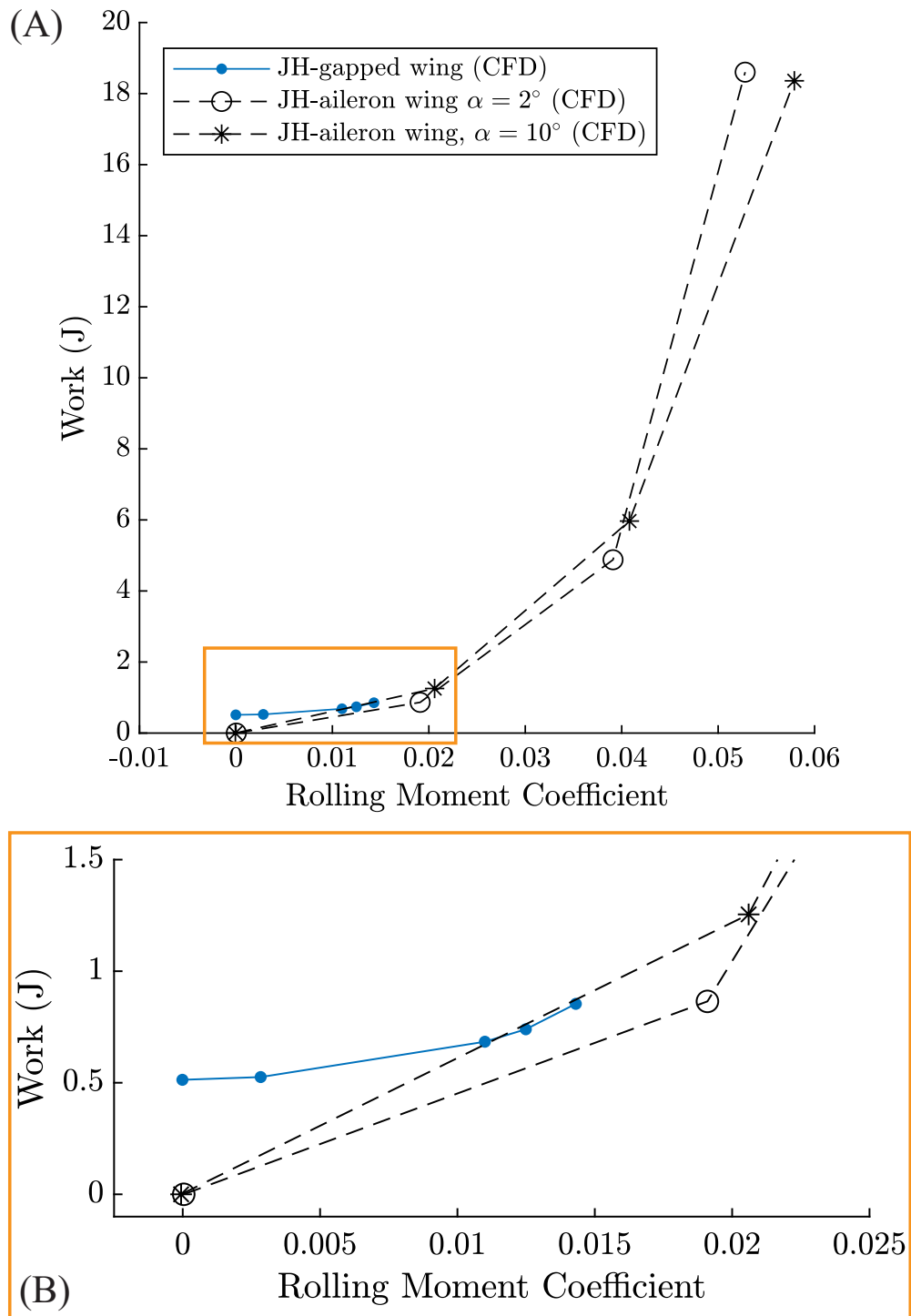


Figure 4.5: (A) The JH-gapped wing required more work than the two-aileron JH-wing at low rolling moment coefficients. At its higher coefficients, the gapped wing required comparable work to the ailerons at  $10^\circ$  angle of attack. (B) Detail view.

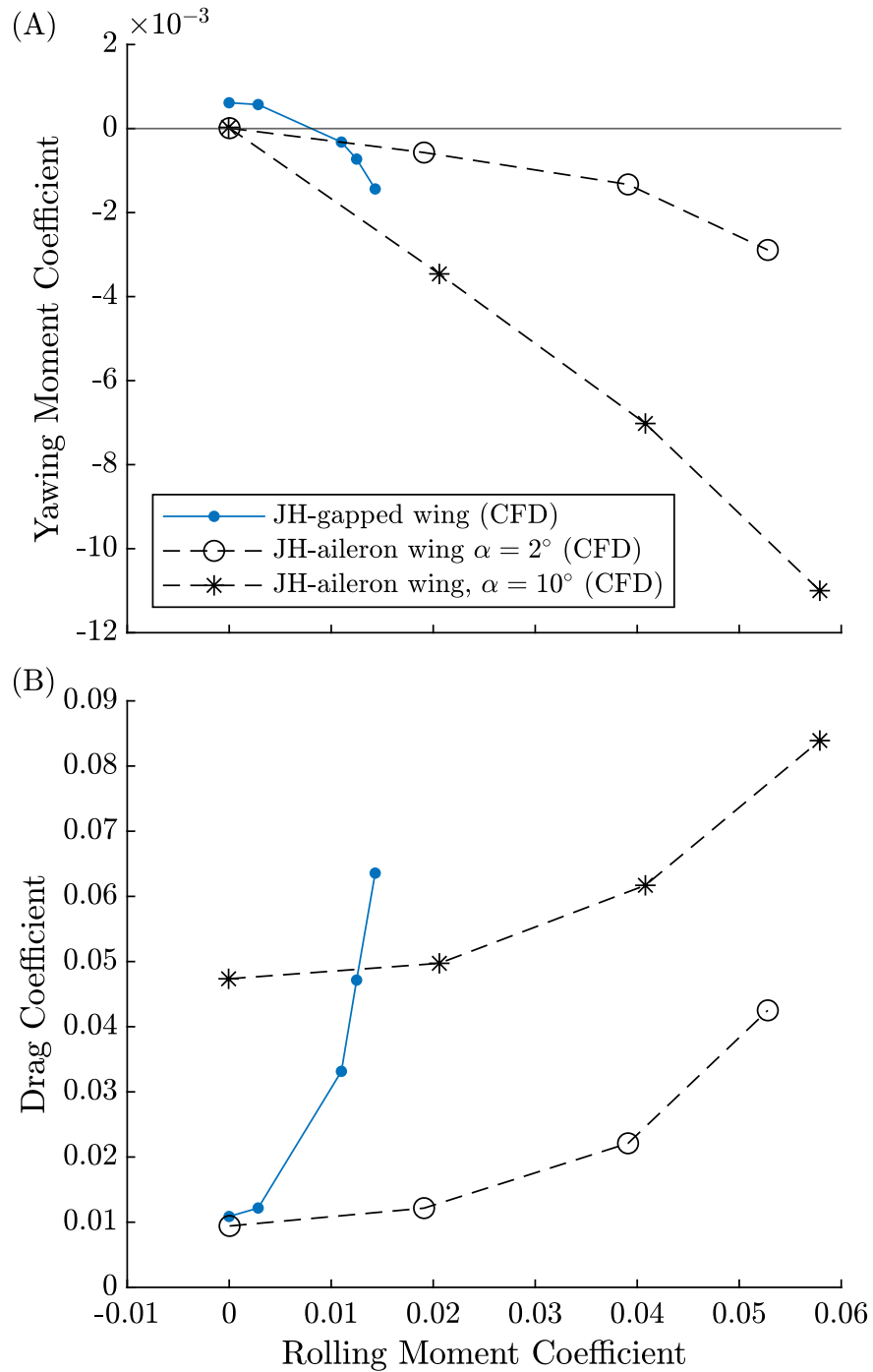


Figure 4.6: The JH-gapped wing provided some drag and yaw benefits over the two-aileron JH wing. (A) The two aileron wing produced adverse yaw across all rolling moment coefficients, while the JH-gapped wing produced favorable yaw at low rolling moment coefficients. (B) The JH-gapped wing produced less drag than the two-aileron wing at  $10^\circ$  angle of attack for low rolling moment coefficients.



from roll, and is generally detrimental to coordinated and efficient flight. Favorable yaw is in the same direction (sign) as the roll, and is typically helpful in establishing a coordinated bank or turn.

The JH-gapped wing provided some benefits over the two-aileron JH-wing in terms of yawing moment coefficient. The two-aileron JH wing only produced adverse yaw at non-zero rolling moment coefficients (Fig. 4.6 (A)). Conversely, the gapped wing produced favorable yaw at low rolling moment coefficients. Above a rolling moment coefficient of  $8 \times 10^{-3}$ , the yaw of the JH-gapped wing became adverse. But, the magnitude of the adverse yaw was comparable to that produced by the two-aileron JH-wing at  $5^\circ$ , and far less than that produced by the two-aileron JH-wing at  $10^\circ$  angle of attack. The JH-gapped wing was also beneficial in some cases with respect to the drag coefficient (Fig. 4.6 (B)). At low rolling moment coefficients, the JH-gapped wing produced a smaller drag coefficient than the two-aileron wing at  $10^\circ$  angle of attack. However, at the gapped wing's upper range of rolling moment coefficients, specifically above 0.0126, it did produce a higher drag coefficient than the two-aileron wing.

The comparison of the JH-gapped wing to the two-aileron JH-wing highlighted several conclusions. Firstly, the gapped wing was not as ideal for roll control compared to a more realistic two-aileron configuration, because it produced lower rolling moment coefficients. This was counter to what the results indicated for the single aileron comparison in Chapters II and III. The gapped wing still required more work than the two-aileron JH-wing for low rolling moment coefficients. However, in the upper range of gapped wing rolling moment coefficient, it required comparable work to the ailerons at  $10^\circ$  angle of attack. Furthermore, the JH-gapped wing produced favorable yaw at low rolling moment coefficients, and less adverse yaw than the ailerons at higher coefficients, and  $10^\circ$  angle of attack. Similarly, the JH-gapped wing produced less drag than the ailerons at  $10^\circ$  angle of attack and low rolling moment coefficients. As with Chapter II, these conclusions are specific to the  $\frac{2c}{3} \times \frac{b}{48}$  gaps. Chapter V discussed how varying the gap size, number of gaps, and other parameters, could

improve the performance of the JH-gapped wing compared to the two-aileron JH-wing.

Finally, this chapter provided important information on the advantages and disadvantages of using the gapped wings in varying flight conditions. For instance, the gapped wings could still be useful for UAVs flying at a high angle of attack, as the gaps allowed moderate roll in this regime while increasing the stall angle of attack. However, the aircraft designer should be cognizant that the gapped wings were not capable of producing as much rolling moment coefficient as a two-aileron wing. In other words, the gapped wings offered an increased stall angle of attack at the cost of rolling moment coefficient magnitude. Alternatively, the gapped wings could be useful for a UAV at moderate angles of attack, where lower rolling moment coefficients are required. In this situation, the gapped wing required comparable work to the two ailerons and offered much lower yawing moments. This in turn may decrease the need for a larger rudder or yaw control surface.

## 4.7 Chapter summary

Here, I sought to provide practical context and a more holistic picture of the gapped wings for future aircraft designers. Using STAR-CCM+, I simulated a JH wing with two ailerons (“two-aileron JH-wing”) and compared its roll performance and work requirements to a JH wing with nine gaps on one semi-span (“JH-gapped wing”). I validated the two-aileron JH-wing simulations against semi-empirical estimates from single aileron data [2]. The CFD results of the two-aileron JH-wing agreed well with the semi-empirical data, with respect to rolling and yawing moment coefficient versus deflection angle, as well as work versus rolling moment coefficient. The two-aileron wing was capable of producing much larger rolling moment coefficients with negligible increases in work requirements compared to the single aileron wing. This highlighted both disadvantages and advantages of the JH-gapped wing, relative to the two-aileron JH-wing. Firstly, the JH-gapped wing did not produce as high of rolling moment coefficients as the two-aileron JH-wing. However, the gapped wing required comparable actuation work to the  $10^\circ$ -deflected two-aileron wing for

rolling moment coefficients above 0.0115. The gapped wings also provided some benefits over the two-aileron wing at lower rolling moment coefficients by reducing drag and producing favorable yaw. As with any control surface, this work demonstrated that the gapped wings were faced with both advantages and disadvantages. Understanding each of these, and their associated costs and benefits, will provide important context and knowledge for further investigating, designing, and implementing the gapped wings as control surfaces.

## **4.8 Data availability**

The data and scripts that support the findings of this study are openly available on figshare at DOI: [10.6084/m9.figshare.c.6489496.v1](https://doi.org/10.6084/m9.figshare.c.6489496.v1).

## CHAPTER V

# Refining Gap Dimensions Could Maximize Roll per Work

### 5.1 Overview

A wing with nine gaps measuring  $\frac{2c}{3}$  long and  $\frac{b}{48}$  wide was previously found to provide effective roll control at high lift coefficients. However, it was difficult to generalize the behavior of this wing to all gap configurations because of the dependence of aerodynamics on wing geometry. Motivated by this lack of generality, I performed a parameter sweep of the gapped wings using a commercial computational fluid dynamics solver. I simulated wings with varying gap length, gap width, and number of gaps, and measured the forces and moments of each configuration at several angles of attack. Using the resulting data I built linear models of the rolling moment coefficient, gap cover actuation work, and rolling moment coefficient normalized by work, all as functions of relevant parameters. Gap width and aspect ratio had large impacts on roll and work. Both rolling moment coefficient and work increased as gap width increased and gap aspect ratio decreased, leading to competing effects. Furthermore, gap length was less impactful than gap width on wing performance, and angle of attack was a larger driver for roll production than work. Examining the normalized roll also confirmed previous conclusions that the gapped wings maximized roll per work at high angles of attack. Finally, varying the gap width showed that the gaps could be gradually opened for smooth roll control, similarly to an aileron. Overall, this work demonstrated that altering gap parameters changed rolling moment coefficient and actuation work of the

gapped wing. The results also corroborated that, for a given gap dimension, the gaps were most effective for roll control at high angles of attack. Ultimately, the parameter sweep implied that gap configuration could be designed to maximize rolling moment coefficient per actuation work. Gap geometry could thus be tailored for specific mission objectives.

## 5.2 Motivation and background

Chapters II and III investigated gapped wings that all shared the same gap dimensions:  $\frac{2c}{3}$  long by  $\frac{b}{48}$  wide (subsequently written as *gap length*  $\times$  *gap width*). While these results provided an informative starting point for evaluating the gapped wing control surface, the findings could not be generalized to all gapped wing geometries. Even small differences in wing geometry, such as blunted versus sharp trailing edges, can cause large differences in flow behavior and wing performance. I speculated that changing the geometry of the gaps—including gap length, gap width, and the number of gaps—could therefore impact the behavior of the gapped wing control surface. Motivated by this hypothesis, I performed a parameter sweep of gap configuration. In particular, I examined how gap geometry and angle of attack impacted rolling moment coefficient, gap cover actuation work, and rolling moment coefficient per work of the gapped wings. The results provided important context for future aircraft design, and could be a foundation for optimization studies. Furthermore, the parameter sweep demonstrated that the gaps could be gradually opened or closed to allow for smooth roll control, like in a real-world setting.

Note that this parameter sweep was not a true optimization study, because only a limited number of discrete gap configurations were simulated. In reality, an infinite number of gap configurations are possible. Thus, this chapter was still specific to the selected gap configurations. Based on this limited data set, conclusions could not be explicitly drawn on an overall optimal gap configuration. Instead, the discussion was confined solely to the domain of included gap configurations.

## 5.3 Methods

### 5.3.1 Conducting the parameter sweep

I performed the parameter sweep using the commercial CFD solver Siemens STAR-CCM+. The validated simulations of the SI-gapped wing from Chapter III served as a starting point, enabling rapid and cost-effective iterations of gap configuration. I investigated all possible combinations of various gap lengths and widths, including gap lengths of  $[\frac{1}{2}, \frac{2}{3}, \frac{3}{4}] \times c$  and gap widths of  $[\frac{1}{192}, \frac{1}{96}, \frac{1}{64}, \frac{1}{48}, \frac{1}{32}, \frac{1}{19}, \frac{1}{16}] \times b$ . The initial gaps used in Chapters II and III were  $\frac{2c}{3} \times \frac{b}{48}$ , so I included both larger and smaller dimensions than these. Varying both gap width and gap length also meant that a wide range of gap aspect ratios were captured (Fig. 5.1). Gap aspect ratio was calculated by dividing gap width by gap length:

$$AR_g = \frac{b_g}{c_g} \quad (5.1)$$

Note that in this chapter, the phrase “gap dimensions” refers to the combination of gap width and gap length.

Each gap dimension was simulated on a wing with nine evenly spaced gaps, as well as a wing with five gaps (Fig. 5.2). The five-gap wing used the same gap spacing as the nine-gap wing, but only the five most outboard gaps were cut out of the wing. I chose this configuration because ailerons are known to be most effective for roll control when positioned closer to the wingtips [2]. As an extreme edge case, I also simulated a wing with two  $\frac{2c}{3} \times \frac{b}{5}$  gaps evenly spaced across the semi-span (Fig. 5.2). Here, the results focused on the five- and nine-gap configurations, since the two-gap wing constituted very different geometry and only featured one data point. The results of the two-gap wing are discussed in Appendix G.

Each gapped wing was simulated at  $0^\circ$ ,  $2^\circ$ ,  $7^\circ$ , and  $10^\circ$  angle of attack to provide representative data at high and low angles. I used the SI wing configuration (Table 3.1), because it was able to be experimentally validated (Section 3.3.1). The wings were simulated as asymmetric full spans (Fig. 5.2) to avoid reflection plane corrections in post-processing.

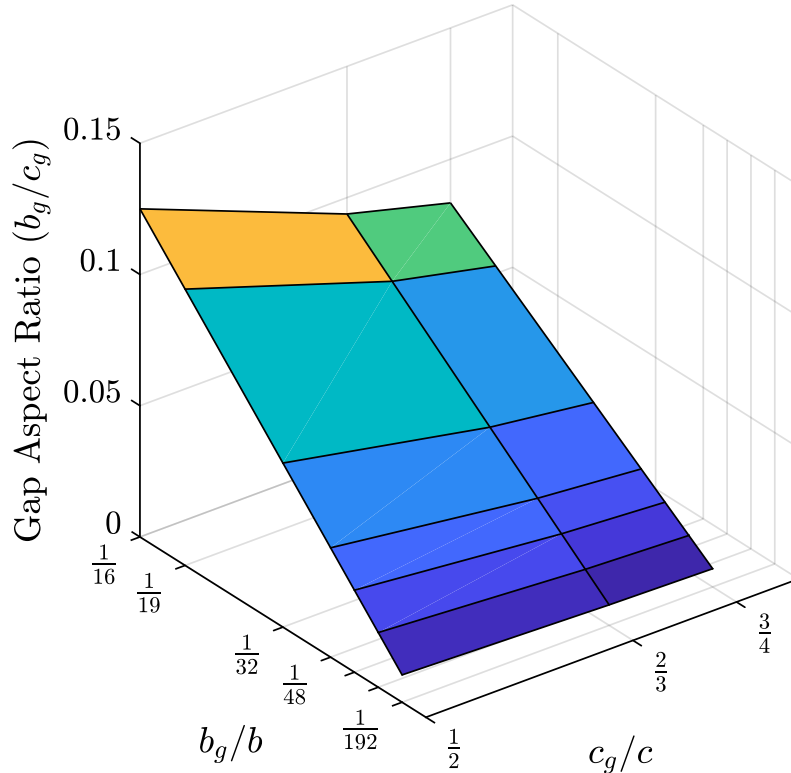


Figure 5.1: A range of gap widths and gap lengths were simulated, resulting in various gap aspect ratios. The initial gaps were  $\frac{2c}{3}$  long and  $\frac{b}{48}$  wide (Chapters II and III).

From each simulation I collected six-axis force and moment data. The rolling moment coefficient was measured about the quarter-chord at the wing root (Chapter III). I also measured the spanwise force acting on the vertical gap faces (teal shaded in Fig. 3.2 (C)) and calculated the gap cover actuation work of each wing according to Eqn. 3.1. Then, I calculated the rolling moment coefficient normalized by gap cover actuation work (“normalized roll”) according to:

$$C_l^{norm} = \frac{C_l^{wing}}{W_{gc}} \quad (5.2)$$

All of the parameter sweep simulations used a coupled solver, and the domain boundaries were 12.3 times the wingspan. The simulations were terminated after the unscaled residuals of  $x$ -momentum,  $y$ -momentum,  $z$ -momentum, continuity, and turbulent kinetic energy

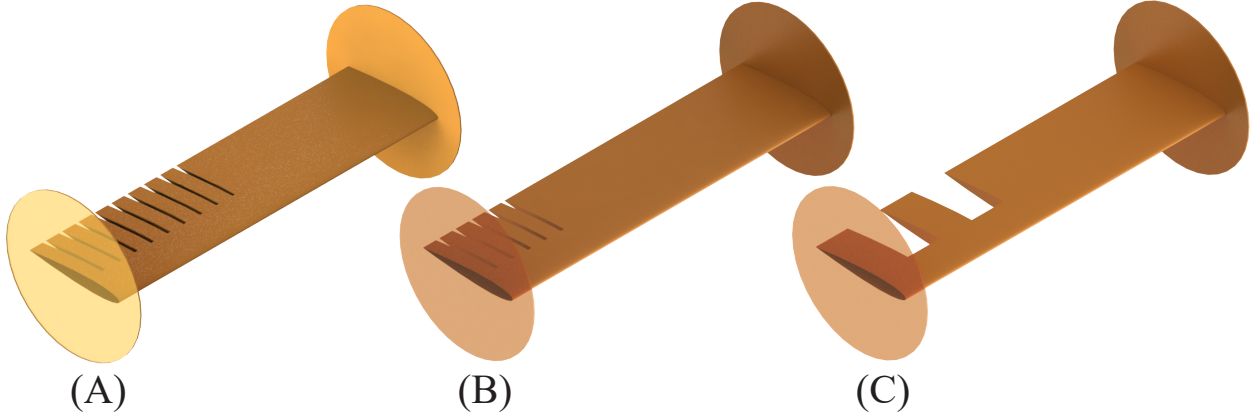


Figure 5.2: Each gap dimension was tested on (A) a wing with nine gaps and (B) a wing with five outboard gaps. (C) A two-gap wing with  $\frac{2c}{3} \times \frac{b}{5}$  gaps was also simulated. Parts (A) and (B) show wings with  $\frac{2c}{3} \times \frac{b}{48}$  gaps for illustrative purposes.

(TKE) were all below  $1 \times 10^{-4}$ , and specific dissipation rate (SDR) was reduced by at least four orders of magnitude. In seven cases, SDR only relatively fell below  $4.1 \times 10^{-4}$ . Reaching convergence typically took 100 to 200 iterations. Further details on the simulation method, meshing, and experimental validation can be found in Chapter III in the sections regarding the SI-gapped wing configuration.

### 5.3.2 Building the linear models

To better quantify the relationship between the gap configuration and wing performance, I fit the parameter sweep CFD data to linear models. I calculated separate models of rolling moment coefficient and gap cover actuation work using multiple linear regressions at a 95% confidence level in MATLAB. The predictor variables were gap width, gap length, gap aspect ratio, the number of gaps, angle of attack, a constant intercept term, and several interaction terms. The number of gaps was treated as a categorical, rather than continuous, variable. The number of gaps must be a whole number. Furthermore, only observations from five- and nine-gap wings were included in the model fit. These assumptions indicated that a categorical variable was appropriate.

Gap aspect ratio was included as an predictor variable. Based on the fluid mechanics



within a gap (Chapter III), I suspected that the interaction between gap length and gap width would be important to the gapped wing's performance. Thus, I modelled the gap width and gap length with units of meters, rather than dimensionless quantities normalized by wing semi-span and wing chord (respectively). This approach enabled me to more accurately capture gap aspect ratio effects in the linear models. To avoid redundant, linearly dependent, or higher order predictor terms, I did not include interaction terms between gap length, gap width, and gap aspect ratio. The gap aspect ratio predictor variable served as the interaction term between gap length and gap width. I also did not include interaction terms between aspect ratio and gap number, and between aspect ratio and angle of attack. Both of these interaction terms were encompassed in the interactions between gap width, gap length, gap number, and angle of attack.

All of the parameter sweep CFD data from the five- and nine-gap wings were used as observations to fit the models. I did not include the two-gap wing in the linear fit because only one data point on the two-gap wing was available. Furthermore, the gaps on the two-gap wing were centered around the middle of the semi-span instead of concentrated at the wingtip. The models did not account for varying the position of the gaps in this manner. Note that the parameter sweep only simulated angles of attack up to  $10^\circ$ , below the point where CFD predicted stall (Chapter III). This was acceptable because linear models would not be appropriate for capturing nonlinear stall behavior.

Given the above assumptions, the linear models were initially formulated as follows:

$$\begin{aligned}
C_\ell^{wing} = & (A_0 + A_1^*) + (A_2 + A_3^*)b_g + (A_3 + A_4^*)c_g + (A_5 + A_6^*)AR_g \\
& + (A_5 + A_6^*)\alpha + A_7\alpha^2 + A_8b_g\alpha + A_9c_g\alpha + (A_{10} + A_{11}^*)AR_g\alpha
\end{aligned} \tag{5.3}$$

and

$$\begin{aligned}
W_{gc} = & (B_0 + B_1^*) + (B_2 + B_3^*)b_g + (B_3 + B_4^*)c_g + (B_5 + B_6^*)AR_g \\
& + (B_5 + B_6^*)\alpha + B_7\alpha^2 + B_8b_g\alpha + B_9c_g\alpha + (B_{10} + B_{11}^*)AR_g\alpha
\end{aligned} \tag{5.4}$$

The superscript \* indicated that the corresponding coefficient was only included for the model of the nine gap wing, and set to zero for the five gap model. This is typically how categorical variables are handled by MATLAB.

I first ran the regressions with all of the predictor variables in Eqn. 5.3 and Eqn. 5.4. These initial models identified terms with a deficit rank, indicating a coefficient value of zero. To determine statistically insignificant predictors, I then re-ran the regressions a second time, excluding the deficit-rank terms. Predictors with a p-value greater than the significance level of 0.05 were deemed statistically insignificant. I performed the regressions a final time excluding both the deficit-rank and insignificant terms, resulting in the final linear models of rolling moment coefficient and gap cover actuation work.

It was difficult to directly interpret the model coefficients, because of the prevalence of the interaction terms and their physical significance. Nevertheless, the magnitudes and signs of the coefficients were used to qualitatively assess the relative impact of the predictor variables.

## 5.4 Effects on rolling moment coefficient

As the gaps became larger in either dimension, both the five- and nine-gap wings produced greater rolling moment coefficients (Fig. 5.3). At  $2^\circ$ ,  $7^\circ$ , and  $10^\circ$  angle of attack, the maximum rolling moment coefficient was produced by the largest gap of dimensions  $\frac{3c}{4} \times \frac{b}{16}$ . These gap dimensions were the maximum values, on the boundary of the domain. Interestingly, the resulting aspect ratio was an intermediate value—neither the smallest nor largest aspect ratio (Fig. 5.2). I expected that the selected range of gap dimensions would capture a clear peak in rolling moment coefficient. However, the maximization at the domain boundaries suggested that greater rolling moment coefficients may exist outside of the simulated gap dimensions. In other words, the highest rolling moment coefficient produced within this domain is not necessarily the maximum rolling moment coefficient across all infinite possible gap configurations.

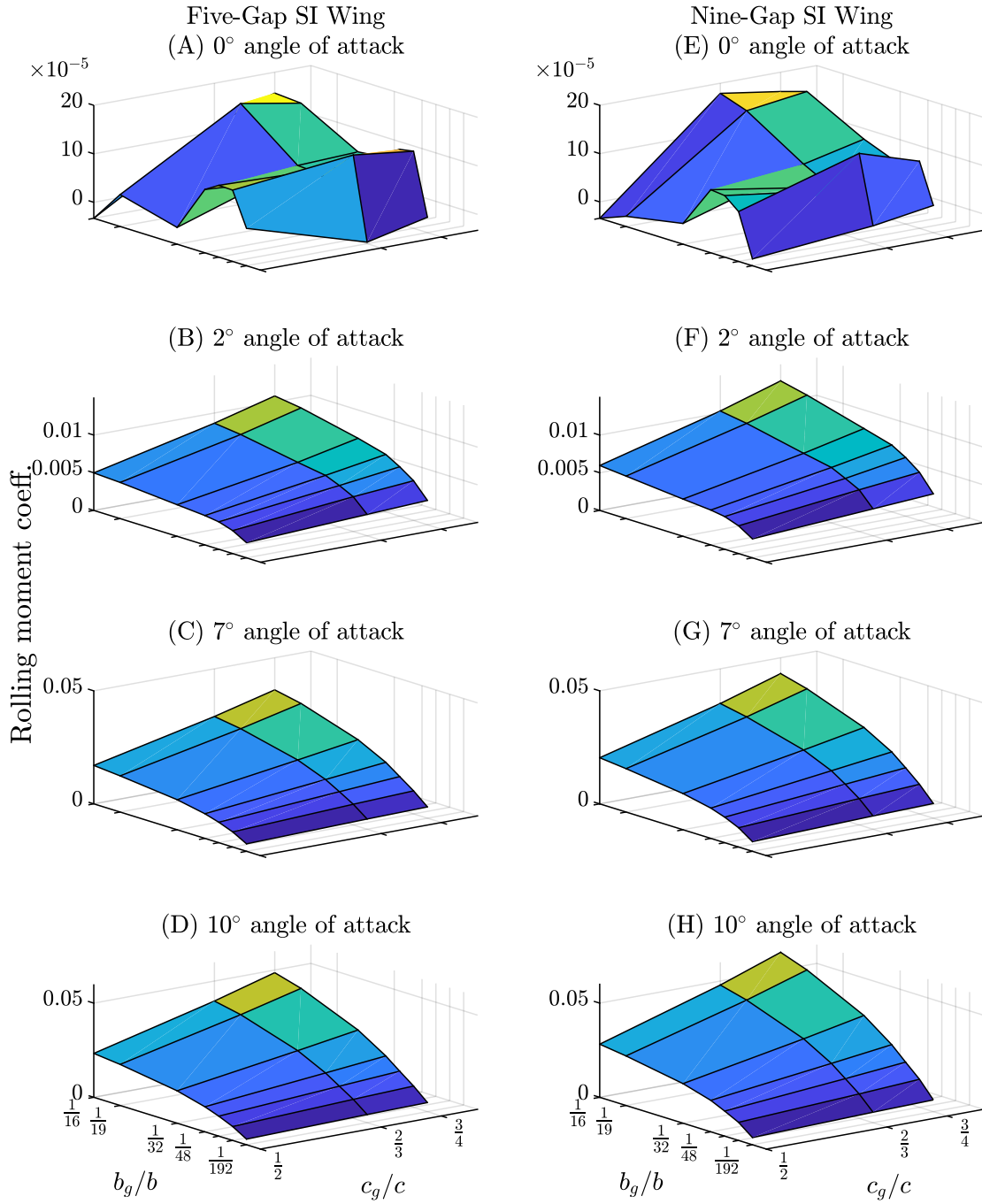


Figure 5.3: Rolling moment coefficient increased as gap length and gap width increased. Five- and nine-gap wings with various gap lengths and widths were simulated at 0°, 2°, 7°, and 10° angle of attack.

Furthermore, it appeared that gap width had a stronger influence on rolling moment coefficient than gap length (Fig. 5.3). There also was a noticeable interaction between gap width and gap length: varying the length of a wider gap produced greater changes in rolling moment coefficient than for a narrower gap.

As expected from Chapter II, increasing the angle of attack typically increased rolling moment coefficient for a given gap configuration (Fig. 5.3). Additionally, increasing angle of attack typically affected wings with larger gaps more than wings with smaller gaps. This result implied interaction effects between angle of attack and gap dimensions. However, gap dimensions appeared to have a larger impact on roll than angle of attack alone. In some cases, varying the gap dimensions caused changes in rolling moment coefficient that were an order of magnitude larger than the changes due to angle of attack. For example, the nine-gap wing with  $\frac{3c}{4} \times \frac{b}{16}$  gaps produced a rolling moment coefficient of 0.043 at  $7^\circ$  angle of attack, and a rolling moment coefficient of 0.0594 at  $10^\circ$  angle of attack—an increase of 38% due to changing the angle of attack. However, holding angle of attack constant at  $10^\circ$  and widening the gap from  $\frac{b}{192}$  to  $\frac{b}{16}$  increased the rolling moment coefficient from 0.00623 to 0.0594, or 853% due to widening the gaps.

For a given angle of attack and gap dimensions, increasing the number of gaps from five to nine did not drastically change the rolling moment coefficient of the wing (Fig. 5.3). The nine-gap wing only produced slightly higher rolling moment coefficients than the five-gap wing. This trend implied that the gaps at the wingtip were more effective at producing roll than gaps closer to the wing root. In other words, removing the inboard gaps did not substantially decrease the rolling moment coefficient. This further suggested that the position of the gaps along the span could be designed to maximize rolling moment coefficient.

The  $0^\circ$  angle of attack case did not follow the above trends (Fig. 5.3). Airfoil symmetry caused the rolling moment coefficient to be negligibly small regardless of gap configuration. These results were still included in the figure for completeness.

From the data in Figure 5.3, the rolling moment coefficient linear model was found to be:

$$C_\ell^{wing} = 0.0141 + 1.19b_g - 0.0923c_g - 0.175AR_g - (0.00219 - 0.000496^*)\alpha + 0.153b_g\alpha + 0.0233c_g\alpha - 9.648 \times 10^{-5}\alpha^2 \quad (5.5)$$

where the superscript \* indicated that the corresponding term should only be included for the model of the nine gap wing, and neglected for the five gap model. For example, the term  $0.000496^*\alpha$  described the interactions between angle of attack and including nine gaps in the wing, relative to the five-gap wing. The model had an adjusted  $R^2$  value of 0.959 and all stated terms were significant based on their p-values.

The rolling moment coefficient linear model (Eqn. 5.5) generally agreed with the conclusions from Figure 5.3. Based on coefficient magnitude, gap width had the strongest impact on the rolling moment coefficient, followed by gap aspect ratio and the interaction between gap width and angle of attack. Figure 5.3 implied that the interactions between angle of attack and gap length ( $c_g\alpha$ ) may have also had a large impact on roll production. However, the magnitude of this coefficient was not as large as that of gap length alone ( $c_g$ ). This suggested that the gap length-angle of attack interaction may not have been as important to roll production. Based on the signs of the coefficients, gap width was positively correlated with rolling moment coefficient, while gap aspect ratio was negatively correlated.

## 5.5 Effects on actuation work

The gap cover actuation work decreased as gap length, gap width, angle of attack, and number of gaps decreased (Fig 5.4). The smallest  $\frac{c}{2} \times \frac{b}{192}$  gaps required the least work of all the simulated configurations. Similarly to the rolling moment coefficient, the fact that actuation work was minimized on the domain boundary suggested that lower-work configurations may exist outside of the simulated gap dimensions.

In general, gap width and the number of gaps appeared to have the strongest impact

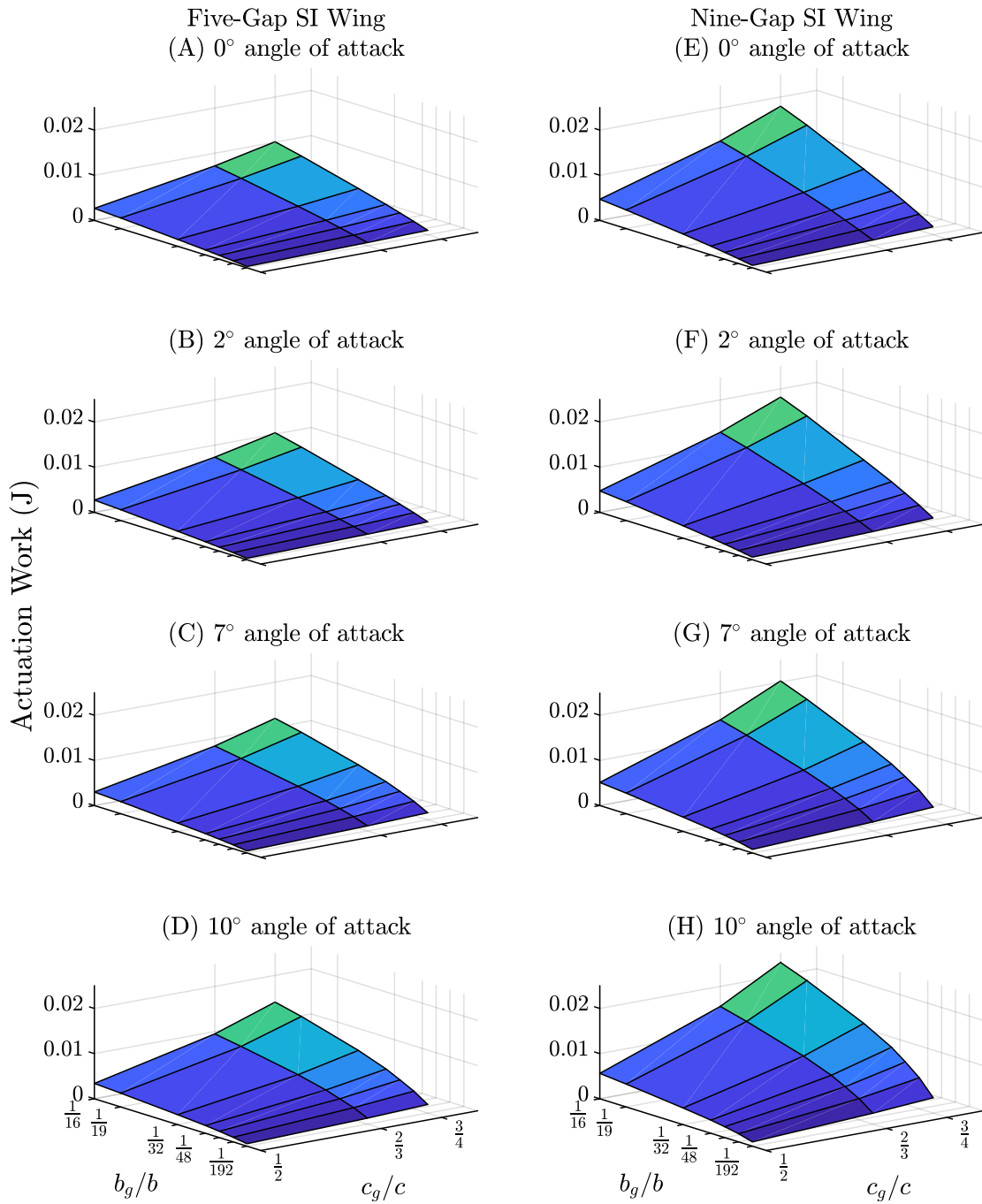


Figure 5.4: Gap cover work increased as gap length and gap width increased. Each gap configuration was simulated at 0°, 2°, 7°, and 10° angle of attack on five- and nine-gap wings.

on actuation work (Fig. 5.4). The magnitude of the work generally increased proportionally with the number of gaps. This trend was expected based on the formula for gapped wing actuation work (Eqn. 3.1). There was also a visible interaction between gap length and width: lengthening the wider gaps increased work more than lengthening the narrower gaps. Angle of attack appeared to play a small role in actuation requirements. While rolling moment coefficient was more dependent on angle of attack, the work requirements stayed fairly constant as angle of attack varied.

From the data in Figure 5.4, the linear model of gap cover actuation work was:

$$\begin{aligned}
 W_{gc} = & 0.411 - 0.750^* + (114 + 21.6^*)b_g - (2.45 - 5.05^*)c_g - 13.0AR_g + 0.0017\alpha^2 \\
 & - (0.0741 - 0.0152^*)\alpha + 0.864b_g\alpha + 0.436c_g\alpha - 0.0918^*AR_g\alpha
 \end{aligned} \tag{5.6}$$

Again, the superscript \* indicated that the corresponding term should only be included for the model of the nine gap wing, and neglected for the five gap model. For example, the term  $-0.750^*$  described the effects of using a nine-gap wing relative to the five-gap wing. The term  $21.6^*b_g$  quantified the interactions between nine gaps and gap width, relative to the five-gap wing. The model had an adjusted  $R^2$  value of 0.973 and all stated terms were significant based on their p-values.

The gap cover work model (Eqn. 5.6) generally confirmed the effects of the predictor variables on gapped wing performance (Fig. 5.4). Based on the relative magnitudes of the coefficients, gap width, gap length, and gap aspect ratio had a greater impact on work compared to angle of attack. Gap width was generally positive correlated with work while gap aspect ratio was negatively correlated, according to the signs of the coefficients. This result implied that the most effective method of reducing gap actuation work could be narrowing the gaps, or simultaneously narrowing and lengthening the gaps.

The work model also identified several trends that were not readily apparent in Figure 5.4. The interaction between number of gaps and gap width ( $21.6^*b_g$ ) and number of gaps and gap length ( $5.05^*c_g$ ) were the strongest factors in terms of comparing the five- to the nine-

gap wing. Finally, the interaction between gap width and angle of attack was an important driver of actuation work. According to the magnitude of the coefficients, this interaction term was slightly more prevalent than the number of gaps alone.

The effects of gap dimensions on roll and work could be related to the fluid mechanics within a gap. For example, shortening the gaps and starting them further aft along the chord reduced the actuation work (Fig. 5.4). Previously, we found that the flow in a gap recirculated, then vented to the suction side of the trailing edge (Chapter III). Due to this flow behavior, the majority of the vertical gap face experienced negative pressure coefficients. It required work to overcome this aerodynamic loading and actuate the gaps. Shortening the gaps could effectively decrease the area exposed to the suction pressures in the gap. The more aftward position could also reduce the overall suction force on the gaps, since the pressure coefficient increased towards the trailing edge (Fig. 3.9). While shortening the gaps also lowered the rolling moment coefficient (Fig. 5.3), the normalized roll overall increased (Fig. 5.5). Thus, the length of the gap could be selected to balance actuation costs with the desired maximum rolling moment coefficient.

I also used these work results to refine the previous work estimates of the gap covers and aileron (Appendix F). Previous methods assumed that the gap force and aileron hinge moment were constant across displacement (Eqn. 3.1 and 2.14), likely leading to conservative overestimates of the actuation work. Here, I applied the data from the parameter sweep to estimate the actuation work using integral approximations. As expected, the refined work estimates were lower than the previous constant force/hinge moment estimates. Furthermore, the intersection of the refined work curves shifted to a higher rolling moment coefficient compared to Figure 3.11. However, the relative work curves ultimately confirmed that the constant force/hinge moment assumption made in Chapter III was appropriate. Due to practical limitations of the integral approximations, the constant force/hinge-moment work estimates were used in this dissertation. The integral approximation methods and results are discussed in in Appendix F.



## 5.6 Gap configuration could be designed to maximize normalized roll

Finally, I investigated the effects of the gap parameters on rolling moment coefficient per actuation work (“normalized roll”). Both roll and work individually tended to increase with gap dimensions, number of gaps, and angle of attack. Thus, increasing the value of these parameters had opposing effects: the rolling moment coefficient increased at the cost of higher work requirements. This led to a classic optimization problem. The gap configuration could be designed to balance rolling moment coefficient with actuation work for a given mission. Ideally, the gaps would maximize normalized roll, or produce the greatest rolling moment coefficient for the least actuation work. Given the novel nature of the gapped wing, the goal of the parameter sweep was not to find this optimal geometry, but rather build intuition of the gapped wing design space. As there were infinite possible combinations of gap dimensions, number, and position, this parameter sweep merely scratched the surface. A true optimization study would be required to find the ideal gap configuration for any given UAV mission.

Normalized roll generally increased as angle of attack increased (Fig. 5.5). This relationship confirmed that the gapped wings were best suited for roll control at high angles of attack, irrespective of gap dimensions. That is, the gapped wings produced the highest normalized roll at high angles of attack (which corresponded to high lift coefficients for the gapped wings, per Figure 2.5). The previous experimental (Chapter II) and computational (Chapter III) work demonstrated this same trend for the initial gap dimensions.

In addition to the magnitude, the general shape of the normalized roll surface also varied with angle of attack (Fig. 5.5). This phenomena differed from that of the work and rolling moment coefficient surfaces, whose shapes remained fairly constant across angle of attack (Fig. 5.3 and 5.4). The varying effects also implied that the interactions between angle of attack and the gap dimensions were significant. The maximum normalized roll was produced

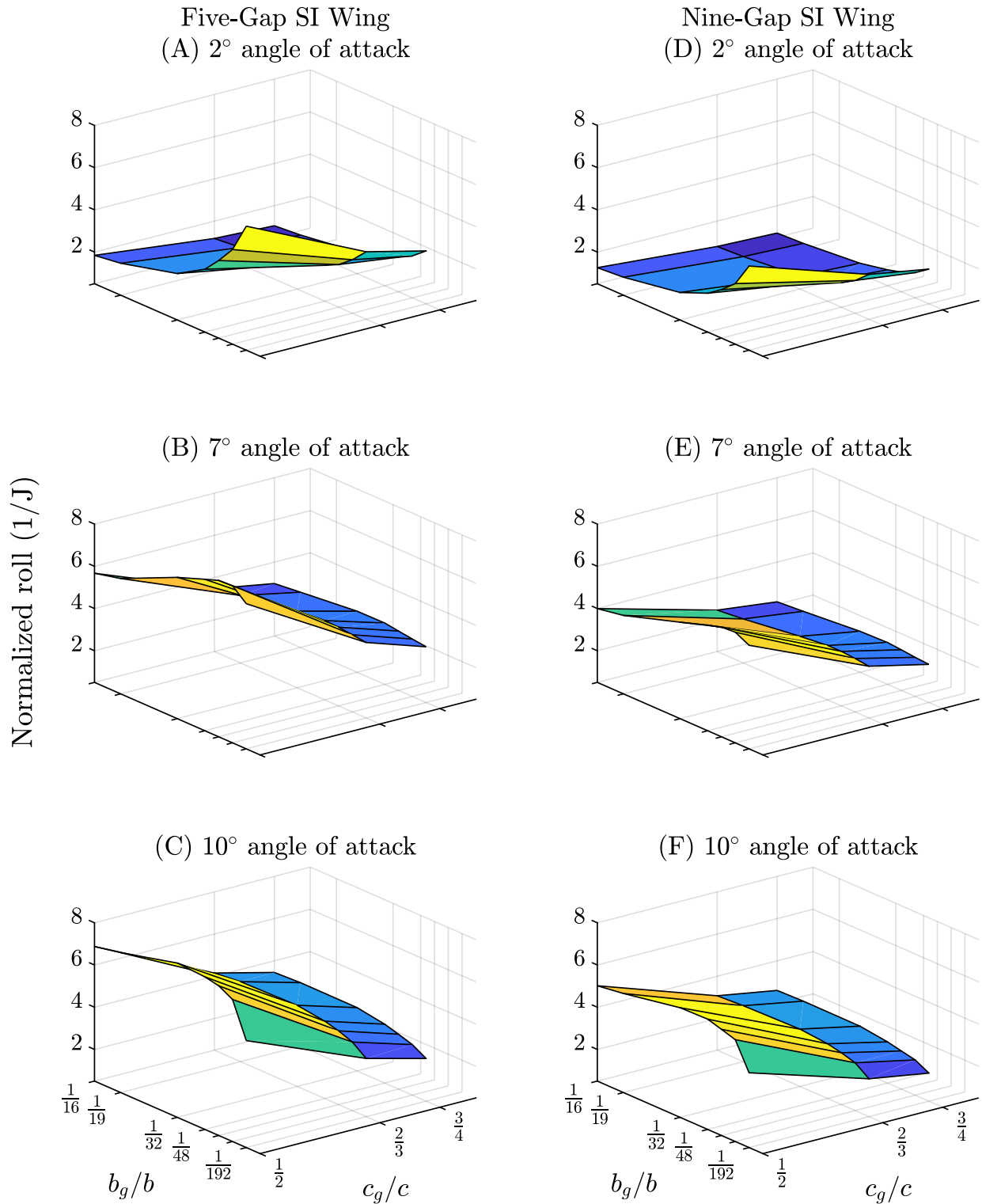


Figure 5.5: Normalized roll increased as gap length and width increased. Wings were simulated at 2°, 7°, and 10° angle of attack on five- and nine-gap wings. Wings at 0° angle of attack produced negligible roll and were excluded.

by different gap dimensions at each angle of attack. For instance, both the five- and nine-gap wings maximized the normalized roll with the smallest  $\frac{c}{2} \times \frac{b}{192}$  gaps at  $2^\circ$  angle of attack. However, the five-gap wing maximized the normalized roll with  $\frac{c}{2} \times \frac{b}{96}$  gaps at  $7^\circ$  and  $\frac{c}{2} \times \frac{b}{32}$  gaps at  $10^\circ$  angle of attack. The nine-gap wing also maximized normalized roll with  $\frac{c}{2} \times \frac{b}{96}$  gaps at  $7^\circ$ , but with  $\frac{c}{2} \times \frac{b}{48}$  gaps at  $10^\circ$  angle of attack. Note that the maximum normalized roll was produced by intermediate gap widths at  $7^\circ$  and  $10^\circ$ . Conversely, the rolling moment coefficient and actuation work were both maximized on the domain boundaries of gap dimensions. Overall, these trends implied that the gaps could be designed to maximize the normalized roll.

The normalized roll was also higher for the five-gap wing compared to the nine-gap wing (Fig. 5.5). This result was expected given that the nine-gap wing only slightly increased rolling moment coefficient, but nearly doubled actuation work compared to the five-gap wing. Relatedly, this also confirmed that the gaps could be more efficient (produce more roll per unit of work) when positioned on the outboard portion of a wing.

From the limited gap configurations and angles of attack that were simulated here, the maximum normalized roll was produced by a five-gap wing with  $\frac{c}{2} \times \frac{b}{32}$  gaps at  $10^\circ$  angle of attack (Fig. 5.5). This result was specific to the discrete parameter values used. However, this work demonstrated an important general conclusion: varying gap width, gap length, number of gaps, and angle of attack effectively changed the rolling moment coefficient, actuation work, and normalized roll of the gapped wing. In short, the gap parameters could be tailored for specific performance requirements or mission objectives. Optimization studies are required to confirm this conclusion, and find a true optimal gap geometry and layout for a given set of criteria.

## 5.7 Linear model validation

To validate the linear models of roll and work, I compared them to a subset of the CFD parameter sweep data consisting of the five- and nine-gap wings with the initial gap

dimensions  $\frac{2c}{3} \times \frac{b}{48}$  (Fig. 5.6). The work model fit the data well. However, the rolling moment coefficient model had noticeable residuals. At  $10^\circ$  angle of attack, the absolute error in rolling moment coefficient was 0.0022 for the nine-gap wing (9.1% relative error), and 0.0021 (10.9% relative error) for the five-gap wing. Investigating various combinations of additional predictor variables (such as lift coefficient, total planform wing area, and others) did not improve the fit of the rolling moment coefficient model. However, I successfully fit a linear rolling moment coefficient model based solely on the data of the five- and nine-gap wings with the initial gap dimensions (Appendix H). This exercise demonstrated that the model-building process was reliable, and that the errors between the model and CFD data were likely from another source.

The model error highlighted the difficulty in predicting the rolling moment coefficient of the gapped wings, especially at higher angles of attack. Given the complexity of the flow field and inherent challenges of RANS (Chapter III), the residuals between the linear model and CFD data could have been due to errors from the CFD simulations themselves. Since it is difficult to model the gap flow in RANS, it is likely that there were errors between the simulations of different gap configurations. This could have led to errors between the linear model and the validation data that could not be explained by the model. Since the error of the rolling moment coefficient model was relatively low, I included it for completeness and to build a qualitative understanding of the effects of gap dimensions. In the future, higher fidelity CFD simulations may improve the fit of the rolling moment coefficient model.

## 5.8 Gaps could be gradually actuated for smooth roll control

Conventional control surfaces like ailerons and spoilers are able to deflect in a graduated fashion. They can be deflected all at once, or little by little, providing smooth control forces. This allows the aircraft to adjust its performance and initiate maneuvers of varying specifications. For example, deflecting the ailerons by a smaller angle leads to a lower roll rate than larger deflections.

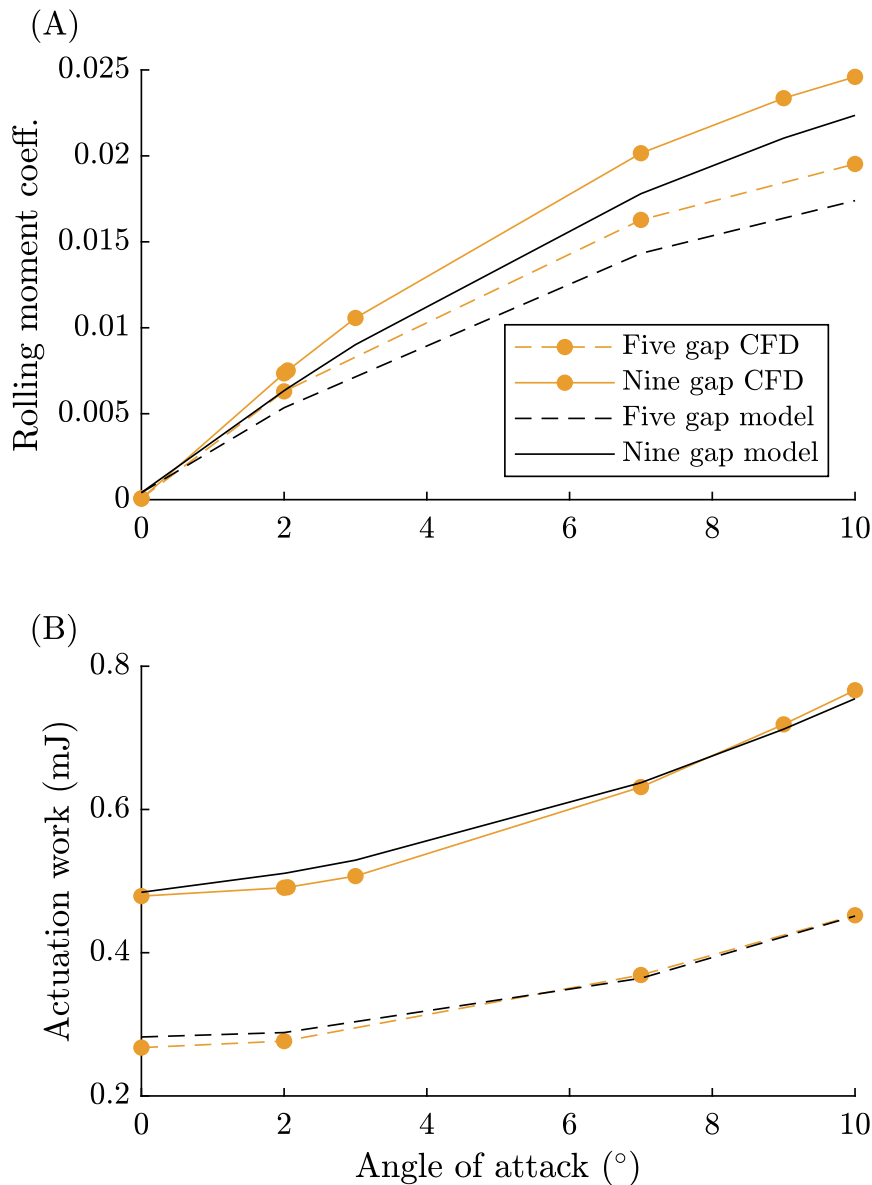


Figure 5.6: (A) The linear model for the rolling moment of the five- and nine-gap wings fit with higher residuals at higher angles of attack. (B) The linear model for the actuation work of the five- and nine-gap wings fit very accurately.

The parameter sweep illustrated that gapped wings could be gradually actuated in a similar manner. For example, given a gap length of  $\frac{2c}{3}$ , widening the gaps from  $\frac{b}{192}$  to  $\frac{b}{16}$  produced smooth increases in both rolling moment coefficient (Fig. 5.3) and actuation work (Fig. 5.4). Widening the gaps could be likened to opening them—as the gap covers retract into

the wing, the a wider gap span becomes exposed to the airflow. Conversely, narrowing the gaps is akin to closing them. Thus, like conventional deflecting control surfaces, the results suggested that gaps were capable of providing smooth changes in aerodynamic moments and actuation requirements. This effect is advantageous because it reduces the potential complexity of a flight controller. The controller would not necessarily need to account for sharp jumps or discontinuities in aerodynamic forces and moments as the gaps are opened.

## 5.9 Chapter summary

Here, I performed a parameter sweep in CFD to explore the effects of gapped wing parameters on control surface performance. I simulated various gap widths, gap lengths, and number of outboard gaps on asymmetric gapped wings, and collected forces and moments at several angles of attack. Then, I fit linear models of the gapped wing rolling moment coefficient and gap cover actuation work. The linear models were limited as predictive tools, but were useful in characterizing the relative effects of gap parameters on control surface performance. Widening the gaps and decreasing gap aspect ratio typically increased both rolling moment coefficient and actuation work. This opposing effect led to an opportunity for optimization in future studies. Gap width had a greater impact on performance than gap length. Angle of attack was more prevalent in roll production than work requirements. The five-gap wing data also implied that outboard gaps were more effective at producing roll than inboard gaps, similarly to an aileron. The results further supported that the gapped wings were most effective for roll control at high angles of attack. While this chapter constituted a parameter sweep as opposed to a true optimization study, it suggested that the gap configuration could be designed to maximize normalized roll (rolling moment coefficient per actuation work). Finally, the parameter sweep implied that the gaps could be gradually actuated, leading to smooth variations in rolling moment and work requirements.

## 5.10 Data availability

The data and codes used to perform the parameter sweep are openly available on figshare at DOI: [10.6084/m9.figshare.c.6487942.v2](https://doi.org/10.6084/m9.figshare.c.6487942.v2).

## CHAPTER VI

# Gapped Wings Altered Trim and Alleviated Gusts

### 6.1 Overview

The novel gapped wings have now been studied in terms of rapid descent and roll control. However, their potential as gust alleviation devices and overall impact on aircraft dynamics remain unknown. Here, we analytically determined the trim state, free response, and gust response of aircraft with varying gapped wings. The gaps shifted the aerodynamic center of the wing forward but in general beneficially decreased the wing's overall contribution to the aircraft pitching moment. This effect resulted in a steeper glide angle and higher velocity at trim. The gaps also reduced the phugoid mode by decreasing its natural frequency and increasing damping. However, all of the aircraft could require a controller for the short period mode due to a higher natural frequency. Finally, we showed that the gapped wings improved the aircrafts' response to transverse and streamwise gusts by increasing damping and reducing the maximum amplitude of oscillations. Despite some practical design challenges associated with the gapped wings, they ultimately benefited the aircraft's dynamic response and effectively mitigated gusts. Thus, the gapped wings could be a suitable control surface for gust alleviation. This result implied that the gapped wings could be advantageous by providing multifunctionality as a control surface for adjusting trim, providing roll control, and mitigating gusts.



## 6.2 Motivation and background

The gapped wings have now been investigated for rapid descent and lateral movement, and showed promise for roll control in certain situations (Chapter II). Furthermore, we built a solid understanding of the effect of the gaps on the flow over the wing, and the flow mechanics within a gap (Chapter III). The roll performance and actuation requirements of a gapped wing were additionally modelled as functions of gap geometry (Chapter V). Here, we evaluated the whiffing-inspired gapped wings with respect to a third hypothesized whiffing function [12]: gust alleviation. This work presented the first application of gapped wings as a gust alleviation device, and the first investigation into how gaps along the length of the chord may affect the rigid body dynamics of an aircraft. Ultimately, we built a qualitative understanding of how whiffing-inspired gaps affect the dynamics of a simple idealized aircraft.

## 6.3 Methods

To assess the effects of the gapped wings on aircraft dynamics, we employed a combination of computational, analytical, and semi-empirical methods. Computational work was performed in Seimen's STAR-CCM+ software, and we created custom MATLAB scripts in version r2022a for the analytical modelling.

### 6.3.1 Modelling the equations of motion

We analytically modelled the rigid body equations of motion for an aircraft following common aerodynamic texts [73], [88]. We employed small disturbance theory and linearized the equations about an equilibrium, or trim, condition. Further, we assumed that the trim condition was symmetric: side slip angle, sideways velocity, roll rate, pitch rate, yaw rate, yaw angle, and roll angle were zero. This approach enabled us to investigate the longitudinal behavior of the aircraft decoupled from the lateral behavior. To avoid making limiting

assumptions on the powerplant of a hypothetical aircraft, we assumed the plane was in a gliding scenario. At the initial time  $t = 0$ , we redefined the body axes to align with the stability axes, such that all incoming velocity was along the  $x$ -axis and the initial heave velocity  $w_0$  was zero (Fig. 6.1) [73], [88], [89]. Since the flight condition was symmetric, we further assumed that the wind axes and stability axes coincided. We treated the aircraft as “stick fixed,” such that there was no input control vector. This problem definition led to the following equations of motion, written in the state space representation [73], [88], [89]:

$$\dot{\mathbf{x}} = \mathbf{A}\mathbf{x} + \mathbf{C}\xi \quad (6.1)$$

The aircraft state vector ( $\mathbf{x}$ ) was defined as:

$$\mathbf{x} = \begin{bmatrix} \Delta u \\ \Delta w \\ \Delta q \\ \Delta \theta \end{bmatrix} \quad (6.2)$$

where  $\Delta u$  is the change in forward velocity (m/s),  $\Delta w$  is the change in heave velocity (m/s),  $\Delta q$  is the change in pitch rate (rad/s), and  $\Delta \theta$  is the change in pitch angle (rad). The gust velocities along each stability axis were defined by the gust disturbance vector:

$$\xi = \begin{bmatrix} v_{gx} \\ v_{gz} \\ v_{gq} \end{bmatrix} \quad (6.3)$$

where  $v_{gx}$  is the gust velocity along the  $x$ -axis,  $v_{gz}$  is the gust velocity along the  $z$ -axis, and  $v_{gq}$  is the rotational gust velocity about the  $y$ -axis (all in m/s). Solving Eqn. 6.1 yielded the change in each state variable over time, after the aircraft was perturbed by a gust. Setting the gust disturbance vector  $\zeta$  to zero and solving the homogeneous system  $\dot{\mathbf{x}} = \mathbf{A}\mathbf{x}$  resulted

in the free response of the aircraft (Section 6.3.3).

Following Nelson's derivation for the equations of motion resulted in [88]:

$$\begin{aligned}
 \mathbf{A} &= \begin{bmatrix} A_{11} & A_{12} & A_{13} & A_{14} \\ A_{21} & A_{22} & A_{23} & A_{24} \\ A_{31} & A_{32} & A_{33} & A_{34} \\ A_{41} & A_{42} & A_{43} & A_{44} \end{bmatrix} \\
 &= \begin{bmatrix} X_u & X_w & 0 & -g \cos \gamma_0 \\ Z_u & Z_w & U_0 + Z_q & -g \sin \gamma_0 \\ M_u + M_{\dot{w}}Z_u & M_w + M_{\dot{w}}Z_w & M_q + M_{\dot{w}}U_0 & 0 \\ 0 & 0 & 1 & 0 \end{bmatrix}
 \end{aligned} \tag{6.4}$$

$A_{14}$  and  $A_{24}$  can be defined as  $-g$  and zero, respectively, by assuming straight and level flight [88]. However, to account for the nonzero trim pitch angle of our gliding configuration, we calculate these terms with respect to the glide angle [73], [89]. The terms  $Z_q$  in  $A_{23}$  and  $M_{\dot{w}}$  in  $A_{31}$ ,  $A_{32}$ , and  $A_{33}$  are also sometimes neglected [88] but we included them for completeness.

Similarly per Nelson [88], the  $\mathbf{C}$  matrix was:

$$\mathbf{C} = \begin{bmatrix} -X_u & -X_w & 0 \\ -Z_u & -Z_w & 0 \\ -(M_u + M_{\dot{w}}Z_u) & -(M_w + M_{\dot{w}}Z_w) & -(M_q + M_{\dot{w}}U_0) \\ 0 & 0 & 0 \end{bmatrix} \tag{6.5}$$

and the aircraft stability derivatives were:

$$\begin{aligned}
X_u &= -(C_{D_u} + 2C_{D0}) \frac{Q_0 S_{fs}}{m U_0} \\
X_w &= -(C_{D_\alpha} - C_{L0}) \frac{Q_0 S_{fs}}{m U_0} \\
Z_u &= -(C_{L_u} + 2C_{L0}) \frac{Q_0 S_{fs}}{m U_0} \\
Z_w &= -(C_{L_\alpha} + C_{D0}) \frac{Q_0 S_{fs}}{m U_0} \\
Z_\alpha &= Z_w U_0 \\
Z_q &= C_{Z_q} \frac{c}{2U_0} \frac{Q_0 S_{fs}}{m} \\
M_u &= C_{M_u} \frac{Q_0 S_{fs} c}{U_0 I_y} \\
M_w &= C_{M_\alpha} \frac{Q_0 S_{fs} c}{U_0 I_y} \\
M_q &= C_{M_q} \frac{c}{2U_0} \frac{Q_0 S_{fs} c}{I_y} \\
M_{\dot{w}} &= C_{M_{\dot{\alpha}}} \frac{c}{2U_0} \frac{Q_0 S_{fs} c}{U_0 I_y}
\end{aligned} \tag{6.6}$$

where  $Q_0$  is the dynamic pressure (N/m<sup>2</sup>) evaluated at the trim velocity  $U_0$  ( m/s),  $m$  is the mass of the total aircraft (kg),  $S_{fs}$  is the planform area of the wing (m<sup>2</sup>),  $c$  is the wing chord (m), and  $I_y$  is the mass moment of inertia of the aircraft about the  $y$ -axis at its center of gravity (kg·m<sup>2</sup>). The relevant aircraft aerodynamic properties are  $C_{D_u}$  the change in drag coefficient with forward speed,  $C_{D0}$  the drag coefficient at trim,  $C_{D_\alpha}$  the slope of the drag curve,  $C_{L0}$  the lift coefficient at trim,  $C_{L_u}$  the change in lift coefficient with forward velocity,  $C_{L_\alpha}$  the slope of the lift curve,  $C_{Z_q}$  the change in the  $Z$ -force coefficient due to pitch rate,  $C_{M_u}$  the change in pitching moment coefficient with forward speed,  $C_{M_\alpha}$  the slope of the pitching moment curve,  $C_{M_q}$  the change of the pitching moment coefficient with pitch rate, and  $C_{M_{\dot{\alpha}}}$  the change of the pitching moment coefficient with the time rate of change of angle of attack. The coefficients were evaluated for each aircraft at its trim state (Section 6.3.5.3). We neglected the control derivatives because the aircraft were static and rigid.

### 6.3.2 Defining the trim state

From small disturbance theory, the aircraft equations of motion were evaluated about an equilibrium state, also known as trim [73], [88]. Trim was defined according to [89]:

$$\begin{aligned} F_{x,0} &= -\frac{1}{2}\rho U_0^2 S_{fs} C_{D0} - mg \sin \gamma_0 = 0 \\ F_{z,0} &= -\frac{1}{2}\rho U_0^2 S_{fs} C_{L0} + mg \cos \gamma_0 = 0 \end{aligned} \tag{6.7}$$

and

$$M_{y0} = 0 \tag{6.8}$$

where  $\gamma_0$  is the trim glide angle (rad).

To satisfy Eqn. 6.8, we first found the angle of attack at which the aircraft pitching moment coefficient  $C_M$  equalled zero, yielding the trim angle of attack  $\alpha_0$ . Given our no-thrust gliding configuration, we only considered positive angles of attack to ensure positive lift. Furthermore, we limited our analysis to trim states achieved at small angles of attack,  $\alpha \leq 2.5^\circ$ . This assumption kept our calculations within the linear range of the lift and pitching moment coefficient curves [73], [88], [90]. Furthermore, we only compared stable aircraft, stipulating a negative pitching moment slope about the aircraft's center of gravity [73], [88].

We then solved the system represented by Eqn. 6.7 for the trim forward velocity  $U_0$  and the trim glide angle  $\gamma_0$ . Solving Eqn. 6.7 generally yielded several pairs of velocities and glide angles. To give our results practical meaning, we selected the trim conditions with positive real velocities. We also required aircraft to trim at shallow glide angles ( $0^\circ \leq \gamma_0 \leq -45^\circ$ ) to model realistic gliding flight [89]. Per convention, we defined  $\gamma_0$  as positive upwards, such that  $\gamma_0 < 0$  for gliding flight [73], [89].

### 6.3.3 Characterizing the free response

The longitudinal free response of an aircraft is typically comprised of two modes: a higher-frequency highly damped motion called the short period mode, and a lower-frequency less damped motion called the phugoid mode [73], [88], [89]. We found the modes by solving the eigenvalue problem corresponding to Eqn. 6.1, in other words, by solving the homogeneous system  $\dot{\mathbf{x}} = \mathbf{A}\mathbf{x}$ . We calculated the eigenvalues of each aircraft's  $\mathbf{A}$  matrix using MATLAB. While there are mathematical approximations for the phugoid and short period modes [73], [88], we solved the whole fourth-order system for increased accuracy [89].

The eigenvalues for a dynamically stable system are typically complex conjugate pairs [73], [88]:

$$\lambda_i = -\Re \pm j\Im \quad (6.9)$$

where  $\Re$  is the real part of the eigenvalue and  $\Im$  is the imaginary part of the eigenvalue. For each mode, we calculated the natural frequency (rad/s), damping ratio, and the time to halve the initial amplitude (s) according to:

$$\omega_n = \sqrt{\Re^2 + \Im^2} \quad (6.10)$$

$$\zeta = \frac{\Re}{\omega_n} \quad (6.11)$$

$$t_a = \frac{0.69}{|\Re|} \quad (6.12)$$

### 6.3.4 Defining the gust profile

After characterizing the free responses, we found the response of each trimmed aircraft to a streamwise and a transverse gust disturbance. The streamwise gust acted solely along the  $x$ -axis in the stability frame, and the transverse gust acted only along the  $z$ -axis in the stability frame (Fig. 6.1). Per specification MIL-F-8785C, we used a  $1-\cos$  profile for both gusts, with the gust ultimately reaching a maximum value of  $w_g$  [89], [91]. While the

specification defined the gust in terms of distance travelled, we modelled it in terms of time elapsed [89]. We applied a maximum gust velocity  $w_g$  of 1.53 m/s, which was 2% of the highest gapped aircraft trim velocity and a reasonable value for UAVs [89], [92]. This value also complied with the low-magnitude assumption inherent to small disturbance theory. We further defined that the gust reached this maximum velocity at  $t_m = 5$  seconds [89]. The gust velocity at any time  $t$  was calculated as:

$$U_g(t) = \begin{cases} 0 & \text{for } t \leq 0 \\ \frac{w_g}{2} \left(1 - \cos\left(\frac{\pi t}{t_m}\right)\right) & \text{for } 0 < t < t_m \\ w_g & \text{for } t \geq t_m \end{cases} \quad (6.13)$$

where  $w_g$  is the maximum gust velocity magnitude (m/s) and  $t_m$  is the gust time constant (s). To find the gust responses of the aircraft, we solved the forced equations of motion Eqn. 6.1, with a gust disturbance vector of:

$$\xi_{\text{streamwise}} = \begin{bmatrix} U_g(t) \\ 0 \\ 0 \end{bmatrix} \quad (6.14)$$

for the streamwise gust, and:

$$\xi_{\text{transverse}} = \begin{bmatrix} 0 \\ U_g(t) \\ 0 \end{bmatrix} \quad (6.15)$$

for the transverse gust.

We solved Eqn. 6.1 numerically using MATLAB's *ode45* Runge-Kutta solver. The solution was calculated from 0 seconds to 60 seconds with a timestep of 0.005 seconds. It was important to ensure that the solver accurately captured the continuity of the gust profile (Eqn. 6.13), especially at its transition from transient to steady state. Therefore, we stopped

the solver at  $t = t_m$  then restarted the solver with the final timestep of the previous run as the initial conditions. For both the streamwise and transverse gusts, all of the changes in state variables were initialized as zero per [89]:

$$\mathbf{x}_{\text{init}} = \begin{bmatrix} 0 \\ 0 \\ 0 \\ 0 \end{bmatrix} \quad (6.16)$$

### 6.3.5 Modelling the aircraft

We modelled a series of aircraft, each featuring a different gapped wing with unique gap dimensions. Following Harvey and Inman, we treated each aircraft as rigid, static, and independent of the other aircraft configurations [89]. This approach simplified the dynamic analysis by neglecting the action of changing the gap configuration (i.e. actuating the gaps mid-flight like a control surface). In compliance with our dynamic modelling assumptions, the aircraft were symmetric about the vertical plane [73], [88], [89]. To achieve trim, the aircraft were modelled with a wing, tail, and point-mass fuselage (Fig. 6.1). Furthermore, we varied the tail and fuselage to find a single configuration for which all of the aircraft achieved trim. Since this was a comparative study between gapped wings, we held this successful tail and fuselage configuration constant and varied only the gapped wing across the aircraft. This approach allowed us to directly compare the effects of different gapped wings on an aircraft’s dynamics. The properties of the wings and tails were determined separately, then combined to estimate the inertial and aerodynamic properties of the full aircraft.

#### 6.3.5.1 Wing-alone properties

We first used computational and analytical methods to determine the inertial and aerodynamic properties of the various SI-gapped wings. In accordance with previous experimental and computational work, each wing was rectangular with a 9 in. chord and 32 in. span



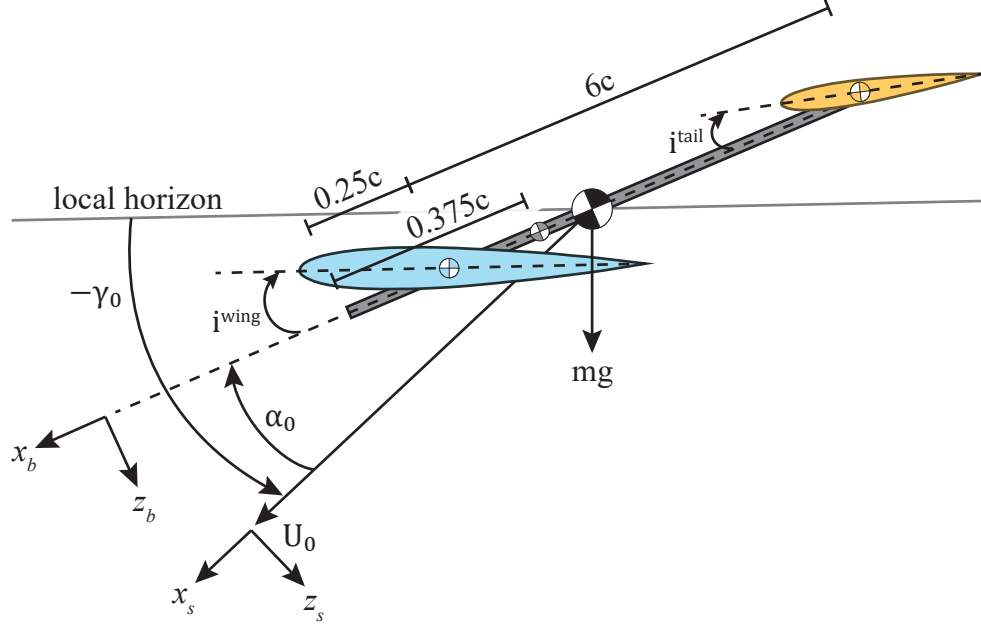


Figure 6.1: The aircraft consisted of a wing, tail, and a stringer fuselage. The wing and tail were mounted by their respective centers of gravity at incidence angles  $i^{wing}$  and  $i^{tail}$ . In trim, the aircraft glided at an angle  $\gamma_0$  below the local horizon with velocity  $U_0$ . The longitudinal axis of the fuselage was at an angle of attack  $\alpha_0$  with respect to the velocity vector. The weight of the aircraft  $mg$  acted down towards the center of the Earth. The body axes, denoted by the subscript  $b$ , were respective to the aircraft longitudinal axis. The stability axes, denoted with the subscript  $s$ , were taken with respect to the velocity vector.

(Chapters II, III, and V). The wings were unswept, untapered, and capped with circular endplates. We considered 43 distinct SI-gapped wings by varying gap width, gap length, and number of gaps. We simulated every combination of gap widths:

$$b_g = b \times \left[ \frac{1}{192}, \frac{1}{96}, \frac{1}{64}, \frac{1}{48}, \frac{1}{32}, \frac{1}{19}, \frac{1}{16} \right] \quad (6.17)$$

and gap lengths:

$$c_g = c \times \left[ \frac{1}{2}, \frac{2}{3}, \frac{3}{4} \right] \quad (6.18)$$

Each unique gap size was then simulated on a wing with nine gaps equally spaced across a semi-span, as well as on a wing only the five most outboard gaps present (Fig. 5.2 (A) and (B)). We also included a baseline wing without gaps as a comparison point. Note that these

gap configurations are the same as those simulated for the parameter sweep (Chapter V). However, here we considered symmetric wings with the same gap configuration on both semi-spans, to preserve the symmetric aircraft assumption. The planform area of each symmetric wing, neglecting the endplates, was calculated according to:

$$S_{fs} = 2(bc - nb_g c_g) \quad (6.19)$$

The lift, drag, and pitching moment curves of each wing were determined from the CFD data collected during the parameter sweep of Chapter V. We conducted three-dimensional RANS simulations in Siemens STAR-CCM+, a commercial CFD code. We simulated each wing at  $0^\circ$ ,  $2^\circ$ ,  $7^\circ$ , and  $10^\circ$  angle of attack. We used the  $k - \omega$  SST turbulence model for its ability to capture flow separation, especially at low Reynolds numbers [71], [72]. We also used the coupled solver. The simulation was terminated after the unscaled residuals of the  $x$ -momentum,  $y$ -momentum,  $z$ -momentum, continuity, and TKE were all below  $1 \times 10^{-4}$ , and after SDR was reduced by at least four orders of magnitude. In nine instances, SDR only relatively fell below  $7.5 \times 10^{-4}$ . Convergence was typically reached between 200 and 500 iterations. The domain boundaries were 12.3 times the wingspan, and the mesh consisted of approximately 3.5 million cells. In accordance with previous experimental work, the simulations were run with an air density of  $1.1565 \text{ kg/m}^3$ , a dynamic viscosity of  $1.58 \times 10^{-5} \text{ Pa}\cdot\text{s}$ , and a velocity of  $16 \text{ m/s}$  based on the experiments of Chapter II. For further details on the simulation setup and meshing, refer to Chapters III and V.

The gapped wings were simulated as asymmetric, with gaps on the right semi-span and a baseline wing without gaps on the left semi-span (Chapter V). The baseline wing was simulated symmetrically, with no gaps on either semi-span. Thus, for the current dynamic analysis, the gapped wing aerodynamic data needed to be corrected to a symmetric gapped wing—the same gap configuration on both semi-spans. First, we measured the force and moment coefficients of each asymmetric wing at the quarter-chord of the wing root. We

normalized the coefficients by their respective asymmetric gapped wing area (Eqn. 2.5). Note that the asymmetric planform area Eqn. 2.5 was only used for the calculation of the coefficients with the superscript *meas* in Eq. 6.20 below. Eqn. 6.19 was used for all other instances of the wing planform area. The pitching moment coefficient was further normalized by the wing chord [88]. We then corrected the measured lift, drag, and pitching moment coefficient curves to symmetric wingspans according to [59]:

$$\begin{aligned}
C_L^{wing} &= 2C_L^{meas} - C_L^{base} \\
C_D^{wing} &= 2C_D^{meas} - C_D^{base} \\
C_{M_{QC}}^{wing} &= 2C_{M_{QC}}^{meas} - C_{M_{QC}}^{base}
\end{aligned} \tag{6.20}$$

where the superscript *meas* indicates measured values from the full asymmetric wingspan, and the superscript *base* indicates values measured from the full symmetric baseline wing. The results of these asymmetric-to-symmetric corrections were validated against a gapped wing configuration that was directly simulated symmetrically (Appendix I).

Once corrected to the symmetric span, we also transferred the wings' pitching moment coefficient from the quarter-chord to the aerodynamic center (AC). While the theoretical AC of a two-dimensional NACA 0012 is at the quarter-chord [56], [73], [93], we anticipated that the finite aspect ratio, endplates, and gaps would shift the location of the wing AC. For each wing, we calculated the location of the AC relative to the leading edge as [56], [73]:

$$x_{AC}^{wing} = \left( -\frac{C_{M,QC}^{wing}}{C_{L_\alpha}^{wing}} + 0.25 \right) c \tag{6.21}$$

where  $C_{M,QC}^{wing}$  is the slope of the wing's moment curve about the quarter-chord (per rad),  $C_{L_\alpha}^{wing}$  is the slope of the wing's lift curve (per rad), and  $c$  is the wing chord (in m). The pitching moment coefficient was then transferred from the quarter-chord to the AC by [56]:

$$C_{MAC}^{wing} = \left( \frac{x_{AC}^{wing}}{c} - 0.25 \right) C_L^{wing} + C_{M_{QC}}^{wing} \tag{6.22}$$

where  $C_L^{wing}$  is the wing’s lift coefficient, and  $C_{M_{QC}}^{wing}$  is the wing’s pitching moment coefficient about its quarter-chord (determined by the CFD simulations).

The wings’ lift curves remained linear up to  $10^\circ$  angle of attack. However, the gapped wings’ pitching moment curves (about the quarter-chord) were not all linear. Pitching moment is usually assumed linear with angle of attack, and the definition of the aerodynamic center requires a constant pitching moment slope [56], [73], [88]. To overcome this challenge, we capped the wings’ linear regime at  $3.5^\circ$  angle of attack. Furthermore, we estimated the slopes of the lift and pitching moment curves as finite differences of the data points at  $0^\circ$  and  $2^\circ$  angle of attack. These calculations are discussed in Appendix J.

The CFD data showed that all of the gapped wings had a positive pitching moment coefficient slope. Thus, a wing-alone plane would not be statically stable [73], [88]. This result is typical, as most conventional wings have a de-stabilizing effect. Since we were only interested in exploring stable aircraft configurations, we added a tail and fuselage to our general aircraft layout.

We measured the inertial properties of each wing directly from Solidworks models of the symmetric wings, including the mass, center of gravity location, and mass moment of inertia. The density of the wings was taken to be  $1010 \text{ kg}\cdot\text{m}^{-3}$  as in Chapter II [62].

### 6.3.5.2 Tail-alone properties

We added a tail to each aircraft in order to achieve statically stable trim. The tail properties were calculated using semi-empirical methods from the U.S. Air Force Data Compendium (DATCOM) [90], and analytical methods. We modeled the tail with a NACA 0012 airfoil and no endplates. The airfoil ordinates were obtained from an online database [65]. The trailing edge was blunted by connecting the two data points at the edge with a vertical line segment. The lift and drag curves for the NACA 0012 airfoil were taken from previous empirical data [93]. We assumed that the aerodynamic center of each airfoil section was at its quarter-chord, in accordance with lifting line theory and empirical results [56], [73],

[93]. To ensure that the aircraft's lift curve remained linear even with the tail present, we assumed the tail span was  $\frac{2}{3}$  of the wing span [90]. We further assumed an elliptical tail with a corresponding elliptical lift distribution, such that the tail's planform efficiency factor equaled unity ( $e = 1$ ) [56], [73].

We created a custom script in MATLAB to discretize the tail and analytically estimate its inertial properties, including CG location, mass moment of inertia, planform area, and mass. As with the wings, we assumed the tail had a density of  $1010 \text{ kg/m}^3$ . Further details on this process can be found in Appendix J.

The aerodynamic properties of the tail were estimated using lifting line theory [73], [88]. The lift curve slope (per rad) was:

$$C_{L\alpha}^{tail} = \frac{a_0}{1 + a_0/(\pi e AR_t)} \quad (6.23)$$

where  $a_0$  is the two-dimensional NACA 0012 lift curve slope (per rad),  $e$  is the planform efficiency factor, and  $AR_t$  is the aspect ratio of the tail. Then, the lift coefficient of the tail was:

$$C_L^{tail} = C_{L\alpha}^{tail} \alpha \quad (6.24)$$

where  $\alpha$  is angle of attack (in rad). The drag coefficient of the tail was [56]:

$$C_D^{tail} = C_{Di}^{tail} + c_d \quad (6.25)$$

$$C_{Di}^{tail} = \frac{(C_L^{tail})^2}{\pi e AR_t} \quad (6.26)$$

where  $C_{Di}^{tail}$  is the induced drag of the tail and  $c_d$  is the two-dimensional NACA 0012 profile drag. We estimated  $a_0$  and  $c_d$  as discussed in Appendix J. Note that the tail aerodynamic variables were first calculated for arbitrary angles of attack in the linear regime, from about  $-3^\circ$  to about  $6^\circ$  [93].

### 6.3.5.3 Complete aircraft properties

With the aerodynamic and inertial properties of the wing and tail defined, we determined the properties of each complete aircraft. Since we sought to compare the effects of different gapped wings, we wanted all of the aircraft parameters to remain constant, except for the wings themselves. Thus, we needed a single tail and fuselage configuration for which all of the gapped wings achieved trim. We began by varying the tail aspect ratio and tail incidence angle of each aircraft. We modelled all combinations of tail aspect ratios:

$$AR_t = [6, 7, 8, 9, 10] \quad (6.27)$$

and tail incidence angles:

$$i^{tail} = [-2, -1, 0, 1, 2]^\circ \quad (6.28)$$

Per lifting line theory, varying the tail aspect ratio allowed us to alter the lift curve slope of the tail [73], [88]. In turn, both the tail lift curve slope and tail incidence angle had a large bearing on aircraft stability and trim. All other tail properties were held constant. The volume fraction of each tail was:

$$V_H = \frac{S^{tail} x_{ac}^{tail}}{S_{fs} c} \quad (6.29)$$

where  $S^{tail}$  is the planform area of the tail (in  $\text{m}^2$ ),  $x_{ac}^{tail}$  is the distance from the aerodynamic center of the tail to the CG of the full aircraft (in m),  $S_{fs}$  is the planform area of the wing (in  $\text{m}^2$ ), and  $c$  is the wing chord (in m).

We found multiple tail configurations that successfully enabled all the gapped wings to trim. However, some of these tail configurations led to three free response modes for the aircraft, instead of the canonical short period and phugoid modes. This can happen for some aircraft when the characteristic roots of the system fall on the real axis, instead of in the complex plane [73], [88]. However, we were interested in studying the effects of the gaps on the two classic longitudinal aircraft modes. Per Nelson, moving the CG forward to reduce

the static margin can move the roots off the real axis [88]. We added a “fuselage” point mass as a means of adjusting the static margin without drastically changing the rest of the aircraft configuration. Practically, the the forward-most location of the CG is often limited by the elevator’s control effectiveness [73]. Moving the CG too far forward could exceed the elevator’s ability to pitch the aircraft. Here, the center of gravity remained aft of the aerodynamic center for all of the gapped wings. Further, the addition of the fuselage mass enabled all the aircraft to achieve statically stable trim with the typical short period and phugoid modes.

In line with the point mass assumption, we modelled the fuselage as a thin stringer connecting the wing and tail. The fuselage mass was concentrated at 3/8 of a chord length from the tip of the stringer (the “nose”) (Fig. 6.1). For each gapped wing and tail combination, we varied the fuselage mass as fractions of the baseline wing mass according to:

$$m^{fuse} = m^{base} \times [0, 0.15, 0.25, 0.5] \quad (6.30)$$

where  $m^{base}$  is the mass of the baseline wing (in kg). We accounted for the inertial properties of the fuselage in the full aircraft, including the CG location, total mass, and mass moment of inertia. However, we neglected the aerodynamic contributions of the fuselage due to its negligible body width. Specifically, we assumed that the fuselage did not contribute to the lift, drag, pitching moment, and pitching moment slope of the aircraft [88], [90]. Additionally, the thin stringer assumption meant that the exposed wing and tail areas were equal to the full wing and tail planform areas, respectively ( $S_e = S_{fs}$ ) [73], [90].

The wing was mounted by its CG (Fig. 6.1). We also assumed a wing incidence angle of  $i^{wing} = 1^\circ$ , due to the symmetric airfoil and need to produce lift at small angles of attack. The tail was also mounted at its CG, six chord lengths aft of the wing’s center of gravity (Fig. 6.1). Mounting the tail far aft increased its influence on aircraft stability without requiring an excessively large surface area [73], [88]. From a practical perspective, increasing

the tail size or distance also increases the weight and drag of the aircraft, thus decreasing its performance [88]. This could be overcome by using a tail airfoil with a higher lift curve slope, among other solutions.

We then analytically determined the inertial properties of each aircraft. The total aircraft mass was:

$$m = m^{wing} + m^{tail} + m^{fuse} \quad (6.31)$$

where  $m^{wing}$  is the mass of the wing,  $m^{tail}$  is the mass of the tail, and  $m^{fuse}$  is the fuselage mass (all in kg). The location of the aircraft's center of gravity (in m from the nose) was:

$$x_{CG} = \frac{x_{CG}^{wing} m^{wing} + x_{CG}^{tail} m^{tail} + x_{CG}^{fuse} m^{fuse}}{m} \quad (6.32)$$

where  $x_{CG}^{wing}$  is the distance from the nose to the wing's center of gravity (in m),  $x_{CG}^{tail}$  is the distance from the nose to the tail's center of gravity (in m), and  $x_{CG}^{fuse}$  is the distance from the nose to the fuselage's center of gravity (in m). We employed the parallel axis theorem to calculate the  $y$ -axis mass moments of inertia of the wing, tail, and fuselage about the aircraft's CG. Then we summed them to find the aircraft's mass moment of inertia about the  $y$ -axis acting at its CG:

$$I_{y,CG} = I_{y,CG}^{wing} + I_{y,CG}^{tail} + m^{fuse} (\ell^{fuse})^2 \quad (6.33)$$

where  $I_{y,CG}^{wing}$  is the mass moment of inertia of the wing about the  $y$ -axis at the aircraft's CG (in  $\text{kg}\cdot\text{m}^2$ ),  $I_{y,CG}^{tail}$  is the mass moment of inertia of the tail about the  $y$ -axis at the aircraft's CG (in  $\text{kg}\cdot\text{m}^2$ ), and  $\ell^{fuse}$  is the distance from the fuselage point mass to the aircraft CG (in m).

The aerodynamic properties and stability derivatives of each aircraft configuration were determined through semi-empirical methods, following common procedures outlined in aerodynamic texts and DATCOM [73], [88], [90]. All of the derivatives and coefficients were



calculated per radian. To assist with finding trim, we calculated the aerodynamic properties of each plane at angles of attack  $\alpha$  from  $0^\circ$  to  $10^\circ$ , in  $1^\circ$  increments.

The downwash from the wing at the horizontal tail was [73], [90]:

$$\epsilon = \frac{d\epsilon}{d\alpha} \alpha^{wing} \quad (6.34)$$

where the variation of the downwash with angle of attack (per rad) was estimated according to:

$$\frac{d\epsilon}{d\alpha} = 4.44 \left( K_A K_\lambda K_H \cos^{\frac{1}{2}}(\Lambda) \right)^{1.19} \quad (6.35)$$

and

$$\begin{aligned} K_A &= \frac{1}{AR_w} - \frac{1}{1 + (AR_w)^{1.7}}, \\ K_\lambda &= \frac{10 - 3\lambda}{7}, \\ K_{h_H} &= \left( 1 - \frac{h_H}{2b} \right) \left( \frac{l_h}{b} \right)^{-\frac{1}{3}} \end{aligned} \quad (6.36)$$

where  $\Lambda$  is the sweep angle of the wing (zero for all wings in this work),  $AR_w$  is the wing's aspect ratio,  $\lambda$  is the taper ratio of the wing (unity for all wings),  $h_H$  is the height between the tail's aerodynamic center and the wing's chord line (in m), and  $l_h$  is the distance between the wing and the tail's aerodynamic centers parallel to the wing's chord line (in m). We assumed that the wake from the wing did not affect the dynamic pressure at the tail, since the tail was far aft of the wing. Thus, the tail efficiency factor  $\eta = 1$  [73], [88].

The lift, drag, and pitching moment coefficients of the wing and tail were combined to find those of the full aircraft [73], [88]. We first interpolated the wing and tail aerodynamic coefficients to the appropriate angles of attack to account for incidence angles and downwash. The tail aerodynamic coefficients were interpolated to the following angles of attack:

$$\alpha^{tail} = \alpha^{wing} - i^{wing} - \epsilon + i^{tail} \quad (6.37)$$

and the wing aerodynamic coefficients were interpolated to the following angles of attack:

$$\alpha^{wing} = \alpha + i^{wing} \quad (6.38)$$

where  $\alpha^{wing}$  is the wing angle of attack and  $\alpha$  is the angle of attack of the aircraft with respect to the longitudinal axis of the fuselage (both in rad). The lift and pitching moment coefficients were interpolated linearly. The drag coefficient was interpolated with the spline method to account for its quadratic nature. Then, the aircraft lift coefficient, drag coefficient, and pitching moment coefficient (about the aircraft CG) were calculated as [88]:

$$\begin{aligned} C_L &= C_L^{wing} + \eta V_H \frac{S^{tail}}{S_{fs}} C_L^{tail} \\ C_D &= C_D^{wing} + \eta V_H \frac{S^{tail}}{S_{fs}} C_D^{tail} \\ C_M &= C_{MCG}^{wing} + C_{MCG}^{tail} \end{aligned} \quad (6.39)$$

where

$$\begin{aligned} C_{MCG}^{wing} &= C_{MAC}^{wing} + C_L^{wing} \frac{\ell_{AC}^{wing}}{c} \\ C_{MCG}^{tail} &= V_H \eta C_L^{tail} \end{aligned} \quad (6.40)$$

and where  $C_{MCG}^{wing}$  is the pitching moment coefficient of the wing about the aircraft's center of gravity,  $C_{MCG}^{tail}$  is the tail's pitching moment coefficient about the aircraft's CG, and  $\ell_{AC}^{wing}$  is the distance from the wing's aerodynamic center to the aircraft's center of gravity (in m).

The slopes of the aircraft coefficient curves were then calculated according to:

$$\begin{aligned} C_{L_\alpha} &= \frac{C_L(\alpha = 2.5^\circ) - C_L(\alpha = 0^\circ)}{2.5^\circ \frac{\pi}{180}} \\ C_{D_\alpha}(\alpha) &= \begin{cases} \frac{C_D(\alpha + \Delta\alpha) - C_D(\alpha)}{\Delta\alpha} & \text{for } \alpha = 0^\circ \\ \frac{C_D(\alpha + \Delta\alpha) - C_D(\alpha - \Delta\alpha)}{2\Delta\alpha} & \text{for } \alpha = 2^\circ, 7^\circ, 10^\circ \end{cases} \end{aligned} \quad (6.41)$$

given that: [73], [88]

$$C_{M_\alpha} = C_{L_\alpha}^{wing} \left( \frac{\ell_{AC}^{wing}}{c} \right) - C_{L_\alpha}^{tail} \left( 1 - \frac{d\epsilon}{d\alpha} \right) \eta V_H \quad (6.42)$$

where  $C_{L_\alpha}^{wing}$  is the slope of the wing's lift curve (per rad),  $C_{L_\alpha}^{tail}$  is the lift curve slope of the tail (per rad),  $\alpha$  is the aircraft angle of attack (in rad), and  $\Delta\alpha$  is an arbitrary angle of attack increment (taken to be  $1^\circ = 0.0175$  rad). As shown in Eqn. 6.41 the lift curve slope was estimated as the finite difference between  $0^\circ$  and  $2.5^\circ$  angle of attack, to keep the wings within the linear regime of their pitching moment coefficient curves. The drag curve slope was similarly estimated as finite differences at several angles of attack, since the drag curve was not linear (Eqn. 6.41). Note that the lift curve, drag curve, and drag curve slope needed to be interpolated to specific angles of attack in several instances, notably for calculating the finite differences above as well as for finding the trim state. In these instances, we interpolated the lift linearly, and the drag and drag slope with a spline interpolation.

The aircraft stability coefficients were [88]:

$$\begin{aligned} C_{M_q} &= 1.1 \left( -2C_{L_\alpha}^{tail} \eta V_H \frac{\ell_{AC}^{tail}}{c} \right) \\ C_{M_{\dot{\alpha}}} &= 1.1 \left( -2C_{L_\alpha}^{tail} \eta V_H \frac{\ell_{AC}^{tail}}{c} \frac{d\epsilon}{d\alpha} \right) \\ C_{Z_q} &= 1.1 \left( -2C_{L_\alpha}^{tail} \eta V_H \right) \end{aligned} \quad (6.43)$$

As recommended by Nelson, we calculated  $C_{M_q}$ ,  $C_{M_{\dot{\alpha}}}$ , and  $C_{Z_q}$  for the tail, then increased those value by 10% to account for the contribution from the wing as shown in Eqn. 6.43 [88]. The wing CFD simulations were run at low speeds and the calculated trim velocities were within the subsonic regime, so we assumed that the changes in lift, drag, and pitching

moment coefficient with forward speed were zero [88], [89]:

$$\begin{aligned}
 C_{L_u} &= 0 \\
 C_{D_u} &= 0 \\
 C_{M_u} &= 0
 \end{aligned}
 \tag{6.44}$$

## 6.4 Results and discussion

The gapped wings produced drastic changes in the location of the wing’s aerodynamic center, as well as the aircraft’s trim state, free response, and gust response. Despite several practical aircraft design challenges, the data indicated that the gapped wings could be a beneficial control surface for gust alleviation.

Firstly, we varied the tail incidence angle, tail aspect ratio, and fuselage mass to find a configuration for which all of the gapped wings trimmed. We found two configurations for which all the gapped wings met our trim criteria:

1.  $i^{tail} = 0^\circ$ ,  $m^{fuse} = 0.5m^{base}$ , and  $AR_t = 9$
2.  $i^{tail} = 0^\circ$ ,  $m^{fuse} = 0.5m^{base}$ , and  $AR_t = 10$

The second configuration produced aperiodic longitudinal modes rather than the typical short period and phugoid modes [88]. Therefore, we used the first configuration with a tail aspect ratio of nine. The results of this study are specific to this aircraft configuration, and further investigation is needed to determine if these results can be generalized to other aircraft configurations.

Note that we also investigated aircraft configuration for which the wing and tail were mounted to the fuselage at their respective aerodynamic centers. We found that these results were largely similar to the results presented here. The AC-mounted aircraft is discussed further in Appendix L.

### 6.4.1 Gaps shifted the aerodynamic center forward

The gaps shifted the aerodynamic center (AC) of the wing forward. According to lifting line theory, the aerodynamic center of a NACA 0012 airfoil occurs at the quarter-chord [56], [73]. The CFD data showed that the AC of the baseline wing was close to this theoretical value, at 23.6% chord. However, the AC of gapped wings varied: the  $\frac{3c}{4} \times \frac{b}{19}$  nine-gap wing shifted the aerodynamic center the furthest forward to 7.57% chord. The  $\frac{c}{2} \times \frac{b}{192}$  five-gap wing had the smallest impact on AC location, with the aerodynamic center at 21.3% chord. Overall, the AC location largely depended on the wing's planform area (Eqn. 6.19), which was directly related to the size and number of gaps.

Overall, the gaps had positive implications on the stability of the full aircraft. Typically, a forward-shift of the aerodynamic center indicates less stability. For wing-alone stability, the aerodynamic center must lie aft of the center of gravity [88]. The CG of the wings remained largely constant irrespective of the gap configuration, at 37% to 43% wing chord. Thus, the aerodynamic center of the baseline wing (at 23.6% chord) was already positioned far forward of its CG. The gaps increased this distance by shifting the AC further forward. However, the gapped wings also produced both a lower pitching moment about their respective aerodynamic centers and a lower lift coefficient than the baseline wing. While  $\ell_{AC}^{wing}$  increased,  $C_{MAC}^{wing}$  and  $C_L^{wing}$  decreased, generally leading to a net decrease in  $C_{MCG}^{wing}$  of the gapped wings compared to the baseline (Eqn. 6.40). Thus, the destabilizing effects of the gapped wings were typically not as great as that of the baseline wing (Fig. 6.2).

### 6.4.2 Gapped wings steepened glide, increased velocity at trim

The gaps generally decreased the pitching moment coefficient of the wing about the aircraft's center of gravity (Fig. 6.2). This resulted in a net decrease of the aircraft's pitching moment at any given angle of attack, per Eqn. 6.39. Thus, the aircraft achieved equilibrium at a lower angle of attack (Fig. 6.3).

Relatedly, the aircraft with gapped wings trimmed at a much steeper glide angle than the

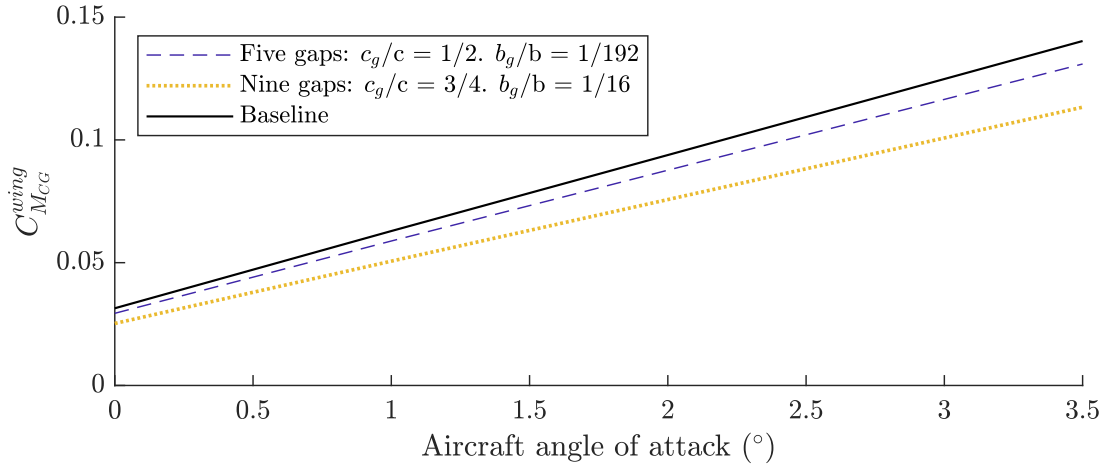


Figure 6.2: Gaps generally decreased the wing’s pitching moment coefficient about the aircraft’s center of gravity ( $C_{M_{CG}}^{wing}$ ). The solid black line is the baseline wing, the dashed blue line is the gapped wing with the smallest impact on gust response, and the dotted yellow line is the gapped wing with the largest impact on gust response. The  $C_{M_{CG}}^{wing}$  curves of all the aircraft are plotted in Appendix K.

baseline aircraft (Fig. 6.3). A lower trim angle of attack typically results in a lower lift-to-drag ratio. This trend is especially true for the gapped wings, which were found in Chapter II to decrease lift with negligible changes in drag. Glide angle is inversely proportional to the lift-to-drag ratio, as can be derived from the trim equations Eqn. 6.7 [73]. Thus, the lower lift-to-drag ratios of the gapped-wing aircraft resulted in steeper glide angles than the baseline aircraft.

The gapped-wing aircraft also trimmed at higher velocities than the baseline aircraft (Fig. 6.3). In combination with the steeper trim glide angle, this implies that the gapped wings could be useful for a rapid descent situation. Previously, it was determined that the gapped wings were not as effective as a spoiler at decreasing the lift-to-drag ratio of a wing (Chapter II). The present results provide a more complete picture for assessing the gaps as rapid descent control surfaces, compared to a baseline wing with no control surface.

The trim state was highly dependent on the size and number of gaps (Fig. 6.3). Larger gaps had a stronger impact on the trim state. For example, gaps of length  $\frac{c}{2}$  did not decrease the angle of attack, steepen the glide angle, or increase velocity at trim as dramatically as

gaps of length  $\frac{3c}{4}$ . Changing the gap length also had a greater effect on trim for wider gaps compared to narrower gaps. For example, lengthening the gaps from  $\frac{c}{2}$  to  $\frac{3c}{4}$  at a constant gap width of  $\frac{b}{16}$  resulted in a much greater change in trim velocity than lengthening the gaps at a constant gap width of  $\frac{b}{192}$ . This implied that trim state was greatly affected by the aspect ratio of the gaps. In addition, for a given gap dimension, the nine-gap wing had a larger impact on the trim state than the corresponding five-gap wing (Fig. 6.3).

Finally, there was a point of diminishing returns for gap widths greater than  $\frac{b}{32}$ , after which widening the gaps did not drastically change the trim state. Interestingly, this gap width corresponds to the results from Chapter V. In Chapter V, I showed that gap widths of  $\frac{b}{32}$  or  $\frac{b}{48}$  maximized the rolling moment coefficient per unit work in several scenarios. At a high angle of attack of  $10^\circ$ , the maximum rolling moment coefficient per unit work was produced by  $\frac{c}{2} \times \frac{b}{32}$  gaps on the five-gap wing, and  $\frac{c}{2} \times \frac{b}{48}$  gaps on the nine-gap wing.

### 6.4.3 Natural modes were generally benefited by gaps

The gapped wings decreased the natural frequency of the aircraft's phugoid mode and increased its damping ratio (Fig. 6.4). This resulted in a much shorter time to halve the amplitude of the phugoid mode, compared to the baseline aircraft. Conversely, the gapped wings typically increased the natural frequency of the aircraft's short period mode and decreased the damping ratio (Fig. 6.4). This dramatically increased the time to halve the amplitude of the short period mode.

As seen with the trim state, the size and number of the gaps had a large bearing on the free response characteristics of the aircraft (Fig. 6.4). Overall, the natural frequencies, damping ratios, and time to halve the short period amplitude varied largely depending on gap dimensions and number. The time to halve the phugoid amplitude was strongly affected simply by the presence of gaps in the wing. The half-time decreased slightly as the number of gaps increased and lengthened, but the width of the gaps did not substantially impact this parameter. Larger gaps did result in greater changes to the natural frequency and damping

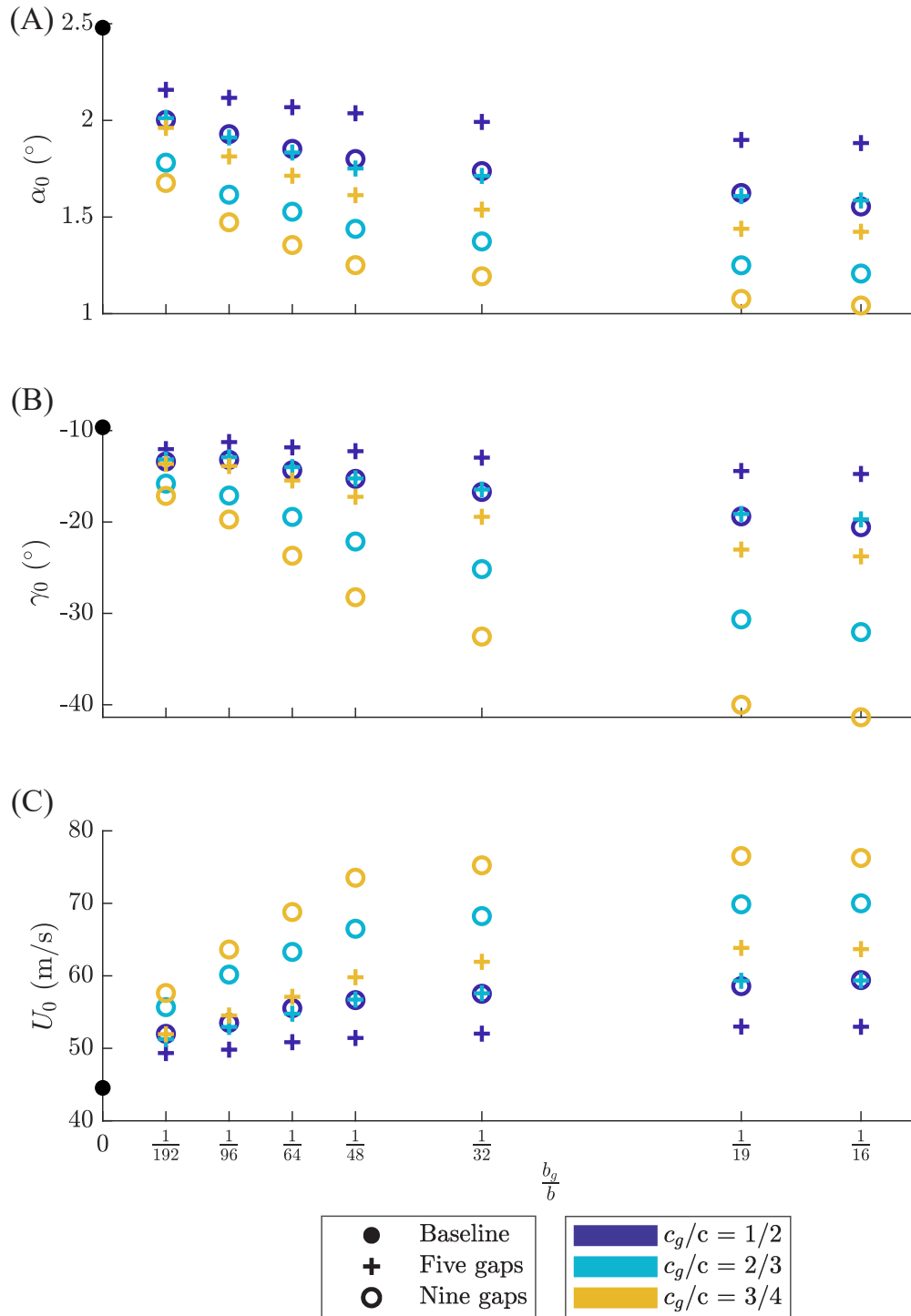


Figure 6.3: The gapped wings (A) decreased trim angle of attack, (B) steepened trim glide angle, and (C) increased trim velocity. The filled dot is the baseline aircraft, + are five-gap aircraft, and o are nine-gap aircraft. Aircraft are color-coded based on gap length and plotted against gap width on the  $x$ -axis.



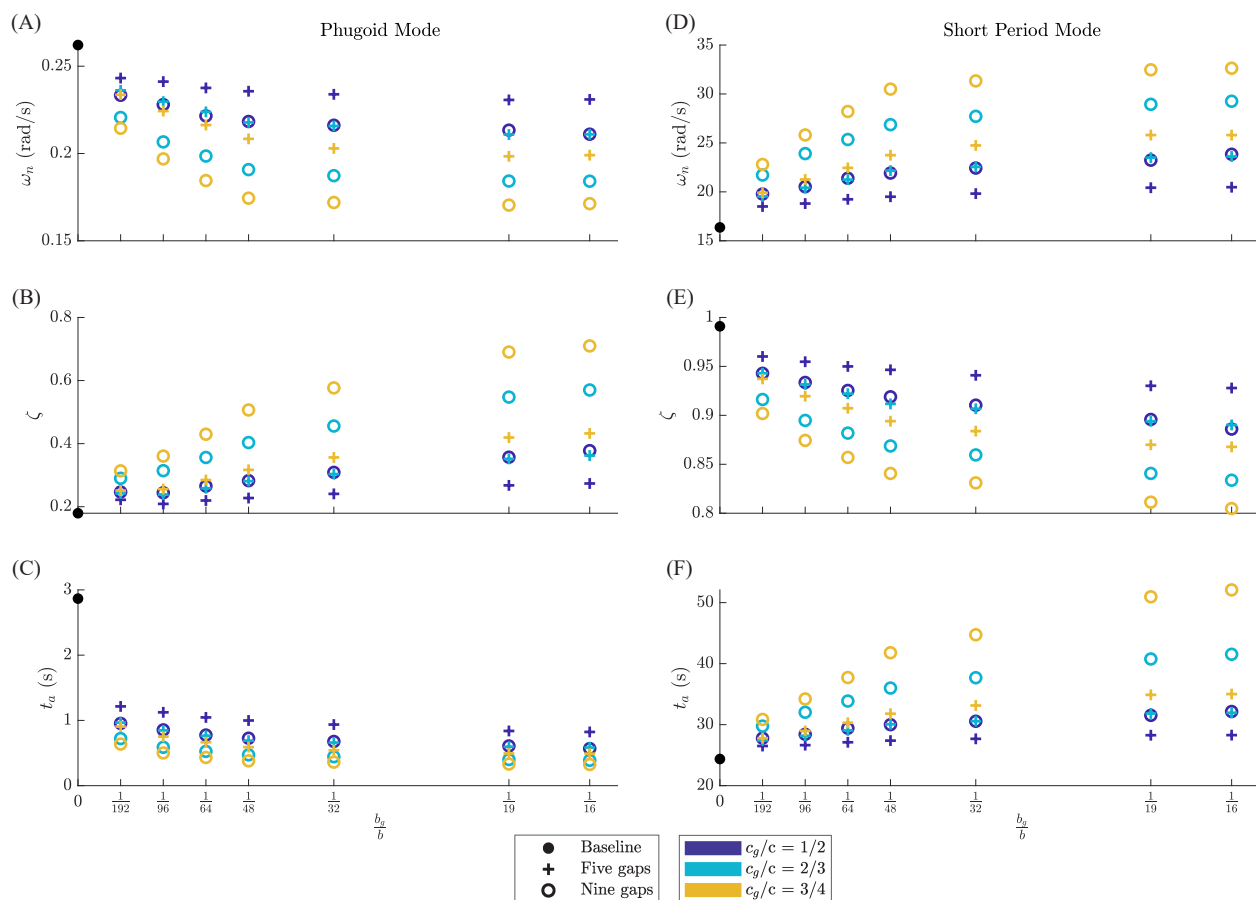


Figure 6.4: The gapped wings decreased the natural frequency and increased the damping of the phugoid mode. They also increased the natural frequency and decreased the damping of the short period mode. The filled dot is the baseline aircraft. Each + is five-gap aircraft and each o is a nine-gap aircraft. The aircraft are color-coded by their gap length and plotted against their gap width on the  $x$ -axis.

ratio of the two modes. But, widening the gaps past  $\frac{b}{32}$  did not result in substantial changes in these parameters. Longer gaps caused greater changes to the natural modes than shorter gaps. The gap aspect ratio also played a strong role in determining the natural modes, as seen with the trim state. Finally, the nine-gap wings had a greater impact on the natural modes compared to their five-gap counterparts. However, this difference was much smaller for the time to halve the phugoid amplitude.

These results had positive implications on aircraft control. Typically, for the purposes of control and safety, it is desirable to have an aircraft with a high natural frequency and heavily-damped short period [88]. Here, the gapped wings beneficially increased the short period mode natural frequency, but decreased its damping, which could make it difficult to control the aircraft. The gapped wings also increased the damping of the phugoid mode, which was beneficial from a controls perspective.

The Cooper-Harper scale presents standard recommendations for the damping ratios of the short period and phugoid modes [73], [88]. The scale specifies the flying qualities of aircraft in terms of three levels. The highest level, Level I, indicates that the aircraft's flight qualities are clearly adequate for aircraft control and mission completion. Level III is the poorest level, and indicates that the flight can be completed safely but with excessive pilot workload and/or inadequate mission effectiveness. The flight phases are broken down into three categories. Category A refers to nonterminal flight phases with rapid maneuvering and precision flight-path control. Category B corresponds to nonterminal flight phases with gradual maneuvering and lower-precision flight path control. Category C includes terminal flight phases like take-off and landing. For Level I control, phugoid damping ratios must be greater than 0.04. Short period damping ratios for Level I must fall between 0.35 and 1.30 (Category A and C phases of flight) or between 0.3 and 2.0 (Category B phases of flight). MIL-F-8785C further defines limits for the natural frequency of the short period mode [73], [91]. Each flight category has a different minimum value, but the maximum values are

defined as:

$$\left(\frac{\omega_{n,SP}^2}{N}\right)_{max} = \begin{cases} 3.6 & \text{Level I} \\ 10.0 & \text{Level II} \\ \text{N/A} & \text{Level III} \end{cases} , \quad (6.45)$$

where

$$N = Q_0 S_{fs} C_{L\alpha} \frac{1}{W} \quad (6.46)$$

and  $Q_0$  is the dynamic pressure at trim (in  $\text{N/m}^2$ ), and  $W$  is the aircraft weight (in  $\text{N}$ ).

All of the gapped-wing aircraft, as well as the baseline aircraft, satisfied the Cooper-Harper Level I criteria for the phugoid damping ratio. Additionally, all of the aircraft met the Cooper-Harper Level I requirement for short period damping. Even though the gaps decreased the aircraft's short period damping, the aircraft remained well within the range for adequate control. Conversely, all of the aircraft fell within the Level III criteria for the short period natural frequency. Typically, the high frequency of the short period mode is beneficial because it helps the aircraft respond rapidly to control inputs [88]. However, increasing the frequency of the short period beyond a certain point exceeds the pilot's response time, impeding effective aircraft control. The baseline aircraft value of  $\omega_{n,SP}^2/N$  was  $15.7 \text{ (rad/s)}^2$ , and the gapped aircraft values ranged from  $18.1 \text{ (rad/s)}^2$  to  $39.8 \text{ (rad/s)}^2$ . The high value of the baseline aircraft suggested that the noncompliance with Level I was not necessarily a result of the gapped wings; the aircraft configuration itself (tail and fuselage) likely contributed to the poorer aircraft control. In the future, the fuselage and tail could be carefully designed to bring all the aircraft in compliance with Level I for the short period natural frequency. However, care would still need to be taken for the gapped wings, given the large increase in  $\omega_{n,SP}^2/N$  of the gapped-wing aircraft compared to the baseline aircraft.

Importantly, note that the Cooper-Harper scale provides recommendations for piloted aircraft, based on feedback and input from human pilots [73], [88]. Thus, the guidelines are based on the human response bandwidth of approximately  $4 \text{ rad/s}$  [73]. A stability

augmentation system could be implemented to improve the controllability of all the aircraft if human-piloted. Alternatively, an autopilot could effectively mitigate the lower short period damping. Thus, while the short period natural frequencies of the aircraft were not desirable, they did not hold large bearing on the controllability of a UAV. Ultimately, the gaps did not negatively impact the controllability of the aircraft, and even provided some beneficial impacts to the natural modes.

#### 6.4.4 Gapped wings improved aircrafts' gust responses

Gap configuration played a large role in the aircraft's gust response, for both streamwise and transverse disturbances (Fig. 6.5). Increasing the number of gaps increased the damping and decreased the amplitude of the response. The aircraft with nine-gapped wings were more heavily damped than the baseline aircraft and aircraft with five-gapped wings. In most cases, the changes in state variables of the nine-gapped aircraft oscillated between smaller peak amplitudes compared to the five-gapped and baseline aircraft. Gap dimension was also an important factor (Fig. 6.5). Gaps of length  $\frac{3c}{4}$  dampened the gust response more strongly than gaps of length  $\frac{c}{2}$ . Furthermore, wider gaps had greater damping than narrower gaps. Overall, the aircraft with a  $\frac{c}{2} \times \frac{b}{192}$  five-gapped wing made the smallest difference in gust response compared to the baseline wing (blue dashed line in Fig. 6.5). The aircraft with a  $\frac{3c}{4} \times \frac{b}{16}$  nine-gapped wing exhibited the largest change compared to the baseline, and the most heavily damped gust response (yellow dotted line Fig. 6.5). We refer to this aircraft as the "optimal gapped aircraft," since it provided the best gust mitigation in terms of both damping and amplitude.

The exception to these trends was the change in heave velocity ( $\Delta w$ ) after a transverse gust. All of the aircraft experienced similar changes in heave velocity after the transverse disturbance (Fig. 6.5). This effect was likely because of our dynamics modelling. We assumed that each aircraft started from a nonzero forward velocity (the trim velocity) and zero heave velocity before encountering the gust. When the streamwise gust perturbed the aircraft,

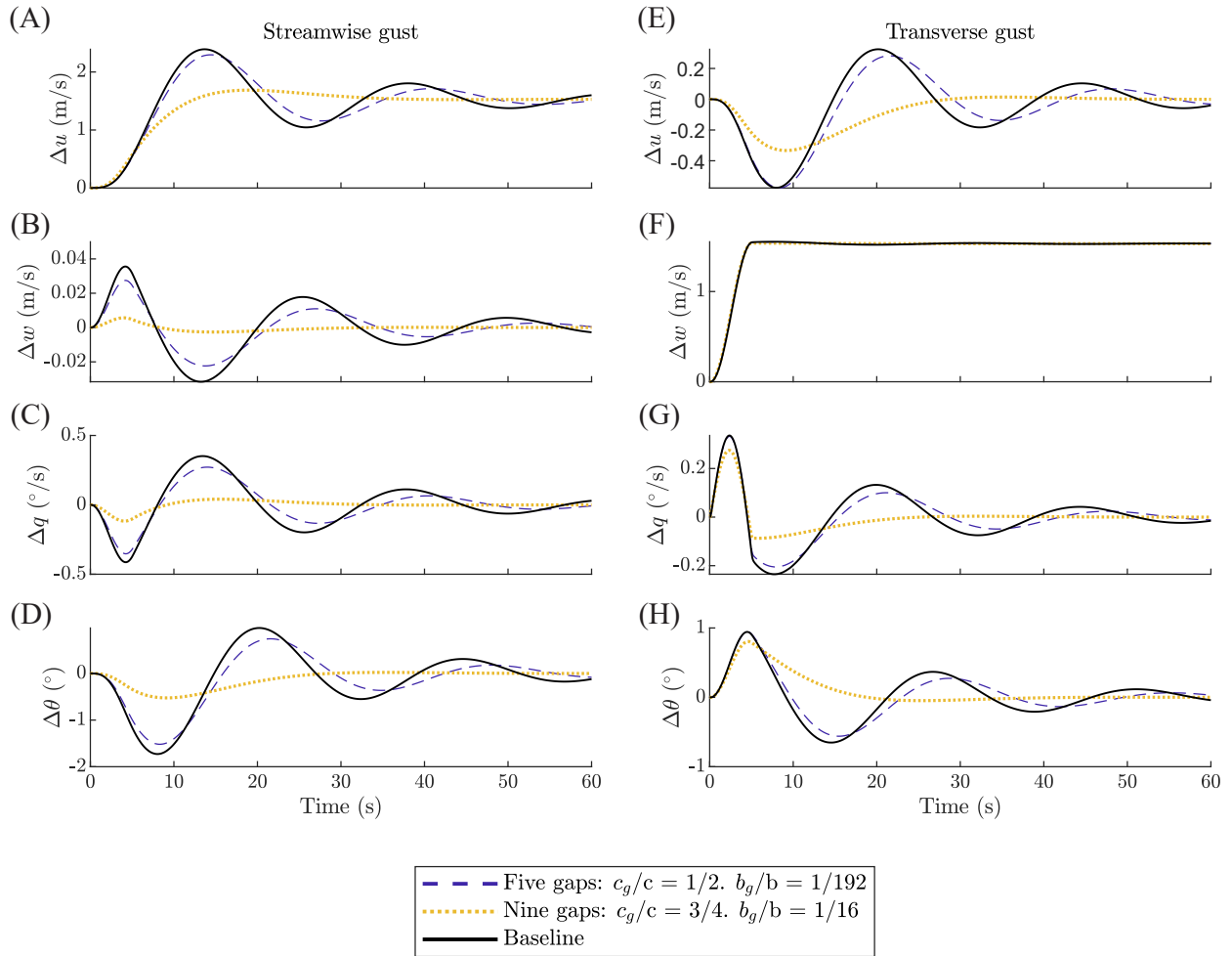


Figure 6.5: Gapped wings improved the aircraft’s gust response by reducing the amplitude and increasing the damping of oscillations. The changes in (A),(E) forward velocity; (B),(F) heave velocity; (C),(G) pitch rate; and (D),(H) pitch angle are plotted against time in response to streamwise and transverse 1–cos gusts. The solid black line is the baseline aircraft, the dashed blue line is the gapped wing with the smallest impact on response, and the dotted yellow line is the gapped wing with the largest impact. All aircraft responses are in Appendix K.

the sudden increase in forward velocity altered the lift and drag, causing the aircraft to experience an oscillatory change in heave velocity. In the case of a transverse gust, the change in heave velocity was roughly equal to the velocity profile of the gust, since that was the driving cause of heave.

After subjection to the streamwise gust, the changes in state variables of the baseline aircraft oscillated then damped back to equilibrium (Fig. 6.5). The changes in state variables of

the optimal gapped aircraft oscillated slightly, but at a much lower amplitude. Furthermore, this aircraft reached steady state much faster than the baseline. This result makes sense, because the optimal gapped aircraft's phugoid damping ratio was close to critically damped at 0.7, and was nearly four times greater than the baseline phugoid damping ratio.

Each aircraft's response to the transverse gust was similar (Fig. 6.5). The changes in state variables of the baseline aircraft oscillated before damping back to equilibrium. The change in heave velocity closely followed the velocity profile of the gust. The changes in state variables of the optimal gapped aircraft oscillated at a much lower amplitude than the other aircraft, and reached steady state faster due to the higher damping ratio.

It is currently unknown if avian whiffing is a passive or active gust response [12]. There are ways in which the gapped wings could be used to either passively or actively alleviate gusts. Firstly, the gaps could be actively opened or closed in response to gusts, similarly to how ailerons and flaps are used as gust mitigation solutions. Alternatively, the gaps could be covered with a material that is sensitive to velocity, pressure, or other atmospheric conditions. The material would be calibrated for some threshold gust velocity, pressure change, or another trigger. Like a check valve, this material would become porous or give way to expose the gaps when experiencing a gust that exceeds the threshold [54], [55].

In all, gapped wings improved aircrafts' response to streamwise and transverse  $1-\cos$  gusts. In almost every case, the changes in state variables of the gapped-wing aircraft experienced higher damping and lower-amplitude oscillations than the baseline aircraft. The exception was the change in heave velocity in response to a transverse gust, which the gapped wings negligibly impacted compared to the baseline. These responses were open-loop, without a controller or autopilot. This implied that aircraft with static gapped wings were naturally less susceptible to gust disturbances than a baseline aircraft. Alternatively, a UAV controller could use the gapped wings for effective gust mitigation.

## 6.5 Chapter summary

Here, we assessed whiffing-inspired gapped wings as a gust alleviation control surface. To accomplish this, we analytically estimated the open-loop response of various aircraft to transverse and streamwise gusts. The aircraft properties were calculated using a combination of computational, analytical, and semi-empirical methods. Each aircraft had the same tail and fuselage configuration, but a unique gapped wing with varying gap dimensions and numbers of gaps. First, we found the trim state of each aircraft. Then, we assessed the impact of the gapped wings on the short period and phugoid modes. Finally, we calculated the time history of each aircraft's response to transverse and streamwise  $1-\cos$  gusts. We found that the gapped wings had a further forward aerodynamic center, but generally were less destabilizing than the baseline wing. The lower pitching moment contribution from the gapped wings resulted in steeper glide angles and increased velocities at trim. The gapped-wing aircraft had a more heavily damped and lower frequency phugoid mode, well within Level I flying quality limits by the Cooper-Harper scale. However, all of the aircraft (including the baseline) fell within Level III flying quality for the short period mode, and could require an autopilot to handle the lightly damped short period mode. Finally, the gapped wings improve the aircraft response to gust disturbances by reducing the amplitude and increasing the damping of oscillations of the changes in state variables. This result signified that the gapped wings could be an effective control surface for gust alleviation.

Overall, the aircraft experienced some design challenges, such as the high frequency of the short period mode. However, there were reasonable and practical solutions to these problems. Furthermore, these problems arose even for the baseline aircraft configuration, and not as a result of the gaps themselves.

## 6.6 Data availability

The data and scripts that support the findings of this study are openly available on figshare at DOI: [10.6084/m9.figshare.c.6487966.v1](https://doi.org/10.6084/m9.figshare.c.6487966.v1).



## CHAPTER VII

### Conclusion

This dissertation provided an initial assessment of a novel whiffing-inspired gapped wing control surface. The gapped wing was specifically based on feather rotation, which had not been previously applied to aircraft design. In the avian realm, birds whiffle to lose altitude, move laterally, and respond to gusts [12]. I speculated that gapped wings could be an alternative UAV control surface for those same purposes. I employed experimental, computational, and analytical approaches to build confidence in the results and develop a variety of analysis tools. The work focused on understanding the impact of gaps on the forces and moments produced by a wing, and the underlying fluid mechanics. Furthermore, I identified key advantages and disadvantages of the gapped wings. Both the inspiration and control surface design were novel, so these results provided important context and knowledge for future biologists and engineers. Overall, I found evidence that the gapped wings could be beneficial for gust alleviation, and roll control in certain situations. The gapped wings could be useful for energy-constrained UAVs flying at high angle of attack, due to the delayed stall of the gapped wings. Alternatively, the gapped wings could provide yaw benefits for a UAV that requires moderate roll at lower angles of attack. They would also be beneficial to UAVs operating in very gusty environments.

## 7.1 Summary of results and impact

### 7.1.1 A gapped wing created roll at high lift coefficients

We first conducted wind tunnel experiments of static gapped wing models, and measured the forces and moments they produced (Chapter II). The work to actuate a model of the gapped wings was also analytically estimated based on friction forces. Two speculated uses of avian whiffling are descent and lateral movement [12]. Thus, we used the work estimates and experimental data to compare the gapped wings to a conventional spoiler and aileron. The gapped wings were unsuitable for rapid descent, because they required more work than a spoiler and did not drastically reduce the lift of the wing. Conversely, the gapped wings were promising for roll control at high lift coefficients. At a high angle of attack, the nine-gapped wing was capable of producing a greater rolling moment coefficient than the maximum deflection of a single aileron. Furthermore, the gapped wing required less work than the aileron to produce this rolling moment coefficient.

This work was important for characterizing the performance of the gapped wing control surface with respect to conventional alternatives. We presented our findings at the 2020 AIAA SciTech Conference [94], in a poster at the 2020 GRC Smart Materials and Structures Conference [95], and in a *Bioinspiration & Biomimetics* journal article [96].

### 7.1.2 Gaps reenergized flow and produced high rolling moment coefficients

In Chapter III, we performed CFD simulations of various gapped wings and aileron wings. We used previous experimental data to validate the simulations, and found good agreement. Then, we leveraged the simulations to study the effects of the gaps on the flow over a wing, as well as the flow behavior within a gap itself. The gaps re-energized the flow over the suction side of the trailing edge, and each gap produced a pair of vortices. Within a gap, the flow recirculated then vented to the suction side of the wing. Based on the CFD data, we estimated the work required to overcome aerodynamic loading on gaps and a

single aileron. The gapped wing required higher actuation work than the single aileron for low rolling moment coefficients. However, the gapped wing did require less work at higher rolling moment coefficients, and produced a greater maximum coefficient.

In this work, we performed the first simulations of flow over this wing geometry. A subset of the results were presented at the 2022 ASME SMASIS conference [97]. Some of this work was also featured in a poster at the 2022 GRC Smart Materials and Structures Conference [98]. A manuscript is currently under review for journal publication [99].

### **7.1.3 A gapped wing produced less roll than two ailerons, but favorable yaw in some cases**

The previous chapters focused on comparing the gapped wing to a wing with a single aileron. However, it is more realistic for ailerons to be implemented in oppositely deflecting pairs. Chapter IV expanded the CFD simulations to a JH-gapped wing and two-aileron JH-wing. The results showed that the two-aileron JH-wing produced much higher rolling moment coefficients than the JH-gapped wing. This represented one of the largest disadvantages of the gapped wing as a control surface. However, in its upper range of rolling moment coefficients, the JH-gapped wing required comparable work to the two-aileron JH-wing at  $10^\circ$  angle of attack. Furthermore, the JH-gapped wing beneficially decreased the drag coefficient compared to the two-aileron JH-wing at low rolling moment coefficients. The JH-gapped wing also produced favorable yaw at low rolling moment coefficients, while the two-aileron JH-wing produced only adverse yaw at non-zero rolling moment coefficients.

### **7.1.4 Gap dimensions could be optimized for roll per work**

Using the validated CFD models, I performed a parameter sweep across several gap dimensions in Chapter V. The previous work had focused on a single gap dimension, and thus the results could not be generalized to other geometries. Thus, this parameter sweep was important for understanding the affects of gap geometry on the rolling moment coefficient

and actuation work of the gapped wing. From the parameter sweep data, I fit linear models of the rolling moment coefficient and actuation work. I also examined the rolling moment coefficient normalized by actuation work (“normalized roll”) of each gap configuration. Larger gaps increased both the rolling moment coefficient and work. In addition, the results implied that the gap configuration could be designed to maximize normalized roll. Comparing five- and nine-gapped wings confirmed that the gaps may be most effective when positioned closer to the wing tip. Furthermore, the results corroborated that the gapped wings were most effective at producing normalized roll at high angles of attack.

### 7.1.5 Gapped wings effectively altered trim and mitigated gusts

Finally, we analytically modelled the rigid body dynamics of a series of aircraft with the gapped wings from the parameter sweep. We used the models to study the effects of the gaps on the aircraft’s trim state, natural longitudinal modes, and response to  $1-\cos$  streamwise and transverse gusts. All of the aircraft with gapped wings were capable of achieving dynamically stable trim. While the gaps shifted the aerodynamic center of the wing forward, they overall decreased the pitching moment contribution from the wing. Thus, the gapped wings were less destabilizing than a baseline wing without gaps. In general, wings with larger and more gaps had a greater impact on aircraft dynamics than wings with smaller and fewer gaps. The gapped wings generally decreased trim angle of attack and increased trim velocity. Furthermore, they tended to increase the damping and decrease the frequency of the phugoid mode, while decreasing the damping and increasing the natural frequency of the short period mode. The gapped wings tended to improve these longitudinal modes. However, all of the aircraft—including the baseline aircraft—exhibited poor flying qualities for the short period mode. Finally, the gapped wings were effective at mitigating the aircraft’s response to gusts, especially the nine-gap wing with  $\frac{3c}{4} \times \frac{b}{16}$  gaps.

While the previous chapters focused on wing-alone configurations, this analytical study quantified the impacts of the gapped wings on overall aircraft dynamics. This work was

presented at the 2023 SPIE Smart Structures & NDE Conference [100].

## 7.2 Limitations of the gapped wings

As with any control surface, the gapped wings were faced by several real-world challenges. Firstly, the gapped wings exhibited varying control effectiveness across angle of attack (Chapter II). This drawback would require creative solutions to minimize burdens on the flight controller, while taking advantage of the gaps' region of higher performance. Relatedly, the gaps performed best at higher lift coefficients, outside of the typical cruise angles of attack. However, this could be interpreted as evidence that the gapped wings expanded the control envelope of UAVs. Finally, a gapped wing produced much lower rolling moment coefficients compared to a wing with two ailerons (Chapter IV). The gapped wing also did not provide substantial work benefits in this case. However, the parameter sweep implied that the gap geometry could be altered to minimize these effects (Chapter V).

## 7.3 Future work

There is a need for further research and development on the gapped wings before they can be effectively incorporated on a UAV. Firstly, an appropriate actuation method needs to be designed and prototyped. The proposed sliding covers may be more mechanically complex to implement than an equivalent aileron. Therefore, prototyping would require studies into the most efficient actuation systems and manufacturing techniques. Further, the sliding covers are not physically similar to the rotating feather mechanism, and thus research into a more feather-inspired actuation method may be required. Additionally, the actuators employed in the prototype must be lightweight and small enough to be housed within the aircraft. These constraints indicate smart materials as an appropriate solution, including macrofiber composites, shape memory alloys, flexible skins, or 3D-printed metamaterials. The gaps could also be manufactured with intelligent or smart materials, with integrated sensors to

provide control feedback. Building a prototype would also enable more accurate estimates of the actuation work, through experimental measurement and validation. In addition, developing strategies to augment the gapped wing's performance at low angles of attack would be useful for future aircraft designers. This work could include research into complex controllers, new flight maneuvers, or special control surfaces as discussed in Chapter II.

The developed CFD models could be leveraged to more thoroughly explore the gapped wing design space, enabling more rapid prototype iterations. More advanced computational tools like Large Eddy Simulation (LES) could better predict forces in the post-stall region. LES could also resolve smaller and more complete flow structures within the gaps themselves. In addition, higher fidelity simulations could inform more accurate work estimates for the gapped wings. These CFD models could also be the basis for future optimization studies. True optimization studies should be run on the gapped wings to determine the best geometry for a given flight mission. For example, the parameter sweep results indicated that the gap dimensions would need to balance desired roll capabilities with work requirements.

Gapped wing dynamics could also be further studied. Finding an aircraft configuration that meets the Level I Cooper-Harper requirements for the short period mode would be desirable. Relatedly, it would be beneficial to develop strategies for mitigating the higher short period natural frequency of the gapped wings. Given that the gaps could make the wing structure more compliant, it would also be important to characterize their aeroelastic behavior. The actuation of the gapped wings could also be modelled to investigate transient behavior as the gaps are opened or closed.

Further research in the biological domain is equally important. The results of this work could not be directly applied to birds, because the bio-inspired gapped wings were simplified, static, and not necessarily representative of bird wings. However, the code, analysis, and experiments developed here may help avian biologists understand whiffing. Furthermore, the tools we developed could help explore the relationship between planar and deflecting morphing in biological fliers. Birds can morph their wings and tails both in- and out-of-plane

to control their flight path and stability [8], [101]. Further studies could identify if there are aerodynamic or energetic advantages to this ability to morph both in- and out-of-plane. It would also be useful to understand the relationship between camber inversion and feather rotation, the affects of feather dynamics, the energy costs of whiffling, and underlying passive or active mechanisms. Whiffling is a unique and complex avian maneuver, and biological studies will provide ornithologists deeper insight into avian flight, and engineers further opportunities to leverage the behavior for bio-inspired work.

## APPENDICES



## APPENDIX A

### Airfoil ordinates

For both the experimental work (Chapter II) and computational work (Chapters III and V), we used the follow equation for the NACA 0012 airfoil ordinates for the SI-gapped wing and SI-aileron wing [102]:

$$y = 0.594689181 \cdot c \left( 0.298222773 \sqrt{\frac{x}{c}} - 0.127125232 \left(\frac{x}{c}\right) - 0.357907906 \left(\frac{x}{c}\right)^2 + 0.291984971 \left(\frac{x}{c}\right)^3 - 0.105174606 \left(\frac{x}{c}\right)^4 \right) \quad (\text{A.1})$$

Using this modified NACA 0012 formula ensured that airfoil closed with a sharp trailing edge at  $\frac{x}{c} = 1$  [102].

The ordinates of the NACA 64A010 (used by the JH-aileron wing and JH-gapped wing) were obtained from Selig's database [103]. The 64A010 also closed with a sharp trailing edge.

The tail plane used for the gust alleviation work (Chapter VI) used a blunted NACA 0012 airfoil as described in Appendix J.

## APPENDIX B

# Aerodynamic Effects of Endplates, and Comparison of SI- and JH-Wings

In this appendix, we used the CFD results to show that the endplates present on the SI-wings successfully reduced the tip effects of the SI-gapped wing and encouraged two-dimensional flow. We also found that the behaviors of the SI-gapped wing and JH-gapped wing were very similar, despite the tip effects present on the JH-gapped wing. This result implied that the endplates ultimately did not have a large effect on the aerodynamics of the gaps. Furthermore, the gaps had similar aerodynamic effects (relative to their corresponding aileron wing) for two different Reynolds numbers and baseline wing geometries. Ultimately, examining the JH-configuration and the SI-configuration side by side helped us study the effects of endplates on the experimental data (Chapter II) and computational results (Chapters III, IV, and V).

### Work curve of the JH-gapped wing

As with the SI-gapped wing, the roll performance and work requirements of the JH-gapped wing were highly dependent and nonlinear with angle of attack (Fig. B.1 (A)). Recall that the JH-aileron wing was simulated at a  $10^\circ$  angle of attack as a representative

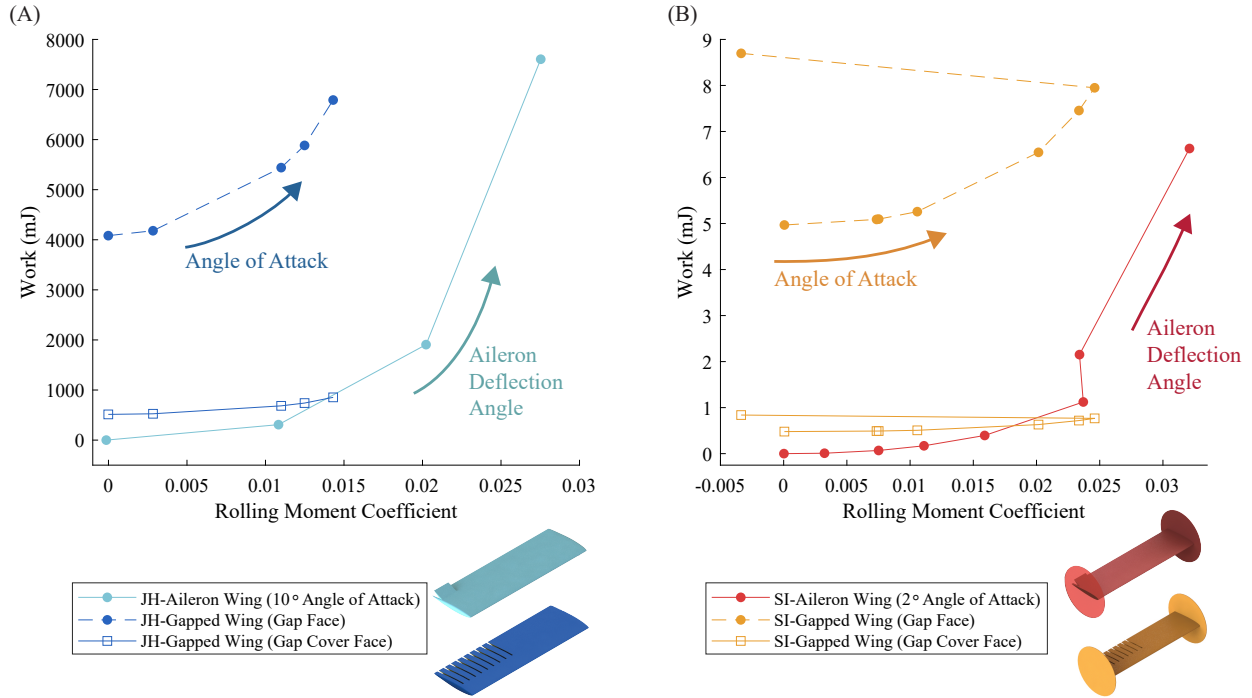


Figure B.1: The gapped wings and aileron wings exhibited similar work curves in both the SI and JH configurations, despite differences in geometry and flow. (A) Work versus rolling moment coefficient of the JH wings. (B) Work curves of the SI wings. The work to actuate the full gap face (before scaling by  $R$ ) is included as dashed lines. We varied deflection angle for the aileron wings and angle of attack for the gapped wings.

set (Section 3.3). Additionally, the JH-gapped wing gap cover work (dark blue solid line) was higher than the JH-aileron wing work (light blue solid line) for rolling moment coefficients below 0.0139 (Fig. B.1 (A)). The JH-gapped wing work curve did not extend far past this point because we limited its simulations to  $12^\circ$  angle of attack. In our simulations, neither the JH-gapped wing nor the aileron wing stalled below  $12^\circ$  angle of attack. We did not exceed this angle of attack because RANS generally suffers from poor convergence and inaccurate results in the post-stall region [76]. Furthermore, the simulations were known to under-predict the stall angle of SI-gapped wing (Section 3.5). In an experimental environment, we expected that the JH-gapped wing could follow similar pre-stall trends to a higher rolling moment coefficient than shown in Figure B.1 (A).

As discussed in Section 3.6.3, the gap cover work estimates could have large error bars

due to the the choice of RANS-based simulations and turbulence model [76]. The work values in Figure B.1 were also likely overestimates because we assumed that the force on the gaps and the hinge moment coefficient were constant across gap position and aileron deflection, respectively. Finally, per Eqn. 3.1, the gap cover work was dependent on the area ratio  $R$  and the assumed geometry of the gap covers and wing. Therefore, the gap face work of the JH-gapped wing was also shown (dark blue dashed line) before scaling by the area ratio  $R$ , for completeness (Fig. B.1 (A)).

## Comparison of the JH- and SI- configurations

Figure B.1 shows the work curves of the SI-gapped wing and the JH-gapped wing compared to their respective aileron configurations. While the magnitude of the work varied due to geometric and flow differences, the curves' patterns were very similar across both configurations. The JH-gapped wing and SI-gapped wing were both highly dependent on angle of attack, required more work at lower rolling moment coefficients, and stall later than the ailerons. One difference between the configurations was that the SI-gapped wing produces a greater maximum rolling moment coefficient than the JH-gapped wing. This was likely due to the endplates on the SI-wing approximating an infinite wing: decreasing aspect ratio tends to decrease rolling moment coefficient [57]. Ultimately, the tip effects on the JH-gapped wing did not affect the wing's general behavior or its ability to produce rolling moment. Additionally, the effects of the gaps on the wing were very similar even at two different Reynolds numbers and for two different baseline wing geometries.

## Effects of endplates

In the SI-gapped wing experiment, endplates were used to approximate two-dimensional flow and avoid conflating the aerodynamic effects of the gaps with tip effects (Chapter II). We found that the pressure distribution along the chord was consistent at various spanwise

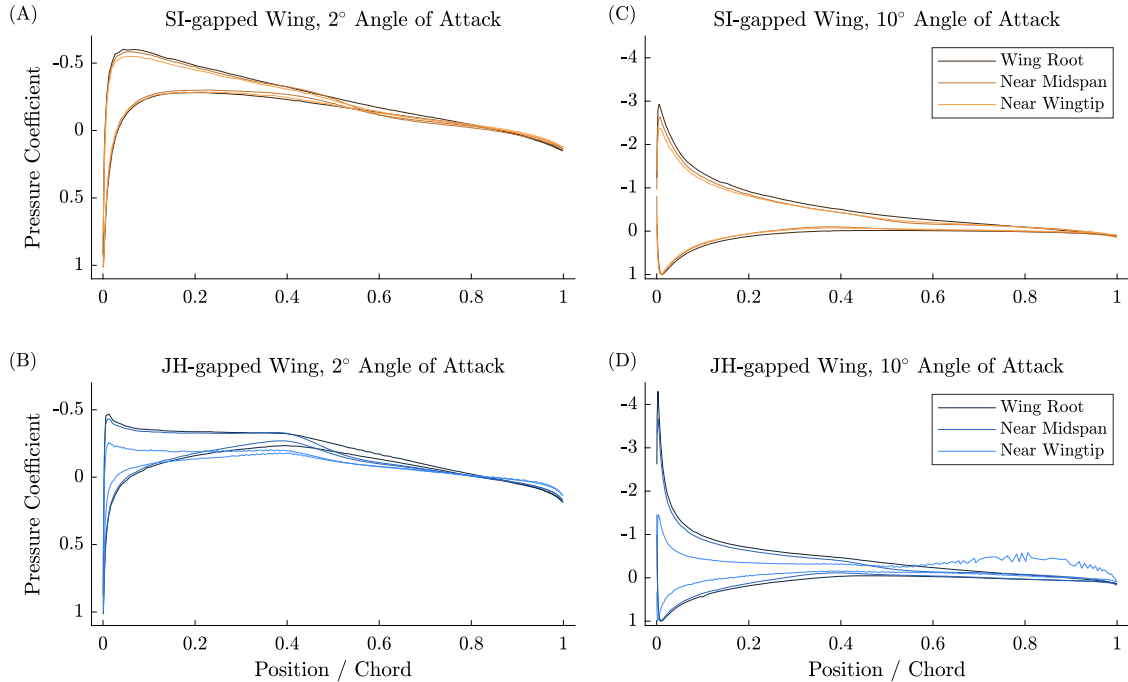


Figure B.2: The pressure distribution along the chord of the SI-gapped wing was not significantly affected by spanwise location, but varied more greatly along the span of the JH-gapped wing. Data were taken at 2° and 10° angles of attack, at three spanwise locations near the root, midspan, and wingtip of each wing as indicated with dashed lines in Figure B.3.

locations on the SI-gapped wing, but more varied over the span of the JH-gapped wing (Fig. B.2). Thus, the endplates on the SI-gapped wing successfully approximated two-dimensional flow and reduced tip effects. Note that the pressure coefficient data from the wingtip of the JH-gapped wing at 10° angle of attack exhibited very different behavior from the baseline airfoil at the wing root; this was likely due to the presence of tip vortices.

Figure B.3 illustrated pressure contours on the upper surfaces of the SI-gapped wing and JH-gapped wing at 2° and 10° angles of attack. At both angles of attack, the SI-gapped wing experienced more negative pressure coefficients near the third-chord of the gapped semi-span compared to the baseline semi-span. The leading edge pressure distribution was more consistent across the span of the JH-gapped wing at both angles. Thus, while endplates reduced tip effects, they had a greater bearing on the pressure distribution over the baseline semi-span. The endplates did not severely impact the pressure distribution over the upper

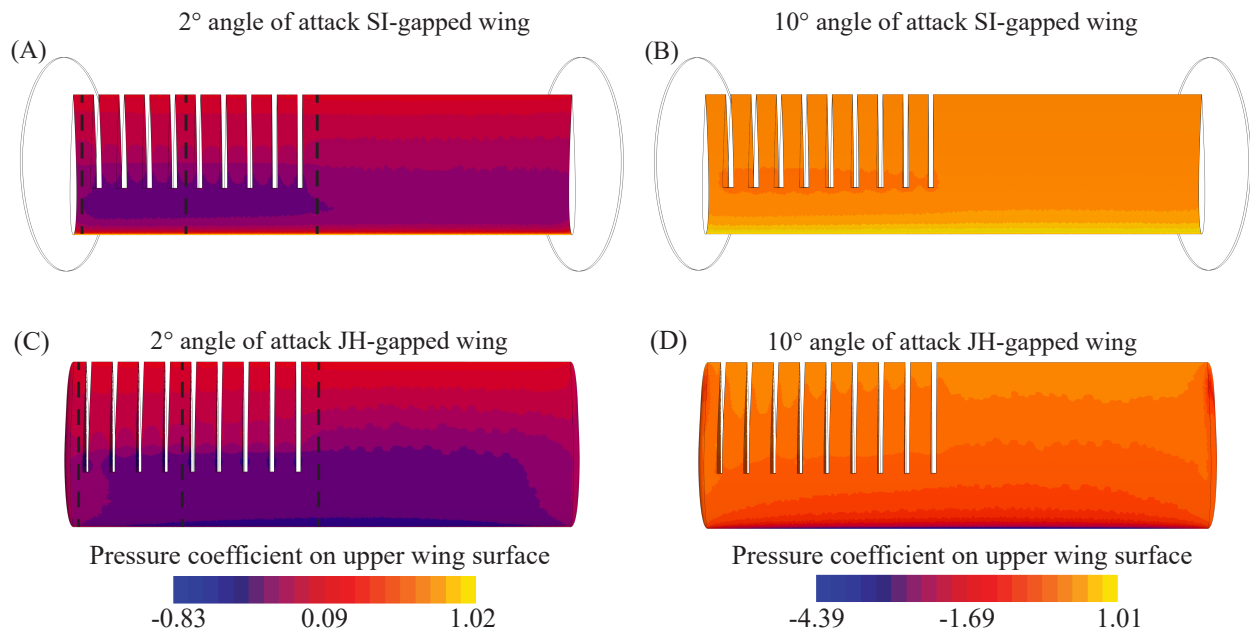


Figure B.3: Tip effects did not substantially impact the pressure distribution over the upper surface of the gapped semi-spans. (A) SI-gapped wing at 2° angle of attack. (B) SI-gapped wing at 10° angle of attack. (C) JH-gapped wing at 2° angle of attack. (D) JH-gapped wing at 10° angle of attack. The black dotted lines in (A) and (C) show the sampling locations used for Figure B.2.

surface of the gapped semi-span.

## APPENDIX C

### Experimental Uncertainty Analysis

The standard combined uncertainty of the data (“uncertainty”) was calculated according to the Guide to the Expression of Uncertainty in Measurements (GUM) [1]. We then determined and reported the expanded uncertainty of the data using a coverage factor of two, yielding an interval with a level of confidence of approximately 95%.

We included both Type A and Type B sources of variance in our uncertainty calculations, excluding the Type B variance of the load cell. The Type B variance of the load cell was specified by the manufacturer on the calibration certificate: the maximum measurement uncertainty was 1.00% of full-scale load at the 95% confidence level for all channels except moment about the  $z$ -axis, for which the maximum measurement uncertainty was 1.50%. The Type B variance of the load cell represented one of the largest sources of relative uncertainty for the data. However, this uncertainty was mitigated by running multiple trials per wing and presenting the data in a cumulative averaged format. The Type B variance of the load cell was therefore excluded from the plotted uncertainty.

The Type A variation (standard error, or standard deviation of the mean) of the force, pressure, and temperature data were calculated using Zięba’s time series analysis method [104]. This method generally yielded more conservative (larger) uncertainty values due to autocorrelation of the data.

We accounted for correlations between the channels of the load cell in the error propagation, but correlations between the dynamic pressure and load cell readings were determined to be negligible and thus were excluded from calculations.

## Statistical significance of experimental data

The results of the experimental gapped wing study were founded on relative data; that is, the differences between mean values of each gapped wing and the baseline wing mean values. In order to draw conclusions about these incremental data, we determined the statistical significance of each incremental data point. To do so, we calculated the expanded uncertainty of each difference of means, at an approximately 95% confidence level, following the methodology outlined in the GUM [1]. Note that this is similar to, but distinct from, a 95% confidence interval of the difference of means [1]. We first calculated the standard combined uncertainty of each gapped wing (mean) value and each baseline wing (mean) value. Then, we took the difference of the gapped wing mean and baseline wing mean, and calculated the corresponding standard combined uncertainty of that difference. Finally, we multiplied the standard combined uncertainty (of the difference of means) by a coverage factor ( $k$ ) of two, per the GUM [1]. This final product was the expanded uncertainty of the difference of means, at an approximately 95% confidence level. We set the null hypothesis to be zero. If the expanded uncertainty included the null hypothesis, we accepted the null, indicating that the difference in means was not statistically significant. In other words, there was no statistical evidence that the mean gapped wing value was different from the baseline wing value. If the expanded uncertainty did not encompass the null hypothesis, then we had evidence that the difference of means was statistically significant. That is, even accounting for the experimental uncertainty, there was statistical evidence that the gapped wing mean values were different from the baseline wing mean values. Determining the statistical significance of the incremental data provided a measure of certainty in our comparative results and conclusions. In summary, determining the statistical significance



of the data provided a measure of reliability, and allowed us to compare the measurement results and accurately draw conclusions. In Chapter II, the statistically significant points are demarcated in the figures by a circled dot ( $\odot$ ), and the insignificant points are marked with a dot ( $\cdot$ ).

## APPENDIX D

### Validation of Experimental Setup

We validated our experimental setup used in Chapter II by comparing the coefficient of lift curve of the baseline wing to previously published data.

The coefficient of lift curve often depends on parameters such as aspect ratio, Reynolds number, and wind tunnel data corrections [56], [59]. There was no single previously published experiment that matched all of our wing geometry and flow conditions. Therefore, we compared the baseline wing data with other previously published results that shared similar parameters to our experimental setup: Jacobs and Sherman tested at an  $Re$  of  $3.3 \times 10^5$  and corrected their data to an infinite wing [93]. Pankonien et al. used an  $Re$  of  $2.1 \times 10^5$  and a low aspect ratio wing with endplates, corrected for blockage [6]. Goett and Bullivant tested a wing of aspect ratio six at a Reynolds number of  $3.3 \times 10^6$ , and corrected for blockage and jet boundaries [105]. Each previously published lift curve shared a similar parameter with the current work, or in the case of the thin airfoil curve, provided an upper bound for the expected lift coefficient results. Including these curves highlighted that the baseline wing coefficient of lift fell within a reasonable range to the previously published data, despite geometric and flow differences.

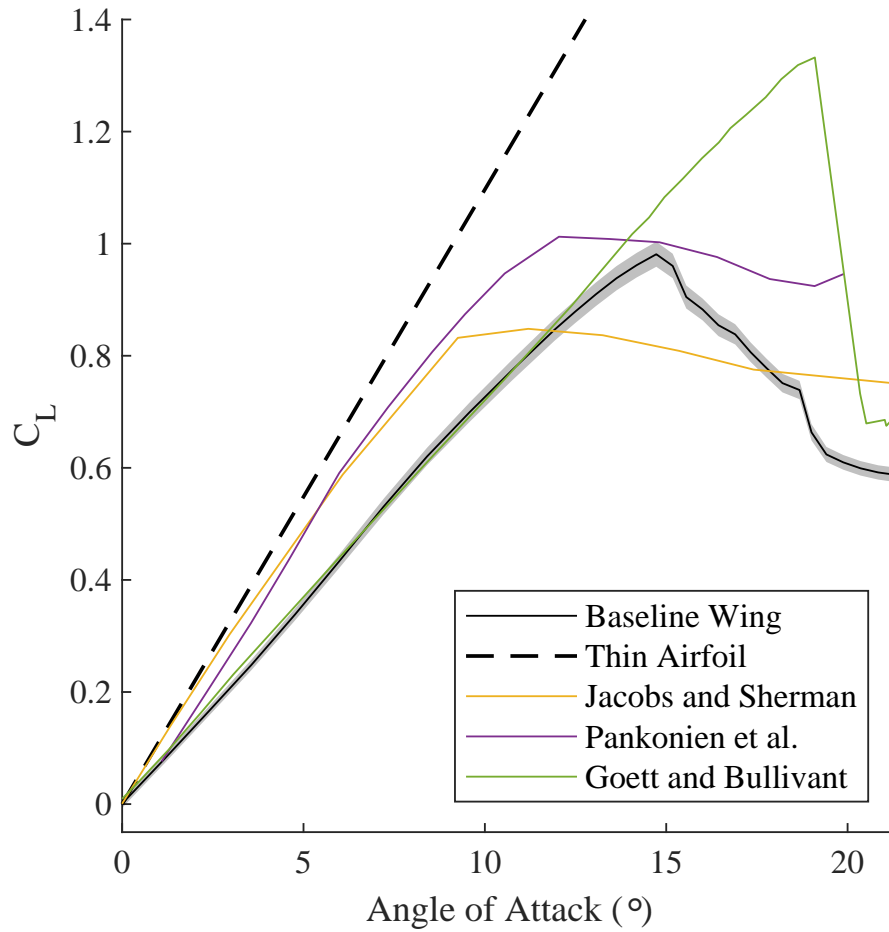


Figure D.1: Validation of the experimental SI-baseline wing lift curve, compared to previously published NACA 0012 data [6], [93], [105]. The experimental data agreed well with the previously published data

## APPENDIX E

### Comparison of SI-Gapped Wing and SI-Baseline Wing

Both the previous experimental study (Chapter II) and the current work investigated a baseline SI wing without gaps (SI-baseline wing) as a comparison to the gapped wing. Here, we experimentally validated CFD results of the SI-baseline wing. We also compared the pressure coefficients at a gap section with pressure coefficients at a baseline wing section. Note that differences in aerodynamic forces and moments between the SI-baseline wing and SI-gapped wing were thoroughly discussed in the previous experimental work, and are not repeated here (Chapter II). The CFD results of the SI-baseline wing agreed well with the previous experimental data from Chapter II (Fig. E.1). This matching was expected, given the good agreement between CFD and experimental data for both the SI-gapped wing (Fig. 3.4) and JH-aileron wing (Fig. 3.5). The baseline wing was simulated as a SI-aileron wing with a  $0^\circ$  aileron deflection, at angles of attack ranging from  $0^\circ$  to  $10^\circ$ .

Figure E.2 compared the pressure coefficients along the gap with the pressure coefficients over a baseline wing section. The baseline pressure distribution appeared nominal for a NACA 0012 section. Comparatively, the pressure coefficients along the chord in the central gap fluctuated to local maxima and minima before returning to a near-nominal value at the trailing edge. The baseline wing reached a slightly higher pressure coefficient at the trailing edge than the gapped wing. The pressure coefficients along the gap (yellow line) were the

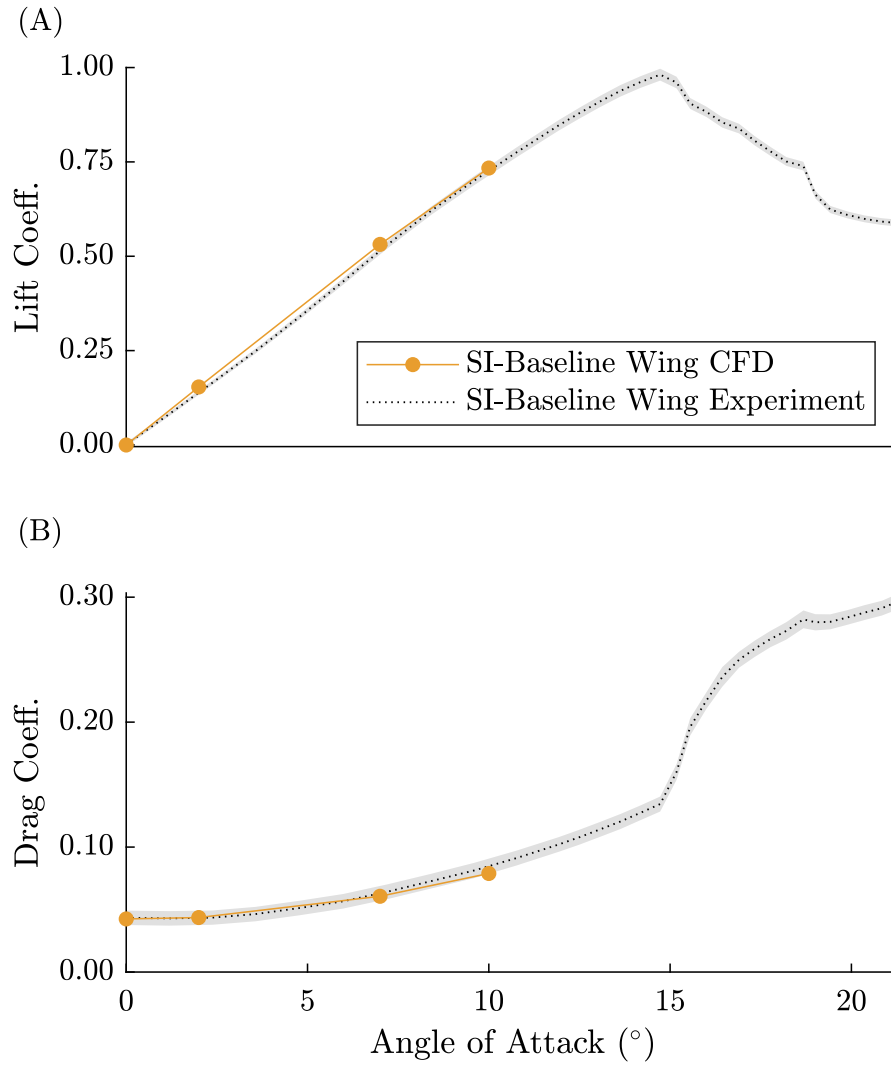


Figure E.1: The SI-baseline wing CFD data agreed well with the previous experimental results, comparing (A) lift coefficient and (B) drag coefficient. The baseline wing was simulated as the SI-aileron wing with a  $0^\circ$  deflection at angles of attack from  $0^\circ$  to  $10^\circ$ .

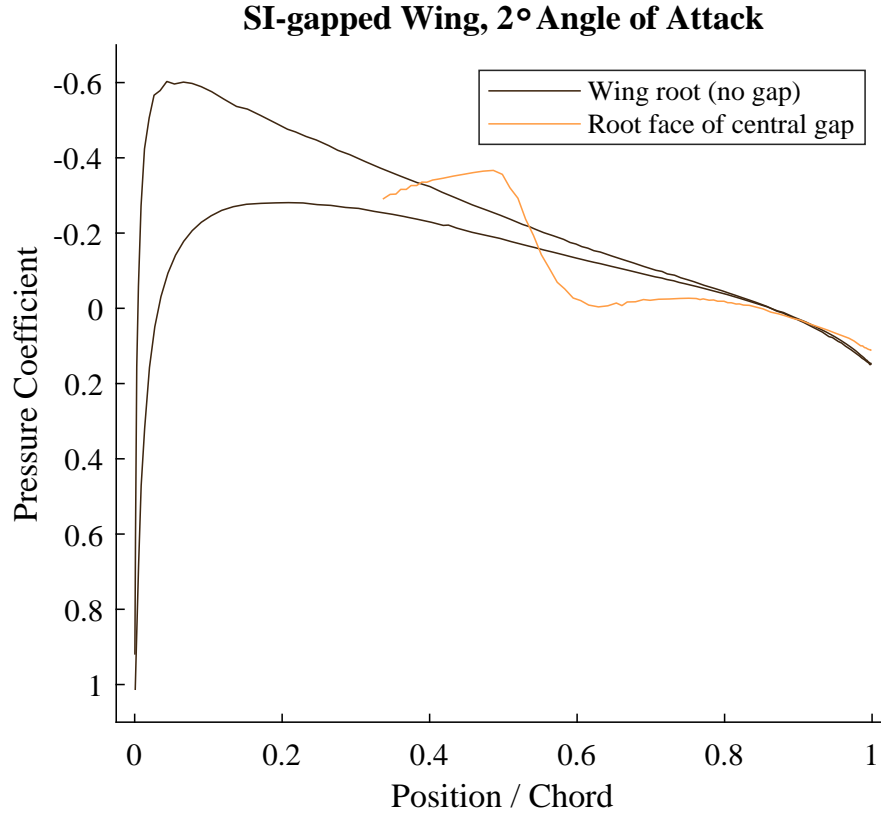


Figure E.2: Compared to the pressure coefficients over the SI-baseline wing (brown), the pressure coefficients over the SI-gapped wing (yellow) oscillated to local minima and maxima. The SI-baseline wing also experienced a slightly higher pressure coefficient at the trailing edge than the SI-gapped wing.

same as those plotted in Figure 3.9 (B), measured along the chord line of the root face of the central gap. The pressure coefficients of the baseline section (dark brown line) were measured from the SI-gapped wing at the wing root, away from the gaps.

## APPENDIX F

# Refined Work Estimates Based on Integral Approximations

Previously, the work of the gapped wings and aileron were estimated assuming that the force on the gap covers and the hinge moment of the aileron were constant across displacement and deflection. However, ailerons experience higher hinge moments at larger deflection angles [2]. I speculated that the force on the gap covers would similarly change across their displacement. Thus, the previous work calculations were likely conservative over-estimates. Here, I used the parameter sweep data (Chapter V) to refine the work estimates of the gap covers and aileron as integral approximations. The refined work estimates were lower than the constant force/hinge moment estimates as anticipated. The intersection of the refined work curves also increased from previous estimates—that is, the gapped wing required less work than the aileron at a higher rolling moment coefficient than before. Despite this discrepancy, the relative work curves confirmed that the constant force/hinge moment assumption (Chapter III) was appropriate. Due to practical considerations, the approximations were not used in this dissertation; the constant force/hinge-moment estimates were used.

## Methods

I previously assumed a constant force across the displacement of the gap cover (Eqn. 3.1). To keep the work estimates of the gaps and aileron directly comparable, I also assumed that the aileron hinge moment coefficient was constant across deflection angle (Eqn. 3.3). However, hinge moments are known to increase with deflection angle [2]. I expected that the force on the gap faces would also change with gap width (actuation position).

Thus, I refined the work estimates for both the SI-gapped wing and SI-aileron wing, using Riemann sum integral approximations based on the parameter sweep data (Chapter V). The Riemann sum method allowed me to vary the force on the vertical gap faces at each simulated gap width. I only included gap widths narrower or equal to  $\frac{b}{48}$  in the integral approximation, because this was the maximum gap width tested experimentally (Chapter II) and simulated in the previous computational work (Chapter III). Thus, basing the refined work estimate on this range of gap widths enabled me to directly compare it to the constant-force work estimate. At each angle of attack, I calculated the work (in mJ) to actuate the gap covers using MATLAB's *trapz* function, which was equivalent to:

$$W_{gc}^R(\alpha) = \sum_{b_i=b/192}^{b/48} \frac{F_g(b_{i+1}) + F_g(b_i)}{2} (b_{i+1} - b_i) \cdot R \cdot 1000 \quad (\text{F.1})$$

Similarly, I applied the Riemann sum estimate to the SI-aileron wing. I summed the products of hinge moment and deflection angle to calculate the work to deflect the aileron to a given angle. Using MATLAB's *trapz* function:

$$W_a^R(\delta_a) = \sum_{\delta_i=0^\circ}^{\delta_a} \frac{M_a(\delta_{i+1}) + M_a(\delta_i)}{2} (-(\delta_{i+1} - \delta_i)) \frac{\pi}{180} \cdot 1000 \quad (\text{F.2})$$

The negative sign in Eqn. F.2 was required to model the work done by the hypothetical actuator. The product  $M_a \delta_a$  represented the work “done” by the airflow on the aileron surface. Thus, the negative of that product represented the work required to overcome this



aerodynamic loading.

The hinge moment coefficient is also known to vary across angle of attack [2]. Therefore, I estimated the aileron work at several angles of attack  $\alpha = [2^\circ, 8^\circ, 10^\circ]$ . Each angle of attack was held constant while the aileron deflection angle was varied. Not all of the same aileron deflections were simulated for each angle of attack. For the angles of attack, the following aileron deflection angles ( $\delta_a$ ) were simulated:

- $\alpha = 2^\circ$ :  $\delta_a = [0^\circ, -2^\circ, -4.7^\circ, -7^\circ, -10^\circ, -15.3^\circ, -18.3^\circ, -30^\circ]$
- $\alpha = 8^\circ$ :  $\delta_a = [-4.7^\circ, -15.3^\circ, -17.5^\circ, -19.5^\circ, -30^\circ]$
- $\alpha = 10^\circ$ :  $\delta_a = [0^\circ, -15.3^\circ, -17.5^\circ, -18.3^\circ, -19.5^\circ]$

## Work estimates were refined using integral approximations

I applied the parameter sweep data to refine the SI-gapped wing work estimates, using Riemann sum integral approximations (Fig. F.1). The force on the vertical gap faces increased as the gaps became narrower. Recall that gap width was limited to those narrower than or equal to  $\frac{b}{48}$  (solid lines in Fig. F.1 (B)). The work to open the gap covers from fully closed to the  $\frac{b}{48}$  position ultimately decreased (solid black line) compared to the constant-force work estimate (dashed black line). The difference between the Riemann sum work estimate and the constant-force work estimate was approximately constant across angle of attack.

I also applied the Riemann sum integral approximation to the SI-aileron work estimates (Fig. F.2). At all angles of attack, the Riemann sum estimate was lower than the constant hinge moment estimate. Furthermore, both the hinge moment and work varied more with deflection angle than angle of attack.

Both the SI-gapped wing and SI-aileron wing required less actuation work based on the Riemann sum estimates compared to the constant force/hinge moment estimates, as expected (Fig. F.3). However, the Riemann-estimated work curves intersected at a higher

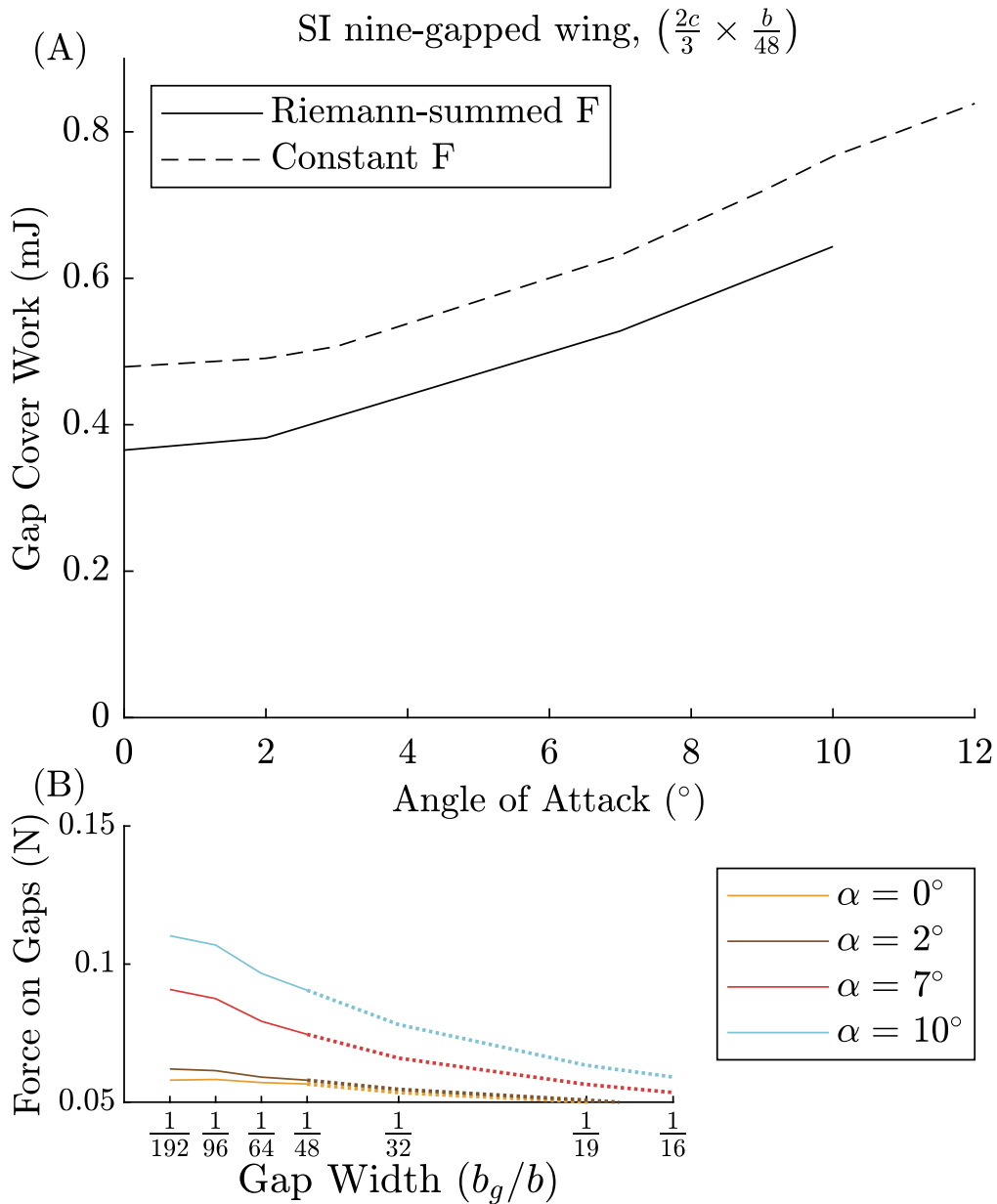


Figure F.1: (A) The Riemann sum work estimate was lower than the constant force estimate for the SI-gapped wing with  $\frac{2c}{3} \times \frac{b}{48}$  gaps. (B) The force on the vertical gap faces decreased as the gaps widened. The gap widths used for the Riemann sum estimates are shown with solid lines, and unused gap widths are shown as dotted lines. The force is plotted at each simulated angle of attack:  $\alpha = [0^\circ, 2^\circ, 7^\circ, 10^\circ]$

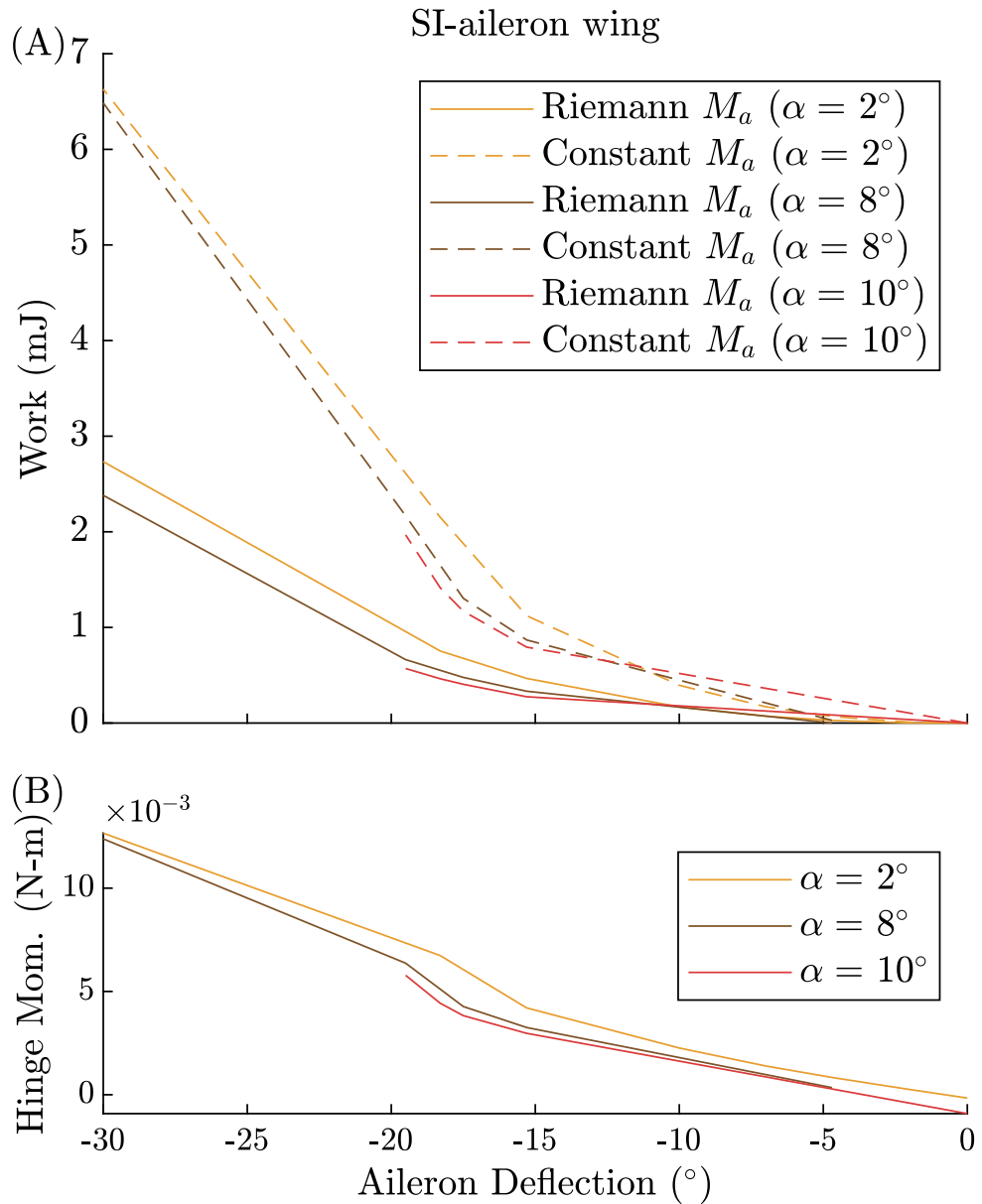


Figure F.2: (A) The Riemann sum work estimates were lower than the constant hinge moment estimates. (B) Hinge moment coefficient decreased as aileron deflection magnitude decreased. Hinge moment and work are plotted against aileron deflection angle at several representative angles of attack.

rolling moment coefficient compared to the constant force/hinge moment work curves. When using the integral approximation, the SI-gapped wing required less work than the SI-aileron wing for rolling moment coefficients above 0.0236 (compared to 0.0182 from Figure 3.11). This new intersection point did not occur until after the SI-aileron wing had partially stalled, indicated by the vertical jump in the aileron work curve. Under the constant force/hinge moment assumption, the gapped wing broke even with the aileron work before the aileron stalled (Fig. 3.11). For ease of comparison with Figure 3.11, note that only the aileron work curve at  $2^\circ$  angle of attack was plotted in Figure F.3.

While the values of the work curves changed with the Riemann sum estimates, their general shapes and values relative to one another remained fairly constant (Fig. F.3, Fig. 3.11). This consistency implied that the constant force/hinge moment assumption was appropriate in the comparative context of Chapter III. However, it would be important to increase the fidelity of the integral approximation when designing and drawing specifications for an aircraft or actuation system. The accuracy of the Riemann sum work estimates were dependent on simulated gap cover positions and aileron deflection angles, as well as the resolution between these points. As with any discrete approximation, the accuracy of the estimates could be improved by including additional intermediate gap positions and aileron deflections. Ultimately, the most accurate method would be to measure the work required to move the gap covers and aileron directly over time, either through dynamic simulations or wind tunnel testing. This topic will be the subject of future investigations. Additionally, the Riemann estimates for the gapped wing in particular may have had large errors, due to the challenges of resolving flow near small geometry with RANS simulations. These errors could have been especially high for the narrower gap widths. To minimize the impact of these potential errors, the CFD-based work estimates outside of this section all employed the constant gap force and constant hinge moment coefficient assumption from Chapter III.

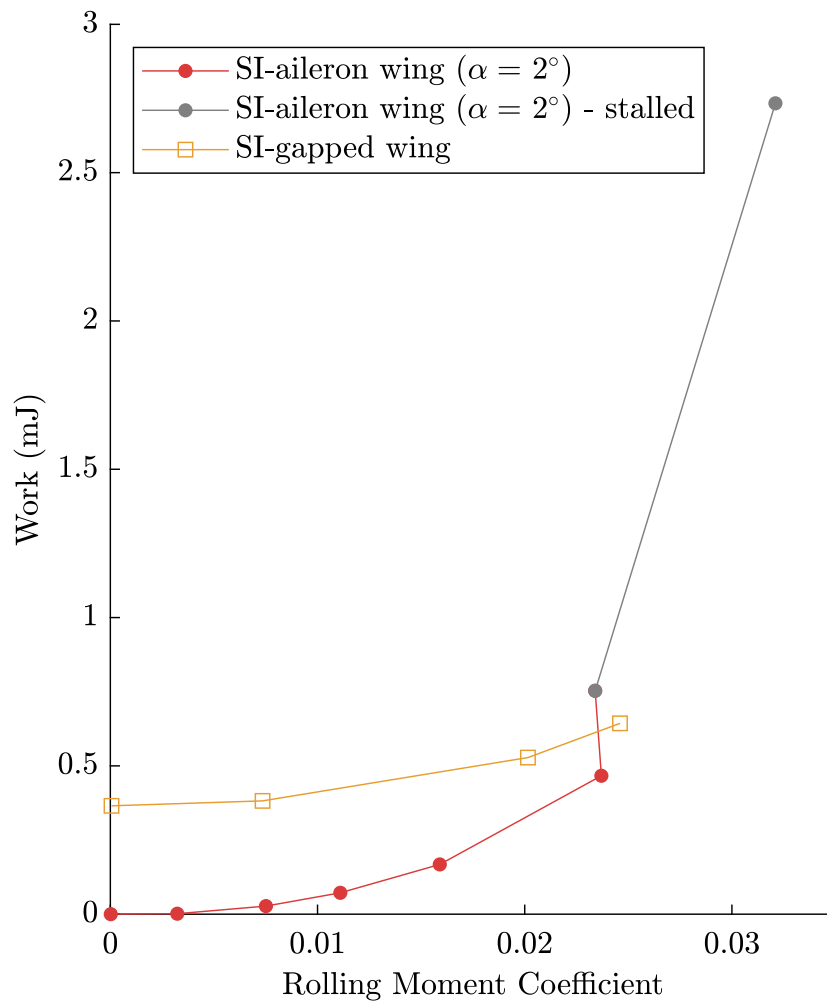


Figure F.3: Comparing the Riemann sum work estimates of the SI-gapped wing and SI-aileron wing, the intersection increased to a rolling moment coefficient of 0.0236 (compared to 0.0182 in Figure 3.11). Grey points indicate partial aileron stall.

## Data availability

The data and codes used to perform the parameter sweep and refine the work estimates are openly available on figshare at DOI: [10.6084/m9.figshare.c.6487942.v2](https://doi.org/10.6084/m9.figshare.c.6487942.v2).

## APPENDIX G

### Parameter Sweep With the Two-Gap Wing

The two-gap edge-case wing was not included in the main results of Chapter V. The gaps of this wing were centered along the semi-span rather than being concentrated at the wingtip, and the models did not account for the relative position of the gaps. Here, we discuss the results of the two-gap wing, alongside the five- and nine-gap wings, all with a gap length of  $\frac{2c}{3}$ . Conclusions were drawn carefully, to avoid conflating effects from the position of the gaps (centered versus outboard) with the number of gaps (two, five, or nine).

The gapped wings appeared to produce greater rolling moment coefficients as the gaps widened, however, this value levelled off to some value (dependent on angle of attack, gap length, and number of gaps) as the gaps became wider (Fig. G.1). As noted from Figure 5.3, the rolling moment coefficient produced by the nine-gap wing was only slightly higher than that of the five-gap wing, implying that the outboard gaps were more effective at producing roll. Visually, the rolling moment coefficient produced by the two-gap wing appeared to follow a similar asymptotic pattern. However, further simulations would be needed to confirm this hypothesis. The high degree of variation in rolling moment coefficient at  $0^\circ$  angle of attack was due to the symmetry of the wing and subsequently negligible roll production.

Figure G.2 confirmed the work requirement trends of the five- and nine-gap wings with  $\frac{2c}{3}$ -long gaps. Specifically, the actuation work of the nine-gap wing was roughly twice that

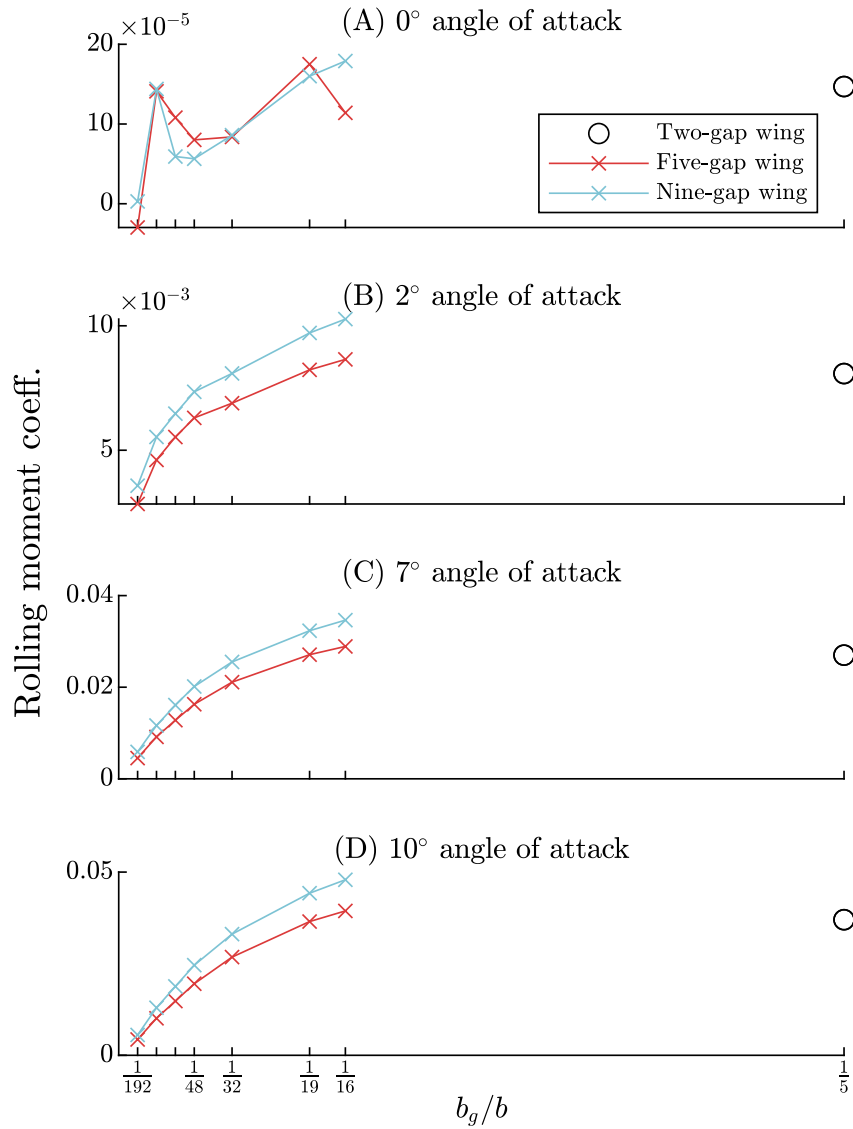


Figure G.1: The rolling moment coefficient versus gap width for the five- and nine- gap wings, as well as the two-gap wing, all with a gap length of  $\frac{2c}{3}$ . Data are plotted at (A)  $0^\circ$ , (B)  $2^\circ$ , (C)  $7^\circ$ , and (D)  $10^\circ$  angle of attack.

of the five-gap wing, because it had nearly twice as many gaps (Eqn. 3.1). Similarly to roll, the actuation work appeared to reach an asymptote as the gaps widened. The two-gap data may follow a similar trend. In particular, Figure G.2 suggested that the actuation cost continued to increase as the gaps widened towards  $\frac{b}{5}$ . Further simulations would be needed to confirm this hypothesis.

Finally, I examined the impact of the two-gap wing on the normalized roll (Eqn. 5.2). Figure G.3 highlighted that the maximum normalized roll existed on the domain boundaries for some cases, but not others. For example, both the five- and nine-gap wings locally maximized the normalized roll with the narrowest gap in the  $2^\circ$  case. However, they maximized normalized roll with intermediate gap widths ( $\frac{b}{48}$  and  $\frac{b}{32}$ ) for  $7^\circ$  and  $10^\circ$  angle of attack. There was also a visible interaction effect between the number of gaps and angle of attack. For example, the normalized roll increased more from the five- to the nine-gap wing at high angles of attack ( $7^\circ$  and  $10^\circ$ ) than at a low  $2^\circ$  angle of attack. From the limited available data, the two-gap wing also appeared to follow similar asymptotic trends for normalized roll.



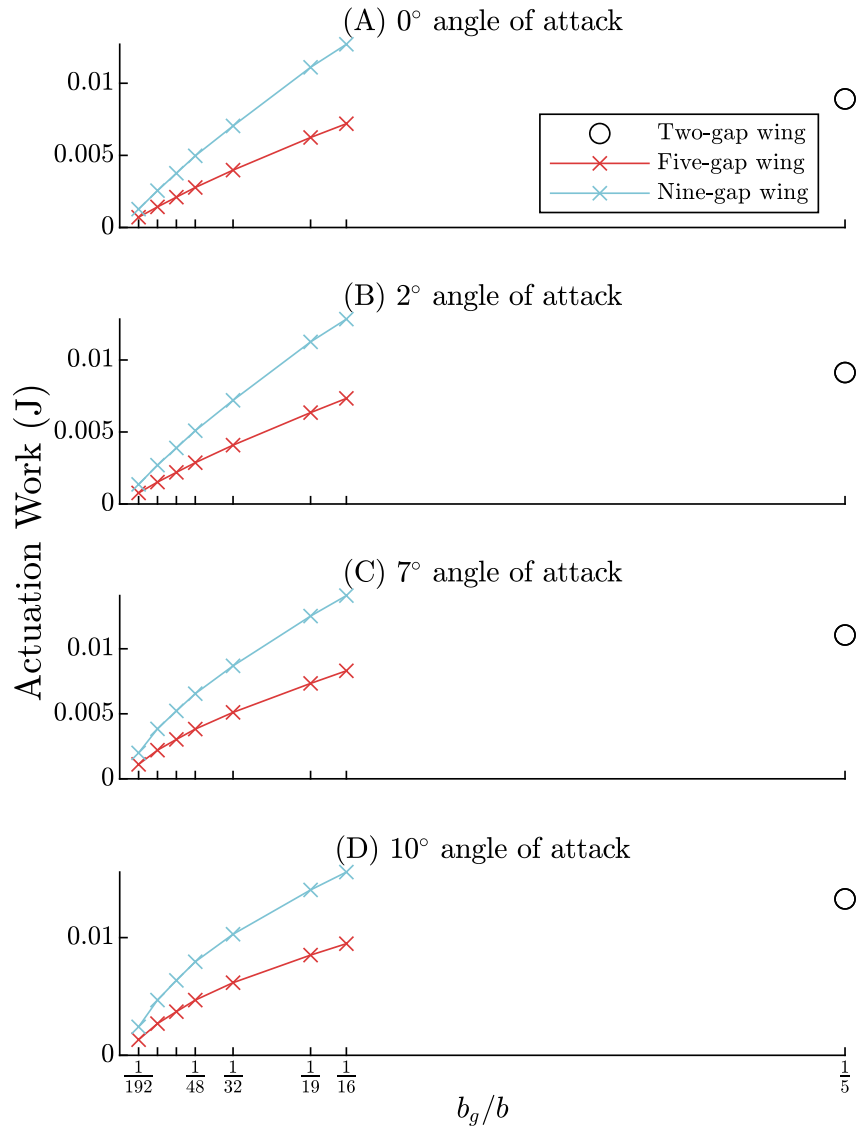


Figure G.2: The actuation work versus gap width for the five- and nine- gap wings, as well as the two-gap wing, all with  $\frac{2c}{3}$ -long gaps. Data are plotted at (A) 0°, (B) 2°, (C) 7°, and (D) 10° angle of attack.

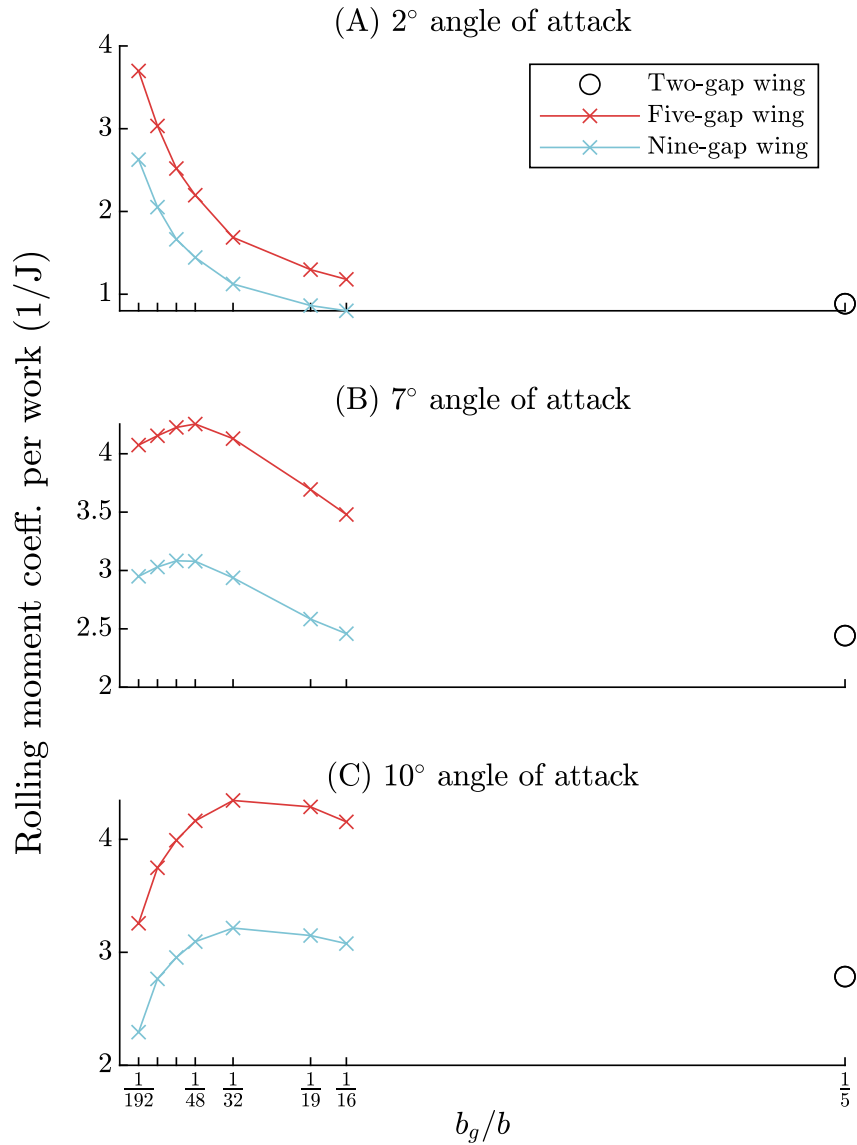


Figure G.3: The normalized roll versus gap width for the five- and nine- gap wings, as well as the two-gap wing, all with a gap length of  $\frac{2c}{3}$ . Data are plotted at (A) 2°, (B) 7°, and (C) 10° angle of attack.

## APPENDIX H

# Simplified Linear Models of Roll and Work, for Validation

The multi-variate linear models for the rolling moment coefficient and actuation work of the five- and nine- SI-gapped wings were initially based on all of the CFD parameter sweep data (excluding the two-gap wing data). I validated the models using just the CFD data from the five- and nine-gap wings with the initial gap dimensions  $\frac{2c}{3} \times \frac{b}{48}$ . The work model fit the data well. However, there were errors between the roll model and validation data. To investigate, I fit simplified versions of the linear models solely using the CFD validation data (the five- and nine-gapped wings with the initial gap dimensions).

Both the simplified rolling moment coefficient model and simplified actuation work model agreed well with the validation data (Fig. H.1). This result built confidence in the approach used to build the full models in Chapter V. However, it also highlighted the difficulty in modelling the effects of gap dimensions on the rolling moment coefficient in particular.

The errors seen in the full rolling moment coefficient model (Chapter V, using all of the parameter sweep data as observations) could be due to the challenges of resolving complex flow around the gaps in RANS CFD simulations. Since it is difficult to model the gap flow in RANS, it is likely that there are errors or residuals between the CFD simulations of different

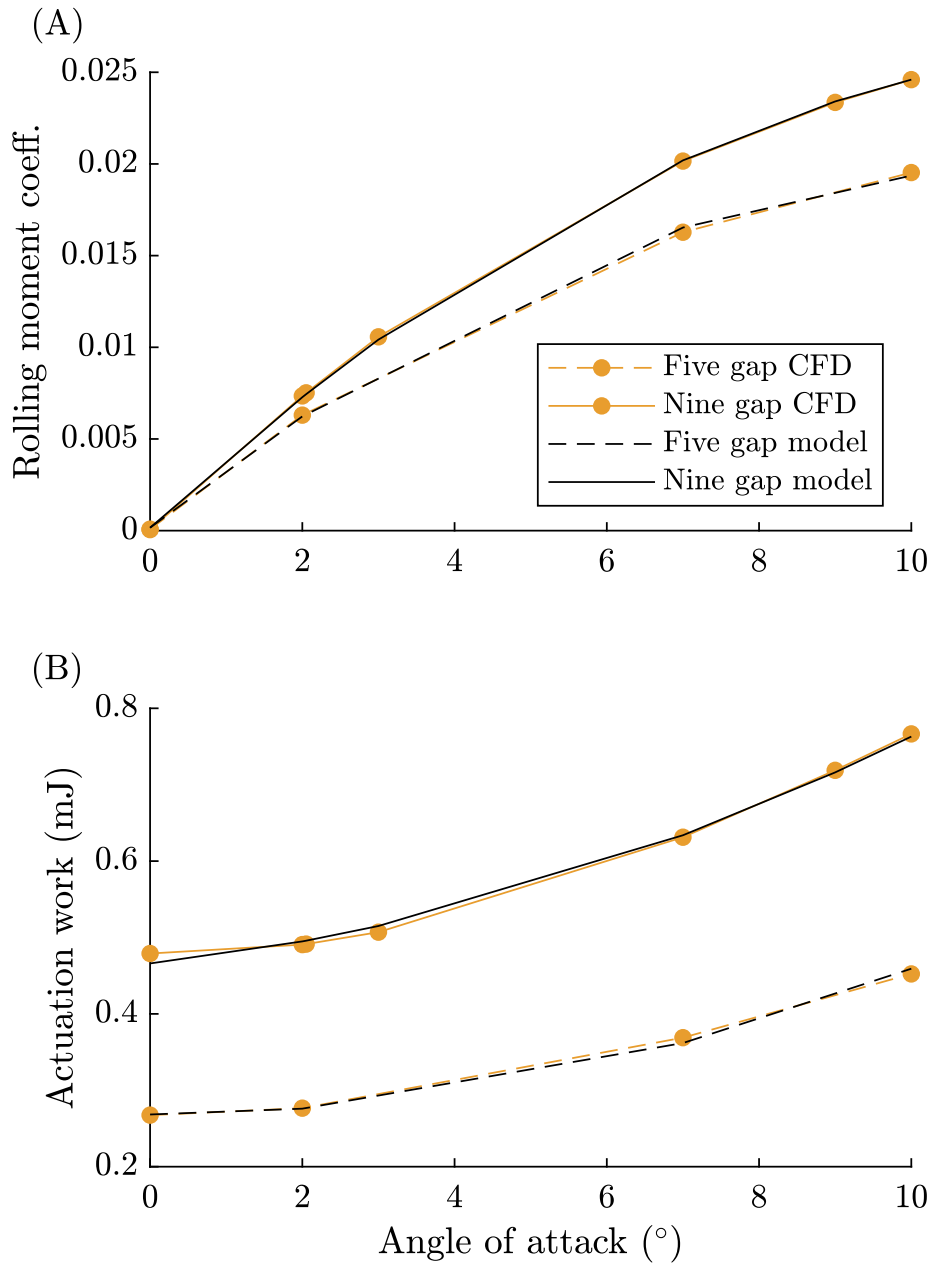


Figure H.1: The linear models for (A) rolling moment coefficient and (B) actuation work of the SI-gapped wing agreed well with the validation data (five- and nine-gap wings with  $\frac{2c}{3} \times \frac{b}{48}$  gaps), when the models were built only using those same validation data points.

gap dimensions. This could lead to the larger errors (between the full model in Section 5.7 and the validation data) that cannot be explained by the linear model.

## APPENDIX I

### Validation of Symmetric Wing Data Corrections

Chapter VI used asymmetric gapped wing data from the parameter sweep (Chapter V) corrected to a symmetric gapped wing, following Barlow et al. (Eqn. 6.20) [59]. To validate this method, I simulated one symmetric gapped wing directly in STAR-CCM+ at  $7^\circ$  and  $10^\circ$  angle of attack. I validated the nine gap wing with  $\frac{3c}{4} \times \frac{b}{16}$  gaps, since it had the largest change in planform area due to the gaps and could thus be the most susceptible to errors in the correction method. I followed the simulation and meshing procedures for the SI-gapped wing from Chapter III and Chapter V. Force and moment coefficients of the validation wing were normalized by symmetric planform area (Eqn. 6.19), and pitching moment coefficient was also normalized by wing chord. The symmetric wing was simulated with 3.6 million cells. The simulations reached convergence after 130 to 140 iterations.

The symmetric validation data agreed well with the corrected estimates (Fig. I.1). The lift and pitching moment coefficients agreed well. There were larger errors in drag coefficient, but this was expected: the large size of the gaps likely led to more turbulent and vortical flow, which added to the difficulty of predicting drag with RANS simulations [76]. In all, the asymmetric-to-symmetric correction method (Eqn. 6.20) was appropriate for use in Chapter VI.

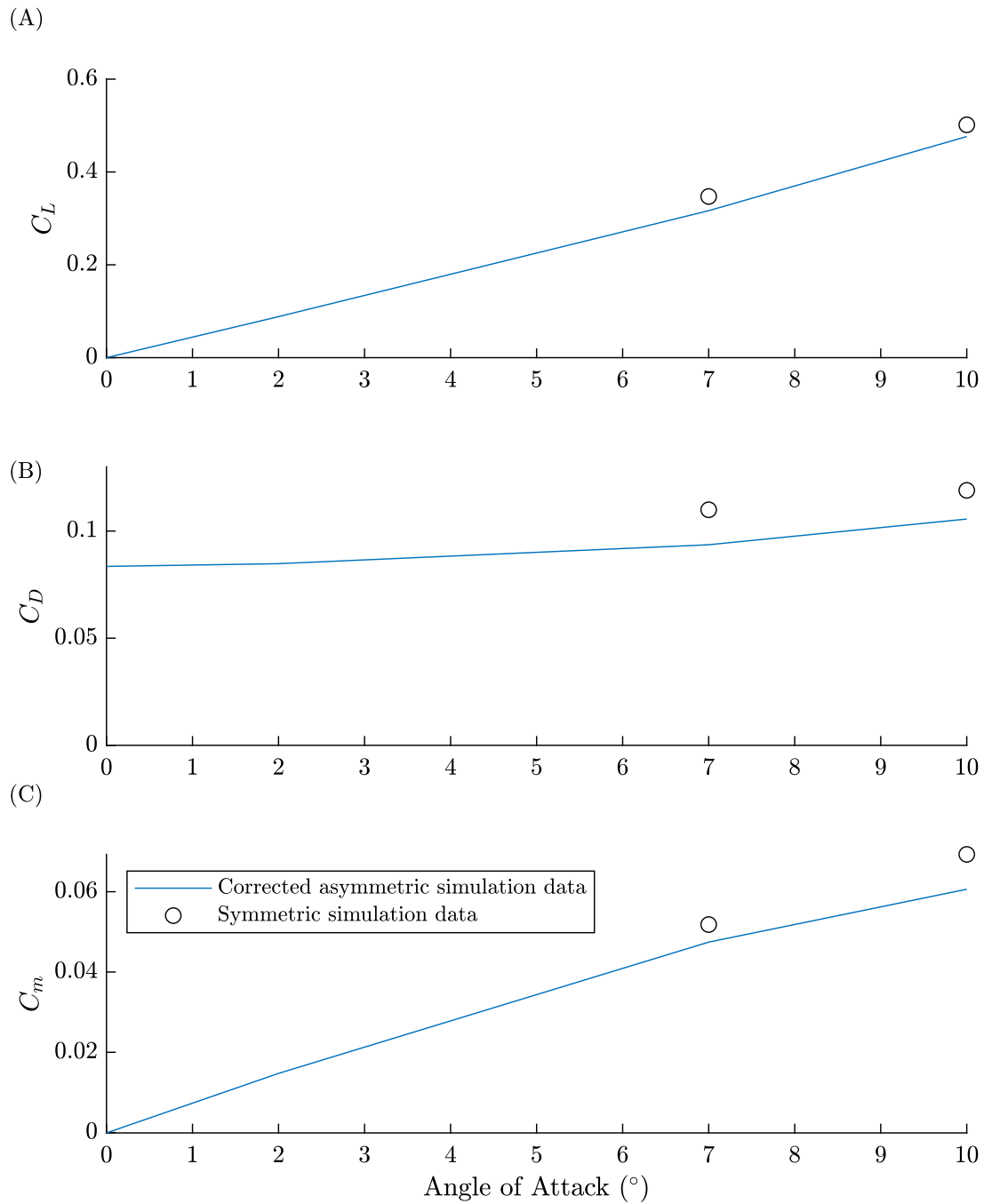


Figure I.1: The asymmetric parameter sweep data was corrected to a symmetric configuration (blue line). I validated the corrected estimates with direct CFD simulations of a symmetric gapped wing (black circles). I validated the gapped wing configuration with nine  $\frac{3c}{4} \times \frac{b}{16}$  gaps. (A) lift coefficient, (B) drag coefficient, and (C) pitching moment coefficient about the quarter-chord.

## APPENDIX J

# Modeling Aircraft Wing and Tail for Rigid Body Dynamics

### Wing aerodynamic properties

We leveraged simple analytical methods to estimate the aerodynamic properties of each wing from the CFD results. We calculated the slopes of the lift and pitching moment curves of each wing as finite differences. Due to the non-linearity of the gapped wings' pitching moment curves, we used the CFD data from  $0^\circ$  and  $2^\circ$  angle of attack as the bounds of the finite difference. Constraining our calculations to these very low angles of attack ensured that we remained within the linear regime of each wing's pitching moment curve. For example, we estimated the slope of the linear regime of the lift curve using:

$$C_{L\alpha}^{wing} = \frac{C_L^{wing}(\alpha = 2^\circ) - C_L^{wing}(\alpha = 0^\circ)}{2^\circ \frac{\pi}{180}} \quad (\text{J.1})$$

where  $\alpha$  is angle of attack (in radians) and  $C_L$  is the coefficient of lift of the wing. We calculated the slope of the pitching moment coefficient (about the quarter-chord) in the



same manner:

$$C_{M,QC\alpha}^{wing} = \frac{C_{MQC}^{wing}(2^\circ) - C_{MQC}^{wing}(0^\circ)}{2^\circ \frac{\pi}{180}} \quad (\text{J.2})$$

## Airfoil lift and drag curves for tail

To model the tail, we used a symmetric NACA 0012 airfoil. The two-dimensional lift ( $c_l$ ) and two-dimensional drag ( $c_d$ ) curves of this airfoil were determined with experimental data from Jacobs and Sherman [93]. We analytically estimated the slope of the linear regime of the lift curve from their data as:

$$a_0 = \frac{c_l(\alpha = 6^\circ) - c_l(\alpha = -3^\circ)}{9^\circ \frac{\pi}{180}} \quad (\text{J.3})$$

We visually determined that the linear range of the lift curve extended from approximately  $-3^\circ$  to  $6^\circ$  angle of attack. We used this range of angles of attack for calculating the aerodynamic properties of the tail-alone. Then, we interpolated the tail's aerodynamic properties to the appropriate  $\alpha^{tail}$  to calculate the properties of the full aircraft (Section 6.3.5.3).

## Tail inertial properties

Given the uncoupled dynamics model, we assumed the tail was symmetric about the vertical plane. We modeled the planform such that the aerodynamic center of each airfoil section fell along the spanwise axis of the tail, parallel to the  $y$ -axis (Fig. J.1).

We modelled the tail planform as two ellipses with the same major axis  $D$  and different minor axes ( $d_{LE}$  and  $d_{TE}$ ), halved then concatenated at the major axis. One half-ellipse represented the leading edge portion of the tail, and the other represented the trailing edge portion. Per our assumption on the tail span, the major axis  $D$  was  $2/3$  of the wing semi-span. By definition, the sum of the minor axes at the tail root equalled the tail root chord:

$$c_{root}^{tail} = d_{LE} + d_{TE} \quad (\text{J.4})$$

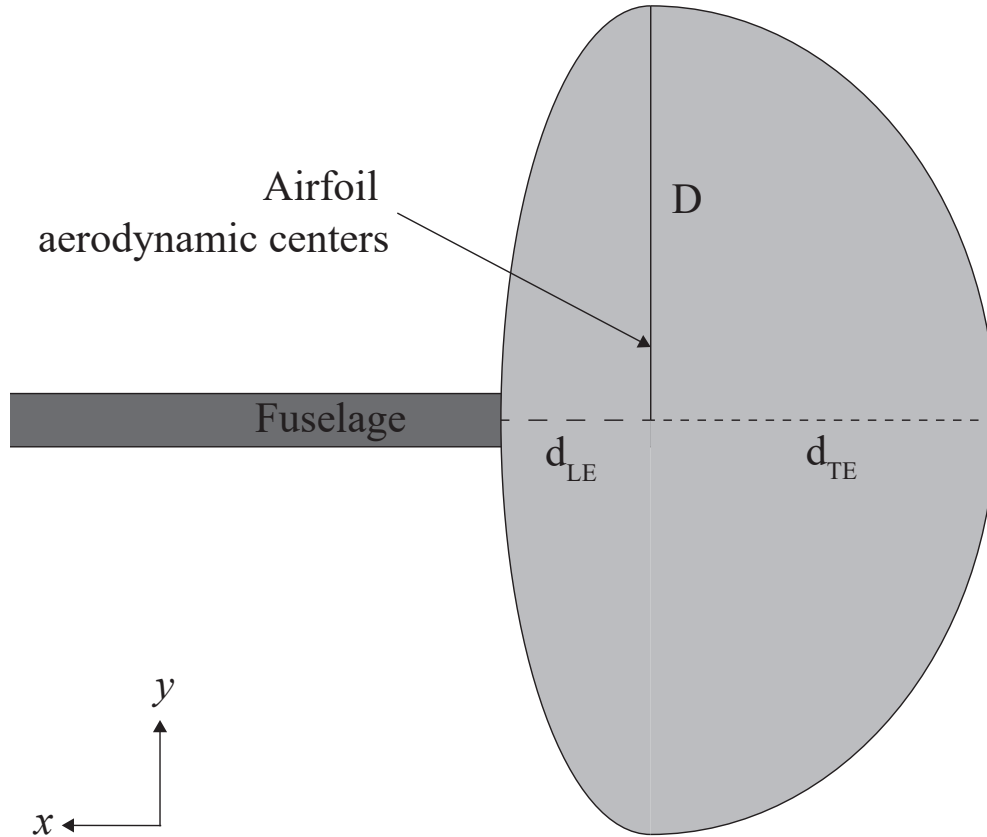


Figure J.1: The tail planform was elliptical, with different minor axes  $d_{LE}$  and  $d_{TE}$  for the leading edge and trailing edge portions, respectively. Both ellipses had a major axis  $D$ . The aerodynamic centers of the airfoil sections fell along the same spanwise axis of the tail.

where  $d_{LE}$  is the minor axis of the leading edge ellipse and  $d_{TE}$  is the minor axis of the trailing edge ellipse (both in m). We aligned the AC's of the airfoil sections, yielding:

$$d_{LE} = \frac{c_{root}^{tail}}{4} \quad (J.5)$$

We combined these relations with the desired tail aspect ratio and the tail planform area to calculate the root chord of the tail as:

$$c_{root}^{tail} = \frac{8D}{\pi AR_t} \quad (J.6)$$

Then, the planform area of the tail was calculated analytically using the formula for the area of two ellipses:

$$S^{tail} = \frac{\pi D(d_{LE} + d_{TE})}{2} \quad (J.7)$$

To calculate the inertial properties of the tail, we discretized the tail along the  $y$ -axis into 100 airfoil slices of equal span. For each slice, we calculated the chord of the airfoil at that spanwise location based on the corresponding dimensions of the planform. Then, we used MATLAB's built-in *polyshape* function to estimate the area and centroid of the slice. We estimated the volume of the slice by multiplying the airfoil area by the slice's thickness, and calculated the slice mass assuming a density of 1010 kg/m<sup>3</sup>. We summed the volumes and masses of all of the slices to estimate the total volume and mass of the tail. The location of the tail's center of gravity along its chord was then estimated according to:

$$x_{CG}^{t0} = \frac{\sum_{i=1}^{100} x_{CG,i} m_i g}{\sum_{i=1}^{100} m_i g} \quad (J.8)$$

where  $x_{CG,i}$  is the location of the  $i^{\text{th}}$  slice's center of gravity along its chord (in m),  $m_i$  is the mass of the  $i^{\text{th}}$  slice (in kg), and  $g$  is the acceleration due to gravity (in m/s<sup>2</sup>). We assumed that the tail's center of gravity was centered along its  $y$ - and  $z$ -axes due to symmetry, and fell along the  $x$ -axis.

We estimated the mass moment of inertia of the tail about its  $y$ -axis at its CG, using the formula for the moment of inertia of a three-dimensional ellipsoid about its origin and the parallel axis theorem. First, we found the moment of inertia of each half-ellipse about its origin (center) as:

$$I_y^{half} = \frac{1}{2} \frac{m^{tail}}{5} (d^2 + h^2) \quad (J.9)$$

where  $m^{tail}$  is the mass of the tail (in kg),  $d$  is the respective minor axis (in m), and  $h$  is the assumed height of the ellipsoid (in m) taken as the maximum thickness of the tail. Given

that the NACA 0012 is a 12% thick airfoil, we defined:

$$h = 0.12c_{root}^{tail} \quad (\text{J.10})$$

where  $c_{root}^{tail}$  is the root chord of the tail (in m). For simplicity, we assumed that the tail mass was equally split across the two ellipsoids. We then summed the moments of inertia of the two ellipsoids to find the tail moment of inertia at the intersection of the major and minor axes (equivalent to the quarter-chord/AC point):

$$I_y^{tail} = I_y^{LE} + I_y^{TE} \quad (\text{J.11})$$

where  $I_y^{LE}$  is the mass moment of inertia of the leading-edge ellipsoid about the  $y$ -axis at its origin and  $I_y^{TE}$  is the mass moment of inertia of the trailing-edge ellipsoid about the  $y$ -axis at its origin (both in  $\text{kg}\cdot\text{m}^3$ ). Then, we applied parallel axis theorem to find the tail moment of inertia about its center of gravity:

$$I_{y,CG}^{tail} = I_y^{tail} - m^{tail}\ell_{QC-CG}^2 \quad (\text{J.12})$$

where  $I_y^{tail}$  is the moment of inertia of the tail at the quarter-chord (in  $\text{kg}\cdot\text{m}^3$ ),  $m^{tail}$  is the mass of the tail (in kg), and  $\ell_{QC-CG}$  is the distance from the tail's quarter-chord to its center of gravity (in m).

## APPENDIX K

### Gust Responses of all Aircraft

For visual clarity and to highlight the key conclusions of this work, we only presented a subset of the modelled aircraft in Fig. 6.2 and Fig. 6.5. All of the aircraft results for the pitching moment coefficient of the wing and the gust responses are included in Fig. K.1 for completeness.

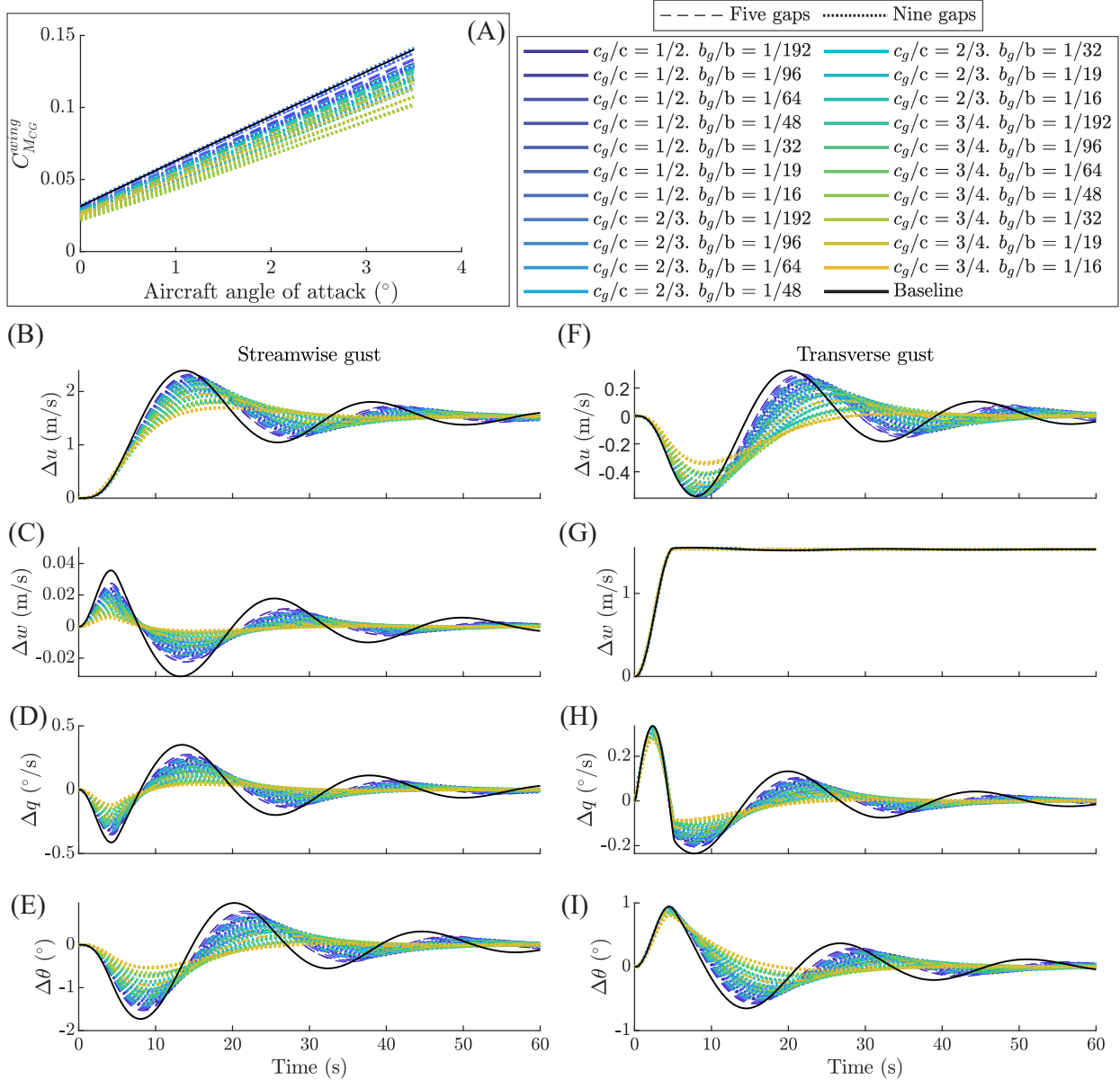


Figure K.1: (A) Gaps decreased the wing’s pitching moment coefficient about the aircraft’s center of gravity. (B) - (I) Gapped wings improved the aircraft gust response by reducing amplitude and increasing damping of the changes in state variables. We plot the changes in forward velocity, heave velocity, pitch rate, and pitch angle in response to streamwise and transverse 1–cos gusts. The solid black line is the baseline aircraft, and each color dashed or dotted line is a different gapped wing aircraft.

## APPENDIX L

### Dynamics of Aircraft With AC-Mounted Wing and Tail

For the gust alleviation analysis (Chapter VI), we modelled the aircraft with the wings and tails mounted by their respective centers of gravity (“CG-mounted aircraft”), as described in Section 6.3. However, common aerodynamic texts model aircraft with their wing and tail mounted by their aerodynamic centers [73], [88]. For completeness, we considered that configuration here (“AC-mounted aircraft”) (Fig. L.1). For the AC-mounted aircraft, we defined the distances from the nose to the aerodynamic center of the wing and tail, rather than the distance from the nose to the center of gravity (Fig. L.1).

The AC-mounted aircraft was easier to trim, because there were more aircraft configurations for which all wings trimmed (compared to the CG-mounted aircraft). The CG-mounted aircraft achieved trim for two configurations, while there were seven AC-mounted aircraft configurations that successfully trimmed:

1.  $i^{tail} = 0^\circ$ ,  $m^{fuse} = 0.15m^{base}$ ,  $AR^{tail} = 10$
2.  $i^{tail} = 0^\circ$ ,  $m^{fuse} = 0.25m^{base}$ ,  $AR^{tail} = 9$
3.  $i^{tail} = 0^\circ$ ,  $m^{fuse} = 0.25m^{base}$ ,  $AR^{tail} = 10$
4.  $i^{tail} = 0^\circ$ ,  $m^{fuse} = 0.5m^{base}$ ,  $AR^{tail} = 7$

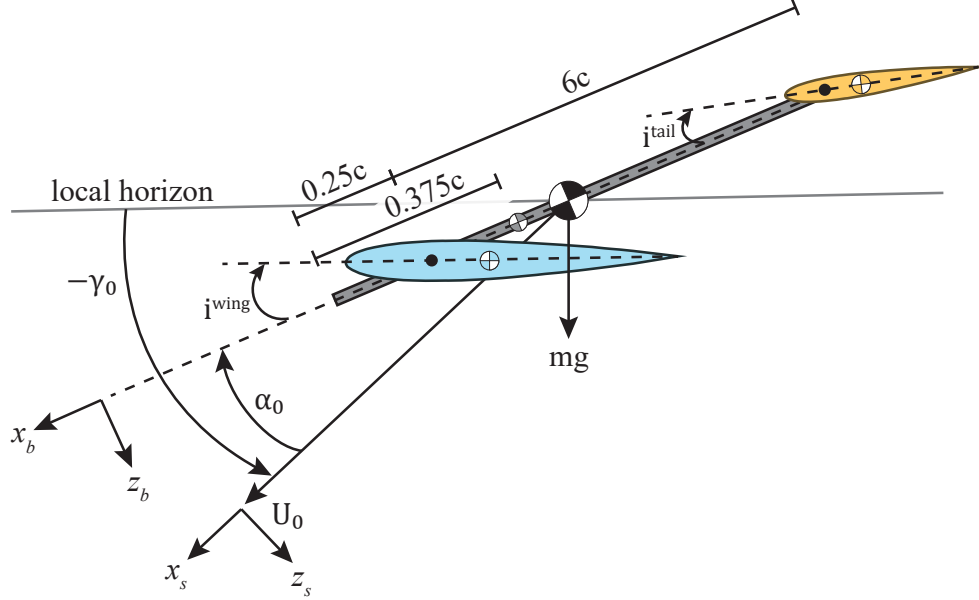


Figure L.1: The AC-mounted aircraft was defined with the wing and tail mounted by their respective aerodynamic centers, per common aerodynamic texts [73], [88].

5.  $i^{tail} = 0^\circ$ ,  $m^{fuse} = 0.5m^{base}$ ,  $AR^{tail} = 8$
6.  $i^{tail} = 0^\circ$ ,  $m^{fuse} = 0.5m^{base}$ ,  $AR^{tail} = 9$
7.  $i^{tail} = 0^\circ$ ,  $m^{fuse} = 0.5m^{base}$ ,  $AR^{tail} = 10$

Only configurations 1. and 3. resulted in aperiodic longitudinal modes. All of the other configurations resulted in the desired short period and phugoid modes. For comparison with the CG-mounted aircraft, we plotted the results of the AC-mounted aircraft described by configuration 6. Due to our definitions of the wing and tail mounting locations for the AC- and CG- mounted aircraft (Fig. L.1 and Figure 6.1), this configuration was similar—but not identical—to the configuration used for the CG-mounted aircraft. Thus, we could not directly compare this AC-aircraft configuration to the CG-aircraft configuration from Chapter VI. However, we made general statements, and addressed the relative effects of the gapped wings on the AC- and CG-mounted aircraft.

In general, the responses of the AC- and CG-mounted aircraft (Chapter VI) differed, but only modestly (Fig. L.2, L.3, L.4, and L.5). For example, the baseline CG-mounted



aircraft trimmed at  $\alpha_0 = 2.5^\circ$ ,  $\gamma_0 = -9.6^\circ$ , and  $U_0 = 44.5$  m/s (Section 6.4 and Figure 6.3). The baseline AC-mounted aircraft trimmed at  $\alpha_0 = 1.9^\circ$ ,  $\gamma_0 = -11.2^\circ$ , and  $U_0 = 48.6$  m/s (Fig. L.2). Similarly small differences between the baseline AC- and CG-mounted aircraft dynamics were also observed for the natural modes (Fig. L.3) and responses to streamwise and transverse gusts (Fig. L.4). These differences were likely due to the previously-mentioned differences in the baseline AC- and CG-mounted aircraft configurations, stemming from the geometrical differences of mounting the wing and tail by their aerodynamic centers as opposed to their centers of gravity. Furthermore, the dynamic effects of AC-mounting were typically much smaller than the impact of the gapped wings on aircraft dynamics.

The selected configuration of the AC-mounted aircraft (Fig. L.2) trimmed at lower angles of attack, higher forward velocities, and comparable glide angles to the CG-mounted aircraft from Chapter VI (Fig. 6.3). This configuration of the AC-mounted aircraft also decreased the natural frequency and the time to halve the amplitude of the phugoid mode, and typically increased the natural frequency and time to halve the amplitude of the short period mode (Fig. L.3 6.4). The AC-aircraft configuration generally had similar phugoid damping ratios and decreased short period damping ratios with respect to the CG-mounted aircraft (Fig. L.3 and 6.4). The differences between the AC- and CG-mounted aircraft gust responses are very subtle (Fig. L.4 and 6.5).

Importantly, the gapped wings had the same pattern of effects on the AC-mounted aircraft as they did on the CG-mounted aircraft: larger and more gaps had a greater impact on trim state, natural modes, and gust alleviation (Fig. L.2, L.3, and L.4). Additionally, the trim state and natural modes did not appear to be greatly affected when widening the gaps past  $\frac{b}{32}$  (Fig. L.2 and L.3). Similarly to the CG-mounted aircraft, the wing with the least and smallest gaps (five  $\frac{c}{2} \times \frac{b}{192}$  gap) had the smallest impact on trim. The wing with the most and largest gaps (nine  $\frac{3c}{4} \times \frac{b}{16}$  gaps) had the largest impact on trim. We plot just the gust responses of those AC-mounted aircraft compared to the baseline AC-mounted aircraft, for visual clarity (Fig. L.4). All aircraft responses are plotted in Figure L.5 for completeness.

In summary, mounting the wings and tails by their aerodynamic centers did not have a large bearing on the aircraft dynamics for the selected configuration. The gaps had similar effects on the AC-mounted aircraft as they did on the CG-mounted aircraft. Furthermore, gap configuration generally had a larger impact on the aircraft dynamics compared to the mounting location of the wings and tail. However, all of the AC-mounted aircraft were able to achieve trim for more tail and fuselage configurations than the CG-mounted aircraft. Thus, mounting the wings and tails by their aerodynamic centers could help overcome some of the practical design challenges discussed in Chapter VI.

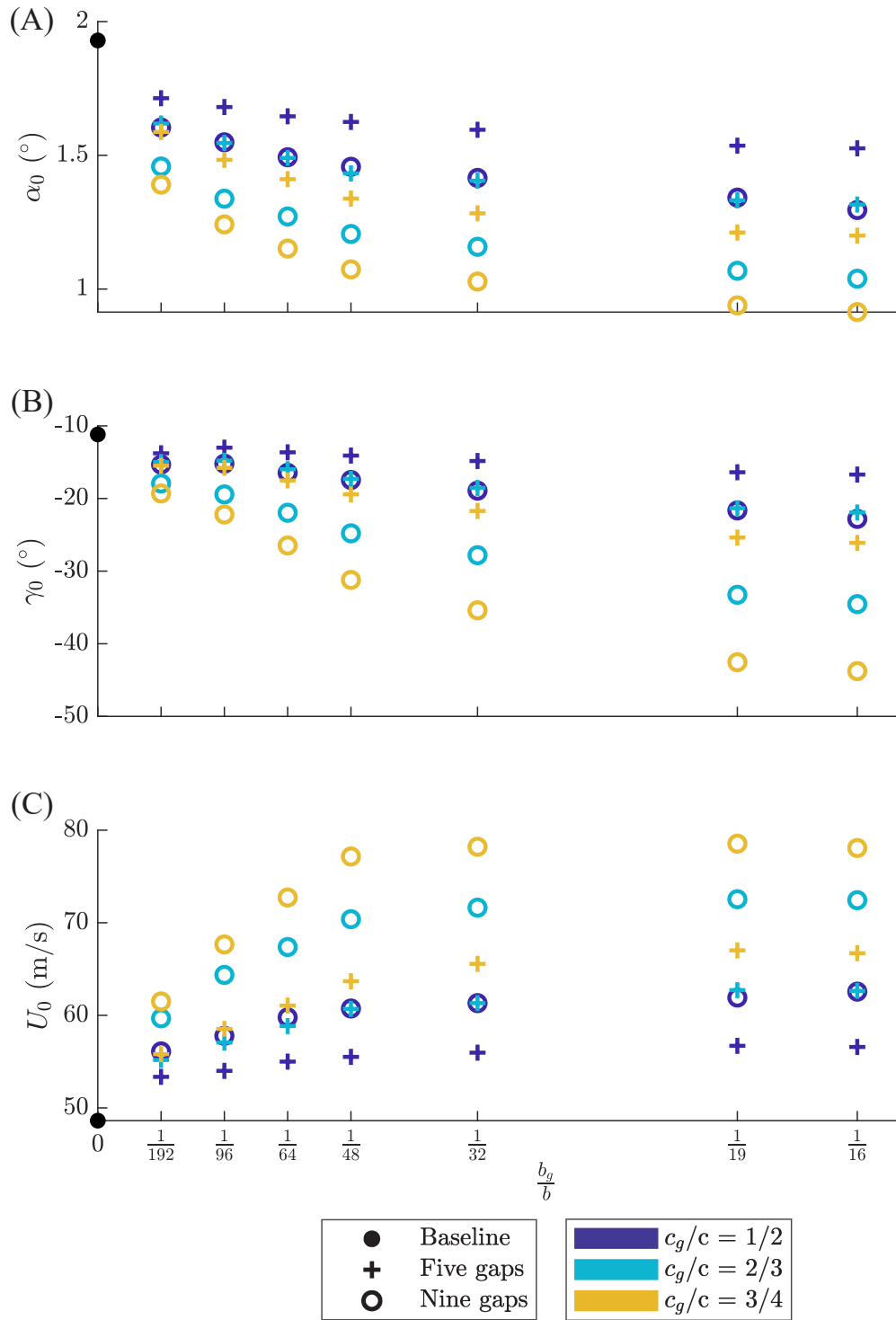


Figure L.2: This configuration of the AC-mounted aircraft trimmed at generally lower angles of attack, similar glide angles, and higher forward velocities compared to the CG-mounted aircraft from Chapter VI. The gapped wings exhibited the same effects on trim state as they did for the CG-mounted aircraft.

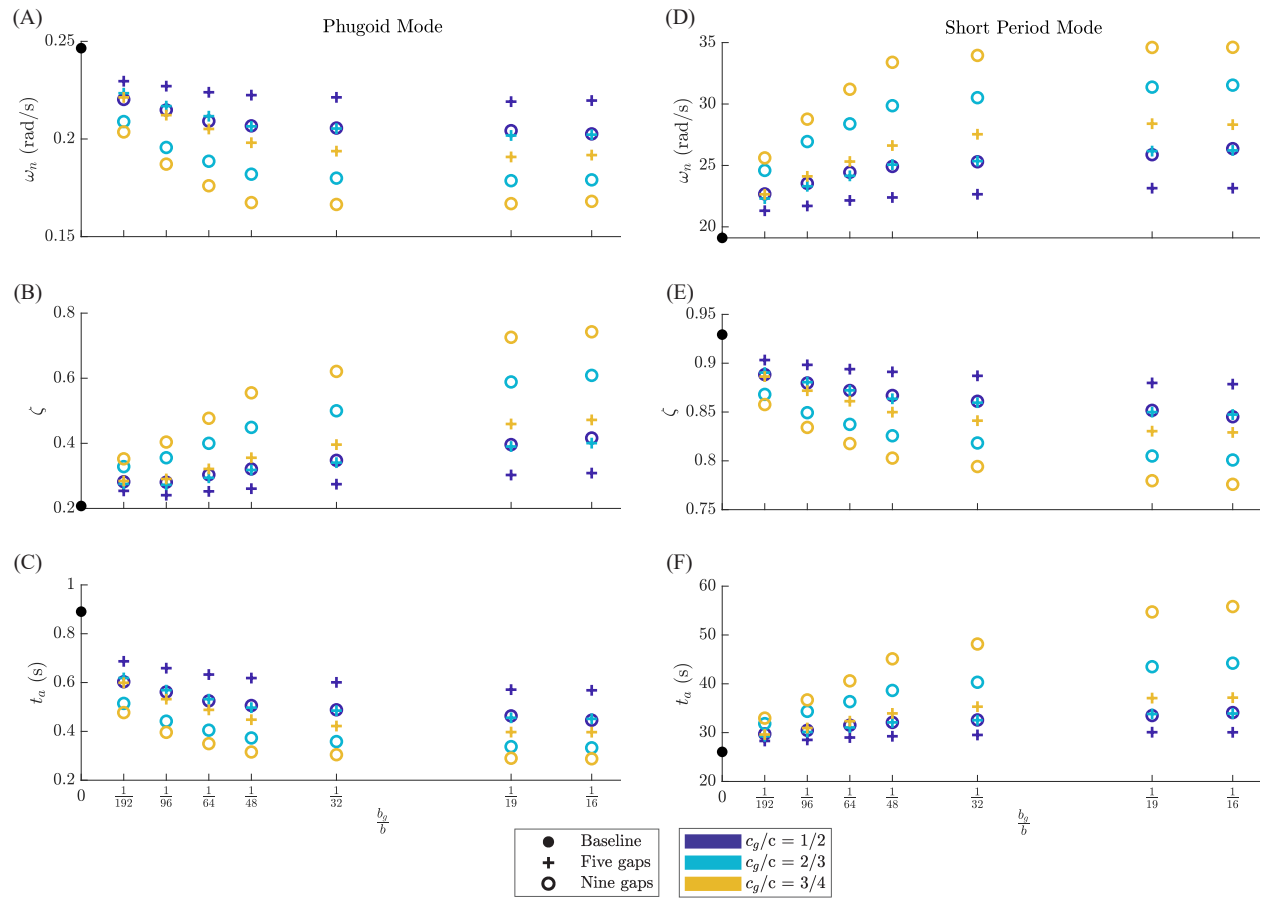


Figure L.3: AC-mounting the wings and tail had modest effects on the natural modes of the aircraft. Notably, the gapped wings exhibited the same pattern of effects on the natural modes as they did for the CG-mounted aircraft.

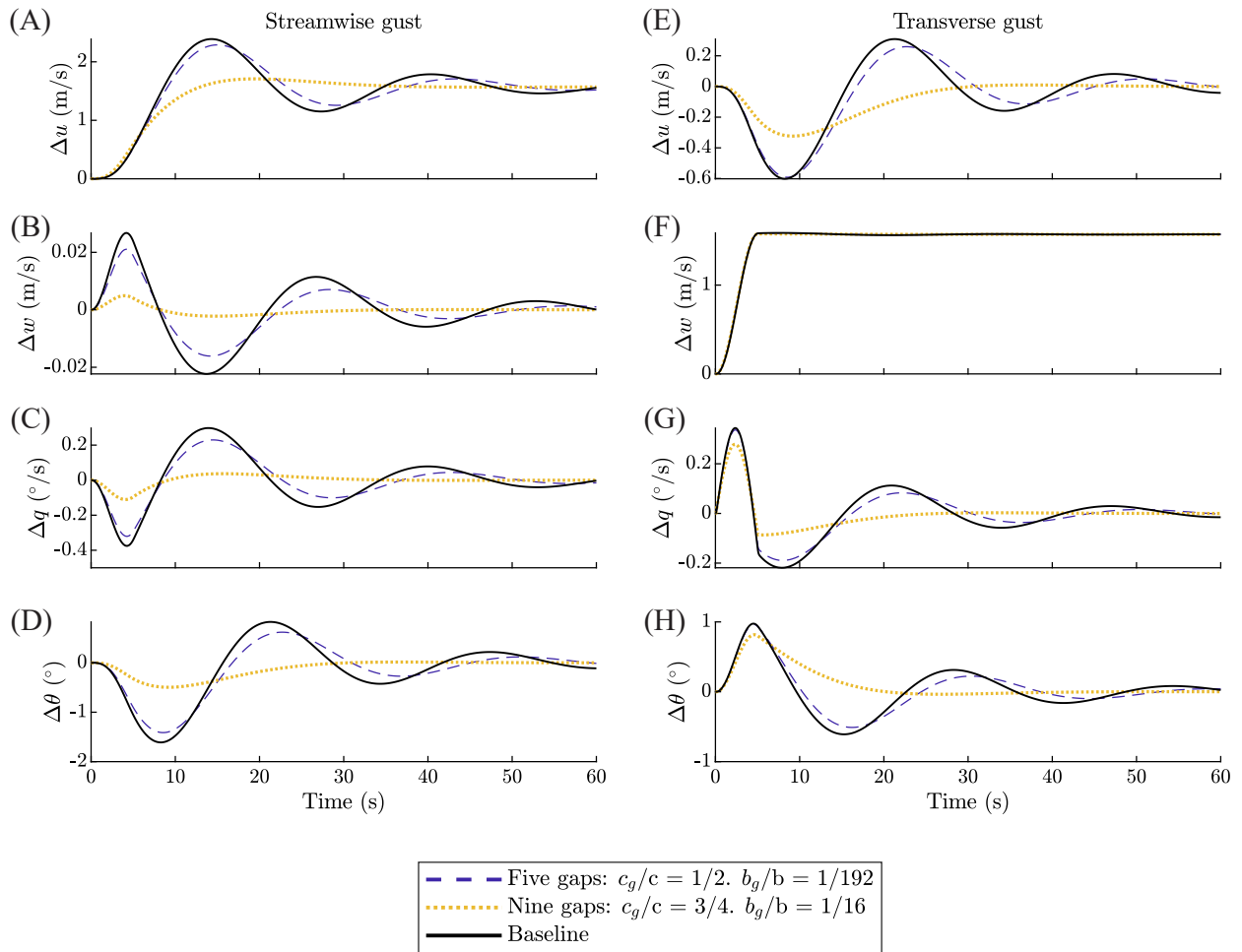


Figure L.4: The gust responses of the AC-mounted aircraft were very similar to those of the CG-mounted aircraft (Chapter VI), and the gapped wings had the same impacts on responses of the AC-mounted aircraft.

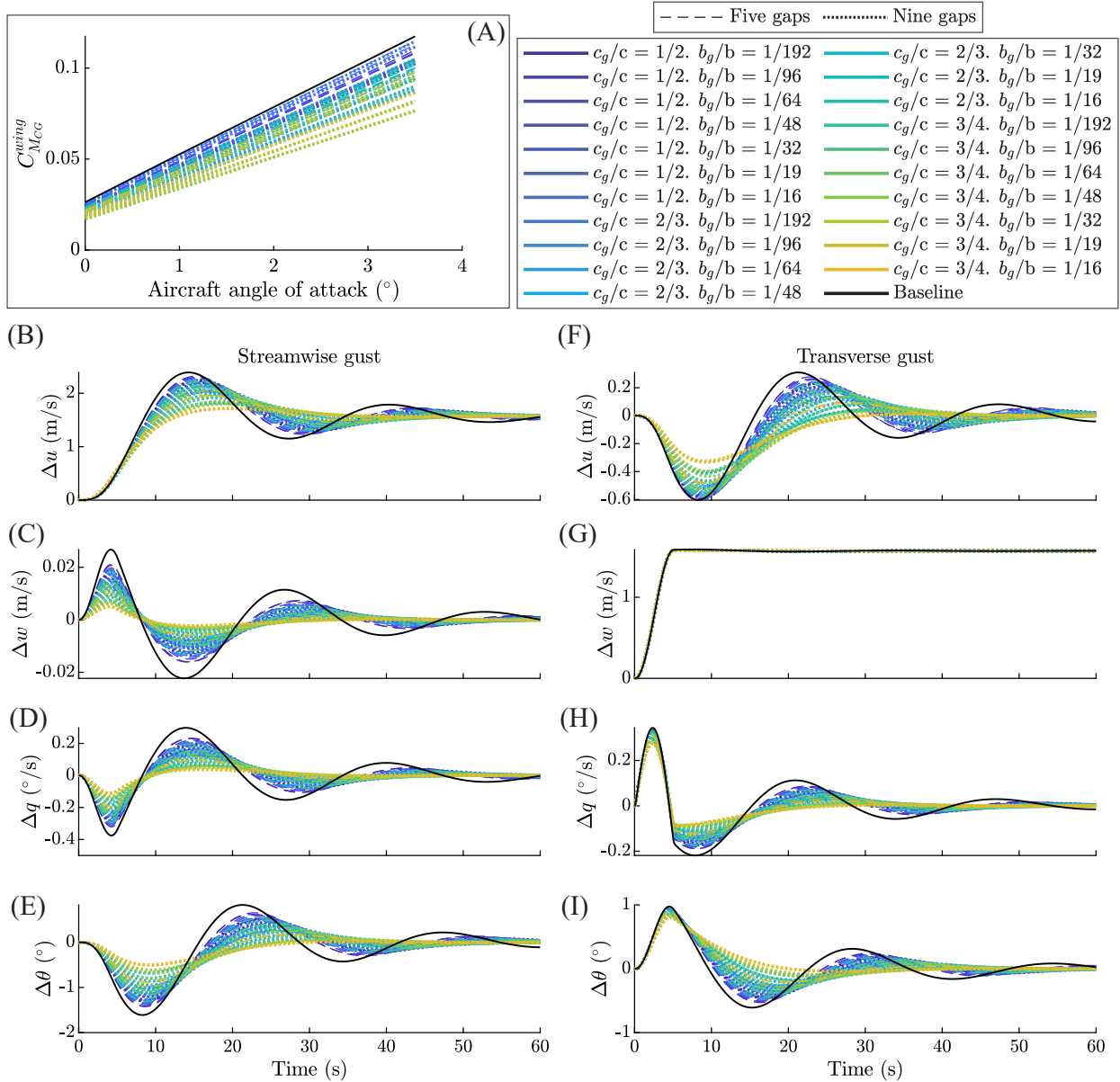


Figure L.5: Gapped wings had similar effects on the gust responses of the AC-mounted aircraft as they did on the CG-mounted aircraft (Chapter VI). (A) Gaps decreased the wing’s pitching moment coefficient about the aircraft’s center of gravity. (B) - (I) Gapped wings improved the aircraft gust response by reducing amplitude and increasing damping of the changes in state variables. We plot the changes in forward velocity, heave velocity, pitch rate, and pitch angle in response to streamwise and transverse 1–cos gusts. The solid black line is the baseline aircraft, and each color dashed or dotted line is a different gapped wing aircraft.

## BIBLIOGRAPHY

## BIBLIOGRAPHY

- [1] J. C. for Guides in Metrology, “Evaluation of measurement data - Guide to the expression of uncertainty in measurement,” JCGM, Technical Report JCGM100:2008, Sep. 2008, p. 134.
- [2] H. S. Johnson and J. R. Hagerman, “Wind-tunnel Investigation at Low Speed of the Lateral Control Characteristics of an Unswept Untapered Semi-span Wing of Aspect Ratio 3.13 Equipped with Various 25-percent-chord Plain Ailerons,” NACA Langley Aeronautical Laboratory, Langley Memorial Aeronautical Laboratory, Technical Note NACA-TN-2199, Oct. 1950.
- [3] C. Harvey, L. L. Gamble, C. R. Bolander, D. F. Hunsaker, J. J. Joo, and D. J. Inman, “A review of avian-inspired morphing for UAV flight control,” *Progress in Aerospace Sciences*, vol. 132, 2022. DOI: 10.1016/j.paerosci.2022.100825.
- [4] A. M. Pankonien and D. J. Inman, “Aerodynamic Performance of a Spanwise Morphing Trailing Edge Concept,” in *25th International Conference on Adaptive Structures and Technologies*, The Hague, The Netherlands, Oct. 2014.
- [5] A. Pankonien and D. J. Inman, “Experimental testing of spanwise morphing trailing edge concept,” in *Active and Passive Smart Structures and Integrated Systems 2013*, vol. 8688, San Diego, CA: SPIE, Apr. 2013. DOI: 10.1117/12.2009400.
- [6] A. M. Pankonien, C. T. Faria, and D. J. Inman, “Synergistic smart morphing aileron: Experimental quasi-static performance characterization,” *Journal of Intelligent Material Systems and Structures*, vol. 26, no. 10, pp. 1179–1190, Jun. 2014, Publisher: SAGE Publications Ltd STM. DOI: 10.1177/1045389X14538530.
- [7] M. Di Luca, S. Mintchev, G. Heitz, F. Noca, and D. Floreano, “Bioinspired morphing wings for extended flight envelope and roll control of small drones,” *Interface Focus*, vol. 7, no. 1, Feb. 2017, Publisher: Royal Society. DOI: 10.1098/rsfs.2016.0092.
- [8] K. P. T. Haughn, L. L. Gamble, and D. J. Inman, “Horizontal Planform Morphing Tail for an Avian Inspired UAV Using Shape Memory Alloys,” in *SMASIS2018*, Volume 2: Mechanics, Behavior of Active Materials; Structural Health Monitoring; Bioinspired Smart Materials, and Systems; Energy Harvesting; Emerging Technologies, Sep. 2018. DOI: 10.1115/SMASIS2018-7986.
- [9] P. C. Withers, “The aerodynamic performance of the wing in Red-Shouldered Hawk *Buteo lineatus* and a possible aeroelastic role of wing-tip slots,” *Ibis*, vol. 123, no. 1, pp. 239–247, Apr. 1981. DOI: 10.1111/j.1474-919X.1981.tb00933.x.



- [10] D. Humphries and P. Driver, “Protean defence by prey animals,” *Oecologia*, vol. 5, no. 4, pp. 285–302, 1970. DOI: 10.1007/BF00815496.
- [11] R. Gillmor and N. G. Blurton Jones, “A goose-watching visit to northern Iceland,” *Wildfowl*, vol. 10, no. 10, pp. 114–117, 1959.
- [12] F. H. Heppner and C. Willard, “Inverted Flight in Canada Geese,” *The Condor*, vol. 77, no. 4, pp. 478–480, 1975, Publisher: American Ornithological Society. DOI: 10.2307/1366095.
- [13] W. Brotherston, “The numbers and behaviour of geese in the Lothians and Berwickshire,” *Wildfowl Trust Annual Report*, vol. 15, no. 15, pp. 57–70, 1964, ISSN: 2052-6458. (visited on 01/21/2021).
- [14] P. Sackl, “Form and function of aerial courtship displays in Black Storks *Ciconia nigra*,” *Acrocephalus*, vol. 21, no. 102/103, pp. 223–229, 2000.
- [15] G. N. Rysgaard, “When Geese Fly North,” *Bios*, vol. 13, no. 3, pp. 175–178, 1942.
- [16] I. Newton, V. M. Thom, and W. Brotherston, “Behaviour and distribution of wild geese in south-east Scotland,” *Wildfowl*, vol. 24, pp. 111–121, 1973.
- [17] P. Blacker, *Canada Geese Whiffing*, Oct. 2011. [Online]. Available: <https://www.youtube.com/watch?v=H46h3ee7TDA>.
- [18] C. Böhmer, O. Plateau, R. Cornette, and A. Abourachid, “Correlated evolution of neck length and leg length in birds,” *Royal Society Open Science*, vol. 6, no. 5, May 2019. DOI: 10.1098/rsos.181588.
- [19] A. E. Pete, D. Kress, M. A. Dimitrov, and D. Lentink, “The role of passive avian head stabilization in flapping flight,” *Journal of The Royal Society Interface*, vol. 12, no. 110, Sep. 2015. DOI: 10.1098/rsif.2015.0508.
- [20] R. H. J. Brown, “The Flight of Birds : II. Wing Function in Relation to Flight Speed,” *Journal of Experimental Biology*, vol. 30, no. 1, pp. 90–103, Mar. 1953. DOI: 10.1242/jeb.30.1.90. (visited on 02/13/2023).
- [21] R. H. J. Brown, “The flight of birds,” *Biological Reviews*, vol. 38, no. 4, pp. 460–489, Nov. 1963. DOI: 10.1111/j.1469-185X.1963.tb00790.x.
- [22] T. L. Hedrick, J. R. Usherwood, and A. A. Biewener, “Wing inertia and whole-body acceleration: An analysis of instantaneous aerodynamic force production in cockatiels (*Nymphicus hollandicus*) flying across a range of speeds,” *Journal of Experimental Biology*, vol. 207, no. 10, pp. 1689–1702, Apr. 2004. DOI: 10.1242/jeb.00933.
- [23] U. M. Norberg, “Hovering flight in the pied flycatcher (*Ficedula hypoleuca*),” in *Swimming and Flying in Nature*, vol. 2, California Institute of Technology: Springer Sciences+Business Media, LLC, Jul. 1974, pp. 869–881. DOI: 10.1007/978-1-4757-1326-8.
- [24] W. Müller and G. Patone, “Air transmissivity of feathers,” *The Journal of Experimental Biology*, vol. 201, no. 18, p. 2591, Sep. 1998.
- [25] J. F. Marchman, “Aerodynamics of Inverted Leading-Edge Flaps on Delta Wings,” *Journal of Aircraft*, vol. 18, no. 12, pp. 1051–1056, Dec. 1981. DOI: 10.2514/3.57599.

- [26] J. Correia, L. S. Roberts, M. V. Finnis, and K. Knowles, “Scale effects on a single-element inverted wing in ground effect,” *The Aeronautical Journal (1968)*, vol. 118, no. 1205, pp. 797–809, 2014. DOI: 10.1017/S0001924000009544.
- [27] P. J. Butler, “The physiological basis of bird flight,” *Philosophical Transactions of the Royal Society B: Biological Sciences*, vol. 371, no. 1704, p. 20150384, Sep. 2016. DOI: 10.1098/rstb.2015.0384.
- [28] J. M. V. Rayner, “A vortex theory of animal flight. Part 2. The forward flight of birds,” *Journal of Fluid Mechanics*, vol. 91, no. 4, pp. 731–763, 1979. DOI: 10.1017/S0022112079000422.
- [29] H. V. Abeywickrama, B. A. Jayawickrama, Y. He, and E. Dutkiewicz, “Empirical Power Consumption Model for UAVs,” in *2018 IEEE 88th Vehicular Technology Conference (VTC-Fall)*, Aug. 2018, pp. 1–5. DOI: 10.1109/VTCFall.2018.8690666.
- [30] M. N. Boukoberine, Z. Zhou, and M. Benbouzid, “A critical review on unmanned aerial vehicles power supply and energy management: Solutions, strategies, and prospects,” *Applied Energy*, vol. 255, Dec. 2019. DOI: 10.1016/j.apenergy.2019.113823.
- [31] J. G. Kang, J. Y. Kwon, and M. S. Lee, “A Dynamic Power Consumption Estimation Method of Electro-mechanical Actuator for UAV Modeling and Simulation,” *International Journal of Aeronautical and Space Sciences*, vol. 23, no. 1, pp. 233–239, Feb. 2022. DOI: 10.1007/s42405-021-00417-4.
- [32] I. Chakraborty, D. Jackson, D. R. Trawick, and D. Mavris, “Development of a sizing and analysis tool for electrohydrostatic and electromechanical actuators for the more electric aircraft,” in *2013 Aviation Technology, Integration, and Operations Conference*, ser. AIAA AVIATION Forum, Los Angeles, CA, USA: American Institute of Aeronautics and Astronautics, Aug. 2013. DOI: 10.2514/6.2013-4282.
- [33] M. H. Sadraey, *Aircraft Design: A Systems Engineering Approach*. John Wiley & Sons, Inc., 2013, ISBN: 978-1-119-95340-1.
- [34] S. Howell, “A basic understanding of moult: What, why, when and how much?” *Dutch Birding*, vol. 23, no. 3, pp. 131–135, 2001.
- [35] A. Hedenström and S. Sunada, “On the aerodynamics of moult gaps in birds,” *Journal of Experimental Biology*, vol. 202, no. 1, pp. 67–76, Jan. 1999.
- [36] E. Williams and J. Swaddle, “Moult, flight performance and wingbeat kinematics during take-off in European starlings *Sturnus vulgaris*,” *Journal of Avian Biology*, vol. 34, no. 4, Nov. 2003. DOI: 10.1111/j.0908-8857.2003.02964.x.
- [37] J. Lind, “Escape flight in moulting Tree Sparrows (*Passer montanus*),” *Functional Ecology*, vol. 15, no. 1, pp. 29–35, Dec. 2001. DOI: 10.1046/j.1365-2435.2001.00497.x.
- [38] Y. Achache, N. Sapir, and Y. Elimelech, “Hovering hummingbird wing aerodynamics during the annual cycle. II. Implications of wing feather moult,” *Royal Society Open Science*, vol. 5, no. 2, Feb. 2018. DOI: 10.1098/rsos.171766.

- [39] Y. Kiat, “Divergent primary moult - A rare moult sequence among Western Palearctic passerines,” *PLOS ONE*, vol. 12, no. 10, Oct. 2017. DOI: 10.1371/journal.pone.0187282.
- [40] *Red-wattled Lapwing: Moulting of primary flight feathers*, Jun. 2010. [Online]. Available: <https://besgroup.org/2010/06/15/red-wattled-lapwing-moulting-of-primary-flight-feathers/>.
- [41] J. P. Swaddle and M. S. Witter, “The effects of molt on the flight performance, body mass, and behavior of European starlings (*Sturnus vulgaris*): An experimental approach,” *Canadian Journal of Zoology*, vol. 75, no. 7, pp. 1135–1146, Jul. 1997. DOI: 10.1139/z97-136.
- [42] J. D. DeLaurier and J. M. Harris, “A study of mechanical flapping-wing flight,” *The Aeronautical Journal*, vol. 97, no. 968, pp. 277–286, Oct. 1993.
- [43] L. B. Scherer, C. A. Martin, B. P. Sanders, *et al.*, “DARPA/AFRL Smart Wing Phase 2 wind tunnel test results,” en, in *Smart Structures and Materials 2002: Industrial and Commercial Applications of Smart Structures Technologies*, vol. 4698, San Diego, CA: SPIE, Jul. 2002. DOI: 10.1117/12.475104.
- [44] M. KleinHeerenbrink and A. Hedenström, “Wake analysis of drag components in gliding flight of a jackdaw (*Corvus monedula*) during moult,” *Interface Focus*, vol. 7, no. 1, Feb. 2017. DOI: 10.1098/rsfs.2016.0081.
- [45] V. A. Tucker, “The Effect of Molting on the Gliding Performance of a Harris’ Hawk (*Parabuteo unicinctus*),” *The Auk*, vol. 108, no. 1, pp. 108–113, Jan. 1991. DOI: 10.1093/auk/108.1.108.
- [46] J. Nedić and J. C. Vassilicos, “Vortex Shedding and Aerodynamic Performance of Airfoil with Multiscale Trailing-Edge Modifications,” *AIAA Journal*, vol. 53, no. 11, pp. 3240–3250, Sep. 2015. DOI: 10.2514/1.J053834.
- [47] H. Davies and F. N. Kirk, “A Resume of Aerodynamic Data on Air Brakes,” National Aeronautical Establishment Library, London, Reports and Memoranda Reports and Memoranda No. 2614, Jun. 1942.
- [48] P. E. Purser and T. R. Turner, “Wind-tunnel investigation of perforated split flaps for use as dive brakes on a rectangular NACA 23012 airfoil,” NACA, Washington, Wartime Report, Jul. 1941.
- [49] E. V. Laitone and J. L. Summers, “An additional investigation of the high-speed lateral-control characteristics of spoilers,” NACA, Washington, Wartime Report ACR 5D28, Jun. 1945.
- [50] Z. Ni, M. Dhanak, and T.-c. Su, “Improved performance of a slotted blade using a novel slot design,” *Journal of Wind Engineering and Industrial Aerodynamics*, vol. 189, pp. 34–44, Jun. 2019, ISSN: 0167-6105. DOI: 10.1016/j.jweia.2019.03.018.

- [51] D. Koss, M. Steinbuch, and M. Shepshelovich, “Design and experimental evaluation of a high-lift, mild-stall airfoil,” in *12th Applied Aerodynamics Conference*, ser. Fluid Dynamics and Co-located Conferences, Colorado Springs, CO, USA: American Institute of Aeronautics and Astronautics, Jun. 1994, pp. 480–488. DOI: 10.2514/6.1994-1867.
- [52] R. Belamadi, A. Djemili, A. Ilinca, and R. Mdouki, “Aerodynamic performance analysis of slotted airfoils for application to wind turbine blades,” *Journal of Wind Engineering and Industrial Aerodynamics*, vol. 151, pp. 79–99, Apr. 2016, ISSN: 0167-6105. DOI: 10.1016/j.jweia.2016.01.011.
- [53] F. E. Weick and J. A. Shortal, “The effect of multiple fixed slots and a trailing-edge flap on the lift and drag of a Clark Y airfoil,” NACA, Langley Memorial Aeronautical Laboratory, Technical Report NACA-TR-427, Jan. 1993.
- [54] J. Kearney and A. Glezer, “Aero-Effected Flight Control Using Distributed Active Bleed,” in *41st AIAA Fluid Dynamics Conference and Exhibit*, ser. Fluid Dynamics and Co-located Conferences, American Institute of Aeronautics and Astronautics, Jun. 2011. DOI: 10.2514/6.2011-3099. (visited on 03/03/2023).
- [55] J. Kearney and A. Glezer, “Aerodynamic Control Using Distributed Bleed,” in *6th AIAA Flow Control Conference*, ser. Fluid Dynamics and Co-located Conferences, American Institute of Aeronautics and Astronautics, Jun. 2012. DOI: 10.2514/6.2012-3246. (visited on 03/03/2023).
- [56] J. D. Anderson Jr., *Fundamentals of Aerodynamics* (McGraw-Hill Series in Aeronautical and Aerospace Engineering), 4th ed. New York, NY: McGraw-Hill, 2007, ISBN: 0-07-125408-0.
- [57] J. Fischel and J. R. Hagerman, “Effect of aspect ratio and sweepback on the low-speed lateral control characteristics of untapered low-aspect-ratio wings equipped with retractable ailerons,” NACA, Langley Memorial Aeronautical Laboratory, Technical Note NACA-TN-2347, May 1951.
- [58] C. Harvey, V. B. Baliga, C. D. Goates, D. F. Hunsaker, and D. J. Inman, “Gull-inspired joint-driven wing morphing allows adaptive longitudinal flight control,” *Journal of The Royal Society Interface*, vol. 18, no. 179, Jun. 2021. DOI: 10.1098/rsif.2021.0132.
- [59] J. B. Barlow, W. H. Rae Jr., and A. Pope, *Low-Speed Wind Tunnel Testing* (Wiley-Interscience), 3rd ed. New York, NY: John Wiley & Sons, Inc., 1999, ISBN: 0-471-55774-9.
- [60] C. Harvey and D. J. Inman, “Aerodynamic efficiency of gliding birds vs. comparable UAVs: A review,” *Bioinspiration & Biomimetics*, vol. 16, 3 2021. DOI: 10.1088/1748-3190/abc86a.
- [61] M. Tasdemir, V. Babat, and U. Yerlesen, “Effect of friction and wear parameters on acrylonitrile butadiene styrene/aluminum-boron carbide-glass spheres polymer composites,” *Mechanika*, vol. 20, no. 4, pp. 407–413, 2014. DOI: 10.5755/j01.mech.20.4.7883.

- [62] *Acrylonitrile Butadiene Styrene (ABS) Typical Properties Generic ABS*, Commercial, 2021. [Online]. Available: <https://plastics.ulprospector.com/generics/1/c/t/acrylonitrile-butadiene-styrene-abs-properties-processing> (visited on 02/23/2021).
- [63] X.-D. Sun, “Active Control of Aircraft Using Spoilers,” Master’s Dissertation, Imperial College of Science, Technology and Medicine, London, Mar. 1993.
- [64] D. Scholz, “Development of a Cae Tool for the Design of Flight Control and Hydraulic Systems,” *Institution of Mechanical Engineers: Avionic Systems, Design and Software*, pp. 1–22, Nov. 1995.
- [65] *Airfoil Tools*. [Online]. Available: <http://airfoiltools.com/compare/index> (visited on 02/09/2022).
- [66] B. H. Carmichael, “Low Reynolds number airfoil survey, volume 1,” Low Energy Transportation Systems, Capistrano Beach, CA, NASA Contractor Report NASA-CR-165803-VOL-1, Nov. 1981.
- [67] P. R. Thomas, S. Bullock, U. Bhandari, and T. S. Richardson, “Fixed-wing approach techniques for complex environments,” *The Aeronautical Journal*, vol. 119, no. 1218, pp. 999–1016, Aug. 2015. DOI: 10.1017/S0001924000004292.
- [68] A. C. Carruthers, A. L. R. Thomas, S. M. Walker, and G. K. Taylor, “Mechanics and aerodynamics of perching manoeuvres in a large bird of prey,” *The Aeronautical Journal (1968)*, vol. 114, no. 1161, pp. 673–680, 2010. DOI: 10.1017/S0001924000004152.
- [69] S. John, A. I. Rasheed, and V. K. Reddy, “ASIC implementation of fuzzy-PID controller for aircraft roll control,” in *2013 International conference on Circuits, Controls and Communications (CCUBE)*, Dec. 2013, pp. 1–6. DOI: 10.1109/CCUBE.2013.6718551.
- [70] Z. Deng, L. Wu, and Y. You, “Modeling and Design of an Aircraft-Mode Controller for a Fixed-Wing VTOL UAV,” *Mathematical Problems in Engineering*, vol. 2021, J. Chen, Ed., Sep. 2021. DOI: 10.1155/2021/7902134.
- [71] P. Catalano and R. Tognaccini, “Turbulence Modeling for Low-Reynolds-Number Flows,” *AIAA Journal*, vol. 48, no. 8, pp. 1673–1685, Aug. 2010. DOI: 10.2514/1.J050067.
- [72] J. Morgado, R. Vizinho, M. Silvestre, and J. Páscoa, “XFOIL vs CFD performance predictions for high lift low Reynolds number airfoils,” *Aerospace Science and Technology*, vol. 52, pp. 207–214, May 2016. DOI: 10.1016/j.ast.2016.02.031.
- [73] B. N. Pamadi, *Performance, Stability, Dynamics, and Control of Airplanes* (AIAA Education Series), 2nd ed. American Institute of Aeronautics and Astronautics, 2000.
- [74] E. N. Tinoco, O. P. Brodersen, S. Keye, *et al.*, “Summary Data from the Sixth AIAA CFD Drag Prediction Workshop: CRM Cases,” *Journal of Aircraft*, vol. 55, no. 4, pp. 1352–1379, Jul. 2018. DOI: 10.2514/1.C034409.
- [75] K. R. Laffin, S. M. Klausmeyer, T. Zickuhr, *et al.*, “Data Summary from Second AIAA Computational Fluid Dynamics Drag Prediction Workshop,” *Journal of Aircraft*, vol. 42, no. 5, pp. 1165–1178, Sep. 2005. DOI: 10.2514/1.10771.

- [76] C. L. Rumsey, J. P. Slotnick, and A. J. Sclafani, “Overview and Summary of the Third AIAA High Lift Prediction Workshop,” *Journal of Aircraft*, vol. 56, no. 2, pp. 621–644, Mar. 2019. DOI: 10.2514/1.C034940.
- [77] X. Liu, H. Kamliya Jawahar, M. Azarpeyvand, and R. Theunissen, “Wake Development of Airfoils with Serrated Trailing Edges,” in *22nd AIAA/CEAS Aeroacoustics Conference*, ser. Aeroacoustics Conferences, Lyon, France: American Institute of Aeronautics and Astronautics, May 2016. DOI: 10.2514/6.2016-2817.
- [78] X. Liu, M. Azarpeyvand, and R. Theunissen, “Aerodynamic and Aeroacoustic Performance of Serrated Airfoils,” in *21st AIAA/CEAS Aeroacoustics Conference*, ser. AIAA AVIATION Forum, Dallas, TX: American Institute of Aeronautics and Astronautics, Jun. 2015. DOI: 10.2514/6.2015-2201.
- [79] T. M. Farabee and M. J. Casarella, “Measurements of Fluctuating Wall Pressure for Separated/Reattached Boundary Layer Flows,” *Journal of Vibration, Acoustics, Stress, and Reliability in Design*, vol. 108, no. 3, pp. 301–307, Jul. 1986, ISSN: 0739-3717. DOI: 10.1115/1.3269343.
- [80] H. Le, P. Moin, and J. Kim, “Direct numerical simulation of turbulent flow over a backward-facing step,” *Journal of Fluid Mechanics*, vol. 330, pp. 349–374, 1997, ISSN: 0022-1120. DOI: 10.1017/S0022112096003941.
- [81] T. C. Wilson, R. KC, N. A. Lucido, *et al.*, “Computational Investigation of the Conformal Vortex Generator,” in *AIAA Scitech 2019 Forum*, ser. AIAA SciTech Forum, American Institute of Aeronautics and Astronautics, Jan. 2019. DOI: 10.2514/6.2019-2138.
- [82] L.-s. Cao, F.-l. Huang, C. Liu, and D.-c. Wan, “Vortical structures and wakes of a sphere in homogeneous and density stratified fluid,” *Journal of Hydrodynamics*, vol. 33, no. 2, pp. 207–215, Apr. 2021, ISSN: 1878-0342. DOI: 10.1007/s42241-021-0032-x.
- [83] N. Yilmaz, B. Aktas, M. Atlar, P. A. Fitzsimmons, and M. Felli, “An experimental and numerical investigation of propeller-rudder-hull interaction in the presence of tip vortex cavitation (TVC),” *Ocean Engineering*, vol. 216, p. 108024, Nov. 2020, ISSN: 0029-8018. DOI: 10.1016/j.oceaneng.2020.108024.
- [84] A. V. Arena and T. J. Mueller, “Laminar Separation, Transition, and Turbulent Reattachment near the Leading Edge of Airfoils,” *AIAA Journal*, vol. 18, no. 7, pp. 747–753, Jul. 1980. DOI: 10.2514/3.50815.
- [85] B. Sanders, F. E. Eastep, and E. Forster, “Aerodynamic and Aeroelastic Characteristics of Wings with Conformal Control Surfaces for Morphing Aircraft,” *Journal of Aircraft*, vol. 40, no. 1, pp. 94–99, Jan. 2003. DOI: 10.2514/2.3062.
- [86] A. J. Fairbanks, “Distribution of Pressure Over Model of the Upper Wing and Aileron of a Fokker D-VII Airplane,” NACA, Langley Memorial Aeronautical Laboratory, Technical Report NACA-TR-254, 1927.

- [87] R. Botez, A. Koreanschi, O. Gabor, *et al.*, “Numerical and experimental transition results evaluation for a morphing wing and aileron system,” *The Aeronautical Journal*, vol. 122, no. 1251, pp. 747–784, 2018. DOI: 10.1017/aer.2018.15.
- [88] R. C. Nelson, *Flight Stability and Automatic Control*, 2nd ed. New York: McGraw-Hill, 1989, ISBN: 0-07-046218-6.
- [89] C. Harvey and D. J. Inman, “Gull dynamic pitch stability is controlled by wing morphing,” *Proceedings of the National Academy of Sciences*, vol. 119, no. 37, Sep. 2022. DOI: 10.1073/pnas.2204847119.
- [90] R. Finck, “USAF Stability and Control Datcom,” McDonnell Douglas Corporation Douglas Aircraft Division, Wright-Patterson Air Force Base, Ohio, Tech. Rep. AFWAL-TR-83-3048, Apr. 1978.
- [91] “Flying Qualities of Piloted Airplanes,” United States Department of Defense, Military Specification MIL-F-8785C, 1980.
- [92] A. R. Jones, O. Cetiner, and M. J. Smith, “Physics and Modeling of Large Flow Disturbances: Discrete Gust Encounters for Modern Air Vehicles,” *Annual Review of Fluid Mechanics*, vol. 54, no. 1, pp. 469–493, Jan. 2022. DOI: 10.1146/annurev-fluid-031621-085520.
- [93] E. N. Jacobs and A. Sherman, “Airfoil section characteristics as affected by variations of the Reynolds number,” NASA Langley Research Center, Hampton, VA, Technical Report NACA-TR-586, 1937, pp. 1–46.
- [94] P. Sigrest and D. J. Inman, “Effect of Spanwise Trailing Edge Gaps on Aerodynamic Performance,” in *AIAA Scitech 2020 Forum*, ser. AIAA SciTech Forum, Orlando, FL: American Institute of Aeronautics and Astronautics, Jan. 2020. DOI: 10.2514/6.2020-2007.
- [95] P. Sigrest and D. J. Inman, “Effect of Whiffing-Inspired Spanwise Trailing Edge Gaps on Aerodynamic Performance of a Wing,” Ventura, CA: Gordon Research Conference, poster, Jan. 2020.
- [96] P. Sigrest and D. J. Inman, “Avian whiffing-inspired gaps provide an alternative method for roll control,” *Bioinspiration & Biomimetics*, vol. 17, no. 4, Jun. 2022. DOI: 10.1088/1748-3190/ac7303.
- [97] P. Sigrest, N. Wu, and D. J. Inman, “Computational Validation that Whiffing-Inspired Gaps Require Less Work for Roll Control than Conventional Ailerons at High Rolling Moment Coefficients,” in *ASME Conference on Smart Materials, Adaptive Structures, and Intelligent Systems*, Dearborn, MI, USA: American Society of Mechanical Engineers, Sep. 2022. DOI: 10.1115/SMASIS2022-89275.
- [98] P. Sigrest and D. J. Inman, “Avian Whiffing-Inspired Gapped Wings as an Energy-Efficient Roll Control Surface,” Ventura, CA: Gordon Research Conference, poster, Sep. 2022.
- [99] P. Sigrest, N. Wu, and D. J. Inman, “Energy considerations and flow fields over whiffing-inspired wings,” *Bioinspiration & Biomimetics*, vol. 18, no. 4, May 2023. DOI: 10.1088/1748-3190/acd28f.

- [100] P. Sigrest and D. J. Inman, “Whiffing-inspired gapped wings alter trim and mitigate gusts,” in *Smart Structures and Materials & Nondestructive Evaluation and Health Monitoring 2023*, Long Beach, CA: SPIE, Mar. 2023. DOI: 10.1117/12.2658539.
- [101] C. Harvey, V. B. Baliga, J. C. M. Wong, D. L. Altshuler, and D. J. Inman, “Birds can transition between stable and unstable states via wing morphing,” *Nature*, vol. 603, pp. 648–653, Mar. 2022. DOI: 10.1038/s41586-022-04477-8.
- [102] *2D NACA 0012 Airfoil Validation*, Report, Aug. 2019. [Online]. Available: [turbmodels.larc.nasa.gov/naca0012\\_val.html](http://turbmodels.larc.nasa.gov/naca0012_val.html) (visited on 05/21/2020).
- [103] M. Selig, *UIUC Airfoil Coordinates Database*, Database. [Online]. Available: [m-selig.ae.illinois.edu/ads/coord\\_database.html](http://m-selig.ae.illinois.edu/ads/coord_database.html).
- [104] A. Zięba, “Effective Number of Observations and Unbiased Estimators of Variance for Autocorrelated Data - an Overview,” *Metrology and Measurement Systems*, no. 1, 2010. DOI: 10.2478/v10178-010-0001-0.
- [105] H. J. Goett and K. W. Bullivant, “Tests of NACA 0009, 0012, and 0018 Airfoils in the Full-Scale Tunnel,” NASA Langley Research Center, Langley Field, Va., Technical Report NACA-TR-647, 1938.